Departamento de Química Física
y Termodinámica Aplicada
Universidad de Córdoba

ENSAMBLAJE DE MATRICES NANOESTRUCTURADAS EN PELÍCULAS DE LANGMUIR

ASSEMBLY OF NANOSTRUCTURED MATRICES IN LANGMUIR FILMS

Tesis Doctoral

Pablo Gómez Argudo

Córdoba, Julio 2019

TITULO: *Ensamblaje de matrices nanoestructuradas en películas de Langmuir*

AUTOR: *Pablo Gómez Argudo*

Campus de Rabanales
Ctra. Nacional IV, Km. 396 A
14071 Córdoba

https://www.uco.es/ucopress/index.php/es/
ucopress@uco.es

ENSAMBLAJE DE MATRICES NANOESTRUCTURADAS EN PELÍCULAS DE LANGMUIR

LOS DIRECTORES,

Fdo.: María Teresa Martín Romero
Profesora Titular del Departamento de Química Física y Termodinámica Aplicada de la Universidad de Córdoba

Fdo.: Juan José Giner Casares
Personal Contratado dentro del Programa Ramón y Cajal

Trabajo presentado para optar al grado de Doctor en Ciencias Químicas

Fdo.: Pablo Gómez Argudo
Graduado en Ciencias Químicas

DEPARTAMENTO DE QUÍMICA FÍSICA
Y TERMODINÁMICA APLICADA
UNIVERSIDAD DE CÓRDOBA

Dª. María Teresa Pineda Rodríguez, Catedrática y Directora del Departamento de Química Física y Termodinámica Aplicada de la Universidad de Córdoba,

INFORMA:

Que el trabajo presentado como Tesis Doctoral por D. Pablo Gómez Argudo, titulado "*Ensamblaje de matrices nanoestructuradas en películas de Langmuir*", ha sido realizado en los laboratorios de este Departamento, así como en las instalaciones del Department of Chemistry and Biochemistry, Ohio State University (Columbus, EE.UU.), y reúne las condiciones exigidas según legislación vigente.

Y para que conste, firmo el presente en Córdoba a 5 de julio de 2019.

Fdo.: María Teresa Pineda Rodríguez

Mediante la defensa de esta Memoria se pretende optar a la obtención de **"Tesis con Mención Internacional"**, habida cuenta que el doctorando reúne los requisitos exigidos para tal mención:

1. Se cuenta con los informes favorables de dos doctores pertenecientes a instituciones de Enseñanza Superior de países europeos distintos al nuestro.
2. En el Tribunal, que ha de evaluar la tesis, existe un miembro de un centro de Enseñanza Superior de otro país europeo.
3. Parte de la defensa de la Memoria se realizará en la lengua oficial de otro país europeo.
4. El doctorando ha realizado una parte del trabajo experimental en las instalaciones del Department of Chemistry and Biochemistry, Ohio State University (Columbus, EE. UU.). Esta estancia, de un trimestre de duración, se ha realizado gracias a la concesión de la beca de movilidad internacional "Doctorado hacia la excelencia" de la Universidad de Córdoba.

El trabajo que engloba la presente Memoria se ha realizado durante el periodo de disfrute del proyecto “Reconocimiento molecular en matrices nanoestructuradas para el diseño de sensores biológicos” (Ref. CTQ2014-57515-C2-2-R) y al contrato Ramón y Cajal “Plasmonic substrates for biomedicine” del Dr. Juan José Giner-Casares (Ref. RyC-2014-14956), financiados por el Ministerio de Economía y Competitividad de España.

MARÍA TERESA MARTÍN ROMERO, Profesora Titular del Departamento de Química Física y Termodinámica Aplicada de la Universidad de Córdoba,

INFORMA:

Que el trabajo presentado como Tesis Doctoral por D. Pablo Gómez Argudo, titulado "Ensamblaje de matrices nanoestructuradas en películas de Langmuir", ha sido realizado bajo mi dirección en los laboratorios de este departamento y reúne las condiciones exigidas según la legislación vigente.

Y para que conste, firmo el presente en Córdoba, a 5 de julio de 2019,

María Teresa Martín Romero

JUAN JOSÉ GINER CASARES, Personal Contratado dentro del Programa Ramón y Cajal, en el Departamento de Química Física y Termodinámica Aplicada de la Universidad de Córdoba,

INFORMA:

Que el trabajo presentado como Tesis Doctoral por D. Pablo Gómez Argudo, titulado "Ensamblaje de matrices nanoestructuradas en películas de Langmuir", ha sido realizado bajo mi dirección en los laboratorios de este departamento y reúne las condiciones exigidas según la legislación vigente.

Y para que conste, firmo el presente en Córdoba, a 5 de julio de 2019,

Juan José Giner Casares

A mis directores, MariTere y Juanjo, por darme a ciegas la oportunidad de hacer esta Tesis, aguantando mis rebuscadas y poco exageradas frases. Muchas gracias por vuestro apoyo, paciencia y confianza.

Gracias a todas las personas del Departamento de Química Física, especialmente a todos los postdoc, doctorandos y demás estudiantes con los que he compartido trabajo y me han ayudado tanto en el laboratorio como fuera de él, las buenas cenas y cervezas nunca se olvidan.

A los amigos que me han tratado como si no hubiera distancia, saludándome como el primer día aun estando a 400 km.

A toda mi familia. A mis tíos por demostrarme que las bellas artes y la ciencia no están separadas; a mis abuelas por demostrar que tener la cabeza bien alta es más que posible y quejarse la mayor parte de las veces es sólo buscar escusas y a mis padres por dejarme mi espacio, entenderme en la forma de enfocar las cosas y nunca en todo este tiempo haber dudado, y menos haber dejado de pensar en mí.

Finalmente, a Marta por apoyarme en todo momento, venir siempre que ha podido y aguantar todo y más de una persona no muy comunicativa. No tengo palabras ni espacio para agradecer todo lo que debería.

"I will do this. I am born in this moment, and if I fail, I will die in this moment."

-Raistlin Majere, "The Soulforge"

A Marcelino, mi abuelo

Índice

Objetivos / *Aims* **1**

Capítulo I: Introducción / *Chapter I: Introduction* **5**

1. Monocapas de Langmuir 7
2. Compuestos objeto de estudio 14
   2.1. Péptidos 15
   2.2. Quantum dots 19
   2.3. Bases nitrogenadas 25
3. Bibliografía 31

Capítulo II: Técnicas experimentales / *Chapter II Experimental techniques* **43**

1. Técnicas de formación y caracterización de monocapas en la interfase aire-agua 45
   1.1. Balanza de Langmuir 45
   1.2. Espectroscopía de reflexión UV-Visible 46
   1.3. Microscopía de ángulo Brewster (BAM) 50
2. Técnicas de formación y caracterización de monocapas en la interfase aire-sólido 54
   2.1. Transferencia de monocapas a sustratos sólidos 54
   2.2. Espectroscopía de absorción UV-Visible 56
   2.3. Dicroísmo circular (CD) 58
3. Técnicas de caracterización en medio líquido 59
   3.1. Dispersión de luz dinámica (DLS) 59
4. Tratamientos de datos 61
5. Bibliografía 64

Capítulo III: Publicaciones / *Chapter III: Publications* 67

Artículo I: *Unravelling the 2D self-assembly of dipepties at fluid interfaces* ...69

Supporting Information 90

Artículo II: *Optimization of aminoacid secuence of Fmoc-dipeptides for interaction with lipid membranes* 127

Artículo III: *Subtle chemical modification for enrichment of Fmoc-amino acid at phospholipid interface* 157

Supporting Information 187

Artículo IV: *Surface-active fluorinated quantum dots for enhanced cellular uptak*e 189

Supporting Information 204

Artículo V: *Fluorinated CdSe/ZnS quantum dots: Interaction with cell membrane* 222

Artículo VI: *Folding of cytosine-based nucleolipid monolayer by guanine recognition at the air-water interface* 239

Supporting Information 267

Conclusiones / *Conclusions* 275

Apéndice / *Appendix* 279

Objetivos

Aims

OBJETIVOS

Los trabajos desarrollados en la presente Memoria de Tesis Doctoral se encuadran en la línea de investigación "*Organización Molecular en Películas Superficiales*" del grupo FQM 204 de la Universidad de Córdoba. Los objetivos globales que se han marcado son:

1. Preparación de películas delgadas de materiales orgánicos (lípidos, dipéptidos y nucleolípido) y caracterización de interacciones entre dichos sistemas y diversos compuestos como son híbridos inorgánicos (quantum dots) o bases nitrogenadas (guanina) en la interfase aire-agua, así como su posterior transferencia a soportes sólidos mediante las técnicas de Langmuir-Blodgett y Langmuir-Schaefer.

2. Planificación y diseño de mecanismos de interacción y ensamblaje de compuestos mencionados en el punto anterior, en función de sus propiedades fisicoquímica, con objeto de desarrollar una determinada estructura deseada.

3. Análisis de las organizaciones moleculares formadas en sistemas bidimensionales 2D, características para cada compuesto, mediante diferentes técnicas de tipo óptico, tanto en la interfase aire-agua como aire-sólido.

4. Estudio del impacto de los distintos compuestos orgánicos e inorgánicos sobre superficies lipídicas construidas en la interfase aire-agua y que actúan como modelo de membranas celulares, y sus posibles aplicaciones biológicas.

AIMS

The work described in this Report presented as Doctoral Thesis belongs to the research line "Molecular Organization in Thin Films" within the group FQM-204 (Universidad de Córdoba). The main goals of this research were as follows:

1. To prepare thin films of organic materials (lipids, dipeptides and nucleolipid) and to characterize the interaction among them and other inorganic hybrids (quantum dots) or nitrogenous bases (guanine) at the air-water interface. Also, their transference to solid supports by Langmuir-Blodgett and Langmuir-Schaefer techniques has been designed.

2. To plan and design several interaction and assembly mechanisms, between the compounds mentioned above, depending on their physicochemical properties, leading to a determinate structure.

3. To analyse the 2D bidimensional systems obtained, due to the specific molecular organization processes for each compound, using different optic techniques at the air-water and air-solid interface.

4. To study the effect of diverse organic and inorganic compounds on lipid surfaces, at the air-water interface, that mimic biological cellular membranes to fathom their biological applications.

Capítulo I

Introducción

Chapter I

Introduction

1. MONOCAPAS DE LANGMUIR

Monocapas en la interfase aire-agua

El estudio de las monocapas en la interfase aire-agua comenzó en 1765 con Benjamin Franklin (1706-1790), tras esparcir una cucharada de aceite en la superficie de un estanque en Clapham Common (Londres)[1]. Allí pudo hacer dos observaciones. La primera fue que el aceite se extendió por la superficie abarcando un área de ~2000 m^2. La segunda fue que, una vez alcanzado este estado, el aceite dejo de extenderse. Haciendo los cálculos hoy en día, y partiendo de que el volumen de una cuchara es de ~5 cm^3, se puede predecir que el espesor de la capa era de 2.5 nm, valor correspondiente a una monocapa insoluble de una molécula de espesor, la primera formada y estudiada. Ya a finales del s.XIX, en 1891, Agnes Pockels (1862-1935) con objetos caseros en la cocina familiar, descubrió como manipular capas de aceite sobre agua, desarrollando la primera balanza o *trough*[2]. Tras ello, escribió a Lord Rayleigh (1842-1919), Ilustración 1, lo que llevó a este último en 1899 a sugerir que las capas eran de una molécula de espesor, origen de los estudios de monocapas insolubles[3].

MY LORD,—Will you kindly excuse my venturing to trouble you with a German letter on a scientific subject? Having heard of the fruitful researches carried on by you last year on the hitherto little understood properties of water surfaces, I thought it might interest you to know of my own observations on the subject. For various reasons I am not in a position to publish them in scientific periodicals, and I therefore adopt this means of communicating to you the most important of them.

First, I will describe a simple method, which I have employed for several years, for increasing or diminishing the surface of a liquid in any proportion, by which its purity may be altered at pleasure.

A rectangular tin trough, 70 cm. long, 5 cm. wide, 2 cm. high, is filled with water to the brim, and a strip of tin about 1½ cm. wide laid across it perpendicular to its length, so that the under side of the strip is in contact with the surface of the water, and divides it into two halves. By shifting this partition to the right or the left, the surface on either side can be lengthened or shortened in any proportion, and the amount of the displacement may be read off on a scale held along the front of the trough.

Ilustración 1: Extracto de la carta de Agnes Pockels a Lord Rayleigh.

Aunque muchos continuaron el trabajo de Pockels, Irving Langmuir (1881-1957) fue el más destacado, desarrollando su método experimental al crear lo que ahora es conocido como balanza de Langmuir, Ilustración 2. Con ella pudo medir la tensión superficial de diversos fluidos, así como la presión superficial de distintas monocapas sobre superficies líquidas. En 1917, Langmuir publicó la determinación de las interacciones de van der Waals y describió la naturaleza anfifílica entre las moléculas, concluyendo que las estructuras eran efectivamente monocapas[4]. Además, determinó las áreas de distintas moléculas a partir de la configuración molecular en la interfase, donde el grupo funcional polar estaba inmerso en el agua y una cadena larga no polar estaba colocada perpendicularmente respecto a la superficie del agua a elevadas presiones superficiales; investigaciones que le llevaron a ser Premio Nobel de Química en 1932[5].

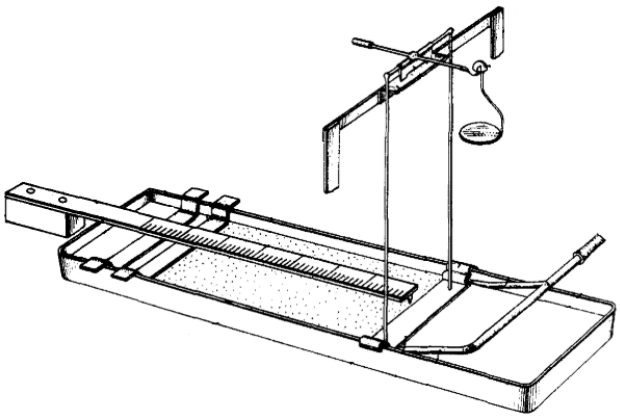

Ilustración 2: Dibujo de la primera balanza diseñada por Langmuir[4].

Mientras, Katherine Blodgett (1898-1979), colaboradora de Langmuir[6], descubrió durante un experimento con estearato cálcico que se pueden depositar monocapas en sustratos sólidos tras sucesivas inmersiones del mismo en interfases acuosas con lípidos depositados, proceso al que se llamó Langmuir-Blodgett (LB)[7,8]. Este proceso fue aplicado en el recubrimiento de cristales para el diseño de cristales anti-reflectantes[9] y, actualmente, es una de las técnicas más utilizadas para la

construcción de dispositivos supramoleculares con aplicaciones en todos los campos de la química[10]. Al poco tiempo, Vincent Schaefer (1906-1993), químico y meteorólogo, que trabajaba en el laboratorio de Langmuir y Blodgett como técnico e investigador en el diseño de equipos desde 1929, tras previas publicaciones en técnicas de análisis de superficies, microscopía electrónica o polarización con aplicaciones en proteínas, partículas submicroscópicas o incluso monocapas, publicó en 1938 junto a Langmuir la técnica que sería nombrada Langmuir-Schaefer (LS)[11]. En ella, establecieron el control de la organización de la monocapa al ser transferida a un sustrato en función de los grupos en contacto con el sustrato, método que usa como partida la técnica Langmuir-Blodgett, pero con una gran diferencia, mientras que en LB el sustrato contacta con la interfase de forma perpendicular o *vertical lifting*, en LS lo hace de forma paralela a la misma u *horizontal touching*.

Formación y caracterización en la interfase aire-agua

Para formar una de estas monocapas, las moléculas utilizadas deben poseer, en principio, un carácter anfifílico. La parte hidrofóbica debe ser lo suficientemente larga para hacer la molécula insoluble en la subfase, normalmente agua; mientras que la parte hidrofílica debe tener una atracción tal que esta región polar se mantenga en la superficie del agua, evitando el apilamiento de las moléculas entre ellas mismas. Debido a estos grupos polares y apolares como son ácidos, alcoholes o aminas o cadenas alifáticas, respectivamente, las moléculas son capas de colocarse en la superficie acuosa de forma estable, formando una monocapa insoluble o monocapa de Langmuir[12–14]. Para su formación, el anfífilo puede ser esparcido o diseminado bien en forma de cristal sobre la superficie, esparciéndose espontáneamente hasta llegar a un punto de equilibrio; o tras disolverse en un disolvente volátil, pero insoluble respecto a la subfase y con un coeficiente de dispersión positivo[15], se esparce espontáneamente hasta llegar a un punto de equilibrio. De esta manera, el disolvente se evapora y la monocapa es formada con una estructura que permita la situación energética más favorable.

En esta situación, la tensión superficial del compuesto en la interfase, γ, disminuye respecto a la tensión superficial en presencia única de agua limpia o γ_0. El cambio en la presión superficial, π, viene dado por:

$$\pi = \gamma_0 - \gamma \quad (1)$$

Estos cambios en la tensión superficial pueden ser medidos mediante distintas técnicas como capilaridad, gota pendiente o presión máxima de burbuja, entre otros. En nuestro caso, y el más usado para este tipo de sistemas, es el método Wilhelmy, donde una placa conocida es suspendida de una balanza mientras está en contacto con la superficie del líquido, midiéndose la fuerza vertical necesaria para levantarla[16]. Si se reduce el espacio entre las moléculas en la interfase aire-agua, se da lugar a la aparición de ciertas fuerzas de repulsión entre ellas, alterándose la presión superficial[12]. La medición de la variación de la presión superficial de las moléculas frente al área, también denominadas isotermas presión superficial-área (π–A) es uno de los mayores indicadores en cuanto a las propiedades de la monocapa se refiere, para la que se utilizan balanzas de Langmuir[17] (detalladas en el *Capítulo II*). Esta área no es el área geométrica de la superficie ocupada ni el área de una molécula, si no el área de la balanza $\hat{A}_M$, entre el número de moléculas en la superficie N_M, dando el área por molécula A:

$$A = \frac{\hat{A}_M}{N_M} \quad (2)$$

Una isoterma presión superficial-área, análoga bidimensionalmente a una isoterma presión-volumen, muestra las 4 principales fases de una monocapa[12,18], si bien no siempre distinguibles, como se representa en la Figura 1:

- Fase gaseosa, *G*. El área por molécula es elevada y por tanto las interacciones intermoleculares son mínimas, al estar las moléculas muy separadas entre sí. Esta fase es también denominada gas bidimensional y

está caracterizada por valores de presión superficial bajos. La ecuación de estado para monocapas en fase gas es reminiscente de la ecuación de gases ideales en tres dimensiones:

$$\pi(A - A_0) = N_M kT \quad (3)$$

donde *Π* es la presión superficial, *A* y A_0 el área final e inicial de la balanza, N_M el número de moléculas en la superficie, *k* es la constante de Boltzmann y *T* la temperatura.

- Fase de líquido expandido, *Le* o L_1. Es característica de moléculas que poseen algún impedimento de empaquetamiento o bajas atracciones entre las cadenas apolares, desordenadas como en un líquido. La presión superficial aumenta ligeramente dando lugar a una fase líquida muy compresible. Las isotermas pueden ser descritas como una ecuación de estado similar a la ecuación de van der Waals:

$$(\pi - \pi_0)(A - A_0) = N_M kT \quad (4)$$

siendo π_0 y A_0 constantes. Entre la fase *G* y *Le* puede existir una transición de fase llamada T_1, donde coexisten ambas.

- Fase de líquido condensado, *Lc* o L_2. Bajo compresión y debido a la aún mayor cercanía entre las moléculas, la monocapa forma una estructura más compacta donde las cadenas apolares se empiezan a colocar buscando el mínimo de energía. Su estructura no está claramente definida al existir modelos que la presentan como una fase algo desordenada, imitando ligeramente a un líquido, mientras que otros la presentan como una estructura sólida donde las cadenas están inclinadas ligeramente respecto de la perpendicular[19]. Entre este sistema casi ordenado y la fase de *Le* puede existir otra transición de fase llamada T_2.

– Fase sólida, *S*. Región de la isoterma de mayor compresión donde la estructura totalmente compactada posee un ordenamiento máximo. La parte hidrofílica de la molécula está en contacto con la superficie acuosa mientras que las cadenas apolares se colocan perpendicularmente a la interfase. Por ello, esta estructura se caracteriza por poseer un área por molécula que sólo se ve afectada por la cabeza polar de la molécula esparcida y no por la longitud de la cadena, denominada área límite y corresponde al valor obtenido extrapolando la pendiente de la fase sólida a valores de presión cero. Por otro lado, si continuásemos comprimiendo la monocapa se alcanzaría la presión de colapso, o presión a la cual la monocapa pierde su estabilidad.

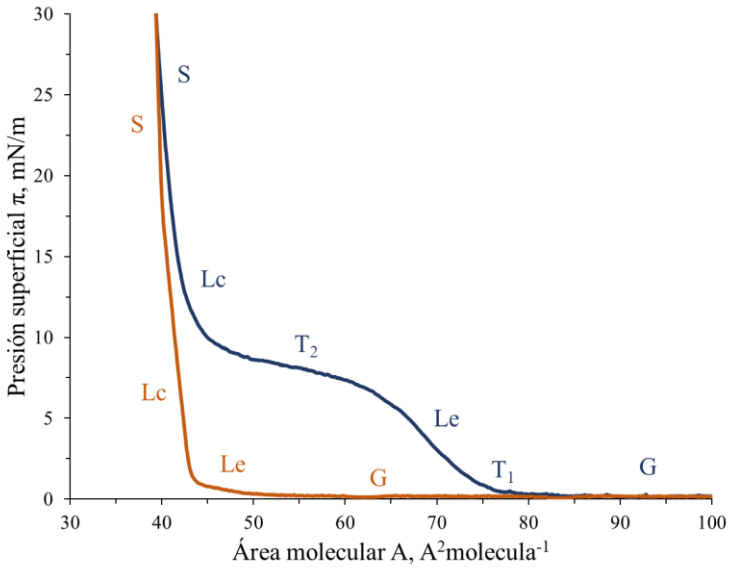

Figura 1: Esquema de isotermas π—A que muestran dos tipos de comportamientos comunes de compuestos anfifílicos con sus fases características: gaseosa (G), líquido expandido (Le), líquidocondensado (Lc), sólida (*S*) y las fases de transición (T_1 y T_2).

Técnicas de caracterización

Debido al aumento en la precisión y sensibilidad de las técnicas desarrolladas hasta la actualidad, es posible medir de forma directa la estructura de una monocapa a cualquier punto de compresión, complementando las originarias medidas indirectas obtenidas de las isotermas π–A, la viscosidad o el potencial superficial[20]. En la Tabla 1 se recogen técnicas instrumentales disponibles que permiten la caracterización de estas estructuras bidimensionales. Algunas de ellas sólo pueden ser realizadas sobre monocapas depositadas en sustratos sólidos, proceso detallado en el *Capítulo II*, y que nos dará información posteriormente relacionada con la monocapa en la interfase aire-agua.

Tabla 1: Técnicas de caracterización de monocapas preparadas en la interfase aire-líquido y aire sólido.

Técnicas	Parámetros	Información
Presión superficial	π frente a A	Área por molécula, presión de colapso, estado de la monocapa
Potencial superficial	ΔV frente a A	Dipolos superficiales, orientación y/o conformación de los grupos
Viscosidad superficial	K^{σ}	Cambios de viscosidad superficial de cizalla
Difracción de rayos X/neutrones	Reflectividad	Ángulo de inclinación de cadenas alifáticas, grosor y densidad electrónica, estequiometría
Difracción de electrones	Interferencia electrónica	Estructuras en el plano de monocapas en soporte sólido
Generación de segundo armónico	Polarización de la susceptibilidad del segundo armónico	Valor medio del ángulo entre el eje de la molécula y la normal a la interfase
Reflexión UV-Vis	ΔR	Densidad, orientación y agregación de las moléculas cromóforo

Espectroscopía FTIR/FTIR-RAS	Absorción/Reflexión	Orientación media de las cadenas alifáticas
Espectroscopía ATR/GIR	Absorción/Reflexión	Orientación molecular sobre sustratos sólidos
Elipsometría	Ángulo de polarización de radiación reflejada	Espesor e índice de refracción de monocapa, coexistencia de fases
Microscopía electrónica	Reflectividad	Sombras que describen la rugosidad de la superficie
Microscopía de fluorescencia	Fluorescencia de la monocapa o molécula sonda	Estructura de la monocapa y/o orientación de las fases
Microscopía de ángulo Brewster, BAM	Reflectividad	Dominios estructurales
Microscopía de barrido STM/AFM	Fuerzas entre punta del equipo y monocapa	Superficie de monocapas en sustratos sólidos

2. COMPUESTOS OBJETO DE ESTUDIO

Como se ha podido ver en la sección 1, el estudio de todo tipo de películas delgadas, capas y monocapas formadas tanto en la interfase aire-agua como en aire-sólido, es de vital importancia de cara a obtener información que nos permita el desarrollo de nuevas estructuras aplicables en el campo de la química, la ingeniería o la medicina, entre otras[21–23]. Conociendo su estructura y origen, dichas películas pueden ser modificadas con objeto de mejorar, alterar o intensificar propiedades específicas que nos permitan alcanzar metas anteriormente imposibles.

Un ejemplo de ello podrían ser los polímeros, macromoléculas formadas por la unión de monómeros mediante enlaces covalentes. Estas cadenas pueden unirse entre sí por fuerzas de van der Waals, puentes de hidrógeno o interacciones

hidrofóbicas que dan lugar a sus futuras aplicaciones ya sean de origen natural, como la celulosa, la seda o el mismo ADN[24,25], o sintéticas, como el polietileno, el propileno o el nailon[26]. Mediante el estudio y alteración de la estructura, pueden llegar a formarse todo tipo de estructuras con infinidad de aplicaciones, ya sea en el campo aeroespacial, del deporte, electrónica e imagen, seguridad, o en la química verde[27].

A continuación, se describe la base de tres tipos de compuestos utilizados como objeto de estudio a lo largo de esta tesis, cada uno de ellos seleccionados por la atracción de una característica determinada de las muchas que disponen. De esta manera: los dipéptidos por su propiedad de auto-ensamblaje; los quantum dots por su uso como marcadores en bioimagen y su aplicación en sistemas vivos; y las bases nitrogenadas por su reconocimiento molecular característico del ARN y del ADN.

2.1. PÉPTIDOS

Estructura e historia

Los péptidos son biomoléculas formadas por la unión de aminoácidos, mediante enlaces peptídicos entre los grupos amino (-NH_2) y carboxilo (-COOH) terminales[28]. En función del número de aminoácidos, los péptidos pueden dividirse en: oligopéptidos, cuando están formados por menos de 10 monómeros (dipéptido, tripéptido, etc.); polipéptidos, cuando contienen entre 10 y 100; o proteínas, cuando contienen más de 100 aminoácidos, como se observa en la Figura 2.

En 1901, Ernest Fourneau (1872-1949) y Emil Fischer (1852-1919) sintetizaron la glicilglicina[29], el primer dipéptido sintético, a partir de la hidrólisis de la dicetopiperazina de glicina, lo que llevó a Fischer a la introducción del término "péptido" en 1902, durante el 14º encuentro de científicos y físicos alemanes en Karlsbad (Alemania)[30]. Entre 1902 y 1907 aparecieron de la mano de Curtius (1857-1928)[31,32], Gumlich (1877-1957)[33] y Müller[34] los primeros procesos de síntesis de péptidos a partir de azidas, pero con ciertos problemas de estabilidad y de una

longitud máxima de 18 aminoácidos. Ya en 1932, Max Bergmann (1886-1944) y Leonidas Zervas (1902-1980)[35] descubrieron el uso del grupo carbobenzoxi (Cbz, ahora "Z" en honor a Zervas) como protector amino, lo que desarrolló rápidamente el campo a partir de 1950. A partir de ese momento, la síntesis de todo tipo de péptidos no ha parado de ser desarrollada, siendo máxima a partir de 1957, con el descubrimiento del grupo protector ter-butiloxicarbonil (Boc) por Akabori (1900-1992)[36,37].

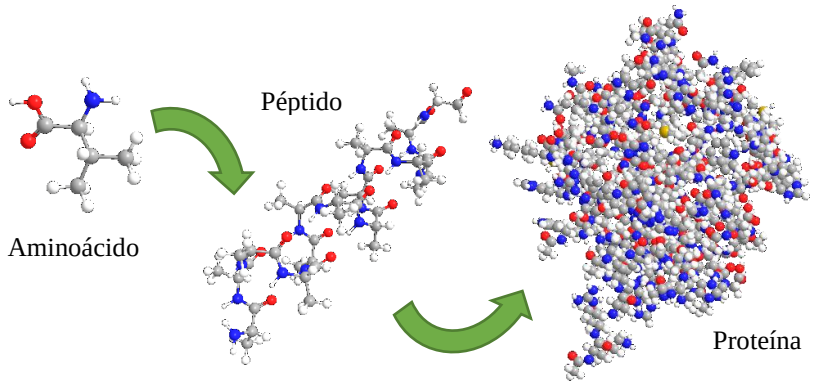

Figura 2: Esquema de formación de proteínas a partir de aminoácidos.

Debido a millones de posibles configuraciones, los péptidos pueden poseer múltiples propiedades y, por ende, aplicaciones. De acuerdo con el *Handbook of Biologically Active Peptides* pueden ser divididos por su fuente (bacterial, cáncer, fúngica, etc) o por su función, más relevante en nuestro caso, como son estructural, reconocimiento celular o marcadora, entre otras. Junto a poderse sintetizar cualquier tipo de péptido, se puede obtener cualquier antígeno o marcador con una estructura única que a su vez sea capaz de llevar a cabo interacciones específicas y únicas con la molécula deseada u objetivo. Adicionalmente, son fáciles de identificar y caracterizar, ya sea en su estructura plegada como tras procesos de fragmentación con técnicas como espectrometría de masas. Todas estas variantes han permitido la aplicación de estos compuestos en multitud de áreas, tales como materiales

(catálisis)[28,38–40], alimentaria (aditivos)[41], cosmética (envejecimiento)[42] o biomédica, siendo esta última el campo estrella por sus aplicaciones estructurales, antioxidantes, inmunoterapéuticas, citomoduladoras, hormonales o de penetración celular.

En particular, como ejemplo de ello, es su aplicación en bioingeniería, donde se usan en la creación de tejidos artificiales regenerativos[19]. Gracias a los péptidos se puede reconstruir la matriz extracelular que permite a las células volver a crecer. Los más utilizados para esta función son hidrogeles peptídicos auto-ensamblados, formados por cadenas cortas anfipáticas, capaces de formar estructuras nano, ya sean fibrilares, tubulares, vesiculares o simplemente de partícula esférica[43]. Por otro lado, por su propiedad de penetración celular, determinados péptidos cortos catiónicos y/o anfifílicos pueden conseguir pasar a través de la membrana celular y nuclear[43], lo que permite su uso como transportadores o sensores vitro incluso junto a otro tipo de estructuras como *quantum dots*, detectados por fluorescencia[44]. En inmunoterapia, se usan tanto para mejorar las técnicas ya existentes como para el desarrollo de nuevas. Esto es debido a su fácil síntesis y uso junto a sus bajos efectos secundarios[45]. En los últimos años, se están estudiando como inhibidores de las proteínas cancerígenas, actuando como antagonistas, es decir, uniéndose a moléculas productoras de hormonas o *LHRH* relacionadas con dicha enfermedad[44]. Otro ejemplo es su uso como vacuna. Por su elevada selectividad permiten la detección de antígenos, en lugar de medicamentos ya obsoletos por la resistencia de los microorganismos a los mismos[46]. Además, determinados péptidos pueden actuar contra virus como el VIH, el Dengue o la gripe a la vez que actúan sobre infecciones bacterianas y/o virales[47].

Debido a la gran variedad de aminoácidos que existen, en función de la distinta longitud y ordenación en la cadena que forman, y sus diversas estructuras de plegamiento, es posible formar una inmensa variedad de péptidos. La presente Memoria se centrará en péptidos de cadena corta, en particular dipéptidos.

Dipéptidos

Un dipéptido, como su propio nombre indica, es una molécula formada mediante la unión de dos aminoácidos por un único enlace peptídico. Sobre esta base, sus funciones pueden ser consideradas desde dos puntos de vista, como un derivado de aminoácido o como un péptido por sí mismo. Es decir, sus propiedades fisicoquímicas son distintas al tener distintos aminoácidos en la cadena, pero sus propiedades fisiológicas en los organismos vivos son las mismas tras degradarse el enlace peptídico[48]. Un ejemplo podría ser la solubilidad en agua. El aminoácido Alanina (Ala) posee una solubilidad de 89 g/L. Si se une a la Tirosina (Tyr), casi insoluble, forma el dipéptido Ala-Tyr con valores de 14 g/L. Sin embargo, si se une a la glutamina (Gln) de solubilidad 36 g/L, se obtiene el dipéptido Ala-Gln con un máximo de solubilidad de 586 g/L. Estos cambios hacen que sea imposible conocer, previo análisis, las propiedades de todos los dipéptidos posibles, ya que incluso algunos poseen propiedades únicas que no están presentes en sus aminoácidos precursores, como es el auto-ensamblaje.

El auto-ensamblaje es un proceso espontáneo de formación de estructuras ordenadas por interacciones no covalentes como son van der Waals, enlace de hidrógeno, π–π, hidrofóbicas o electrostáticas[49,50], que se ven afectadas por el disolvente o medio donde se producen. Por ello, gracias a sintones específicos, se puede llevar a cabo el diseño estructural de dipéptidos que permitan este tipo de interacciones. Los dipéptidos auto-ensamblables están presentes en la naturaleza dando lugar tanto a nano- como a microestructuras, Figura 3. Casi siempre en forma de hidrogeles[51], estos compuestos son de vital importancia en la biología para la formación o rotura de membranas lipídicas[52], plegamiento del ADN o de proteínas[53]. Debido a sus procesos de reconocimiento molecular y a su biocompatibilidad y elevada hidratación, hacen que estos hidrogeles auto-ensamblables puedan ser utilizados en otros campos como en la bioingeniería para recuperación de tejidos[54,55], para actuar como centros de crecimiento para fibras o nervios, en la liberación

controlada de fármacos[56], mediante cambios de temperatura, pH o interacciones, o crecimiento celular[57] al imitar medios biológicos.

En definitiva, los péptidos en general y los dipéptidos en particular están considerados como la nueva generación de compuestos reguladores biológicamente activos y que, a pesar de pequeños obstáculos en su síntesis y estabilidad, no pueden dejarse de lado debido a sus innumerables ventajas.

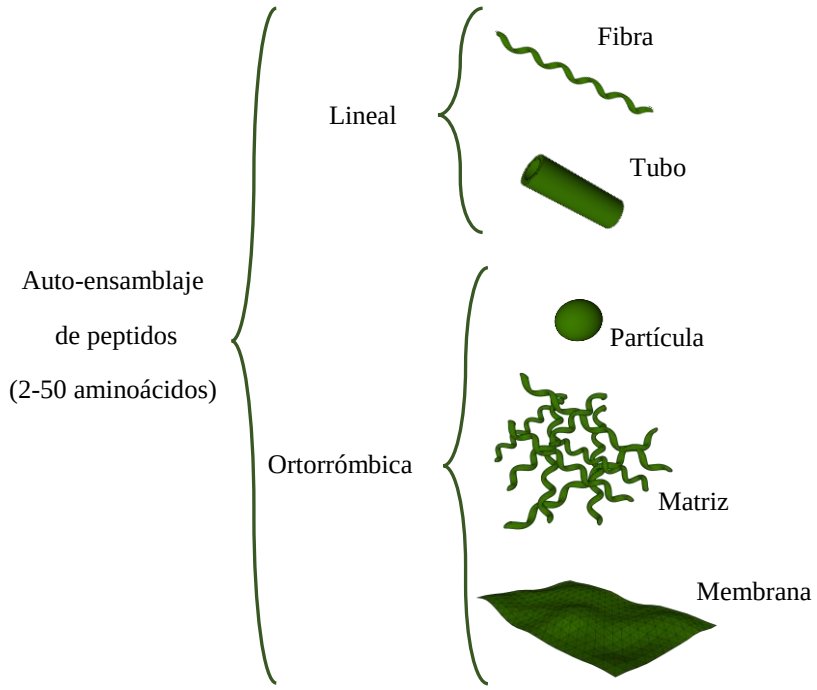

Figura 3: Esquema de topologías de autoensamblaje para nanomateriales.

2.2. QUANTUM DOTS

Origen y propiedades

Los sólidos inorgánicos cristalinos pueden ser divididos desde un punto de vista electrónico en función de su banda prohibida, E_g, en tres grupos ampliamente conocidos: metales (E_g ~ 0.1 eV), semiconductores (E_g ~ 0.5 a 3.5 eV) y aislantes (E_g

> ~ 4 eV), Figura 4.a. A su vez, en los sólidos semiconductores, el salto de banda puede ser directo o indirecto, dependiendo del vector de onda *k* de los electrones al pasar éstos de la banda de valencia o HOMO al LUMO o banda de conducción, Figura 4.b. Así, los semiconductores más iónicos tenderán a ser materiales de salto de banda directo y tendrán mejores aplicaciones en aplicaciones de emisión de luz.

De entre todos los compuestos de la tabla periódica, únicamente la Sílice y el Germanio poseen estas propiedades semiconductoras en el grupo IV[58]. Por ello, a partir de mezclas III-V como el GaN, GaP, GaAs, InP o InAs o II-VI como ZnO, ZnS, CdS, CdSe o CdTe, se pueden obtener propiedades similares, pudiéndose llegar a utilizar mezclas de elementos IV-VI e incluso I-III-VI_2[59]. Y es que estos sólidos inorgánicos cristalinos, en el rango de los nanómetros, dan lugar a partículas semiconductoras con propiedades ópticas y electrónicas únicas, denominadas *quantum dots* (QDs)[60].

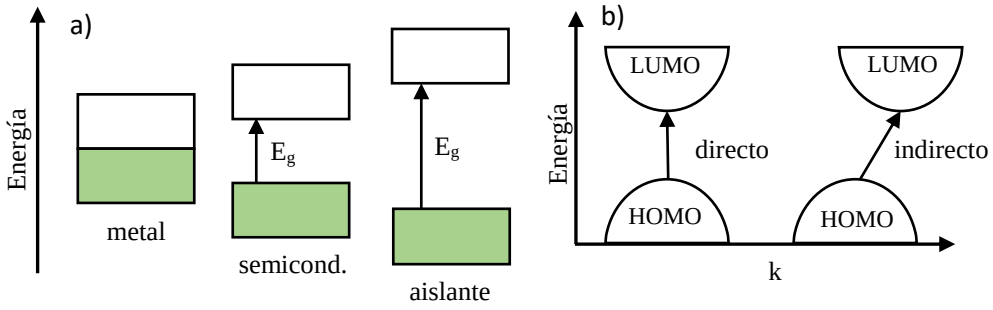

Figura 4: a) diagrama de niveles energéticos para cada sólido inorgánico. La forma coloreada representa la banda de valencia y la vacía la banda de conducción. b) Estructura de bandas de semiconductores. Las flechas representan la transición de menor energía entre ambas bandas[61].

En 1981 Alexey I. Ekimov (1945), físico ruso premiado en 2006 por la Sociedad Americana de Óptica, descubrió los nanocristales semiconductores conocidos como puntos cuánticos o QDs[62]. Más tarde, en 1984, Luis Brus (1943) estudió la relación existente entre su tamaño y el salto de banda mediante el modelo de partícula en una

esfera, prediciendo que materiales con una E_g pequeña deben alcanzar un determinado tamaño cristalino, que varía en función del material, antes de presentar procesos de absorción[63]. Finalmente, Christopher B. Murray (1967) en 1993 descubrió un método de síntesis de QDs basados en mezclas II-VI mediante un proceso *top-down*[64]. Consiguió sintetizar cantidades macroscópicas monodispersas de *quantum dots*, en especial basados en Cd, a través de un único proceso de reacción con un tamaño deseado entre ~12 y 115 Å de diámetro. Desde este momento, el estudio en este tipo de materiales ha vivido un gran auge hasta nuestros días.

Al ser cero dimensionales, estas partículas semiconductoras poseen un número determinado de electrones y unos niveles de energía discretos cuantizados en su densidad de estados. Un efecto claro de ello es el efecto del volumen, representado en la Figura 5, donde pequeñas variaciones en el tamaño dan lugar a cambios drásticos en sus propiedades ópticas de absorción, energías de excitación y efectos de recombinación hueco-electrón[65].

No sólo el tamaño sino factores como la forma, defectos, impurezas o cristalinidad son determinantes en sus propiedades. Además, estas propiedades se verán afectadas por los efectos de confinamiento cuántico y la estructura superficial del QD, debido a su elevado ratio superficie/volumen. Para este tipo de partículas, la superficie de la partícula suele estar formada por enlaces libres que pueden actuar como trampas electrón/hueco o agente oxidante/reductor. Una forma de controlar estos procesos, a la vez de eliminar la toxicidad presente en compuestos como el CdX, es pasivándola, saturando todos los enlaces libres[66] y confinando internamente, desde un punto de vista cuántico, cualquier salto de banda. Además, el uso de cationes como pasivadores de aniones libres permite la formación de radicales que dan lugar a una banda de estados superficiales bajo la banda de conducción[67]. Todos esto permite el diseño de recubrimientos estables que facilitará, a su vez, diseñar QDs para el reconocimiento específico. Una de las formas más utilizadas para pasivar es a partir de moléculas orgánicas que aportan propiedades coloidales a la vez que permiten la bio-conjugación[68]. La mayor parte de los ligandos usados son los fosfenos[64] (como

el óxido de tri-n-octil fosfeno o TOPO) o los tioles[69] (-SH). Mediante moléculas inorgánicas, donde el rendimiento se ve afectado por el grosor del recubrimiento, éstos se realizan con moléculas de elevado E_g tanto de forma epitaxial[70], formando QDs como el CdSe/ZnSe[71], o de forma no epitaxial[72], con recubrimientos de silica[73]. A pesar de todo, estos recubrimientos poseen desventajas como impedimento estérico o distorsiones en la forma y tamaño de la superficie, además, pueden llegar a hacerlos foto-inestables, por lo que se han de seguir desarrollando nuevos compuestos.

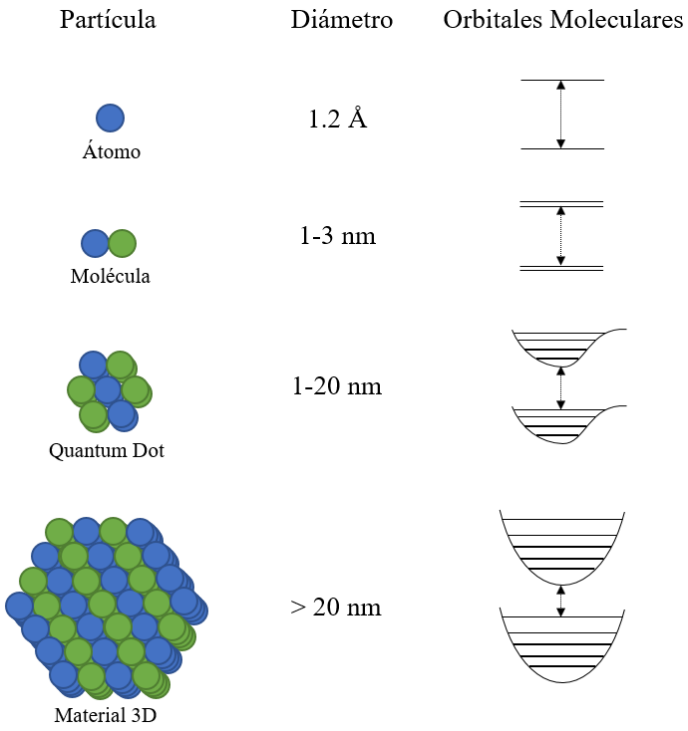

Figura 5: Variación de E_g en función del tamaño de partícula[58].

Aplicaciones en la última década

Los *quantum dots* pueden ser aplicados en múltiples campos. Así, por ejemplo, en la última década están siendo relevantes para la fabricación de "lo último" en dispositivos electroluminiscentes, diodos emisores de luz o QLEDs[74]. Esto es debido

a que su anchura de emisión a la altura media del pico de emisión es de 20-30 nm, siendo ideal para imágenes de alta resolución que mejora a cualquier material orgánico, con valores >50 nm. Más estables térmicamente y con mayor tiempo de vida y eficiencia, estos compuestos inorgánicos pueden producir emisiones de infrarrojo menores a 1μm y con una misma composición, pueden emitir a distintas longitudes de onda al alterarse únicamente el tamaño. Esto hace que sean el futuro, dejando atrás a los leds orgánicos o OLEDs[75]. En la fabricación de células solares, la eficiencia de compuestos inorgánicos es superior a las orgánicas o híbridas en cuanto a movilidad electrónica se refiere y esto influye positivamente, ya que el funcionamiento de célula solar se caracteriza por 4 procesos: la absorción de luz y formación de un excitón, la difusión de este, la separación de sus cargas y el transporte de éstas. Todo ello hace de los QDs sean ideales junto a otros compuestos como nanotubos, buenos transportadores de huecos, al actuar como dadores electrónicos en estado excitado[76]. Asimismo, los QDs están siendo empleados es en la disminución energética de luz, donde la luz emitida posee valores de frecuencia menores a los incidentes. Además, los *quantum dots* son usados en lugar de fotoconversores convencionales por su elevado rango de emisión, su elevada ventana de absorción y su alto rendimiento cuántico[77].

Todas estas aplicaciones no son nada comparadas con una de las más relevantes y clave en los trabajos presentados en esta Memoria: bioimagen o seguimiento de marcadores en sistemas vivos. A día de hoy, la resonancia magnética[78] u óptica[79] son técnicas utilizadas para el seguimiento de este tipo de partículas en función del análisis a realizar, ejemplos de ello se muestran en la Tabla 2. Tradicionalmente, en estas técnicas de detección y/o seguimiento se han usado colorantes, aunque presentan desventajas como inestabilidad bajo irradiación, estrechas ventanas de excitación que dificultan el uso de varios colorantes, alteraciones por cambios de pH o interferencias con las propias células. Por ello, los QDs son cada vez más utilizados por sus elevados coeficientes de extinción, elevados campos quánticos, fácil control de absorbancia y emisión mediante el tamaño, bajo fotoblanqueo, fácil

funcionalización, mayores bandas de excitación y menores de emisión o menor toxicidad[80]. De entre todos los sistemas nanoestructurados, los QDs permiten desarrollar sistemas multicolor, por ejemplo, funcionalizando distintos QDs con diferentes pasivadores[81].

El seguimiento tanto en medidas *in vitro* como *in vivo* puede ser llevado a cabo mediante fluorescencia, raman o resonancia magnética, entre otras, pudiéndose incluso realizarse todas al mismo tiempo[82–85]. Los QDs fluorescentes son clasificados en función de su intensidad, espectro, tiempo de vida y tiempo de desplazamiento o *time-gate*, propiedades estudiadas a la vez para obtener imágenes multimodales[84,86,87].

Tabla 2: Ejemplos de QDs utilizados en bioimagen[58].

Quantum Dots	**Análisis**	**Técnica de imagen**	**QD Emisión/tamaño**
CdSe/ZnS	Detección biológica	Fluorescencia *in vitro*	1-4 nm
CdSe/ZnS	Tumor Vascular y endotelio pulmonar	Fluorescencia *in vitro* & *in vivo*	< 10 nm
CdSe/ZnS/SiO_2	Procesos fagocinéticos	Fluorescencia *in vitro*	554 & 626 nm
CdSe/CdS/SiO_2	Seguimiento de fibroblastos	Fluorescencia *in vitro*	550 & 630 nm
CdSe/ZnS	Unión de maltosa	Fluorescencia de resonancia *in vitro*	560 nm
CdTe/CdSe	Cáncer en ganglios linfáticos	Fluorescencia *in vitro*	NIR

Debido a las distintas emisiones en función del tamaño que poseen, quantum dots como el CdSe, permiten distinguir la presencia de todo tipo de analitos por cambio de color con una tasa de acierto del 99,99%[88]. En espectroscopía Raman o *Surface*

Enhanced Raman Spectroscopy (SERS) se usan QDs de dos formas: 1. usando una molécula que junto a un QD dé un espectro SERS único; 2. midiendo el espectro SERS de agregados de QDs recubiertos con monocapas de analito. De esta manera, se están aplicando QDs basados en ZnO para la detección de cancer *in vivo*[89]. En cuanto a resonancia magnética o *proton nuclear magnetic resonance* (NMR)[90], gracias a los QDs se puede mejorar la señal donde las densidades relativas de protones son similares. Además, pueden ser disueltos en medios acuosos, no como la mayor parte de indicadores orgánicos, lo que permite que sean utilizados en aplicaciones *in vivo* intravenosas[91] junto a su propiedad, anteriormente mencionada, de permitir imágenes multimodales[92].

2.3. BASES NITROGENADAS

Reconocimiento Molecular

Las bases nitrogenadas son moléculas orgánicas con átomos de nitrógeno en su estructura, los cuales actúan como base en las reacciones químicas que intervienen, es decir, como dadores de electrones[93]. Estas moléculas pueden separarse en dos clases: pirimidínicas y púricas. Ambas parten de la estructura de la piridina, no polar y plana, pero, mientras que las bases pirimidínicas están formadas únicamente por variaciones de este anillo orgánico heterocíclico, las bases púricas poseen un doble anillo, formado a partir de la unión de un anillo de imidazol con un anillo de pirimidina. También llamadas nucleobases, estas moléculas son la base de la estructura del ácido desoxiribonucleico o ADN[94] y del ácido ribonucleico o ARN[95], cadenas poseedoras de la información de todo ser vivo. Aunque existen múltiples bases nitrogenadas, sólo las cinco formadoras de estas cadenas, la adenina o A, la guanina o G, la citosina o C, la timina o T y el uracilo o U, son consideradas las más relevantes, Figura 6. Todas ellas fueron descubiertas y nombradas por primera vez entre finales del S.XIX y principios del XX. La guanina fue descubierta en 1844 por Julius Bodo Unger (1819-1885), como mineral a partir del guano de pájaros[96]. La

timina fue descubierta por Albrecht Kossel (1853-1927) junto a Albert Neumann (1851-1938) en 1893 de las moléculas de timo de un carnero[97]. Un año después, en 1894, ambos descubrieron la citosina a partir de la hidrólisis de tejidos de timo de animal[98], la cual fue sintetizada artificialmente por primera vez en 1903. El uracilo, fue descubierto en 1900 por Alberto Ascoli (1877-1957) por la hidrólisis de la nucleína de la levadura[99]. Finalmente, la adenina fue descubierta por Vera Reader (1902-1989) en 1930 bajo el pseudónimo de vitamina B_4[100], aunque mas tarde se descubrió que no era una vitamina y no formaba parte del complejo de Vitamina B.

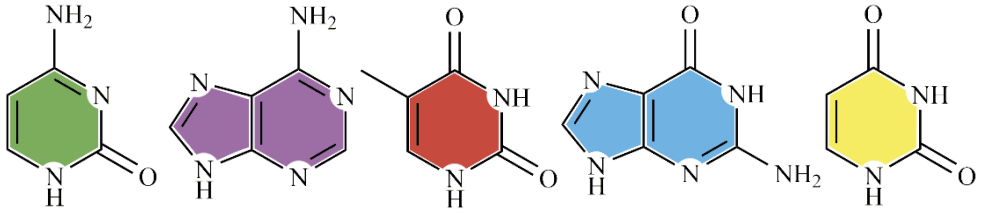

Figura 6: Bases nitrogenadas del ADN, de izquierda a derecha: citosina, timina, adenina, guanina y uracilo

Entre las propiedades primordiales de estas moléculas destaca su reconocimiento molecular o complementariedad, donde específicamente la adenina reconoce a la timina y la guanina a la citosina, formándose uniones A-T y G-C a partir de dos y tres enlaces de hidrógeno respectivamente, características de la doble hélice de ADN[101]. En el caso del ARN, y ya que su estructura no contiene timina, la complementariedad se establece entre A-U mediante dos puentes de hidrógeno[102]. Aun así, las nucleobases no sólo participan en este tipo de enlaces, ya que los pares de electrones existentes tanto en el nitrógeno como en el oxígeno hacen posible la formación de estructuras supramoleculares[103]. Un ejemplo de ello es el uso de esos electrones como ligando de metales[104], campo en constante análisis por sus aplicaciones biológicas, donde ya desde los años 50 se demostró la unión de Hg^{2+} a cadenas de ADN como un proceso reversible[105], y llegó a su punto álgido en los 70 con la demostración del uso del platino como inhibidor tumoral en células

animales[106]. Actualmente, innumerables metales son utilizados en reacciones junto al ADN como el Pd^{2+}, por su elevada reactividad[107], o compuestos organometálicos como el $(NH_3)_5Ru$ por el uso del Ru^{3+} como compuesto de coordinación en el campo farmacéutico en el tratamiento de tumores malignos[108], o para rotura de enlaces glicosídicos en la guanosina[109]. Entre los más importantes, de estos últimos mencionados, se encuentra el Zn^{2+}, por: i. poseer una afinidad similar tanto para el oxígeno como el nitrógeno, los dos átomos dadores de las cadenas de ADN y ARN[110]; y ii. poseer una elevada selectividad con las cinco nucleobases principales anteriormente nombradas, lo que le permite controlar todo tipo de procesos genéticos[111].

Además, junto a la posibilidad de poder crear cualquier cadena de ácidos nucleicos, la propiedad de ensamblaje de las bases nitrogenadas permite aplicar este tipo de sistemas en casi cualquier conformación o proceso de reconocimiento molecular en campos como ciencias de nanomateriales, siempre sin perder un punto de vista biocompatible[112,113]. Por último, las propias bases nitrogenadas poseen propiedades no presentes en sus respectivos ácidos nucleicos, como sus propiedades quirales, lo que les permite ser utilizadas como centros de unión o de auto-ensamblaje en compuestos sintéticos como los polímeros[114,115].

Estos polímeros artificiales son modificados normalmente de dos formas: bien mediante la adición en sus extremos de nucleobases, o bien alterándose la estructura de los monómeros que con lo conforman, dotando al compuesto, en ambos casos, de propiedades únicas. Un ejemplo del primer caso es el uso del oligometileno como espaciador entre moléculas iguales, como puede ser adenina o timina. Estos compuestos forman nanofibras supramoleculares por el reconocimiento de las bases A-T y de las cadenas poliméricas entre sí[116], Figura 7. En cuanto al segundo caso, mediante la modificación de la cadena, moléculas como el poliestireno han sido alteradas en su anillo aromático con unidades de diamidopiridina que pueden unirse de forma no covalente con moléculas de bi-timina, añadidas al medio, dando lugar a estructuras ramificadas[117]. Si el propio poliestireno es modificado con moléculas de

tiamina, vitamina B1, ellas mismas mediante un proceso de reconocimiento se unirán entre sí dando lugar a estructuras vesiculares esféricas[118].

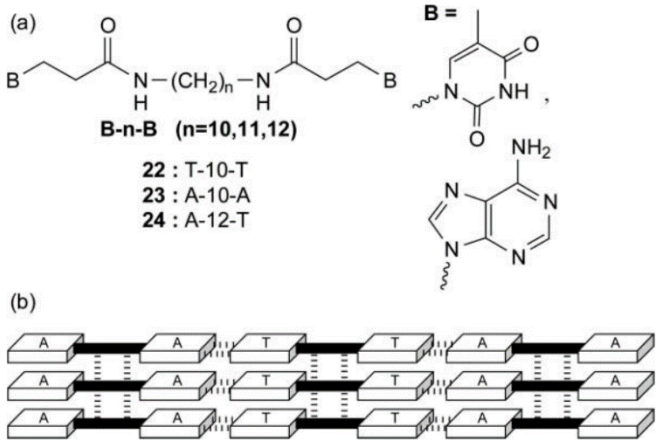

Figura 7: Polímeros sustituidos por nucleósidos: (a) estructura molecular; (b) organización en nanofibras mediante enlaces de hidrógeno[103].

Interacción citosina-guanina

Entre las tres posibles interacciones por reconocimiento existentes entre las bases nitrogenadas, nucleótidos o nucleósidos (A-T, A-U y G-C)[119], la presentae Memoria se centra en el reconocimiento directo entre la base púrica G y la pirimidínica C, Figura 8, caracterizadas por la unión mediante tres puentes de hidrógeno. Esta interacción es relativamente fuerte ($>10^4$ M^{-1} en $CDCl_3$) aunque la baja solubilidad de la guanina limita su uso en procesos de síntesis y futuras aplicaciónes[120]. Por ello, se utiliza la guanosina en su lugar[121], nucleósido de la guanina formado por la unión de una molécula de guanina a un anillo de ribosa mediante un enlace glucosídico. Un ejemplo del uso de la guanosina es en el reconocimiento citidina-guanosina en porfirinas formadoras de estructuras oligoméricas para el estudio de transferencia de carga en procesos fotoinducidos. Gracias a los puentes de hidrógeno, se pueden crear nuevas estructuras basadas en tripletes, interacciones no covalentes que mejora los tiempos de transferencia de carga y las distancias mínimas comparadas con

estructuras singlete, siempre manteniendo una eficiencia de transferencia de, al menos, un 90%[122].

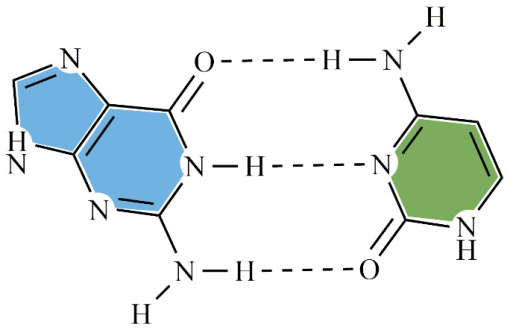

Figura 8: Interacción guanina (izq.) – citosina (drcha.).

Aun así, la guanina es usada en numerosos sistemas por la especificidad de su enlace G-C y porque es un enlace único característico del ADN, cadena poseedora de un espacio en el interior idóneo para la unión de multitud de moléculas. Sin ir más lejos, en una doble hélice mediante interacciones Hoogsteen[123] pueden formarse nuevos puentes de hidrogeno con un ácido nucleico extra formando una triple hélice de ADN[124]. Además, moléculas como la urocanamida, que interaccionan específicamente con la unión G-C y ninguna otra, son utilizadas para reforzar mediante puentes de hidrógeno extra los ya formados por las bases nitrogenadas hasta valores de 10^3 M^{-1} en $CDCl_3$, sirviendo a su vez como protector estérico del mismo[125].Otro uso de este reconocimiento se encuentra en la detección de mutaciones o fallos en la secuencia del ADN. Mediante reconocimiento *host-guest*, moléculas con bases como sustituyentes pueden reconocer partes incompletas en la cadena, al interaccionar de manera selectiva con ella. En este marco, por ejemplo, se utilizan carbohidratos híbridos con grupos sustituyentes de citosina capaces de reconocer grupos guanina libres en cadenas tanto de ADN como ARN[126].

Dejando de lado las disoluciones y centrándose en sistemas 2D, específicamente en interfases aire-agua, el estudio de reconocimiento molecular por puentes de hidrógeno, desde un punto de vista biológico, entre bases nitrogenadas, azúcares o

nucleótidos como el ATP es más que posible[127]. A partir de una membrana celular modelo, se ha podido demostrar la existencia de reconocimiento molecular mediante puentes de hidrógeno entre las moléculas de guanina y citosina existentes en las cabezas polares de las nucleolípidos funcionalizados[128]. Estos procesos de reconocimiento también son posibles entre estos mismos nucleolípidos y sus moléculas complementarias presentes en la subfase acuosa[129].

3. BIBLIOGRAFÍA

1. B. Franklin. Of the stilling of Waves by means of Oil. *Philos. Trans.* **64**, 445-460 (1774).
2. Pockels, A. Surface Tension. *Nature* (1891).
3. Lord Rayleigh. Investigations in Capillarity:—The size of drops.—The liberation of gas from supersaturated solutions.—Colliding jets.—The tension of contaminated water-surfaces. *London, Edinburgh, Dublin Philos. Mag. J. Sci.* **48**, 321–337 (1899).
4. Langmuir, I. The constitution and fundamental properties of solids and liquids. II. Liquids. *J. Am. Chem. Soc.* **39**, 1848–1906 (1917).
5. Langmuir, I. Vapor pressures, evaporation, condensation and adsorption. *J. Am. Chem. Soc.* **54**, 2798–2832 (1932).
6. Langmuir, I. Oil lenses on water and the nature of monomolecular expanded films. *J. Chem. Phys.* **1**, 756–776 (1933).
7. Blodgett, K. B. Monomolecular films of fatty acids on glass. *J. Am. Chem. Soc.* **56**, 495-495 (1934).
8. Blodgett, K. B. Films built by depositing successive monomolecular layers on a solid surface. *J. Am. Chem. Soc.* **57**, 1007–1022 (1935).
9. Blodgett, K. B. A method of extinguising the reflection of light from glass. *Science.* **89**, 60–61 (1939).
10. Hussain, S. A., Dey, B., Bhattacharjee, D. & Mehta, N. Unique supramolecular assembly through Langmuir – Blodgett (LB) technique. *Heliyon* **4**, e01038 (2018).
11. Langmuir, I. & Schaefer, V. J. Activities of urease and pepsin monolayers. *J. Am. Chem. Soc.* **60**, 1351–1360 (1938).
12. Gaines, G. L. *Insoluble monolayers at Liquid-Gas Interfaces*. (Wiley-Interscience, 1966).
13. Adamson, A. W. *Physical Chemistry of Surfaces*. (Interscience, 1967).

14. Tasman Davies, J. & Keightley Rideal, S. E. *Interfacial Phenomena*. (Academic Press, 1963).
15. Gericke, A., Simon-Kutscher, J. & Hühnerfuss, H. Influence of the spreading solvent on the properties of monolayers at the air/water interface. *Langmuir* **9**, 2119–2127 (1993).
16. Kuhn, H., Möbius, D. & Bücher, H. *Physical Methods of Chemistry*. (Wiley-Interscience, 1972).
17. Chechel, O. V. & Nikolaev, E. N. Devices for production of Langmuir-Blodgett Films. *Instruments Exp. Tech.* **34**, 750–762 (1991).
18. Barnes, G. T. & Gentle, I. R. *Interfacial Science: an introduction*. (Oxford, 2005).
19. Knobler, C. M. Condensed monolayer phases at the air/water interface: Phase transitions and structures. *J. Phys. Condens. Matter* **3**, S17–S22 (1991).
20. Dynarowicz-Latka, P., Dhanabalan, A. & Oliveira, O. N. J. Modern physicochemical research on Langmuir monolayers. *Adv. Colloid Interface Sci.* **91**, 221–293 (2001).
21. Zhao, L. & Lin, Z. Self-assembly of non-linear polymers at the air/water interface: The effect of molecular architecture. *Soft Matter* **7**, 10520–10535 (2011).
22. Miller, R. *et al.* Dynamics of protein and mixed protein/surfactant adsorption layers at the water/fluid interface. *Adv. Colloid Interface Sci.* **86**, 39–82 (2000).
23. Kasprzyk-Hordern, B. Chemistry of alumina, reactions in aqueous solution and its application in water treatment. *Adv. Colloid Interface Sci.* **110**, 19–48 (2004).
24. Holmberg, M. *et al.* Surface force studies of Langmuir–Blodgett cellulose films. *J. Colloid Interface Sci.* **186**, 369–381 (1997).
25. Valluzzi, R., Gido, S. P., Muller, W. & Kaplan, D. L. Orientation of silk III at the air-water interface. *Int. J. Biol. Macromol.* **24**, 237–242 (1999).

26. Chen, Z., Shen, Y. R. & Somorjai, G. A. Studies of polymer surfaces by sum frequency generation vibrational spectroscopy. *Annu. Rev. Phys. Chem.* **53**, 437–465 (2002).
27. Aguilar, M. R. & Román, J. S. *Smart Polymers and their Applications. Woodhead Publishing* (Woodhead Publishing, 2014).
28. Sánchez, A. & Vázquez, A. Bioactive peptides: A review. *Food Qual. Saf.* **1**, 29–46 (2017).
29. Fischer, E. & Fourneau, E. Ueber einige derivate des glukocolls. *Ber Dtsch Chem Bunenges* **34**, 2868–2877 (1901).
30. Goodman, M., Cai, W. & Smith, N. C. The bold legacy of Emil Fischer. *J. Pept. Sci.* **9**, 594–603 (2003).
31. Curtius, T. Verkettung von amidosäuren I. Abhandlung. *J. für Prakt. Chemie* **70**, 57–72 (1904).
32. Curtius, T. Synthetische versuche mit hippurazid. *Berichte der Dtsch. Chem. Gesellschaft* **35**, 3226–3228 (1902).
33. Curtius, T. & Gumlich, O. Verkettung von amidosäuren. VII. Abhandlung. Kettenbildung zwischen hippurazid und β-amino-α -oxypropionsäure und β-aminobuttersäure. *J. für Prakt. Chemie* **70**, 195–223 (1904).
34. Curtius, T. & Müller, E. Über hippuryl-y-aminobuttersäure und hippuryl-b-phenyl-a-alanin. *J. für Prakt. Chemie* **70**, 223–229 (1904).
35. Bergmann, M. & Zervas, L. Über ein allgemeines verfahren der peptid-synthese. *Ber Dtsch Chem Ges* **65**, 1192–1201 (1932).
36. Akabori, S., Ikenaka, T. & Matsumoto, K. Asymmetric synthesis of amino acids. *Proc Jpn Acad* **27**, 7–9 (1951).
37. Izumi, Y., Tasumi, S., Imaida, M., Fukuda, Y. & Akabori, S. The preparation of optically active a-c-substituted glutamic acid. *Bull. Chem. Soc. Jpn.* **38**, 1338–1340 (1965).
38. Zhang, Z., Zhu, W. & Kodadek, T. Selection and application of peptide-binding peptides. *Nat. Biotechnol.* **18**, 71–74 (2000).

39. Hajfathalian, M., Ghelichi, S., García-Moreno, P. J., Moltke Sørensen, A. D. & Jacobsen, C. Peptides: Production, bioactivity, functionality, and applications. *Crit. Rev. Food Sci. Nutr.* **58**, 3097–3129 (2018).
40. Hamley, I. W. Small bioactive peptides for biomaterials design and therapeutics. *Chem. Rev.* **117**, 14015–14041 (2017).
41. Keymanesh, K., Soltani, S. & Sardari, S. Application of antimicrobial peptides in agriculture and food industry. *World J. Microbiol. Biotechnol.* **25**, 933–944 (2009).
42. Lupo, M. P. & Cole, A. L. Cosmeceutical peptides. *Dermatol. Ther.* **20**, 343–349 (2007).
43. Pugliese, R. & Gelain, F. Peptidic biomaterials: From self-assembling to regenerative medicine. *Trends Biotechnol.* **35**, 145–158 (2017).
44. Agarwal, R. *et al.* Delivery and tracking of quantum dot peptide bioconjugates in an intact developing avian brain. *ACS Chem. Neurosci.* **6**, 494–504 (2015).
45. Moldaver, D. & Larché, M. Immunotherapy with peptides. *Allergy Eur. J. Allergy Clin. Immunol.* **66**, 784–791 (2011).
46. di Luca, M., Maccari, G. & Nifosí, R. Treatment of microbial biofilms in the post-antibiotic era: Prophylactic and therapeutic use of antimicrobial peptides and their design by bioinformatics tools. *Pathog. Dis.* **70**, 257–270 (2014).
47. Skalickova, S. *et al.* Perspective of use of antiviral peptides against influenza virus. *Viruses* **7**, 5428–5442 (2015).
48. Yagasaki, M. & Hashimoto, S. I. Synthesis and application of dipeptides; Current status and perspectives. *Appl. Microbiol. Biotechnol.* **81**, 13–22 (2008).
49. González-Díaz, N. E., López-Rendón, R. & Ireta, J. Insight into the dipeptide self-assembly process using density functional theory. *J. Phys. Chem. C* **123**, 2526–2532 (2019).
50. Wang, J. *et al.* Trace solvent as a predominant factor to tune dipeptide self-

assembly. *ACS Nano* **10**, 2138–2143 (2016).

51. Ryan, D. M. & Nilsson, B. L. Self-assembled amino acids and dipeptides as noncovalent hydrogels for tissue engineering. *Polym. Chem.* **3**, 18–33 (2012).
52. Schnaider, L. *et al.* Self-assembling dipeptide antibacterial nanostructures with membrane disrupting activity. *Nat. Commun.* **8**, 1365 (2017).
53. Fichman, G. & Gazit, E. Self-assembly of short peptides to form hydrogels: Design of building blocks, physical properties and technological applications. *Acta Biomater.* **10**, 1671–1682 (2014).
54. Drury, J. L. & Mooney, D. J. Hydrogels for tissue engineering: Scaffold design variables and applications. *Biomaterials* **24**, 4337–4351 (2003).
55. Van Vlierberghe, S., Dubruel, P. & Schacht, E. Biopolymer-based hydrogels as scaffolds for tissue engineering applications: A review. *Biomacromolecules* **12**, 1387–1408 (2011).
56. Qiu, Y. & Park, K. Environment-sensitive hydrogels for drug delivery. *Adv. Drug Deliv. Rev.* **53**, 321–339 (2001).
57. Tibbitt, M. W. & Anseth, K. S. Hydrogels as extracellular matrix mimics for 3D cell culture. *Biotechnol. Bioeng.* **103**, 655–663 (2009).
58. Bera, D., Qian, L., Tseng, T. K. & Holloway, P. H. Quantum dots and their multimodal applications: A review. *Materials (Basel).* **3**, 2260–2345 (2010).
59. Ji, X., Peng, F., Zhong, Y., Su, Y. & He, Y. Fluorescent quantum dots: Synthesis, biomedical optical imaging, and biosafety assessment. *Colloids Surfaces B Biointerfaces* **124**, 132–139 (2014).
60. Henglein, A. Small-particle research: Physicochemical properties of extremely small colloidal metal and semiconductor particles. *Chem. Rev.* **89**, 1861–1873 (1989).
61. Murphy, C. J. & Coffer, J. L. QuantumDots: A Primer. *Focal point* **56**, 16A-20A (2002).
62. Ekimov, A. I. & Onushchenko, A. A. Quantum size effect on three-dimensional microscopic semiconductor crystals. *Pis'ma v Zhurnal*

Èksperimental'noi i Teor. Fiz. **34**, 363–366 (1981).

63. Brus, L. E. Electron-electron and electron-hole interactions in small semiconductor crystallites: The size dependence of the lowest excited electronic state. *J. Chem. Phys.* **80**, 4403–4409 (1984).
64. Murray, C. B., Norris, D. J. & Bawendi, M. G. Synthesis and characterization of nearly monodisperse CdE (E = sulfur, selenium, tellurium) semiconductor nanocrystallites. *J. Am. Chem. Soc.* **115**, 8706–8715 (1993).
65. Alivisatos, A. . Semiconductor clusters, nanocrystals, and quantum dots. *Science*. **271**, 933–937 (1996).
66. Wang, Y. & Herron, N. Nanometer-sized semiconductor clusters: Materials synthesis, quantum size effects, and photophysical properties. *J. Phys. Chem.* **95**, 525–532 (1991).
67. Zhu, J.-J., Li, J.-J., Huang, H.-P. & Cheng, F.-F. *Quantum Dots for DNA Biosensing*. *Springer* (2013). doi:10.1007/978-3-642-44910-9
68. Petryayeva, E., Algar, W. R. & Medintz, I. L. Quantum dots in bioanalysis: A review of applications across various platforms for fluorescence spectroscopy and imaging. *Focal Point Rev.* **67**, 215–252 (2013).
69. Barkhouse, D. A. R., Pattantyus-abraham, A. G., Levina, L. & Edward, H. Thiols passivate recombination in colloidal quantum dots leading to enhanced. *ACSNano* **2**, 2356–2362 (2008).
70. Peng, X., Schlamp, M. C., Kadavanich, A. V. & Alivisatos, A. P. Epitaxial growth of highly luminescent CdSe/CdS core/shell nanocrystals with photostability and electronic accessibility. *J. Am. Chem. Soc.* **119**, 7019–7029 (1997).
71. Reiss, P., Bleuse, J. & Pron, A. Highly luminescent CdSe/ZnSe core/shell nanocrystals of low size dispersion. *Nano Lett.* **2**, 781–784 (2002).
72. Pathak, Y. & Thassu, D. Semiconducting Quantum Dots for Bioimaging. in *Drug Delivery Nanoparticles Formulation and Characterization* 416 (2016).
73. Yang, H., Holloway, P. H. & Santra, S. Water-soluble silica-overcoated

CdS:Mn/ZnS semiconductor quantum dots. *J. Chem. Phys.* **121**, 7421–7426 (2004).

74. Coe-Sullivan, S. Optoelectronics: Quantum dot developments. *Nat. Photonics* **3**, 315–316 (2009).
75. C David, M. *et al.* Multi-colour organic light-emitting displays by solution processing. *Nature* **421**, 829–833 (2003).
76. Guldi, D. M. *et al.* CNT-CdTe versatile donor-acceptor nanohybrids. *J. Am. Chem. Soc.* **128**, 2315–2323 (2006).
77. Lee, J., Sundar, V. C., Heine, J. R., Bawendi, M. G. & Jensen, K. F. Full color emission from II-VI semiconductor quantum dot-polymer composites. *Adv. Mater.* **12**, 1102–1105 (2000).
78. Cassidy, P. J. & Radda, G. K. Molecular imaging perspectives. *J. R. Soc. Interface* **2**, 133–144 (2005).
79. Maiti, A. & Bhattacharyya, S. Review : Quantum dots and application in medical science. *Int. J. Chem. Chem. Eng.* **3**, 37–42 (2013).
80. Chunyan, L., Bohua, D. & Qiangbin, W. Properties of quantum dots: A new nanoprobe for bioimaging. In *Handbook of Nanomaterials Properties* 1263–1298 (2014).
81. Martynenko, I. V. *et al.* Application of semiconductor quantum dots in bioimaging and biosensing. *J. Mater. Chem. B* **5**, 6701–6727 (2017).
82. Herbst, R. S. & Shin, D. M. Monoclonal antibodies to target epidermal growth factor receptor-positive tumors. *Cancer* **94**, 1593–1611 (2002).
83. Sharma, P., Brown, S., Walter, G., Santra, S. & Moudgil, B. Nanoparticles for bioimaging. *Adv. Colloid Interface Sci.* **123**–**126**, 471–485 (2006).
84. Gambhir, S. S. & Weiss, S. Quantum dots for live cells, in vivo imaging, and diagnostics. *Science (80-.).* **307**, 538–545 (2005).
85. Lakowicz, J. R. *Principles of Fluorescence Spectroscopy*. (2006).
86. Medintz, I. L., Uyeda, H. T., Goldman, E. R. & Mattoussi, H. Quantum dot bioconjugates for imaging, labelling and sensing. *Nat. Mater.* **4**, 435–446

(2005).

87. Hassan, M. & Klaunberg, B. A. Comparative Medicine Overview Biomedical Applications of Fluorescence Imaging In Vivo. *Comp. Med.* **54**, 635–644 (2004).
88. Han, M., Gao, X., Su, J. Z. & Nie, S. Quantum-dot-tagged microbeads for multiplexed optical coding of biomolecules. *Nat. Biotechnol.* **19**, 631–635 (2001).
89. Haldavnekar, R., Venkatakrishnan, K. & Tan, B. Non plasmonic semiconductor quantum SERS probe as a pathway for in vitro cancer detection. *Nat. Commun.* **9**, 1–18 (2018).
90. Zamborini, F. P., Bao, L. & Dasari, R. Nanoparticles in measurement science. *Anal. Chem.* **84**, 541–576 (2012).
91. Kalangi, S. K. *et al.* Synthesis, Characterization, and Biodistribution of Quantum Dot-Celecoxib Conjugate in Mouse Paw Edema Model. *Oxid. Med. Cell. Longev.* **2018**, 1–8 (2018).
92. Santra, S. *et al.* Synthesis and characterization of fluorescent, radio-opaque, and paramagnetic silica nanoparticles for multimodal bioimaging applications. *Adv. Mater.* **17**, 2165–2169 (2005).
93. Nelson, D. L. & Cox, M. M. *Lehninger Principles of Biochemistry*. (W.H. Freeman and Company, 2017).
94. Miescher, F. Ueber die chemische Zusammensetzung der Eiterzellen. in *Medicinisch-chemische Untersuchungen* 441–460 (1871).
95. Levene, P. A. The Structure of Yeast Nucleic Acid. *J. Biol. Chem* **41**, 19–23 (1919).
96. Magnus. Ueber das Vorkommen von Xanthicoxyd im Guano. *Ann. der Chemie und Pharm.* **51**, 395–397 (1844).
97. Albrecht, K. & Neumann, A. Ueber das Thymin, ein Spaltungsproduct der Nucleïnsäure. *Berichte der Dtsch. Chem. Gesellschaft zu Berlin* **26**, 2753–2756 (1893).

98. Kossel, A. & Neumann, A. Berichte der Deutschen chemischen Gesellschaft zu Berlin. in *Berichte der Deutschen Chemischen Gesellschaft zu Berlin* **27**, 2215–2222 (1894).

99. Ascoli, A., Thymin, D. & Neumann, V. A. K. A. Ueber ein neues Spaltungsprodukt des Hefenucleins. *Zeitschrift für Physiol. Chemie* **31**, 161–164 (1900).

100. Reader, V. The assay of vitamin B(4). *Biochem. J.* **24**, 1827–1831 (1930).

101. Pauling, L. The Nature of the Chemical Bond and the Structure of Molecules and Crystals: An Introduction to Modern Structural Chemistry. *Cornell University Press* 450 (1960). doi:10.1021/ja01500a088

102. Miao, Z. & Westhof, E. RNA Structure: Advances and Assessment of 3D Structure Prediction. *Annu. Rev. Biophys.* **46**, 483–503 (2017).

103. Sivakova, S. & Rowan, S. J. Nucleobases as supramolecular motifs. *Chem. Soc. Rev.* **34**, 9–21 (2005).

104. Lippert, B. & Martin, R. B. *Multiplicity of metal ion binding patterns to nucleobases*. *Coordination Chemistry Reviews* (Wiley-VCH Weinheim, 2000). doi:10.1016/S0010-8545(00)00260-5

105. Katz, S. The Reversible Reaction of Sodium Thymonucleate and Mercuric Chloride. *J. Am. Chem. Soc.* **74**, 2238–2245 (1952).

106. Rosenberg, B., VanCamp, L., Trosko, J. E. & Mansour, V. H. Patinum Compounds: a New Class of Potent Antitumour Agents. *Nature* **222**, 385–386 (1969).

107. Lippert, B. *Cisplatin: Chemistry and Biochemistry of a Leading Anticancer Drug*. *Encyclopedia of Toxicology: Third Edition* (1999). doi:10.1016/B978-0-12-386454-3.00288-8

108. Clarke, M. J., Zhu, F. & Frasca, D. R. Non-Platinum Chemotherapeutic Metallopharmaceuticals. *Chem. Rev.* **99**, 2511–2534 (2002).

109. LaChance-Galang, K. J., Zhao, M. & Clarke, M. J. Disproportionation of [(py)(NH 3)4RuIII] at the N7 of Guanine Nucleosides: Severing the N-

Glycosidic Bond. *Inorg. Chem.* **35**, 6021–6026 (2002).

110. Fusch, E. C. & Lippert, B. [Zn3(OH)2(1-MeC-N3)5(1-MeC-O2)3]4+(1-MeC=1-Methylcytosine): Structural Model for DNA Cross-Linking and DNA Rewinding by Zn(II)? *J. Am. Chem. Soc.* **116**, 7204–7209 (1994).
111. Kimura, E. & Shionoya, M. Zinc complexes as targeting agents for nucleic acids. *Met Ions Biol Syst.* **33**, 29–52 (1996).
112. Wang, F., Liu, X. & Willner, I. DNA switches: From principles to applications. *Angew. Chemie - Int. Ed.* **54**, 1098–1129 (2015).
113. Nayak, A. K. & Subudhi, U. Directed self-assembly of genomic sequences into monomeric and polymeric branched DNA structures. *RSC Adv.* **4**, 54506–54511 (2014).
114. Berti, L. & Burley, G. A. Nucleic acid and nucleotide-mediated synthesis of inorganic nanoparticles. *Nat. Nanotechnol.* **3**, 81–87 (2008).
115. Marino, N. *et al.* Homochiral self-assembly of biocoordination polymers: Anion-triggered helicity and absolute configuration inversion. *Chem. Sci.* **6**, 4300–4305 (2015).
116. Shimizu, T., Iwaura, R., Masuda, M., Hanada, T. & Yase, K. Internucleobase-interaction-directed self-assembly of nanofibers from homo- and heteroditopic 1,ω-nucleobase bolaamphiphiles. *J. Am. Chem. Soc.* **123**, 5947–5955 (2001).
117. Thibault, R. J., Hotchkiss, P. J., Gray, M. & Rotello, V. M. Thermally reversible formation of microspheres through non-covalent polymer cross-linking. *J. Am. Chem. Soc.* **125**, 11249–11252 (2003).
118. Thibault, R. J. *et al.* Specific interactions of complementary mono- and multivalent guests with recognition-induced polymersomes. *J. Am. Chem. Soc.* **124**, 15249–15254 (2002).
119. Pu, F., Ren, J. & Qu, X. Nucleobases, nucleosides, and nucleotides: Versatile biomolecules for generating functional nanomaterials. *Chem. Soc. Rev.* **47**, 1285–1306 (2018).

120. Herskovits, T. T. & Harrington, J. P. Solution Studies of the Nucleic Acid Bases and Related Model Compounds. Solubility in Aqueous Alcohol and Glycol Solutions. *Biochemistry* **11**, 4800–4811 (1972).

121. Wong, A., Ida, R., Spindler, L. & Wu, G. Disodium guanosine 5′-monophosphate self-associates into nanoscale cylinders at pH 8: A combined diffusion NMR spectroscopy and dynamic light scattering study. *J. Am. Chem. Soc.* **127**, 6990–6998 (2005).

122. Sessler, J. L., Wang, B. & Harriman, A. Photoinduced Energy Transfer in Associated but Noncovalently Linked Photosynthetic Model Systems. *J. Am. Chem. Soc.* **117**, 704–714 (1995).

123. Nikolova, E. N. *et al.* Transient Hoogsteen base pairs in canonical duplex DNA. *Nature* **470**, 498–504 (2011).

124. Esguerra, M., Nilsson, L. & Villa, A. Triple helical DNA in a duplex context and base pair opening. *Nucleic Acids Res.* **42**, 11329–11338 (2014).

125. Mertz, E., Mattei, S. & Zimmerman, S. C. Synthesis and duplex DNA recognition studies of oligonucleotides containing a ureido isoindolin-1-one homo-N-nucleoside. A comparison of host-guest and DNA recognition studies. *Bioorganic Med. Chem.* **12**, 1517–1526 (2004).

126. Idutsu, Y., Sasaki, A., Matsumura, S. & Toshima, K. Molecular design, chemical synthesis, and evaluation of cytosine-carbohydrate hybrids for selective recognition of a single guanine bulged duplex DNA. *Bioorganic Med. Chem. Lett.* **15**, 4332–4335 (2005).

127. Ariga, K. & Kunitake, T. Molecular Recognition at Air-Water and Related Interfaces: Complementary Hydrogen Bonding and Multisite Interaction. *Acc. Chem. Res.* **31**, 371–378 (1998).

128. Wang, Y., Du, X., Miao, W. & Liang, Y. Molecular recognition of cytosine- and guanine-functionalized nucleolipids in the mixed monolayers at the air-water interface and Langmuir-Blodgett films. *J. Phys. Chem. B* **110**, 4914–4923 (2006).

129. Miao, W., Du, X. & Liang, Y. Molecular recognition of nucleolipid monolayers of 1-(2-octadecyloxycarbonylethyl)cytosine to guanosine at the air-water interface and Langmuir-Blodgett films. *Langmuir* **19**, 5389–5396 (2003).

Capítulo II

Técnicas experimentales

Chapter II

Experimental techniques

1. TÉCNICAS DE FORMACIÓN Y CARACTERIZACIÓN DE MONOCAPAS EN LA INTERFASE AIRE-AGUA

De todas las técnicas de caracterización existentes para monocapas en la interfase aire-agua, mostradas en la Tabla 1 de la sección 1, se procede a desarrollar aquellas utilizadas a lo largo de la Tesis.

1.1. BALANZA DE LANGMUIR

La tensión superficial es la fuerza por unidad de distancia que se produce sobre un punto en una superficie, en nuestro caso, en la interfase aire-agua. Una balanza de Langmuir nos permite medir esta tensión superficial a la vez que se varía el área del sistema, viéndose el efecto de la molécula anfifílica en la interfase[1], Figura 1. Este equipo consiste en: una cubeta poco profunda de teflón donde se aloja el líquido o subfase sobre la que se va a esparcir el compuesto o compuestos a analizar, normalmente agua ultrapura o una disolución acuosa; una barrera móvil encargada de variar el área disponible por las moléculas para organizarse sobre ésta; y un sistema de medición de presión superficial mediante el método de Wilhelmy. *Wilhelmy plate* es un sistema está basado en una lámina metálica, normalmente de platino, o un papel de filtro sumergido parcialmente en la subfase y conectado a un dispositivo que mide la tensión superficial. De esta manera, en cualquier superficie, si una fuerza F actúa tangencialmente sobre una superficie de dimensiones δx, la tensión vendrá dada por:

$$\gamma = \frac{F}{\delta x} \qquad (5)$$

Como el plato en contacto está orientado verticalmente, el menisco en contacto con la superficie será una línea de longitud $2(\mathrm{x} + \mathrm{y})$, donde x e y son la longitud horizontal y grosor del plato respectivamente:

$$F = \gamma 2(x + y) \qquad (2)$$

donde, pudiéndose medir *F*, *x* e *y*, se obtiene el valor de la tensión superficial de la cual se deduce la presión superficial, que como bien ya se ha establecido en la primera sección del capítulo I, viene descrita por la diferencia entre las tensiones superficiales de la subfase pura con la del compuesto en la superficie de la misma:

$$\pi = \gamma_0 - \gamma \qquad (3)$$

Una vez medido el valor de la presión π para cada área de la balanza, al comprimir la película con la/s barrera/s, ésta se representa frente al área por molécula, A^2/molécula, donde se suele apreciar un aumento de la presión superficial al disminuir el área por molécula, al comprimir con la/s barrera/s.

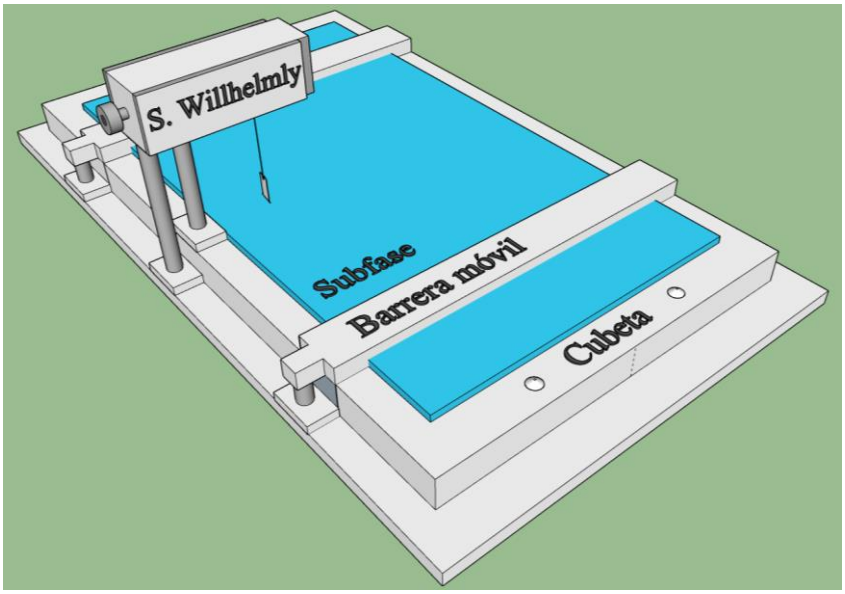

Figura 1: Representación 3D de una balanza de Langmuir tipo Wilhelmy.

Todas las moléculas usadas a lo largo de la presente memoria fueron estudiadas en la interfase aire-agua utilizando dos balanzas comerciales NIMA modelos 611 y 601, con una y dos barreras móviles, respectivamente. La velocidad de compresión

utilizada en las diferentes isotermas oscila entre 0.03-0.1 $nm^2min^{-1}molécula^{-1}$ a una temperatura de 21 ºC.

1.2. ESPECTROSCOPÍA DE REFLEXIÓN UV-VISIBLE

La espectroscopía de reflexión es una técnica utilizada para monocapas de compuestos con alto coeficiente de extinción que mide la diferencia de luz reflejada, en el rango del UV-Visible, en la interfase aire-agua entre un sistema líquido puro y uno con una monocapa en superficie. Por ello, podemos obtener datos de la orientación, asociación, adsorción y cambio químico de cromóforos en la monocapa analizada[2].

La base de esta técnica es la siguiente: La luz no polarizada emitida por dos lámparas incide de forma normal sobre la superficie de la subfase separándose en tres partes: I_A o parte disipada, I_R o parte reflejada e I_T o parte transmitida a través de la interfase. Para casos donde la reflexión y la absorción de luz en la interfase es baja, podemos decir que nuestra I_R es debida a la dispersión coherente de las moléculas, que no cambian de estado al emitir toda la energía recibida. Este total de intensidad es el cuadrado de la suma de todas las amplitudes de dispersión de las moléculas. Para nuestro caso, a partir de la amplitud relativa de campo eléctrico $E_{r,S}/E_0$ de la I_R se puede determinar R_S o la reflexión del agua pura:

$$E_{r,S}/E_0 = \sqrt{R_S} \qquad (4)$$

donde la luz reflejada sufre un cambio de fase de $-\pi$ respecto a la fase de luz incidente. La dispersión de resonancia o cambio de ángulo tras la dispersión debida a las moléculas depositadas en la superficie se puede expresar con un modelo clásico mediante la fuerza del oscilador *f*, intensidad de una banda de absorción electrónica, la cual viene dada por:

$$f = 8\pi^2 m_0 v_0 |D_{12}|^2/(3he_0^2) \qquad (5)$$

siendo m_0 la masa del electrón, v_0 la frecuencia de resonancia del oscilador, D_{12} el momento de transición, h la constante de Planck y e_0 la carga del electrón. Si consideramos que los momentos de transición están estadísticamente orientados en el plano de superficie del agua, la R_D o reflexión de la monocapa viene determinada por:

$$R_D = \left(\frac{3fe_0^2}{2m_0c}\right)^2 N^2 \frac{v^2}{(v_0^2 - v^2)^2 + v^2 v'^2} \quad (6)$$

donde N es el número de moléculas por área, c es la velocidad de la luz, v es la frecuencia de la luz incidente y v' la suma de todas las posibles ratios de decaimiento. Esta capa a su vez genera un cambio en la fase de π/2. Por ello, combinando ambos sistemas se obtiene que la $R_{D,S}$ o reflexión total viene determinada por:

$$R_{D,S} = R_S + 2\sqrt{R_S}\sqrt{R_D}\frac{vv'}{(v_0^2 - v^2) + v^2 v^2} + R_D \quad (7)$$

que, junto a la expresión de la absorción de luz de una monocapa, A:

$$A = 2\left(\frac{3fe_0^2}{2m_0c}\right) N \frac{v^2 v'}{(v_0^2 - v^2)^2 + v^2 v'^2} \quad (8)$$

se puede expresar como:

$$R_{D,S} = R_S + R_D + A\sqrt{R_S} \quad (9)$$

En el punto de absorción máxima, donde la frecuencia de resonancia del oscilador y la frecuencia de la luz incidente son iguales, $v = v_0$, la adsorción puede ser expresada como:

$$A_0 = A_{max} = 2\left(\frac{3fe_0^2}{2m_0c}\right)\frac{N}{v'} \quad (10)$$

por lo que, podemos volver a rescribir la ecuación de reflexión total como:

$$\Delta R = \left(R_{D,S} - R_S\right) = A\sqrt{R_S} + \frac{1}{4}AA_0 \quad (11)$$

De esta forma, en el caso de tener una única monocapa homogénea, y debido a existir una dependencia lineal entre la reflexión y a las moléculas depositadas, el segundo término de la derecha puede ser despreciado obteniéndose:

$$\Delta R = \left(R_{D,S} - R_S\right) = A\sqrt{R_S} \qquad (12)$$

donde se alcanza que el espectro de reflexión de las moléculas en la interfase aire-agua es igual al espectro de absorción. Por ello, podemos asociar la absorbancia con la reflexión por un factor numérico de 2.303, con lo que:

$$\Delta R = 2.303 \cdot 10^3 f_0 \varepsilon \Gamma \sqrt{R_S} \qquad (13)$$

donde ε representa la absortividad molar (mol·cm·L^{-1}), Γ es la concentración superficial (mol·cm^{-2}), f_0 es el factor de orientación del dipolo respecto a la superficie del agua y 10^3 es el factor necesario para hacer ΔR adimensional.

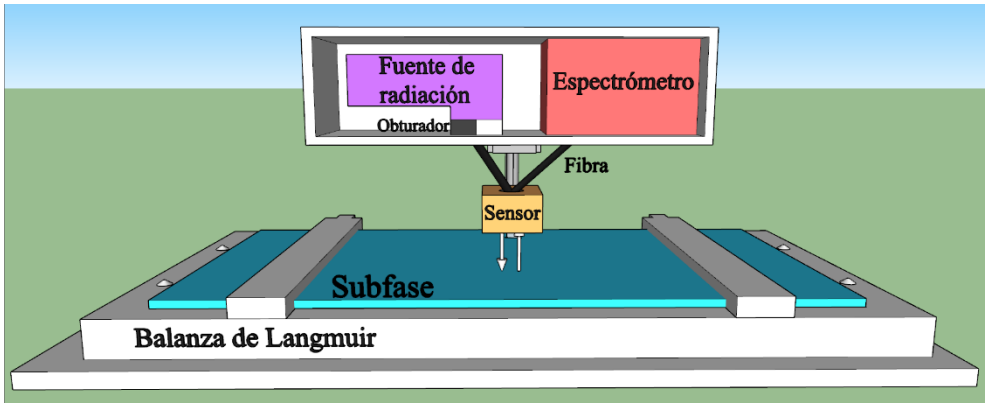

Figura 2: Esquema 3D del equipo de reflexión RefSpec^2.

Las medidas de reflexión (ΔR) en la interfase aire-agua se han realizado con el equipo RefSpec^2, diseñado por Nanofilm (Göttigen, Germany) y mostrado en las Figuras 2 y 3. Los espectros obtenidos el resultado de son la media de 15 medidas con un tiempo de apertura de 200ms. Dos lámparas, una de deuterio y otra de

tungsteno, emiten en el rango de 240 a 1000nm a través de un cristal de cuarzo que colima a una unidad sensor a través de una fibra óptica. Allí, tras pasar por un cromador y gracias a una trampa que elimina la luz reflejada por el fondo de la balanza, la unidad sensor mide la luz reflejada en nuestro sistema que es llevada a través de otra fibra al espectrofotómetro o detector, donde se analiza electrónicamente. Esta unidad sensor tiene un obturador, que permite alternar entre la luz emitida por equipo y la luz reflejada por la interfase y un espejo, que recubre su parte trasera como referencia en caso de oscilaciones de la lámpara.

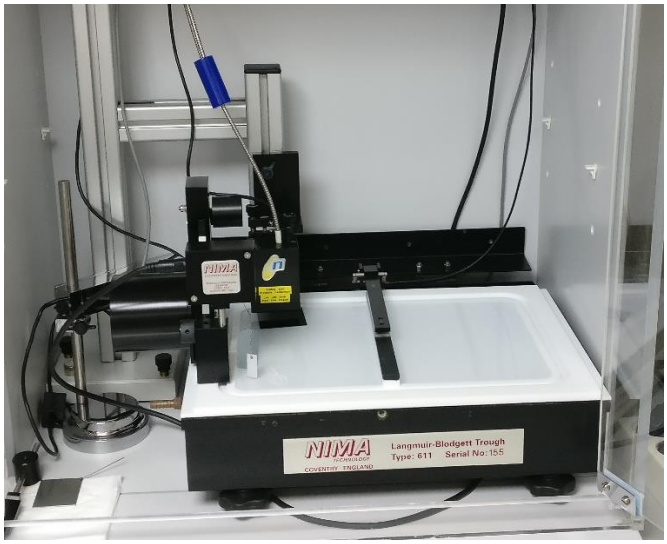

Figura 3: Imagen del equipo de reflexión RefSpec[2].

1.3. MICROSCOPÍA DE ÁNGULO BREWSTER (BAM)

La microscopía de ángulo Brewster, BAM, es una técnica no-invasiva que permite la visualización in situ de monocapas en la interfase aire-agua. Complementaria a las isotermas de Langmuir, posibilita el estudio de estructuras internas o dominios formados a lo largo de los procesos de compresión-expansión. Esta técnica está basada en la reflectividad de la luz bajo el ángulo Brewster[3], ángulo en el que toda radiación p-polarizada que incide en la interfase aire-agua es transmitida, sin producirse reflexión alguna[4].

Cuando la luz produce un cambio entre medios de distintos índices de refracción, parte es reflejada y otra reflectada. Las ecuaciones de Fresnel son conocidas como un conjunto de relaciones matemáticas que relacionan las amplitudes de las ondas reflejadas y refractadas cuando una onda electromagnética sufre dicho cambio, en nuestro caso, entre dos medios isotrópicos con distintos índices de refracción (aire y agua). Esta onda posee una parte p-polarizada, paralela al plano de incidencia, y una parte s-polarizada, orientada perpendicularmente al plano de incidencia.

Las ecuaciones de Fresnel parten de la ley de Snell[5]. Para un haz de luz que cambia de medio según se muestra en la Figura 4:

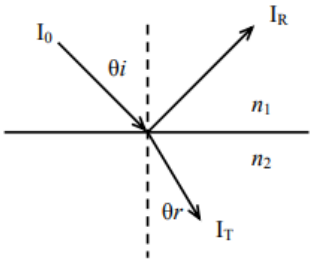

Figura 4: Representación de la ley de Snell.

donde n_1 y n_2 son los índices de refracción de los dos medios, θ_i y θ_r los ángulos de la luz incidida y transmitida, y I_0, I_R e I_T la intensidad de la luz de incidencia, reflejada y transmitida respectivamente. Sobre esta base, se puede estipular que:

$$n_2 \sin\theta_i = n_2 \sin\theta_r \qquad (13)$$

Siendo el valor de la reflectividad $R = I_R/I_0$, se deducen las ecuaciones de Fresnel para la reflectividad de la parte polarizada p o R_p y la parte s o R_s de la luz incidente:

$$R_p = \left[\frac{\tan(\theta_i - \theta_r)}{\tan(\theta_i + \theta_r)}\right]^2 \quad R_s = \left[\frac{\sin(\theta_i - \theta_r)}{\sin(\theta_i + \theta_r)}\right]^2 \qquad (14)$$

De manera que, R_p y R_s son función de la luz incidente θ_i. Siendo n_1=1 para el aire y n_2=1.33 para el agua pura se pueden obtener los distintos valores de reflectividad para cada ángulo, representados en la Figura 5.

Como se puede observar, existe un ángulo θ_B donde el valor de R_p tiende a 0, valor que puede ser deducido de su ecuación de Fresnel, para la que $\tan(\theta_i + \theta_r) = \infty$.

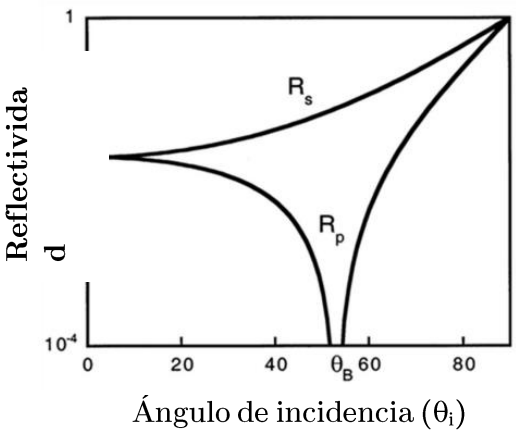

Figura 5: Valores de R_s y R_p como función del ángulo θ_i para una interfase de Fresnel entre aire y agua.

Viendo que para ello $\theta_i + \theta_r = \pi/2$, y junto a la ecuación de Snell anteriormente mencionada, se deduce:

$$n_1 \sin\theta_B = n_2 \sin(\pi/2 - \theta_B) = n_2 \cos\theta_B \quad (15)$$

donde:

$$\theta_B = \tan^{-1}\left(\frac{n_2}{n_1}\right) \quad (16)$$

Así, para un valor de n_1=1 y n_2=1.33 da un valor final de $\theta_B \approx 53.1^{\circ}$, ángulo donde en la interfase aire-agua, toda radiación p-polarizada será transmitida. Sin embargo, si depositamos una monocapa en la interfase ésta producirá un cambio en el índice de refracción y, por tanto, se producirá reflexión.

El equipo I-Elli2000 empleado en este trabajo diseñado por Nanofilm (Göttingen, Alemania), se compone de un láser verde (Nd:YAG, >20 mW, 532nm) que produce un rayo de luz de 1.3 mm de diámetro con polarización p tras atravesar un polarizador. Ese haz incide sobre la interfase con un ángulo de incidencia *i*=53.1º. La intensidad de luz refractada es absorbida por una trampa de luz situada en el fondo de la subfase, mientras que la reflejada pasa a través de un objetivo con distancia focal igual a 20 mm y llega a una cámara CCD de alta sensibilidad. La cámara CCD es capaz de registrar en forma electrónica la intensidad y el punto de llegada de pequeñísimas cantidades de luz, que son convertidas a imágenes de mapa de bits (768 x 562 píxeles), para su representación y análisis a través de la aplicación informática que controla el equipo. Finalmente, se obtiene una imagen con una resolución lateral de 2 µm.

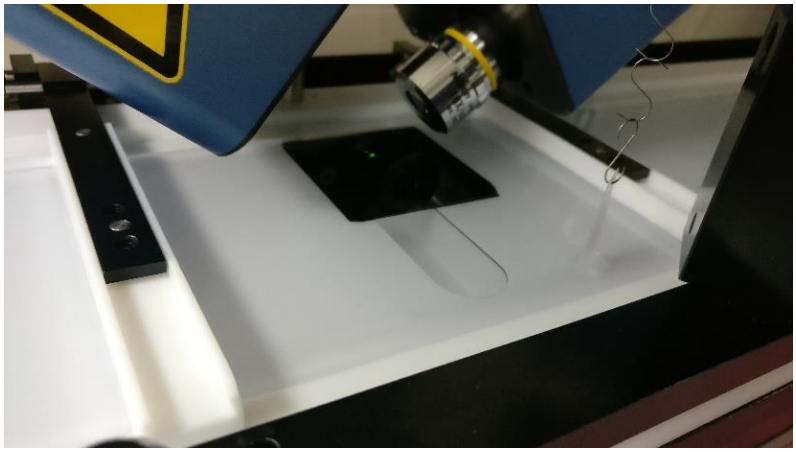

Figura 6: Imagen del equipo de BAM.

Como método para el estudio de posibles anisotropías en los dominios, está equipado con un analizador frente a la cámara. De este modo, mediante un cambio en el ángulo del analizador respecto a la dirección de polarización p, luz incidente, se pueden observar diferencias en el contraste dentro de un mismo dominio, fenómeno indicativo de una diferente orientación molecular.

Para evitar ruido producido por posibles vibraciones, tanto el microscopio como la balanza están sobre una mesa antivibratoria Halcyonics MOD-2S (Göttingen, Alemania).

2. TÉCNICAS DE FORMACIÓN Y CARACTERIZACIÓN DE MONOCAPAS EN LA INTERFASE AIRE-SÓLIDO

Al igual que en el apartado 1 de este capítulo, se procede al desarrollo de las técnicas utilizadas, en este caso, para la caracterización de monocapas en la interfase aire-sólido.

2.1. TRANSFERENCIA DE MONOCAPAS A SUSTRATOS SÓLIDOS

Tras formar una monocapa insoluble en la interfase aire-agua, un soporte sólido o sustrato puede ser puesto en contacto con ésta, siendo, mediante *vertical lifting*, depositada sobre el mismo y dando lugar a una estructura supramolecular con características definidas. Tal y como se ha indicado en la Introducción, este proceso es conocido como Langmuir-Blodgett, LB, en honor a los científicos que descubrieron esta técnica[6]. En caso de repetir el proceso sobre el mismo sustrato, serán depositadas capas adicionales en la superficie del sustrato dando lugar a un sistema de multicapas mientras que la barrera de la balanza comprime para compensar la pérdida de área y realizar todas las transferencias a la misma presión.

Las monocapas de Langmuir-Blodgett son formadas cuando el soporte cruza verticalmente la monocapa depositada en la interfase y existen tres tipos en función de la deposición, denominadas X, Y o Z[7].

La deposición tipo Y se produce cuando, una vez depositada la primera monocapa, se producen nuevas deposiciones al pasar el soporte de forma ascendente y descendente, de forma que la organización molecular es cabeza-cabeza, cola-cola, Figura 7, es decir, un ordenamiento alterno de la parte hidrófila e hidrófoba de las monocapas respecto al sustrato. Para los casos X y Z todas las monocapas son

depositadas con la misma orientación las unas respecto a las otras, con la parte hidrófoba o hidrófila más cercana al soporte respectivamente, Figura 8.

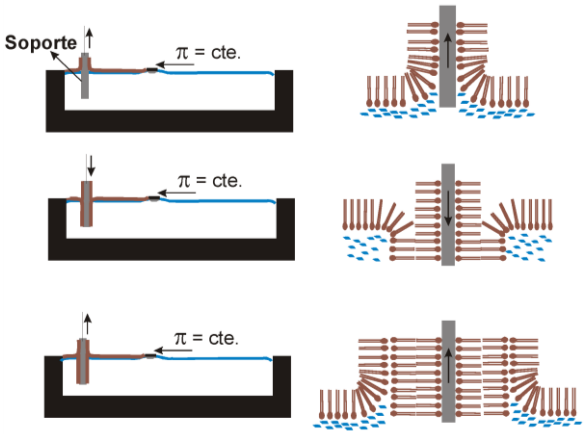

Figura 7: esquema proceso de deposición tipo Y.

Por otra parte, cuando la monocapa es muy rígida para un proceso de LB, se puede llevar a cabo una deposición Langmuir-Schaefer, LS, donde el sustrato toca la monocapa horizontalmente al colocarse de forma paralela. En el caso de multicapas, la mayor parte de deposiciones son de tipo X, aunque también existen deposiciones de tipo Y[8,9]. Además, se pueden encontrar otros métodos alternativos de transferencia como el de Schulman[10] y el de Kossi y Leblanc[11], que usan tanto la deposición vertical como la horizontal anteriormente mencionadas.

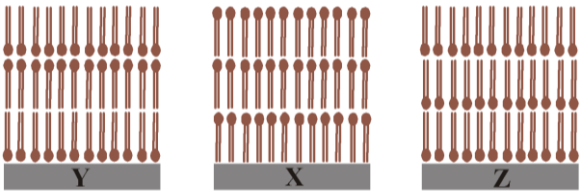

Figura 8: Esquema de deposiciones X, Y, Z.

Adicionalmente a las variables que afectan al proceso de transferencia, como la temperatura, el pH, la velocidad de inmersión y emersión del soporte o la presión de

compresión durante la deposición, entre otros, para el éxito de este proceso, la naturaleza del sustrato y de las moléculas que forman la monocapa son de vital importancia, ya que no todas son válidas.

En relación al tipo de soporte a emplear, el material utilizado dependerá de la técnica con la cual se vaya a caracterizar posteriormente la monocapa depositada, así como de las posibles interacciones existentes entre ambos. Para algunos materiales, la deposición está asociada a un cambio de fase desde una fase bidimensional líquido cristalino (Lc) sobre la interfase acuosa a una forma sólida cristalina (S) sobre el soporte. En cuanto a la eficiencia del proceso, ésta es determinada mediante la ratio de transferencia[12], τ:

$$\tau = \frac{A_L}{A_S} \tag{17}$$

donde A_L es la disminución del área ocupada por la monocapa sobre la interfase aire-agua para mantener la presión constante y A_S es el área del sustrato utilizado en la transferencia. Autores como Honig[13] sugirieron nuevos parámetros con el fin de tener en cuenta efectos como la evaporación, desorción o disolución de las moléculas en la subfase durante la transferencia o colapso:

$$\phi = \frac{\tau_u}{\tau_d} \tag{18}$$

donde τ_u y τ_d son las relaciones de transferencia obtenidas en la emersión e inmersión del soporte sólido, respectivamente. De esta manera, en una transferencia tipo X, Y o Z los valores de ϕ serán de 0, 1 o ∞, respectivamente.

En nuestro caso, la tranferencia tanto de monocapas como de multicapas a soportes sólidos desde la balanza de Langmuir fue realizada mediante la técnica de Langmuir-Schaefer, LS, sobre sustratos de cristal para las medidas de FT-IRRAS y de cuarzo para las medidas de dicroísmo circular y UV-Visible, Para todas las transferencias realizadas en este trabajo, la ratio de transferencia τ ha sido cercano a la unidad.

2.2. ESPECTROSCOPÍA DE ABSORCIÓN UV-VISIBLE

La espectroscopía de absorción es una técnica que estudia la interacción de la radiación electromagnética con la materia, en este caso; comparando su intensidad antes y después de interaccionar con la muestra. Electrónicamente, se basa en la absorción de fotones por las sustancias depositadas en el sustrato y la siguiente promoción electrónica de un nivel fundamental a uno excitado. Cada molécula puede absorber a distintas longitudes de onda, determinada por la diferencia en los niveles de energía disponibles en el compuesto. Finalmente, la energía transferida por los fotones absorbidos es perdida por medios no radiantes, como calor, entre otros[14].

En un espectofotómetro UV-Vis, se hace incidir un haz de luz de Intensidad inicial conocida I_0, y se compara con la intensidad del haz tras atravesar la muestra I. La transmitancia es la relación entre ambos, en la cual la absorbancia *A*, está basada:

$$A = -\log_{10} T = -\log_{10}\left(\frac{I}{I_0}\right) \tag{19}$$

En caso de estar las especies absorbentes en solución, se relaciona esta absorbancia *A* con la concentración *c* mediante la Ley de Lambert-Beer[15-17]:

$$A = -\log_{10}\left(\frac{I}{I_0}\right) = \varepsilon \cdot l \cdot c \tag{20}$$

donde ε es la constante de absortividad molar o coeficiente de extinción específico de ese compuesto, l es el paso de la muestra y c la concentración de la especie absorbente. El haz de luz de un espectrofotómetro suele ser de una bombilla incandescente para las longitudes de onda visibles y de una lámpara de arco de deuterio para el ultravioleta. El haz llega a un monocromador, donde se separa las diferentes longitudes de onda, y se hace incidir sobre la muestra, tras lo que se mida la intensidad I en un detector de fotodiodo o CCD.

Figura 9: Equipo de absorción UV-visible Cary 100 Bio.

Los espectros de absorción UV-visible se obtuvieron en un espectrofotómetro Varian Cary 100 Bio, Figura 9. Las medidas realizadas de las mono- y multicapas fueron realizadas sobre soportes de cuarzo. De igual manera, se realizaron los espectros de disoluciones orgánicas, empleando cubetas de cuarzo Hellma de paso óptico 1 cm.

2.3. DICROISMO CIRCULAR (CD)

Un rayo de luz polarizada en un plano se puede descomponer en dos componentes polarizados circularmente, uno a la derecha (RCP) y otro a la izquierda (LCP). Estos componentes son de la misma amplitud y están en fase. Cuando la luz polarizada pasa a través de un medio ópticamente activo, la velocidad entre RCP y LCP varía, así como la absortividad molar de las mismas. Esto provoca una rotación del plano de polarización que varía en función de la longitud de onda, dando lugar a espectros donde se muestra la rotación o elipticidad frente a dicha la longitud de onda[18].

Partiendo de la ley de Lambert-Beer y sabiendo que el valor obtenido al medir el CD es la diferencia entre la luz polarizada a la izquierda A_L y a la derecha A_R, se obtiene una Absorbancia total para cada longitud de onda:

$$\Delta A(\lambda) = A_{L(\lambda)} - A_{R(\lambda)} = \left[\varepsilon_{L(\lambda)} - \varepsilon_{R(\lambda)}\right] \cdot l \cdot c = \Delta\varepsilon \cdot l \cdot c \qquad (21)$$

donde A es la absorbancia de la muestra, c la concentración del cromóforo, l la longitud de paso óptico que contiene la muestra y ε la absorptividad molar. Al atravesar el medio quiral, la luz deja de estar circularmente polarizada para definir una elipse, Figura 10. El ángulo θ, llamado elipticidad, obtenido de la relación entre el eje menor y el mayor, la tangente, es una consecuencia directa de la presencia de dicroísmo circular.

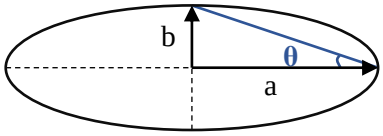

$$\tan\theta = b/a \rightarrow \theta = \tan^{-1}(b/a) \qquad (21)$$

Figura 10: Representación de la elipticidad.

Un equipo de CD consta de una fuente de luz, la cual genera el haz que pasa por un monocromador, donde se separan las distintas longitudes de onda. Tras atravesar un polarizador lineal para polarizar la luz en un plano y un modulador fotoelástico (PEM) para modular la polarización de la luz, la luz incide finalmente sobre la muestra. Por último, un fotomultiplicador mide el cambio de elipticidad producido por la muestra ópticamente activa.

Figura 11: Equipo de dicroísmo circular Jasco J-1500.

Las medidas de dicroísmo circular fueron realizadas usando un espectrofotómetro UV-Vis Jasco J-1500, Figura 11, en el Servicio Central de Apoyo a la Investigación (SCAI) de la Universidad de Córdoba. Los espectros fueron medidos en un intervalo de 190 a 350 nm con una resolución de 0.1 nm. Cada medida se llevó a cabo con 2 segundos como tiempo de respuesta, una velocidad de escaneo de 15 nm/min. La ratio señal/ruido fue mejorado por la acumulación de 3 medidas de la misma muestra.

3. TÉCNICA DE CARACTERIZACIÓN EN MEDIO LÍQUIDO

Para comprender lo que sucede en la interfase aire-agua y comprobar la estabilidad de diversos compuestos se realizaron medidas de dispersión de luz dinámica.

3.1. DISPERSIÓN DE LUZ DINÁMICA (DLS)

En esta técnica se hace incidir un haz láser (λ = 632 nm) a una muestra líquida en una cubeta de cuarzo. Gran parte de éste traspasa la muestra, pero una pequeña parte, como consecuencia de la diferencia de índice de refracción existente entre las partículas y el disolvente, es dispersado por las partículas presentes. Estas fluctuaciones de intensidad de luz dispersada originadas debido al movimiento browniano de las partículas llegan a un detector colocado a 173º. Allí, son transformadas en una función de autocorrelación por medio de un correlador digital[19].

En una medida de DLS se registra la intensidad de luz dispersada en intervalos de tiempo de nanosegundos hasta segundos en expansión logarítmica, lo que da lugar a la función de autocorrelación de intensidades normalizada $g^{(2)}(t)$, directamente relacionada con la función de autocorrelación de campo eléctrico normalizada $g^{(1)}(t)$ mediante la relación de Siegert:

$$g^{(2)}(t) \equiv \frac{G^{(2)}(t)}{\langle i(0)i(0)\rangle} = 1 + \beta\left|g^{(2)}(t)\right|^2 \qquad (22)$$

donde β es un factor óptico cercano a la unidad, denominado factor de coherencia. La función de autocorrelación de campo eléctrico normalizada $g^{(1)}(t)$ está a su vez relacionada con el factor de estructura dinámico $S(q,t)$ o función de dispersión intermedia, en el caso de partículas pequeñas comparadas con q^{-1}:

$$g^{(1)}(t) = \frac{\langle E^*(t)E(t)\rangle}{\langle E^*(0)E(0)\rangle} = \frac{S(q,t)}{S(q)} \tag{23}$$

sabiendo que q está definido como el ventor de onda:

$$q = \frac{4\pi n_0}{\lambda}\sin(\theta/2) \tag{24}$$

siendo λ la longitud de onda del láser incidente, n_0 el índice de refracción de la muestra y θ el ángulo en que el detector está ubicado respecto al haz de luz transmitido. Sólo para muestras donde nuestro sistema en disolución sea esférico, monodisperso y de partículas pequeñas la función de autocorrelación de campo eléctrico normalizada $g^{(1)}(t)$ puede obtenerse el coeficiente de difusión de estas partículas según la ecuación:

$$g^{(1)}(t) = exp(-\Gamma t) = exp\left(-\frac{t}{\tau}\right) = exp(-Dq^2t) \tag{25}$$

donde Γ es la tasa de decaimiento, τ el tiempo de relajación característico y D el coeficiente de difusión de la partícula. En muestras donde haya presente una elevada polidispersidad, se utilizan distintos métodos alternativos para obtener la distribución de coeficientes de difusión y por tanto de tamaños, siendo entre éstos, el más sencillo, el método de cumulantes.

Finalmente, si a las premisas anteriores le añadimos condiciones de alta dilución, envitando así interacciones entre las partículas, se puede aplicar la ecuación de Stokes-Einstein para obtener el tamaño hidrodinámico promedio de las partículas:

$$D = \frac{k_B T}{6\pi\eta r_h} \tag{26}$$

siendo k_B la constante de Boltzmann, T la temperatura absoluta, η la viscosidad de cizalla del disolvente y r_h el radio hidrodinámico de la partícula.

Un sistema de DLS consta de varios componentes. Los principales son, un láser, utilizado como fuente de luz con el que se ilumina la muestra y un detector a un ángulo determinado, que medirá la intensidad recibida, tras pasar por un atenuador para reducirla y no saturarse. Este ángulo, en nuestro caso, es de 173º, cercano a la detección de retrodispersión, tecnología patentada y denominada NIBS[20] (retrodispersión no invasiva). La retrodispersión reduce el efecto conocido como dispersión múltiple, donde la luz dispersada por una partícula es dispersada por nuevas partículas; evita la medición de contaminantes como el polvo, al ser más grandes que nuestras partículas y dispersan hacia adelante, y al pasar el haz por una ruta más corta de la muestra, permitiendo medir a mayores concentraciones[21]. El experimento de dispersión de luz dinámica (DLS) de la alícuota de subfase acuosa tras la realización de isotermas fue llevado a cabo usando un Zetasizer Nano, Figura 12, infraestructura singular perteneciente al Instituto Universitario de Investigación en Química Fina y Nanoquímica (IUNAN) de la UCO.

Figura 12: Equipo de DLS ZetasizerNano.

4. TRATAMIENTO DE DATOS

La interpretación y representación de los datos obtenidos de forma digital en cada técnica fue llevada a cabo con los programas de hoja de cálculo: SigmaPlot 12.0,

OriginPro 9.0c y Microsoft Office: Excel 2016. Para el tratamiento y diseño de imágenes se han usado los editores gráficos: XnConvert, Adobe Photoshop CC 2018, CorelDRAW X7, Adobe Illustrator CC 2019, Autodesk Maya 2018 y SketchUp Pro 2018.

5. BIBLIOGRAFÍA

1. Langmuir, I. The constitution and fundamental properties of solids and liquids. II. Liquids. *J. Am. Chem. Soc.* **39**, 1848–1906 (1917).
2. Grüniger, H., Möbius, D. & Meyer, H. Enhanced light reflection by dye monolayers at the air-water interface. *J. Chem. Phys.* **79**, 3701–3710 (1983).
3. David Brewster, L. IX. On the laws which regulate the polarisation of light by reflexion from transparent bodies. *Philos. Trans. R. Soc. London* 125–159 (1815).
4. Hénon, S. & Meunier, J. Microscope at the Brewster angle: Direct observation of first-order phase transitions in monolayers. *Rev. Sci. Instrum.* **62**, 936–939 (1991).
5. Rashed, R. A pioneer in anaclastics: Ibn Sahl on burning mirrors and lenses. *Isis* **81**, 464–491 (1990).
6. Blodgett, K. B. Monomolecular films of fatty acids on glass. *J. Am. Chem. Soc.* **56**, 495-4995 (1934).
7. Oliveira Jr., O. N. Langmuir-Blodgett Films - Properties and Possible Applicat ions. *Brazilian J. Phys.* **22**, 60–69 (1992).
8. Kato, T. Studies on the fully automatic horizontal lifting deposition of lb films using double gates. *Jpn. J. Appl. Phys.* **27**, L1358–L1360 (1988).
9. Kato, T. Overturn of molecules during the fully automatic horizontal lifting deposition using double gates. *Jpn. J. Appl. Phys.* **27**, L2128–L2130 (1988).
10. Bikerman, J. J. & Schulman, J. H. On the structure of 'built-up' films on metals. *Phys. Rev.* **53**, 909 (1938).
11. N'soukpoé-Kossi, C. N. & Leblanc, R. M. Absorption and photoacoustic spectroscopies of lutein and zeaxanthin Langmuir–Blodgett films in connection with the Haidinger's brushes. *Can. J. Chem.* **66**, 1459–1466 (2011).
12. Bikerman, J. J. On the formation and structure of multilayers. *J. Proc. R. Soc.*

A170, 130–145 (1939).

13. Honig, E. P., Hengst, J. H. T. & Den Engelsen, D. Langmuir-blodgett deposition ratios. *J. Colloid Interface Sci.* **45**, 92–102 (1973).
14. Skoog, D. A., Holler, F. J. & Crouch, S. R. *Principles of Instrumental Analysis*. *Thomson Brooks/Cole* (2007).
15. Bouguer, P. Essai d'optique sur la gradation de la lumière. *Claude Jombert* 19–22 (1729).
16. Lambert, J. H. Photometria sive de mensura et gradibus luminis, colorum et umbrae. *Eberhardt Klett.* 170 (1760).
17. Beer. Bestimmung der Absorption des rothen Lichts in farbigen Flüssigkeiten. *Ann. Phys.* **86**, 78–88 (1852).
18. G.D. Fasman. *Circular Dichroism and the Conformational Analysis of Biomolecules*. (1996).
19. Scattering, L. L. Laser Light Scattering Systems. *Anal. Chem.* **21**, 145–174 (1970).
20. Amin, S. (Norton) & Rega, C. A. (Bromborough). *Dynamic Light Scattering Based Microrheology of Complex Fluids With Improved Single-Scattering Mode Detection.* (2013).
21. Berne, B. J. & Pecora, R. *Dynamic Light Scattering with Applications to Chemistry, Biology, and Physics (Berne, Bruce J.; Pecora, Robert)*. *Courier Dover Publications* (1977).

Capítulo III

Publicaciones

Chapter III

Publications

Published on 20 Sep 2018
DOI: 10.1039/C8SM01508B

Unravelling the 2D Self-Assembly of Dipeptides at Fluid Interfaces

Pablo G. Argudo,[a] Rafael Contreras-Montoya,[b] Luis Álvarez de Cienfuegos,[b] Juan M. Cuerva,[b] Manuel Cano,a David Alba-Molina,[a] María T. Martín-Romero,[a] Luis Camacho,[a] Juan J. Giner-Casares[a]

a. Departamento de Química Física y T. Aplicada, Instituto Universitario de Investigación en Química Fina y Nanoquímica IUIQFN, Facultad de Ciencias, Universidad de Córdoba, Campus de Rabanales, Ed. Marie Curie, E-14071 Córdoba, Spain.
b. Departamento de Química Orgánica, Facultad de Ciencias, Universidad de Granada, (UGR), C. U. Fuentenueva, E-18071 Granada, Spain.

Dipeptides self-assemble onto supramolecular structures showing plenty of applications in nanotechnology and biomedical fields. A set of Fmoc-dipeptides with different aminoacid sequences has been synthesized and their self-assembly at fluid interfaces has been assessed. The relevant molecular parameters for achieving an efficient 2D self-assembly process have been established. The self-assembled nanostructures of Fmoc-dipeptides displayed significant chirality and retained the chemical functionality of the aminoacids. The impact of the sequence in the final supramolecular structure has been evaluated in high detail using *in situ* characterization techniques at air/water interface. This study provides a general route for the 2D self-assembly of Fmoc-dipeptides.

Introduction

Dipeptides are an exciting building block in nanotechnology.[1–8] Dipeptides display some advantageous features among self-assembling organic molecules, such as easy choice in sequence during synthesis, readily available chiral features and high biocompatibility, with Fmoc-dipeptides as highly promising structure, especially in biological applications.[9] Intracellular NO delivery was achieved by a purposefully self-assembling dipeptide.[10] Fmoc (9-fluorenylmethyloxycarbonyl) group contributes to enhance the self-assembly of the dipeptides onto well-defined nanostructures through solvophobic interactions, also providing amphiphilic character.[11–13] Self-assembly of Fmoc-dipeptides in bulk solution is able to render nanowires with excellent chirality and energy transfer features.[14,15] Intriguingly, self-assembled nanowires of dipeptides are connected to the core recognition motif in Alzheimer disease.[16] Supramolecular structures of dipeptides are also promising candidates as antibacterial agents for membrane disruption, alternatively to standard antibiotics that promote acquired bacterial resistance.[17] The amphiphilic character of the Fmoc-dipeptides leads to interesting applications as ultrathin membranes for local control of physicochemical parameters.[18] Remarkably, the local value of pH is crucial for the efficient self-assembly of the dipeptides.[19] Moreover, the Fmoc-dipeptides are highly interesting in technological applications based in self-assembled nanostructures by purposefully designed building blocks.[20] Stable emulsions can be fabricated using Fmoc-dipeptides as stabilizing surfactants at the oil/water interface, with the possibility of tuning the emulsion properties by simply varying the sequence of the dipeptide. The self-assembly process at the oil/water interface is also promoted by other similar groups to Fmoc, *e.g.*, Pyrene, however Fmoc yields optimum results.[21,22] The self-assembly capability of a given dipeptide sequence might determine the actual performance in applications as *in vivo* self-assembly for biomedical purposes.[23,24]

A large body of research is devoted to the self-assembly of dipeptides to render functional and interesting nanostructures. Orientation on the influence of the

aminoacid sequence in the self-assembly process that might guide a purposefully chemical synthesis is highly desirable.[25] Nevertheless much of the published work has been restricted to the isotropic growth in bulk solution mediated by a self-assembly process triggered by different stimuli, such as pH, solvent, temperature or enzymatic.[26] The influence of many experimental factors makes very difficult to predict the gel-forming capacity of specific sequences of aminoacids in bulk solution, although recent works have tried to achieve this goal using a combination of sophisticated computational and true data analysis within families of peptides.[27,28] On the contrary, a systematic study involving the self-assembly of small peptides in 2D and connecting the aminoacid sequence with the achieved nanostructure has never been carried out. The possibility to create functional surfaces simply by coating with small peptides brings many new applications in bio- and nanotechnology, such as biologically active surfaces that can interact with cells, antimicrobial, superhydrophobic, optical or chiroptical surfaces.[29,30]

Here we present a framework for the 2D self-assembly of Fmoc-dipeptides at fluid interfaces. Relevant molecular parameters are defined in terms of aminoacid sequence and experimentally tested. The supramolecular structures were successfully built from the 2D self-assembly of the Fmoc-dipeptides at the air/water interface and studied in detail by utilizing the Langmuir technique. The air/water interface provides a rather experimentally simple and reliable route for the 2D self-assembly of the Fmoc-dipeptides.[31] Note that in all cases we use Fmoc-derived dipeptides herein, thus taking advantage of the amphiphilic character promoted by the self-assembling Fmoc group. The experimental techniques for characterization included herein assured the *in-situ* measure of the nanostructures exclusively placed at the air/water interface, with no contribution from bulk solution. In addition to provide a comprehensive model for 2D self-assembly of dipeptides at fluid interfaces, detailed information on the molecular arrangement of the dipeptide units at the interface is shown.[32] Guiding rules for the chemical design of Fmoc-dipeptides that efficiently self-assemble at fluid interfaces are provided by relating the

aminoacid sequence of the Fmoc-dipeptides with the self-assembling capabilities.

Results and Discussion

A set of Fmoc-dipeptides was synthesized, see Scheme 1, section SI1. Two Fmoc-aminoacids were included as well for further confirming the range of application of the molecular parameters defined in our model, Fmoc-Y (Tyrosine) and Fmoc-F (Phenylalanine). A carboxyl group was included as end group in all cases to assure the sole dependence of the nanostructures on the aminoacid sequence.[33] The aqueous subphase was in all cases a diluted HCl solution (pH = 2) to enhance the self-assembly of the Fmoc-dipeptides on the air/water interface.[34] The Fmoc-dipeptides were not located at the air/water interface when using Milli-Q water with almost neutral pH, see SI6. The following dipeptides were able to self-assemble at the air/water interface: Fmoc-CF (Cysteine-Phenylalanine), Fmoc-MF (Methionine-Phenylalanine), and Fmoc-FF (diphenylalanine). On the other hand, the following dipeptides were not anchored at the air/water interface, instead being solved in the bulk water solution: Fmoc-LG (Leucine-Glycine), Fmoc-AA (dialanine), Fmoc-GG (diglycine), and Fmoc-RF (Arginine- Phenylalanine), see Figures SI2,3.

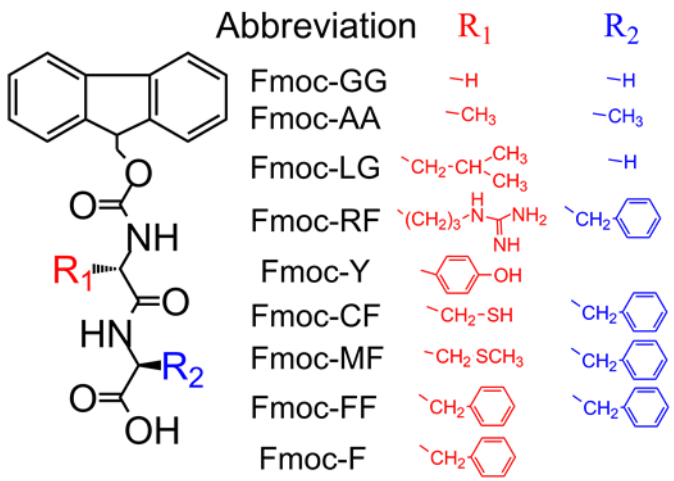

Scheme 1. Molecular structure of the Fmoc-dipeptides.

The presence of the not self-assembling dipeptides at the air/water interface was ruled out according to the absence of UV-vis spectroscopy signal and any observable microstructure, see SI4,5. The layers of Fmoc-dipeptides were compressed at a speed of 0.03 nm^2 min^{-1} $molecule^{-1}$, typically considered in Langmuir studies as a speed value suitable for studying equilibrium structures. Unfortunately, the surface active Fmoc-dipeptides were transferred into the water subphase after compression. Therefore, experiments dealing the kinetics of assembly of the Fmoc-dipeptides could not be performed.

Note all the Fmoc-dipeptides displayed a certain amphiphilic character provided by the hydrophobic and self-stacking Fmoc group and a markedly polar headgroup, *i.e.*, the carboxylic acid. Intriguingly, such amphiphilicity does not guarantee the interfacial self-assembly of all the Fmoc-dipeptides. This finding was in agreement with the report on Fmoc-dipeptides as stabilizing agents for oil/water emulsions by Ulijn *et al.*, who found that the aminoacid sequence strongly determines the residence of the Fmoc-dipeptides at the oil/water interface. The chemical modification of the sequence of the Fmoc-dipeptides could then lead to an enhanced stability of the oil/water emulsions based on Fmoc-dipeptides.[21] Herein we offer insights on the 2D behavior of Fmoc-dipeptides at the air/water interface that can be extended to the formulation of oil/water emulsions stabilized by Fmoc-dipeptides. Inspired by the work by Adams and Frith, the partition coefficient P and water solubility S as relevant and easily calculated molecular parameters were obtained for all Fmoc-dipeptides.[35] The Chemicalize/ChemAxon platform was used for performing the calculations.[36] The log P tool calculates the octanol/water partition coefficient, based on the work by Viswanadhan *et al.* and modified according to Klopman.[37,38] The log S tool uses a fragment-based method that identifies different structural fragments in the molecule and calculates their relative contribution to the solubility coefficient.[39] Note the log P and – log S values of the Fmoc-RF indicate a comparatively higher solubility of Fmoc-RF in water than expected from the partition coefficient. The greater solubility of Fmoc-RF is ascribed to the Arginine

residue, displaying a larger number of sites for H-bond formation with water.

Two regimes of self-assembling capabilities of Fmoc-dipeptides were obtained, see Figure 1. The Fmoc-dipeptides tended to be solved in bulk solution rather than self-assemble at the air/water interface for low values of log P and –log S (high hydrophilicity). The soluble Fmoc-dipeptides formed aggregates in bulk water, as confirmed by dynamic light scattering measurements, see SI7.[40] Oppositely, those Fmoc-dipeptides with high values of log P and – log S were able to self-assemble into well-defined supramolecular structures at the air/water interface (high hydrophobicity). The range of values for the partition coefficient of the tested Fmoc-dipeptides extended *ca.* five orders of magnitude.

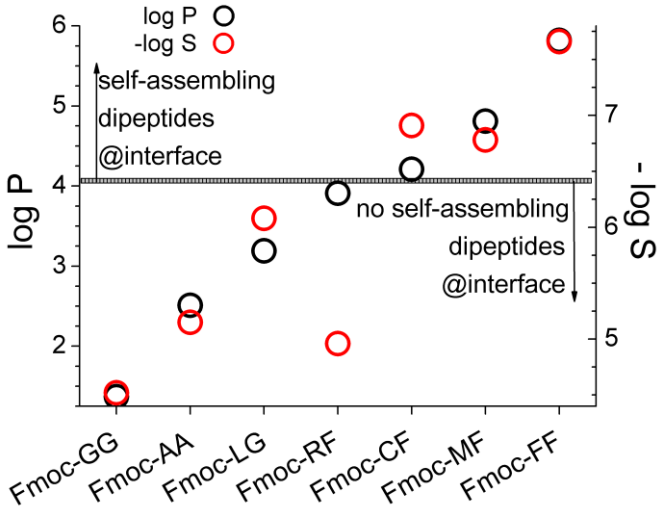

Figure 1. Values of log P (black circles) and log S (red circles) for the Fmoc-dipeptides. Two regimes can be differentiated: Zone of no self-assembling dipeptides for log P and – log S lower than 4.1 and 6.4, respectively; Zone of self-assembling dipeptides for log P and – log S higher than 4.1 and 6.4, respectively. A transition zone is indicated as a dividing box.

A transition zone at log P of *ca.* 4.1 and – log S of *ca.* 6.4 was found as the limit between the two regimes. This limit might serve as an indication when chemically

designing dipeptide derivatives for stabilizing oil/water emulsions. The Fmoc-dipeptides were chosen to fully cover a representative range of values of solubility and partition coefficient. Whereas these findings might not be applied to all derivatives of Fmoc-dipeptides, this criterion is valid for our set of Fmoc-dipeptides and provides a semiquantitative approximation for the chemical design of dipeptides for 2D self-assembly.

This criterion for defining the efficient 2D interfacial self-assembly is exclusive for the Fmoc-dipeptides. Fmoc-Y and Fmoc-F display log P = 4.4 and 4.7 and –log S = 5.5 and 5.9, respectively. Fmoc-F was able to self-assemble at the air/water interface, as opposed to Fmoc-Y, thus probing their distinct behaviour with respect to the Fmoc-dipeptides.

Brewster Angle Microscopy (BAM) is an optical technique that allowed direct visualization solely of the microstructures formed by the Fmoc-dipeptides in situ at the air/water interface. No contribution from bulk solution was recorded in the BAM pictures. The presence of the Fmoc-dipeptides induced the change of refractive index of the air/water interface and therefore the visualization of the microstructures was achieved. Figure 2 and SI8-11 shows the BAM pictures of the Fmoc-dipeptides acquired at the air/water interface. Well-defined elongated ribbon-like microstructures were observed for Fmoc-MF and Fmoc-FF, arising from stacking and lateral packing of the Fmoc-dipeptide molecules. The thickness of the microstructures was 2.6 ± 0.8 and 2.4 ± 0.6 μm for the Fmoc-MF and Fmoc-FF dipeptides, respectively. A modest influence of the sequence on the final morphology of the microstructures was observed.

Electron microscopy measurements confirmed the thickness value of the supramolecular structure, with a thickness of 1.0 ± 0.5 μm, see below. 2D self-assembly led to larger assemblies than those obtained by 3D assembly in bulk solution, typically with a thickness from *ca.* 20 to 200 nm.[40,41] Note the thickness values were obtained by measuring the image with the ImageJ software, and therefore these values might be taken only as a semiquantitative approach. The

apparent discrepancy between the two values of thickness was ascribed to the different conditions for measuring, *e. g.*, the electron microscopy picture was taken under high vacuum and extremely low content of water, whereas the BAM pictures were taken in contact with the water surface in laboratory conditions. Therefore, the lower value of thickness for the nanostructures under vacuum conditions was expected due to the drying of the sample.

Remarkably, decrease of the available surface area was able to reduce the distance between the microstructures formed by the Fmoc-dipeptides with no significant modification of the thickness. Further compression induced packing of the microstructures onto a continuous solid film as observed by BAM, see SI8-11. The temperature was kept constant at 21 ºC, given the significant influence of temperature on the Fmoc-dipeptide nanostructures.[42]

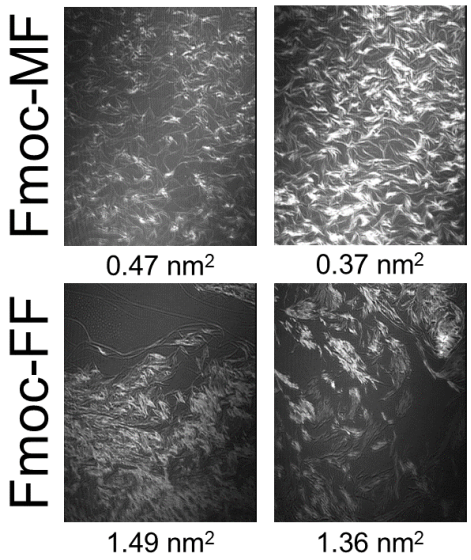

Figure 2. Brewster Angle Microscopy (BAM) pictures at the air/water interface of Fmoc-MF and Fmoc-FF (top and bottom pictures, respectively). The value of available surface area per molecule of Fmoc-dipeptide is included at the bottom of each picture. The width of each frame corresponds to 215 μm.

The Fmoc-dipeptides self-assembled at the air/water interface display chirality.

The supramolecular structures formed by Fmoc-dipeptides could be readily transferred to a solid support by gently touching the air/water interface with a solid support, *i. e*., using the Langmuir-Schaeffer technique. The fidelity of the transfer process Fmoc-dipeptides onto solid substrates was checked by comparing the UV-vis spectra obtained by transmission (solid substrates) and reflection (air/liquid interface) UV-vis spectroscopy. The shape and relative intensity of the band remains constant after the transference, see Figure SI12. We therefore assume that the perturbation induced by the transfer of the layers of Fmoc-dipeptides is not significant.

A significant circular dichroism (CD) signal related to the supramolecular organization of the Fmoc group into highly ordered self-assembled structures was obtained, see Figure 3, SI13,14.

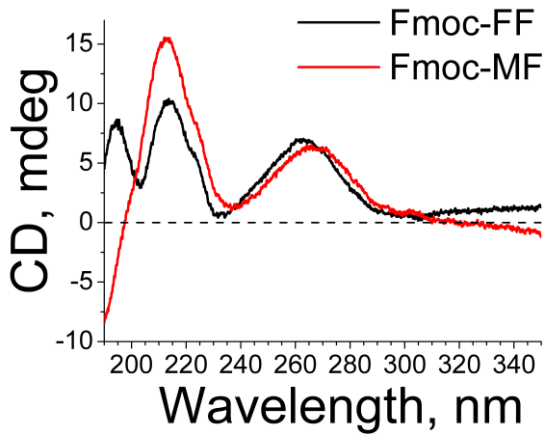

Figure 3. Circular dichroism spectra of the 2D self-assembled Fmoc-FF (black line, 15 layers transferred), Fmoc-MF (red line, 10 layers transferred) transferred to a quartz support by the Langmuir-Schaeffer technique.

Both chiral centers for all the Fmoc-dipeptides included in this study were (S,S). Two positive bands for Fmoc-MF and Fmoc-FF at *ca.* 212 nm and 264 nm was related to n→π* and π→π* transitions of the Fmoc group, respectively. These two

bands indicated a similar self-assembly to related Fmoc-dipeptides.[43] This arrangement was confirmed by the band at *ca.* 194 nm from the Fmoc-FF supramolecular structures, typically arising from the interaction of the π-π* transition of the amide I band with the aromatic rings of the dipeptides.[44] The positive sign of all CD bands indicated a unique supramolecular organization of the Fmoc-FF obtained using this 2D self-assembly route, probably imposed by the arrested organization at the air/water interface in contrast to 3D bulk formation of hydrogels with negative signals in CD, see SI14.[45,46]

Quantitative information on the presence and orientation of the Fmoc groups at the air/water interface could be conveniently obtained by in situ UV-vis reflection spectroscopy. The signal was recorded exclusively at the air/water interface, based on the increase of reflection of incoming radiation from the presence of the Fmoc-dipeptide molecules at the interface according to eq. (1):

$$\Delta R_{norm} = A\ x\ \Delta R = \frac{2.303\ x\ 10^{17}\ f_0 \varepsilon}{N_A}\sqrt{R_S} = 5.41\ x\ 10^{-8} f_0 \varepsilon \qquad (1)$$

where ΔR_{norm} has $nm^2 \cdot molec^{-1}$ units, R_S is the air/water interface reflectivity, A and ε are the available surface area and the absorption coefficient per Fmoc-dipeptide molecule, respectively.[47] f_0 is the orientation factor, accounting for a preferential orientation of the transition dipole of the Fmoc group at the self-assembled supramolecular structures. The value of f_0 was experimentally obtained from the UV-vis reflection spectra. Limit values of f_0 = 1.5 and 0 are defined, indicating that the transition dipole of Fmoc is either parallel or perpendicular to the water surface, respectively, see SI15. This is the first study providing quantitative insights on the molecular arrangement of the Fmoc-dipeptides at fluid interfaces.

Figure 4 shows the 2D UV-vis reflection spectra as well as the 3D bulk transmission spectra for the Fmoc-FF dipeptide. A shift to longer wavelength of *ca.* 4 nm was obtained when comparing the UV-vis reflection spectra with the bulk

spectrum. This shift corresponds to the formation of J-aggregates and local changes in polarizability in the self-assembled supramolecular structure formed by the Fmoc-FF dipeptide. The shape of the band centred at 265 nm of the Fmoc-FF 2D supramolecular structures was slightly modified when compared to the non-assembled Fmoc-FF in bulk solution. The bulk spectrum of Fmoc-FF in bulk solution was formed by four components at a 276, 265, 262, and 255 nm, with the most intense component at 265 nm. The UV-vis reflection spectra of Fmoc-FF at the air/water interface were formed by four components at a 281, 269, 262 and 258 nm, with the most intense component at 262 nm. This change in the shape of the UV-vis band was ascribed to the change of orientation of the polarization axes of the Fmoc group at the air/water interface. The Fmoc-FF molecules might display a preferential orientation at the interface that differs from bulk due to the restricted geometry of the 2D interface, as further confirmed by the CD results, see above. The relative orientation of the Fmoc group of the Fmoc-FF dipeptide at the air/water interface was assessed from the UV-vis reflection spectra. An orientation factor value of f_0 = 1.5 was obtained, indicating a parallel orientation of the longitudinal axis of the Fmoc group to the water surface. No shift in the UV-vis reflection bands is observed at different values of available surface area per Fmoc-FF molecule. Thus, the supramolecular arrangement of the Fmoc group was not modified by the decrease in the surface area of the nanowires, instead being determined by the self-assembly of the Fmoc-dipeptide units.

The aminoacid sequence of the Fmoc-dipeptides showed a significant influence on the supramolecular arrangement at the air/water interface that can be followed by in situ UV-vis reflection spectra, see SI15.1. A shift of *ca.* 4 nm for the 2D reflection spectra compared to the 3D bulk spectrum was obtained for the Fmoc-CF dipeptide, similarly to the Fmoc-FF dipeptide. However, the shape and relative intensity of the bands remained as observed in bulk solution, indicating a fixed parallel orientation of the main axis of the Fmoc group at the interface, see SI15.2. The Fmoc-MF dipeptide showed a reduced UV-vis reflection intensity when compared to the

expected values assuming an $f_0 = 1.5$, as well as further reduction with the decrease of the available surface area. A significant change in morphology of the UV-vis reflection spectra was obtained with the decrease of the available surface area, with the band at 301 nm shifting to 303 nm and a significant modification of the group of bands at 265 nm, probably indicating a change of orientation of the Fmoc group, see SI15.3.

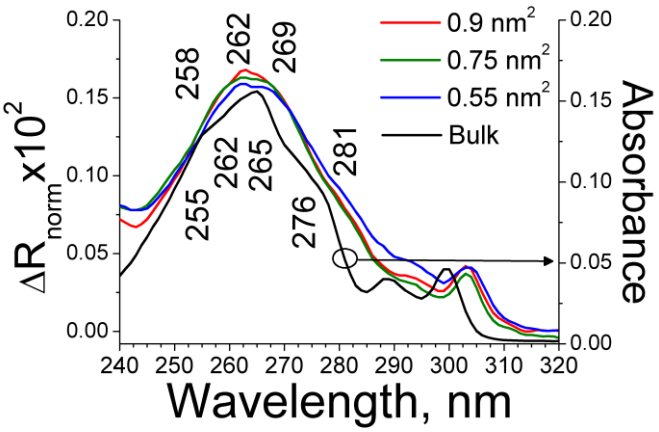

Figure 4. UV-vis reflection (red, green and blue lines indicating different values of available surface area) and bulk solution (black line) spectra for the Fmoc-FF dipeptide. Maximum values of wavelength for each band and available surface area are indicated in the inset.

Fmoc-F showed a greatly reduced intensity of the UV-vis reflection spectra and no modification of the morphology of the bands upon decrease of the available surface area, indicating a diminished residence at the interface, see SI15.4. The residence of the supramolecular structures of the Fmoc-dipeptides at the air/water interface was assessed by monitoring the maximum intensity of the UV-vis reflection band at 263-270 nm upon decrease of the available surface area. Fmoc-FF was the only Fmoc-dipeptide showing no loss of molecules onto the subphase with the decrease of the available surface area. The residence of the Fmoc-dipeptide molecules varied according to: Fmoc-FF > Fmoc-CF > Fmoc-MF, see Figure SI15.5. Therefore, high values of log P and – log S led to persistent assemblies at the

air/water interface. This trend might be applied for designing oil/water emulsions stabilized by Fmoc-dipeptides and requiring high stability against long storage times. Therefore, we conclude that the interfacial self-assembly of the Fmoc-dipeptides was directed by the sequence of each dipeptide and might be tuned by including the adequate residues.

The molecular arrangement of the Fmoc-dipeptide molecules in the self-assembled supramolecular structures was assessed using Fmoc-FF as foremost example. Molecular dynamics (MD) simulations were performed to attain a fine detail in the supramolecular structure, see Figure 5 and section SI16. The relative position of the Fmoc groups obtained by MD is experimentally tested by calculating the shift in the UV-vis spectra of the UV-vis reflection spectra of the 2D self-assembled Fmoc-dipeptides compared to the bulk solution spectrum (λ_N). The extended dipole model was used, see eq. (2) and SI17:

$$\lambda_{i,N} = \frac{\lambda_{mon}\, hc10^7}{hc10^7 + 4\lambda_{mon} \sum_{j=k}^{N} J_{1,k} \frac{(N+1-k)}{N}} \quad (2)$$

λ_{mon} is the maximum wavelength for the Fmoc-FF in bulk solution, N is the number of Fmoc-FF molecules forming the optically active supramolecular unit. $J_{1,k}$ is the interaction energy between the dipoles of the *1* and *k* Fmoc-FF molecules. Remarkably, an excellent agreement between the MD simulation results, predicting a shift of *ca.* 4 nm with the spectroscopic data showing a shift of 4 nm, see above. The Fmoc groups self-assembled in a zipper-like manner on the air/water interface, see Figure 5. The tilting values of the Fmoc groups with respect to the air/water interface were 76.4º and 72.5º for the longitudinal and transversal axis, respectively. The average distance between the rows of Fmoc groups was 3.4 Å and between neighbouring Fmoc was 10.7 Å, see Figure 5. Note that the rows of Fmoc-FF were shifted 2.5 Å upwards with respect to the front row.

The 2D self-assembly led not only to well-defined supramolecular structures, but

also provided a direct route to include additional building blocks, as demonstrated by Banerjee *et al.* in hydrogels based on Fmoc-dipeptides including graphene.[48] Our previous work shows the possibility of combining dipeptides with Fe nanoparticles.[45] The chemical functionality provided by each aminoacid was conveniently maintained in the nanostructures after the 2D self-assembly. The self-assembled Fmoc-dipeptides presented here showed a highly versatile nanostructure that could be combined with inorganic nanoparticles to form composites at the nanoscale.[49–51]

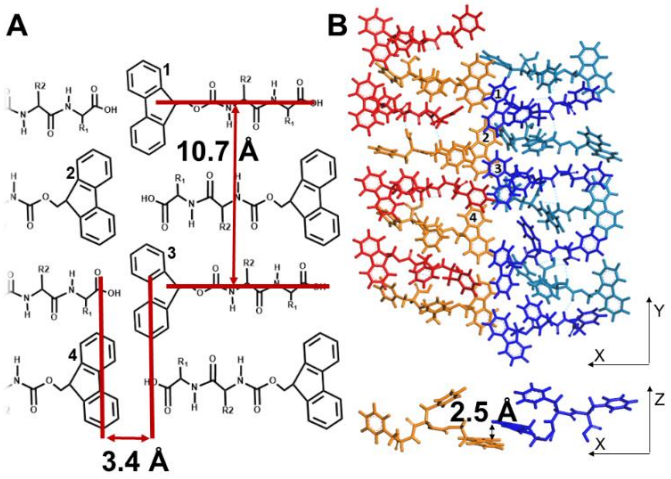

Figure 5. A) Molecular sketch of the arrangement of the inter-molecular distance of Fmoc groups. B) Caption of molecular dynamics simulations for the Fmoc-FF dipeptide on the XY (interface) and XZ planes. Numbers 1 to 4 are included to guide the correspondence of atoms between the two schemes.

The attachment of Au nanoparticles with a diameter of 94 ± 5 nm to the 2D self-assembled Fmoc-CF was achieved under simple immersion in a solution of Au nanoparticles of the ribbon-like structures transferred to a glass support. The Fmoc-CF was selected for its chemical functionality allowing the covalent binding of Au nanoparticles. The cysteine residue of the Fmoc-CF was used as a chemical linker to the Au nanoparticles via thiol chemistry, see scheme 1.[52] The Au nanoparticles were

attached to the surface of the Fmoc-CF supramolecular structures as a dense monolayer, with certain regions showing an additional layer of nanoparticles, see Figure 6. The supramolecular structures of Fmoc-CF showed an average thickness of 1.0 ± 0.5 μm, in agreement with the BAM pictures, see above. The possibility of using the chemical function of the aminoacid residue of the Fmoc-dipeptide even after forming the assemblies is largely appealing. Moreover, this experimental result supports the proposed supramolecular arrangement. Additional chemical functionalities might be included in the Fmoc-dipeptides, allowing the formation of well-defined hybrid nanocomposites.

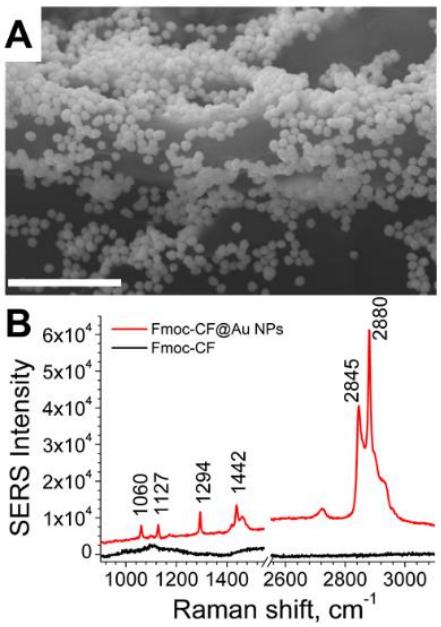

Figure 6. A) Scanning electron microscopy picture of the Fmoc-CF supramolecular structures with attached Au nanoparticles of *ca*. 90 nm diameter. Scale bar is 1 μm. B) SERS performance of the Fmoc-CF supramolecular structures coated by Au nanoparticles. Raman spectrum of self-assembled Fmoc-CF deposited on glass (black line). SERS spectrum of self-assembled Fmoc-CF coated with Au nanoparticles deposited on glass (red line), offset of $5x10^{-3}$ intensity units.

Surface Enhanced Raman Scattering (SERS) could then be per-formed due to the close contact of the tightly packed Au nanoparticles with the Fmoc-dipeptides, associated with the formation of "hot-spots".[53,54] The SERS spectrum of the Fmoc-CF is shown in Figure 6B, demonstrating the dramatic enhancement of the Raman signal over the bare Fmoc-CF supramolecular structures. The strong bands at 2845 and 2880 cm^{-1} could be assigned to the symmetric stretch of the CH_2(CO) group and the C–H stretching mode, respectively.[55,56] The bands at 1060 and 1127 cm^{-1} correspond to the asymmetric stretch of the CCO group and the combination of in-plane bending of the CH ring with the bending of CH(H), respectively. The bands at 1294, 1442 cm^{-1} correspond to the in-plane bending of the CH ring, and the bending of the CH_2(CHCOO) terminal group, respectively.[56]

Conclusions

In summary, the first study on 2D self-assembly of Fmoc-dipeptides at the air/water interface onto well-defined supramolecular structures is presented. General guidelines for selecting the amino-acid sequence of Fmoc-dipeptides that will efficiently self-assemble at fluid interfaces have been introduced. By experimentally testing a set of dipeptides with a variety of aminoacid residue sequences, the values of log P and – log S have been proposed as simple and reliable molecular parameters for deciding whether a given Fmoc-dipeptide would efficiently self-assemble at fluid interfaces. These insights might be extended to the formulation of oil/water emulsions stabilized by Fmoc-dipeptides. The as-obtained supra-molecular structures from the Fmoc-dipeptides retain the chiral features observed in bulk self-assembly. The arrangement of the Fmoc-dipeptide molecules has been convincingly described in high detail by a combination of in situ UV-vis spectroscopy and BAM offering information exclusively from the air/water interface. The chirality transfer from the peptides to solid surfaces allows an easy access to chiral surfaces with potential chiroptical applications. The chemical functionality of the Fmoc-dipeptides is maintained after the 2D self-assembly. Moreover, the possibility of forming

nanocomposites has been demonstrated by combining a cysteine-containing nanostructure with plasmonic Au nanoparticles, showing SERS effect. This work suggests that Fmoc-dipeptides are relevant bioinspired molecules for self-assembling at fluid interfaces and that the required aminoacid sequence for nanostructure design can be efficiently predicted.

References and Notes

1. R. Krishna Kumar, R. L. Harniman, A. J. Patil and S. Mann, *Chem. Sci*. **2016**, 7, 5879–5887.
2. H. Ni, Z. Yu, W. Yao, Y. Lan, N. Ullah and Y. Lu, *Chem. Sci*. **2017**, 8, 5699–5704.
3. R. Xing, C. Yuan, S. Li, J. Song, J. Li and X. Yan, *Angew. Chem. Int. Ed*. **2018**, 57, 1537–1542.
4. L. McDougall, E. R. Draper, J. D. Beadle, M. Shipman, P. Raubo, A. G. Jamieson and D. J. Adams, *Chem. Commun*. **2018**, 54, 1793–1796.
5. B. Sun, H. Riegler, L. Dai, S. Eickelmann, Y. Li, G. Li, Y. Yang, Q. Li, M. Fu, J. Fei and J. Li, *ACS Nano* **2018**, 12, 1934–1939.
6. G. G. Scott, P. J. McKnight, T. Tuttle and R. V. Ulijn, *Adv. Mater*. **2016**, 28, 1381–1386.
7. J. Wang, K. Liu, L. Yan, A. Wang, S. Bai and X. Yan, *ACS Nano* **2016**, 10, 2138–2143.
8. J. Boekhoven, A. M. Brizard, M. C. A. Stuart, L. Florusse, G. Raffy, A. Del Guerzo and J. H. van Esch, *Chem. Sci*. **2016**, 7, 6021–6031.
9. P. Makam and E. Gazit, *Chem. Soc. Rev*. **2018**, 47, 3406–3420.
10. H. A. Pal, S. Mohapatra, V. Gupta, S. Ghosh and S. Verma, *Chem. Sci*. **2017**, 8, 6171–6175.
11. S. Fleming, S. Debnath, P. W. J. M. Frederix, T. Tuttle and R. V. Ulijn, *Chem. Commun*. **2013**, 49, 10587-10589.
12. S. Murillo-Sánchez, D. Beaufils, J. M. González Mañas, R. Pascal and K. Ruiz-Mirazo, *Chem. Sci*. **2016**, 7, 3406–3413.
13. 13 . A. C. Baumruck, D. Tietze, L. K. Steinacker and A. A. Tietze, *Chem. Sci*. **2018**, 9, 2365–2375.
14. D. Yang, P. Duan, L. Zhang and M. Liu, *Nat. Commun*. **2017**, 8, 15727.
15. M. Deng, L. Zhang, Y. Jiang and M. Liu, *Angew. Chem. Int. Ed*. **2016**, 55, 15062–15066.

16. M. Reches and E. Gazit, *Science* **2003**, 300, 625–627.
17. L. Schnaider, S. Brahmachari, N. W. Schmidt, B. Mensa, S. Shaham-Niv, D. Bychenko, L. Adler-Abramovich, L. J. W. Shimon, S. Kolusheva, W. F. DeGrado and E. Gazit, *Nat. Commun.* **2017**, 8, 1365.
18. E. K. Johnson, D. J. Adams and P. J. Cameron, *J. Am. Chem. Soc*. **2010**, 132, 5130–5136.
19. J. Rodon Fores, M. L. Martinez Mendez, X. Mao, D. Wagner, M. Schmutz, M. Rabineau, P. Lavalle, P. Schaaf, F. Boulmedais and L. Jierry, *Angew. Chem. Int. Ed.* **2017**, 56, 15984–15988.
20. K. Tao, A. Levin, L. Adler-Abramovich and E. Gazit, *Chem. Soc. Rev*. **2016**, 45, 3935–3953.
21. S. Bai, C. Pappas, S. Debnath, P. W. J. M. Frederix, J. Leckie, S. Fleming and R. V. Ulijn, *ACS Nano* **2014**, 8, 7005–7013.
22. S. Fleming and R. V. Ulijn, *Chem. Soc. Rev*. **2014**, 43, 8150–8177.
23. A. Lampel, R. V. Ulijn and T. Tuttle, *Chem. Soc. Rev*. **2018**, 47, 3737–3758.
24. A. Baral, S. Roy, A. Dehsorkhi, I. W. Hamley, S. Mohapatra, S. Ghosh and A. Banerjee, *Langmuir* **2014**, 30, 929–936.
25. T. O. Mason, T. C. T. Michaels, A. Levin, C. M. Dobson, E. Gazit, T. P. J. Knowles and A. K. Buell, *J. Am. Chem. Soc*. **2017**, 139, 16134–16142.
26. M. Conejero-Muriel, J. A. Gavira, E. Pineda-Molina, A. Belsom, M. Bradley, M. Moral, J. de D. G.-L. Durán, A. Luque González, J. J. Díaz-Mochón, R. Contreras-Montoya, Á. Martínez-Peragón, J. M. Cuerva and L. Álvarez de Cienfuegos, *Chem. Commun*. **2015**, 51, 3862–3865.
27. P. W. J. M. Frederix, G. G. Scott, Y. M. Abul-Haija, D. Kalafatovic, C. G. Pappas, N. Javid, N. T. Hunt, R. V. Ulijn and T. Tuttle, *Nat. Chem*. **2015**, 7, 30–37.
28. J. K. Gupta, D. J. Adams and N. G. Berry, *Chem. Sci*. **2016**, 7, 4713–4719.
29. X. Zhao, L. Xu, M. Sun, W. Ma, X. Wu, C. Xu and H. Kuang, *Nat. Commun*. **2017**, 8, 2007.
30. B. S. Gomes, B. Simões and P. M. Mendes, *Nat. Rev. Chem*. **2018**, 2, 0120.

31. J. J. Giner-Casares, G. Brezesinski and H. Möhwald, *Curr. Opin. Colloid Interface Sci.* **2014**, 19, 176–182.
32. J. P. Coelho, M. J. Mayoral, L. Camacho, M. T. Martín-Romero, G. Tardajos, I. López-Montero, E. Sanz, D. Ávila-Brande, J. J. Giner-Casares, G. Fernández and A. Guerrero-Martínez, *J. Am. Chem. Soc*. **2017**, 139, 1120–1128.
33. I. R. Sasselli, C. G. Pappas, E. Matthews, T. Wang, N. T. Hunt, R. V. Ulijn and T. Tuttle, *Soft Matter* **2016**, 12, 8307–8315.
34. T. Li, M. Kalloudis, A. Z. Cardoso, D. J. Adams and P. S. Clegg, *Langmuir* **2014**, 30, 13854–13860.
35. D. J. Adams, L. M. Mullen, M. Berta, L. Chen and W. J. Frith, *Soft Matter* **2010**, 6, 1971-1980.
36. www.chemicalize.com (Accessed 12/09/2018)
37. V. N. Viswanadhan, A. K. Ghose, G. R. Revankar and R. K. Robins, J. *Chem. Inf. Comput. Sci.* **1989**, 29, 163–172.
38. G. Klopman, J.-Y. Li, S. Wang and M. Dimayuga, *J. Chem. Inf. Comput. Sci*., **1994**, 34, 752–781.
39. T. J. Hou, K. Xia, W. Zhang and X. J. Xu, *J. Chem. Inf. Comput. Sci*. **2004**, 44, 266–275.
40. M. Li, E. Zellermann and C. Schmuck, *Chem. Eur. J*. **2018**, 24, 9061–9065.
41. N. Brown, J. Lei, C. Zhan, L. J. W. Shimon, L. Adler-Abramovich, G. Wei and E. Gazit, *ACS Nano* **2018**, 12, 3253–3262.
42. E. R. Draper, H. Su, C. Brasnett, R. J. Poole, S. Rogers, H. Cui, A. Seddon and D. J. Adams, *Angew. Chem. Int. Ed*. **2017**, 129, 10603–10606.
43. X. Mu, K. M. Eckes, M. M. Nguyen, L. J. Suggs and P. Ren, *Biomacromolecules* **2012**, 13, 3562–3571.
44. S.-T. Wang, Y. Lin, R. K. Spencer, M. R. Thomas, A. I. Nguyen, N. Amdursky, E. T. Pashuck, S. C. Skaalure, C. Y. Song, P. A. Parmar, R. M. Morgan, P. Ercius, S. Aloni, R. N. Zuckermann and M. M. Stevens, *ACS Nano* **2017**, 11, 8579–8589.
45. R. Contreras-Montoya, A. B. Bonhome-Espinosa, A. Orte, D. Miguel, J. M.

Delgado-López, J. D. G. Duran, J. M. Cuerva, M. T. Lopez-Lopez and L. Álvarez de Cienfuegos, *Mater. Chem. Front*. **2018**, 2, 686–699.

46. B. Adhikari, J. Nanda and A. Banerjee, *Soft Matter* **2011**, 7, 8913-8922.
47. C. Rubia-Payá, G. De Miguel, M. T. Martín-Romero, J. J. Giner-Casares and L. Camacho, *Adv. Colloid Interface Sci*. **2015**, 225, 134-145.
48. B. Adhikari and A. Banerjee, *Soft Matter* **2011**, 7, 9259-9266.
49. Y. Zhou, P. F. Damasceno, B. S. Somashekar, M. Engel, F. Tian, J. Zhu, R. Huang, K. Johnson, C. McIntyre, K. Sun, M. Yang, P. F. Green, A. Ramamoorthy, S. C. Glotzer and N. A. Kotov, *Nat. Commun.* **2018**, 9, 181.
50. H.-E. Lee, H.-Y. Ahn, J. Mun, Y. Y. Lee, M. Kim, N. H. Cho, K. Chang, W. S. Kim, J. Rho and K. T. Nam, *Nature* **2018**, 556, 360–365.
51. V. P. Terrier, H. Adihou, M. Arnould, A. F. Delmas and V. Aucagne, *Chem. Sci.* **2016**, 7, 339–345.
52. S. G. Booth, A. Uehara, S.-Y. Chang, C. La Fontaine, T. Fujii, Y. Okamoto, T. Imai, S. L. M. Schroeder and R. A. W. Dryfe, *Chem. Sci*. **2017**, 8, 7954–7962.
53. G. Bodelón, V. Montes-García, C. Costas, I. Pérez-Juste, J. Pérez-Juste, I. Pastoriza-Santos and L. M. Liz-Marzán, *ACS Nano* **2017**, 11, 4631–4640.
54. S. Paterson, S. A. Thompson, J. Gracie, A. W. Wark and R. de la Rica, *Chem. Sci.* **2016**, 7, 6232–6237.
55. J. K. Sahoo, N. M. S. Sirimuthu, A. Canning, M. Zelzer, D. Graham and R. V. Ulijn, *Chem. Commun*. **2016**, 52, 4698–4701.
56. W. Nuansing, A. Rebollo, J. M. Mercero, J. Zuñiga and A. M. Bittner, J. Raman *Spectrosc*. **2012**, 43, 1397–1406.

Supporting Information

Experimental section

Materials. The initial 0.5 mM solutions of phenyl dipeptides were prepared in dichloromethane, while the rest of the dipeptides were in methanol. Solvents were used without further purification from Aldrich (Germany). Ultrapure water, produced by a Millipore Milli-Q unit, pre-treated by a Millipore reverse osmosis system (>18.2 MΩ cm), was used as subphase. The subphase temperature was 21 ºC with pH 2. The pH 2 subphase was prepared with Hydrochloric acid 37% PRS-Codex purchased from Panreac. All instruments for the study of the dipeptides at the air/liquid interface were located on tables with vibration isolation (antivibration system MOD-2 S, Accurion, Göttingen, Germany) in a large class 100 clean room. Fmoc-LG, Fmoc-AA, Fmoc-GG and Fmoc-FF were purchase from Bachem Co., Switzerland; Fmoc-Y and Fmoc-F were purchase from Sigma-Aldrich.

Surface pressure–area isotherms. Two different models of Nima troughs (Nima Technology, Coventry, England) were used in this work, both provided with a Wilhelmy type dynamometric system using a strip of filter paper: a NIMA 611D with one moving barrier for the measurement of the reflection spectra, and a NIMA 601, equipped with two symmetrical barriers to record BAM images. The layers of Fmoc-dipeptides were compressed at a speed of 0.03 nm^2 min^{-1} $molecule^{-1}$.

UV-vis reflection spectroscopy. UV-visible reflection spectra at normal incidence as the difference in reflectivity (ΔR) of the film-covered water surface and the bare surface were obtained with a Nanofilm Surface Analysis Spectrometer (Ref $SPEC^2$, supplied by Accurion GmbH, Göttingen, Germany).

Brewster angle microscopy. Images of the film morphology were obtained by Brewster angle microscopy (BAM) with a I-Elli2000 (Accurion GmbH) using a Nd:YAG diode laser with wavelength 532 nm and 50 mW, which can be recorded with a lateral resolution of 2 μm. The image processing procedure included a geometrical correction of the image, as well as a filtering operation to reduce interference fringes and noise. The measurement of thickness of the supramolecular structures was performed by ImageJ software.

Langmuir-Schaefer transferred films. The multilayers were transferred onto quartz substrates by sequential monolayer transfer. These monolayers were transferred by Langmuir-Schaefer, *i. e.*, by horizontal dipping at constant surface pressure. The transfer ratio was close to unity for all transfer processes.

UV-Visible absorption spectroscopy of films. The UV-vis spectra of the films were measured locating the substrate directly in the light path on a Cary 100 UV-Vis spectrophotometer.

UV-Visible absorption spectroscopy of solutions. UV-vis spectra of the Fmoc group and Fmoc-dipeptides in bulk solution were measured using an Analytik Jena SPECORD® 200 Plusand.

Circular dichroism (CD) spectroscopy of films. CD measurements were acquired using a UV-Vis Jasco J-1500 spectrophotometer. All spectra were recorded at room temperature. The spectra were measured in the wavelength interval from 190 to 350 nm with a 0.1 nm step resolution. The scanning rate was 15 nm/min with 2 s response time. The signal-to-noise ratio was improved by accumulating 3 scans for each CD spectrum. Data processing was carried out using the software package. The blank spectrum of the bare quartz substrate was subtracted.

Circular dichroism (CD) spectroscopy of the hydrogels. The CD spectra were recorded using an Olis DSM172 spectrofotometer with a xenon lamp of 150W. The hydrogels were gelated into a 0.1 mm quartz cell (Hellma 0.1 mm quartz Suprasil®). All of them were prepared at 2 $mg \cdot mL^{-1}$; Fmoc-CF hydrogel was prepared by solvent-switch with dimethylsulfoxide and water 5:95; Fmoc-MF and Fmoc-FF were prepared by pH-switch by addition of 2 molar equivalents of glucono-δ-lactone (GdL) to a basic peptide solution. Spectra were obtained from 190 to 350 nm with a 1 nm step and 0.1 s integration time per step at 25 ºC, taking 20 averages.

Scanning Electron Microscopy (SEM). SEM images were obtained using an JEOL JSM 7800F with acceleration voltage from 0.5 to 30 kv.

Raman spectroscopy. The spectra of Fmoc-CF were measured with a Raman microscope Renishaw In Via spectrophotometer, equipped with a Leica DM2500 M

confocal microscope. Spectra were obtained by excitation with green laser light (532 nm). The laser beam was focused on the specimen using the 100× lens, which was equivalent to sampling a theoretical spot of 2 μm. Reflected light was scattered through a diffraction slit of 1200 lines/mm and signals recorded by a CCD detector. Raman spectra were acquired over the wavenumber range 100–4000 cm^{-1}, using an acquisition time of 20 s and 10 cumulative scans to improve the signal noise. The laser power used for spectral acquisition is from 50% of the maximum level (100 mW) a preheating of 20 s was carried out avoiding combustion of the compound. The spectra were corrected by the elimination of the cosmic rays, the background subtraction and the signal corresponding to the bare glass.

Nuclear Magnetic Resonance (NMR). NMR Spectra were recorded were recorded on NMR 300 MHz spectrometer (Variant), and 500 MHz spectrometer (Bruker). Chemical shifts (δ), referenced to the residual protonated solvent as an internal standard, are quoted in ppm. Coupling constants (J) are reported in Hz.

High Resolution Mass Spectrometry. Mass spectra were recorded using an Xevo G2-XS QTof (Waters, USA) mass spectrometer.

Dynamic Light Scattering (DLS). DLS experiments were performed using a Zetasizer Nano ZS Instrument (Malvern Instruments Ltd., Malvern, UK). The DLS measurements were performed at 25 ºC using the red line (wavelength, λ = 632 nm) of a He-Ne laser in a quasi-backscattering configuration (scattering angle, θ = 173º). Previously to each measurement, the solutions were filtered in a cleanroom using a 0.45 μm Nylon membrane (Millex®, USA) to remove the dust particles. The filtered samples were transferred to a quartz measurement cell (Hellma®6030-OG Model). In DLS experiments the normalized intensity or second-order autocorrelation function was measured, $g^{(2)}(q,t)$, that is related to the electric field or first-order autocorrelation function, $g^{(1)}(q,t)$, through the Siegert relationship,

$$g^{(2)}(q,t) - 1 = \beta \left| g^{(1)}(q,t) \right|^2$$

where *t* is the time, $q = (4\pi n/\lambda)\ sin(\theta/2)$ is the wavevector, and *n* the solution

refractive index. β is an optical coherence factor and is generally found to be close to 1, except for cases in which the scattered intensity is low. Either because of the low size of the scatterers, low concentration or poor refractive index contrast between the scatterers and the solvent.

Section SI1. Solid phase protocol for the synthesis of Fmoc-CF, Fmoc-MF and Fmoc-RF.

All materials were of analytical grade and used without further purification. Fmoc-Phe-OH, Fmoc-Met-OH, Fmoc-Cys(Trt)-OH, Fmoc-Arg(Pbf)-OH, 4-dimethylaminopyridine (DMAP), trifluoroacetic acid (TFA) and triisopropylsilane (TIS) were purchase from Sigma-Aldrich, USA. 1-hydroxybenzotriazole (HOBt) and N,N'-diisopropylcarbodiimide (DIC) were purchase from FluoroChem, UK.

Step 1 – solid phase peptide coupling conditions used for the first coupling between p-alkoxybenzyl alcohol resin (Wang resin) and Fmoc-L-phenylalanine (Fmoc-Phe-OH):

Dry p-alkoxybenzyl alcohol resin (Wang resin) was placed in a round bottom flask under inert atmosphere. The resin was then swollen in dry dichloromethane (DCM) (10 mL per gram of resin). In another flask under inert atmosphere, Fmoc-Phe-OH (5 equiv) and HOBt (5 equiv) were dissolved in the minimum amount of dry N,N-dimethylformamide (DMF). Immediately after, DIC (5 equiv) was added and the mixture was stirred for 15 min before addition to the resin. After that, DMAP (0.01 equiv) solved in dry DMF was added to the reaction mixture. The mixture was agitated overnight at room temperature to effect coupling. To acetylate the resin hydroxyl free groups, pyridine (2 equiv) and acetic anhydride (2 equiv) were added to the suspension. The mixture was agitated for 15 min and the resin was washed with DMF (x5), DCM (x5) and diethyl ether (x2).

Step 2 – N-terminal Fmoc removal:

Fmoc removal was performed using 20% piperidine in DMF with two sequential treatments of 20 min. The resin was then filtered and washed with DMF (x5),

DCM (x5) and diethyl ether (x2).

Step 3 – coupling of the second Fmoc-aminocid derivative:

The resin previously functionalized with phenylalanine was swollen in DMF. Then, Fmoc protected aminoacids (Fmoc-Cys(Trt)-OH, Fmoc-Met-OH or Fmoc-Arg(Pbf)-OH) (3.5 equiv) and HOBt (5 equiv) were dissolved in DMF. DIC (5 equiv) was added and the mixture and was stirred for 15 min. This mixture was added to the resin and was agitated for 2 h at 60 ºC to effect coupling. The resin was washed with DMF (x5), DCM (x5) and diethyl ether (x2). To test the efficiency of the coupling reaction, a qualitative Ninhydrin Test was carried-out after each coupling.[1]

Step 4 – cleavage of peptides from resin and removal of acid labile protecting groups:

Dry functionalized resin was suspended in 20 mL per gram of resin of TFA/water/1,2-ethanedithiol/TIS (92.5/2.5/2.5/2.5) and agitated for 2 h. The TFA solution was filtered, vacuum concentrated and added to cold (4 ºC) mixture of diethyl ether and hexane (2:1) in a centrifuge tube. The resulting precipitate was collected by centrifugation and washed with the mixture of diethyl ether and hexane (x3).and hexane (2:1) in a centrifuge tube. The resulting precipitate was collected by centrifugation and washed with the mixture of diethyl ether and hexane (x3).

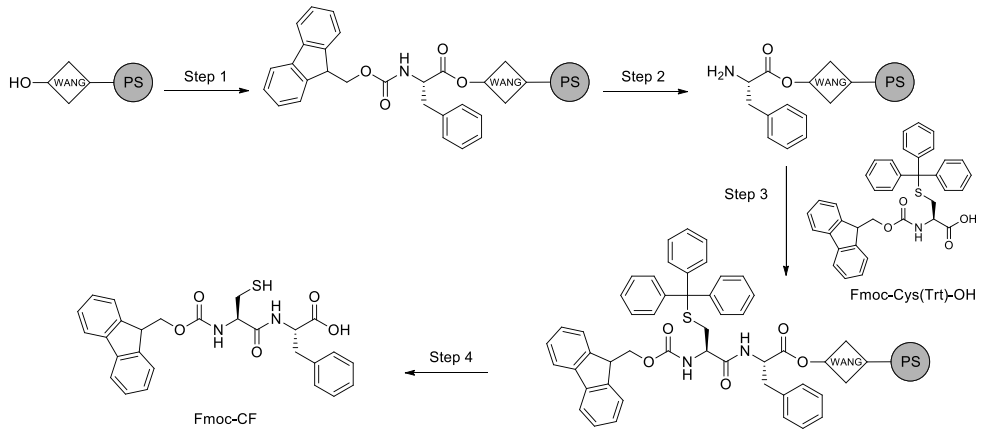

Figure SI1.1. Synthetic scheme and NMR spectra of Fmoc-CF.

Fmoc-CF: ^{1}H NMR (500 MHz, DMSO-d_6) δ 8.20 (s, 1H), 7.89 (d, *J* = 7.5 Hz, 2H), 7.73 (dd, *J* = 7.6, 3.8 Hz, 2H), 7.50 (d, *J* = 8.4 Hz, 1H), 7.41 (td, *J* = 7.5, 1.1 Hz, 2H), 7.35 – 7.30 (m, 2H), 7.25-7.00 (m, 5H), 6.67 (d, J = 8.4, 1H), 4.5-4.35 (m, 1H), 4.34 – 4.19 (m, 2H), 4.13 (s, 1H), 4.03 (s, 1H), 3.06 (dd, *J* = 14.0, 5.1 Hz, 1H), 2.98 – 2.84 (m, 1H), 2.81-2.70 (m, 1H), 2.67 – 2.56 (m, 1H). ^{13}C NMR (126 MHz, DMSO-d_6) δ 173.16, 170.04, 155.87, 143.83, 143.73, 140.68, 137.31, 129.95, 129.11, 128.21, 128.12, 127.62, 127.07, 126.40, 125.30, 120.08, 65.76, 57.04, 53.50, 46.62, 36.53, 26.29. HRMS (ESI): m/z calculated for $C_{27}H_{26}N_2O_5NaS$ $[M+Na]^+$: 513.1460; found: 513.1458.

^{1}H-NMR of Fmoc-CF:

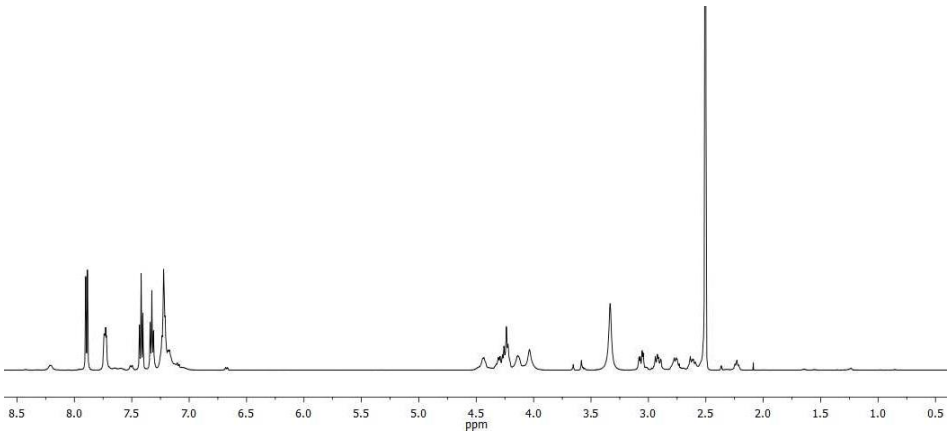

^{13}C-NMR of Fmoc-CF:

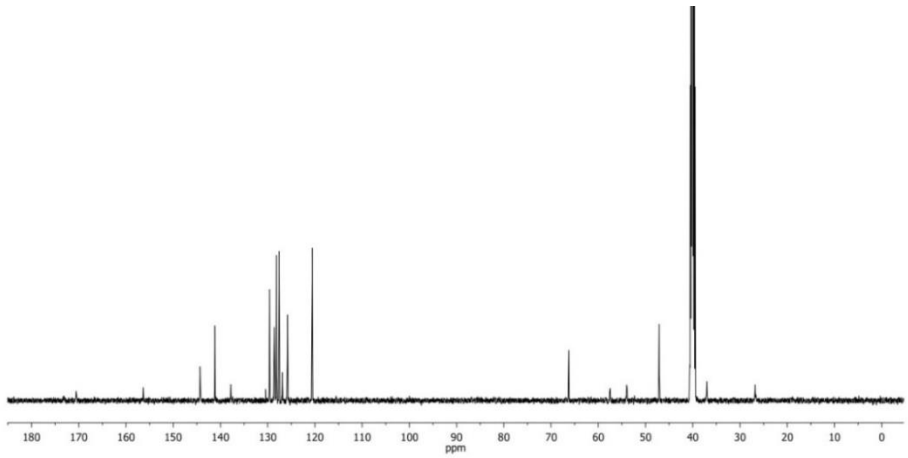

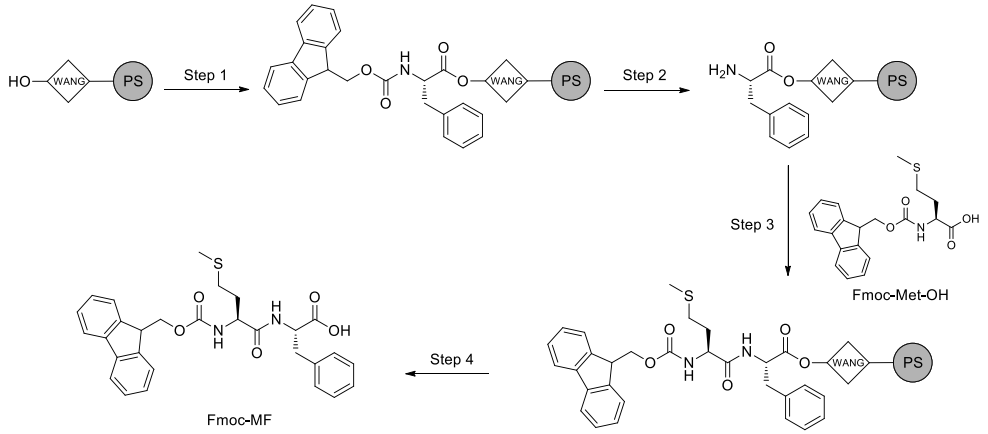

Figure SI1.2. Synthetic scheme and NMR spectra of Fmoc-MF.

Fmoc-MF: ^{1}H NMR (300 MHz, CDCl3-*d*) δ 7.76 (d, *J* = 6.9 Hz, 2H), 7.58 (d, *J* = 6.9 Hz, 2H), 7.40 (t, *J* = 7.0 Hz, 2H), 7.34 – 7.28 (m, 2H), 7.23 – 7.10 (m, 5H), 4.87 – 4.67 (m, 4H), 4.45 – 4.29 (m, 2H), 4.24 – 4.15 (m, 1H), 3.25 – 3.13 (m, 1H), 3.11 – 2.95 (m, 1H), 2.51 (d, *J* = 19.9 Hz, 2H), 2.09 – 1.84 (m, 5H). ^{13}C NMR (126 MHz, CDCl3-*d*) δ 171.32, 156.29, 143.79, 141.46, 135.93, 129.48, 128.75, 127.95, 127.29, 127.26, 125.22, 125.17, 120.18, 67.35, 53.77, 53.57, 47.25, 37.57, 31.69, 30.03, 29.85, 15.24. HRMS (ESI): m/z calculated for $C_{29}H_{30}N_2O_5NaS$ $[M+Na]^+$: 541.1773; found: 541.1772.

^{1}H-NMR of Fmoc-MF:

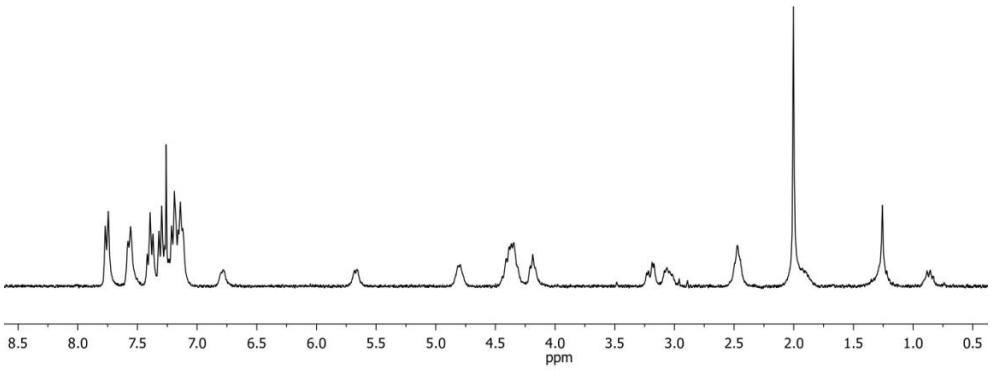

^{13}C-NMR of Fmoc-MF:

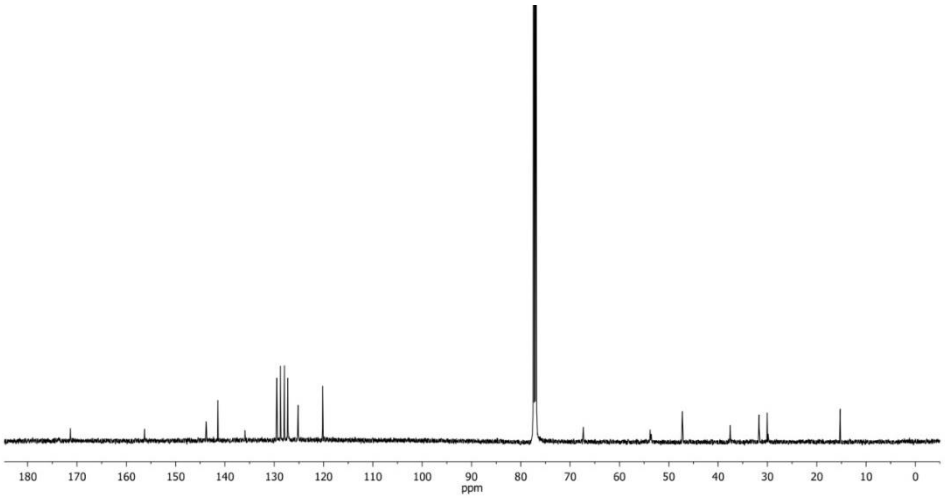

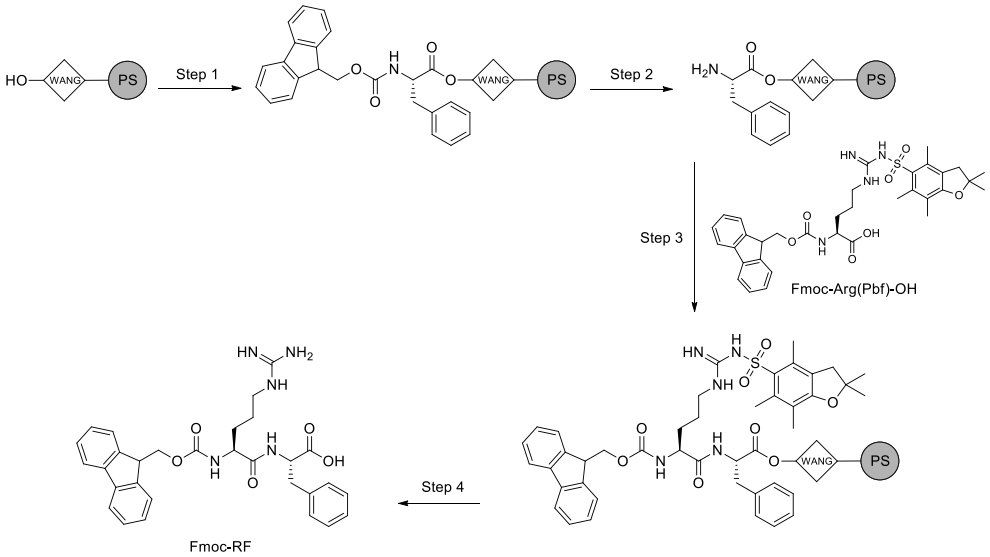

Figure SI1.3. Synthetic scheme and NMR spectra of Fmoc-RF.

Fmoc-RF: ^{1}H NMR (500 MHz, DMSO-d_6) δ 8.36 (d, J = 7.4 Hz), 8.11 (d, J = 7.8 Hz, 1H), 7.90 (d, J = 7.6 Hz, 2H), 7.72 (t, J = 8.1 Hz, 2H), 7.66 – 7.56 (m, 1H), 7.48

(d, *J* = 8.4 Hz, 1H), 7.42 (t, *J* = 7.5 Hz, 2H), 7.33 (t, *J* = 7.4 Hz, 2H), 7.29 – 7.13 (m, 5H), 4.52 – 4.39 (m, 1H), 4.32 – 4.18 (m, 3H), 4.03 (td, *J* = 8.4, 5.1 Hz, 1H), 3.57 (s, 1H), 3.12 – 2.99 (m, 3H), 2.93 (dd, *J* = 13.9, 8.6 Hz, 1H), 1.69-1.57 (m, 1H), 1.57-1.37 (m, 3H). ^{13}C NMR (126 MHz, DMSO-d_6) δ 172.85, 171.77, 171.49, 156.66, 155.81, 143.89, 143.71, 140.70, 137.48, 136.97, 129.16, 129.05, 128.21, 128.09, 127.65, 127.08, 126.55, 126.34, 125.31, 125.27, 120.11, 65.68, 54.05, 53.95, 53.60, 53.55, 51.83, 46.65, 40.38, 36.72, 36.57, 29.08, 24.97. HRMS (ESI): m/z calculated for $C_{27}H_{33}N_5O_5$ $[M+H]^+$: 544.2560; found: 544.2563.

^{1}H-NMR of Fmoc-RF:

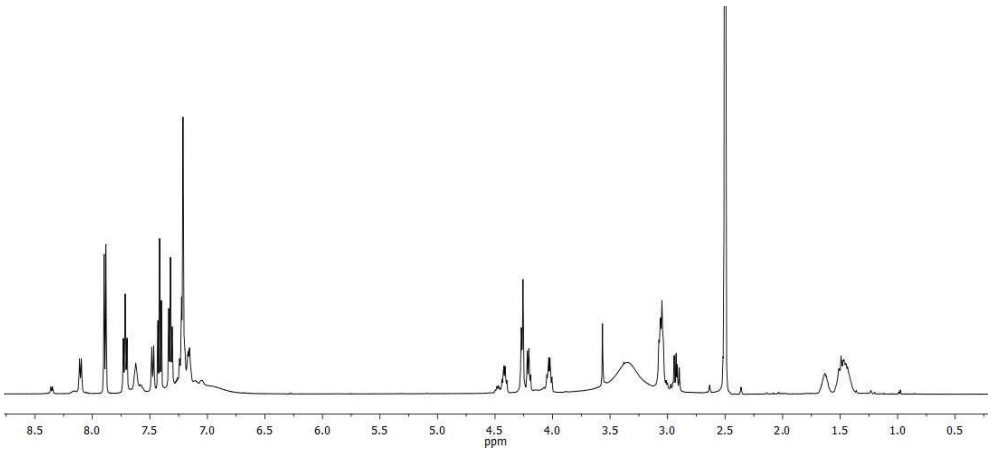

^{13C}-NMR of Fmoc-RF:

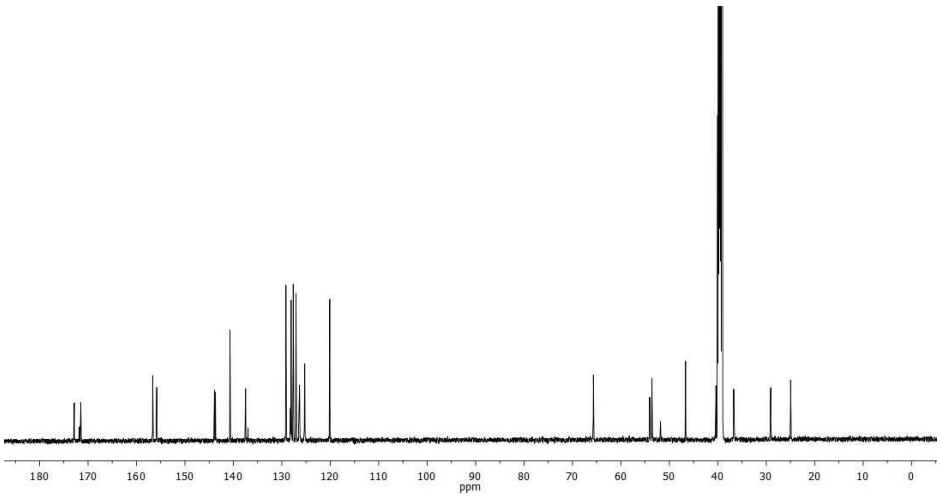

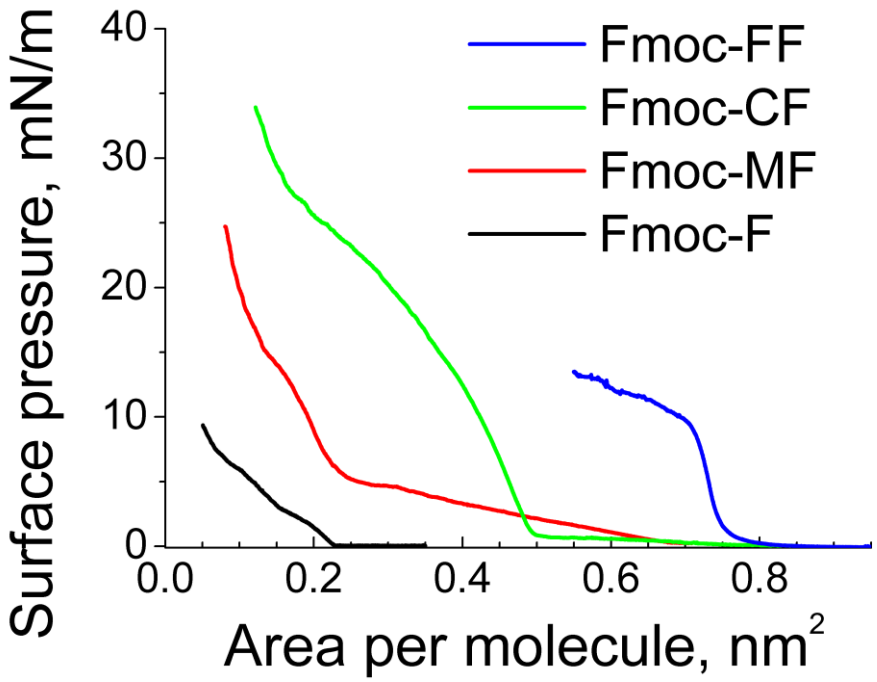

Figure SI2. Surface pressure – molecular area isotherms for the following Fmoc-dipeptides: Fmoc-F (red line), Fmoc-MF (green line), Fmoc-CF (black line), Fmoc-FF (black line). The subphase was in all cases a HCl solution adjusted to pH = 2.

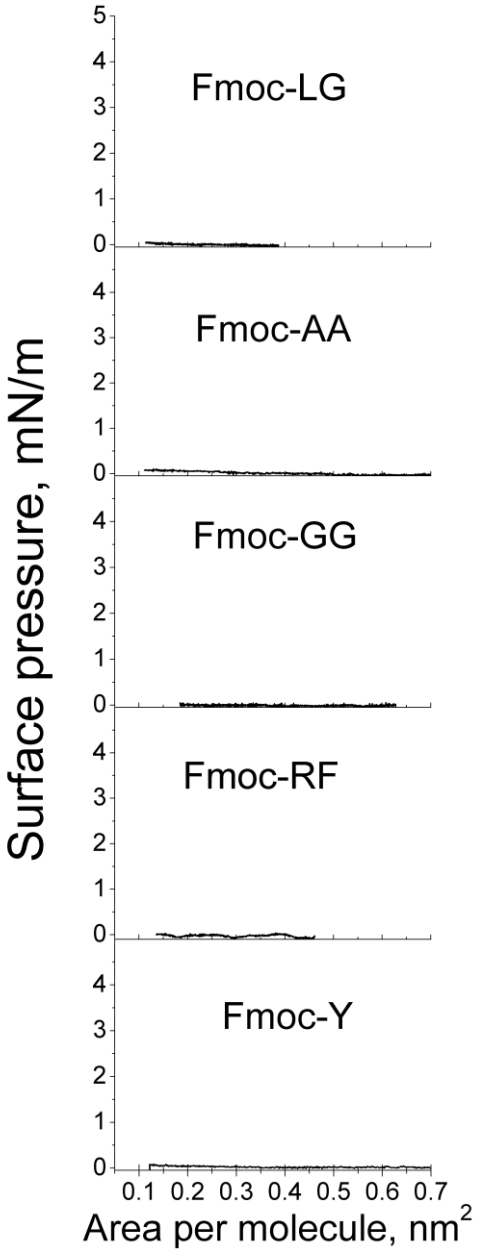

Figure SI3. Surface pressure – molecular area isotherms for the following Fmoc-dipeptides from top to bottom: Fmoc-LG, Fmoc-AA, Fmoc-GG, Fmoc-RF, Fmoc-Y. The subphase was in all cases a HCl solution adjusted to pH = 2.

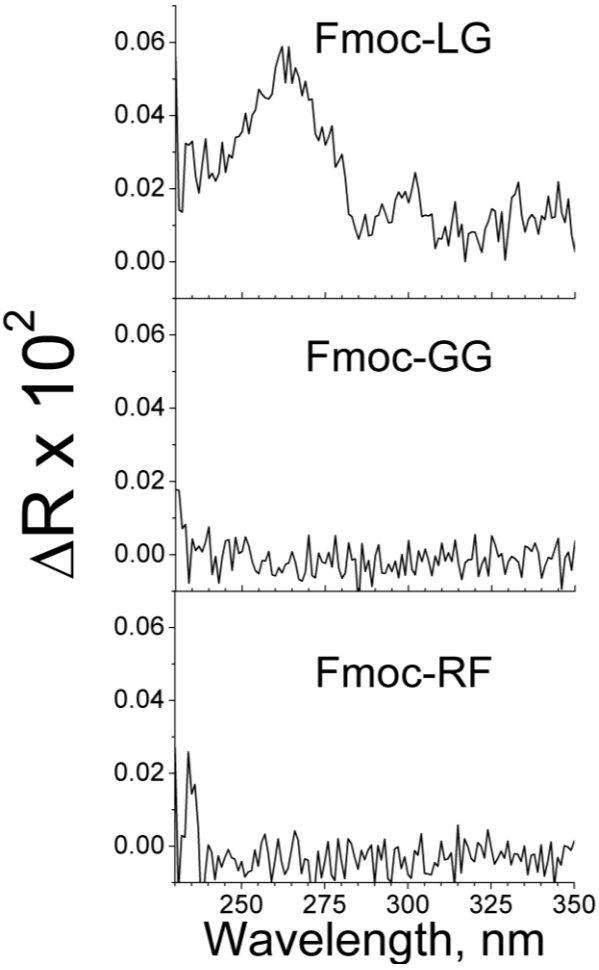

Figure SI4. UV-vis reflection spectra for the following Fmoc-dipeptides from top to bottom: Fmoc-LG (surface area of 0.11 nm^2/molecule), Fmoc-GG (surface area of 0.18 nm^2/molecule), Fmoc-RF (surface area of 0.27 nm^2/molecule). The subphase was in all cases a HCl solution adjusted to pH = 2.

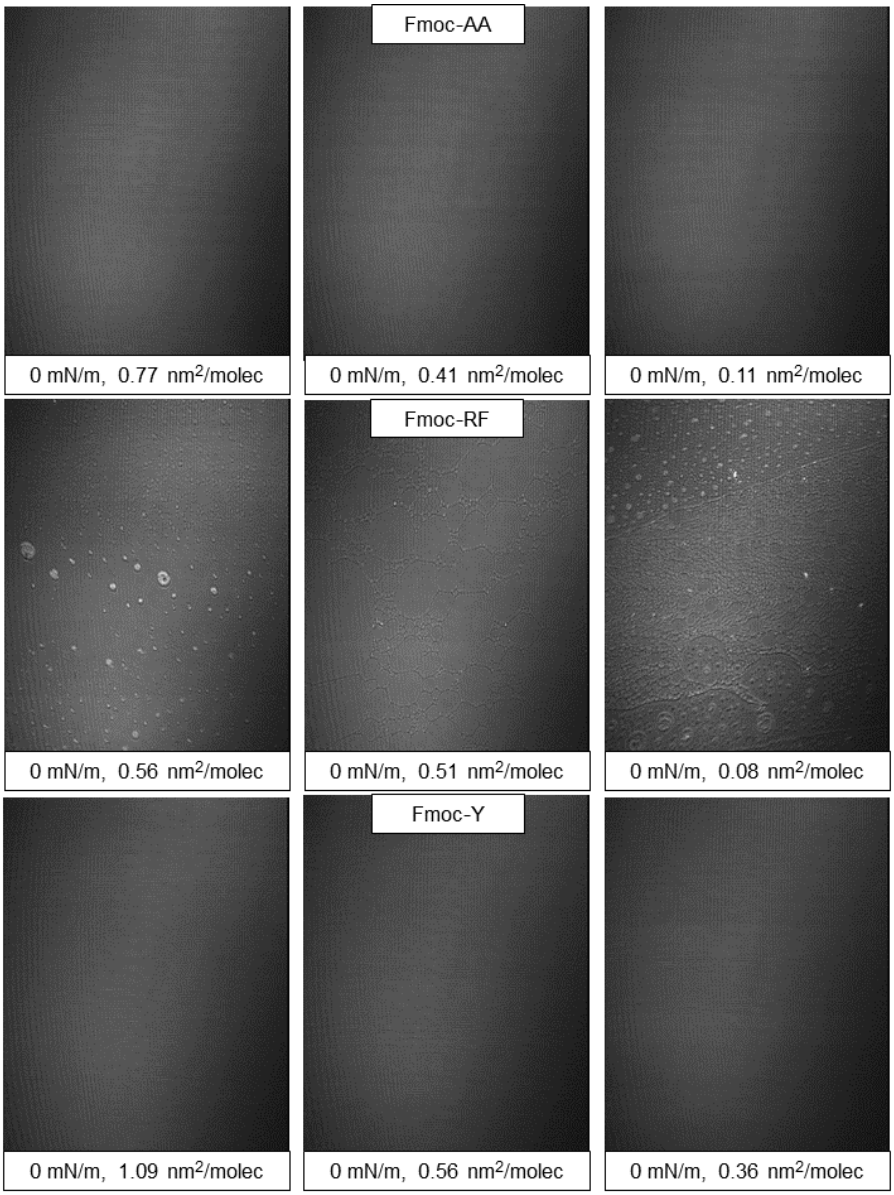

Figure SI5. Brewster angle microscopy pictures for the Fmoc-dipeptides at the air/water interface of Fmoc-AA, Fmoc-RF, Fmoc-Y, from top to bottom, respectively. The subphase was a HCl solution adjusted to pH = 2. The values of surface pressure and available surface area are included for each picture as inset. The width of each frame corresponds to 215 μm.

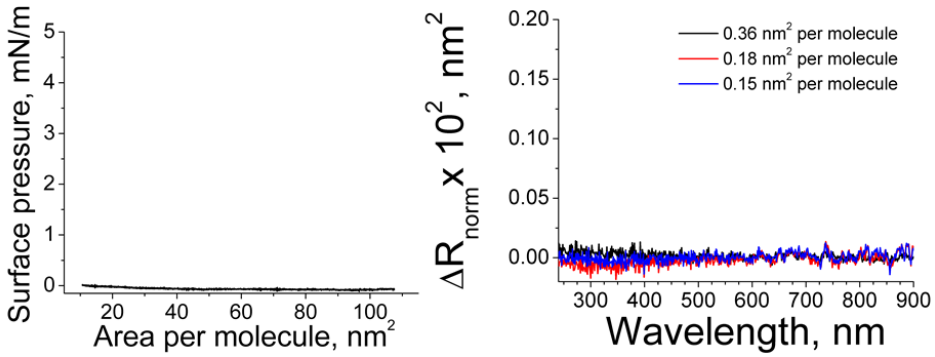

Figure SI6. Figure. Left) Surface pressure – molecular area isotherm of Fmoc-LG on a MilliQ water subphase. Right) UV-vis reflection spectra of Fmoc-LG at different values of available surface area per Fmoc-LG molecule as noted in the inset.

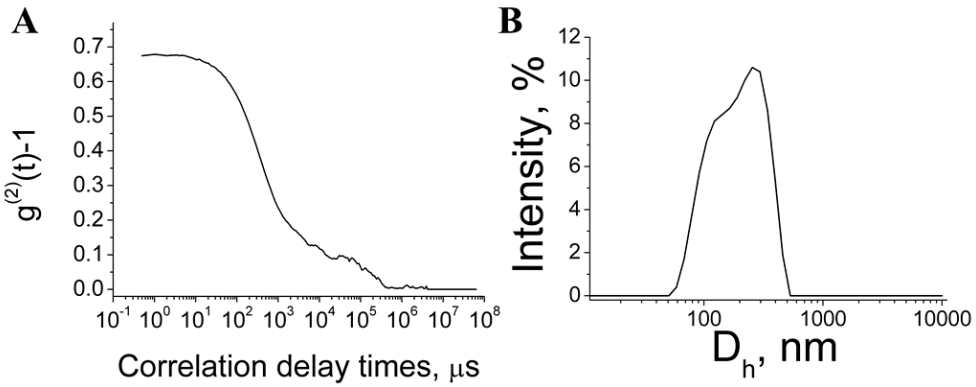

Figure SI7. A) DLS intensity auto-correlation function for bulk water after spreading of Fmoc-LG on the air/water interface. B) DLS spectrum of bulk water after spreading of Fmoc-LG on the air/water interface.

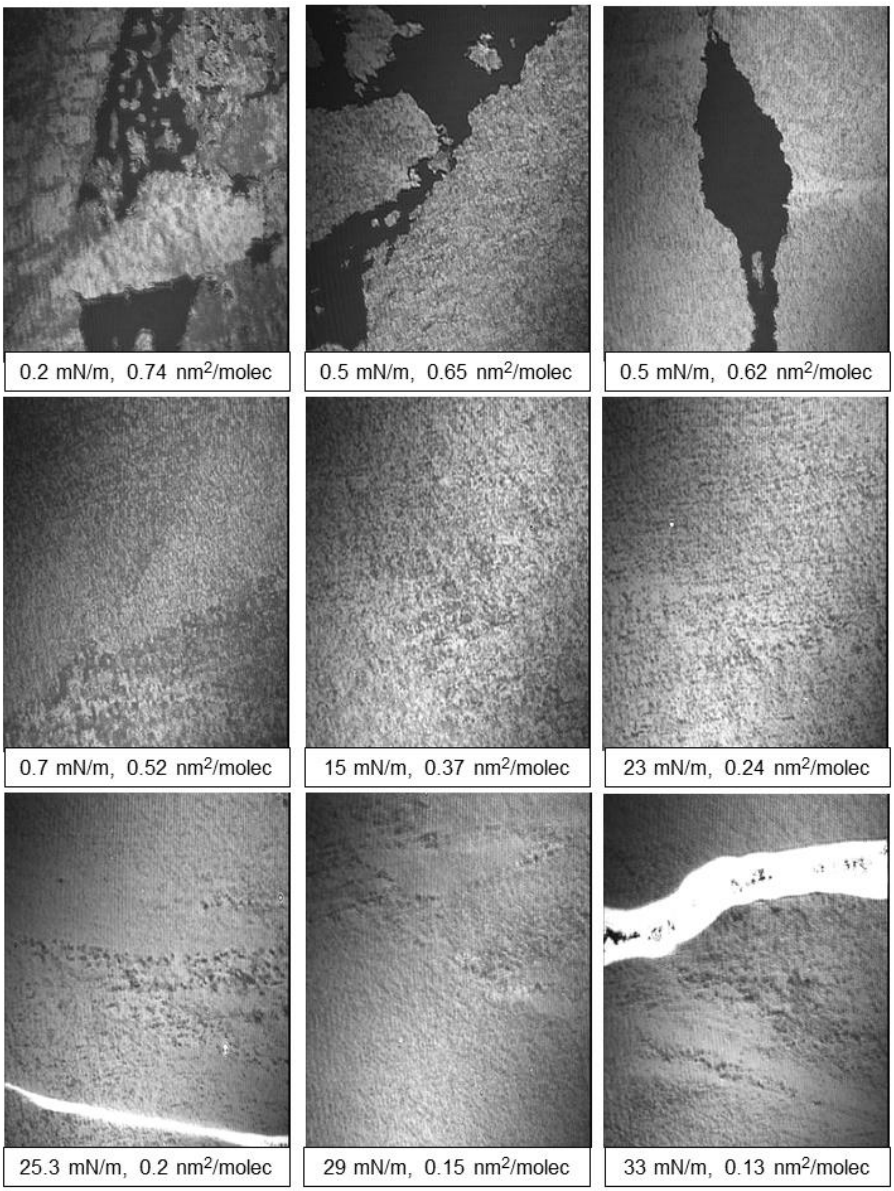

Figure SI8. Brewster angle microscopy pictures for the Fmoc-CF at the air/water interface. The subphase was a HCl solution adjusted to pH = 2. The values of surface pressure and available surface area are included for each picture as inset. The width of each frame corresponds to 215 μm.

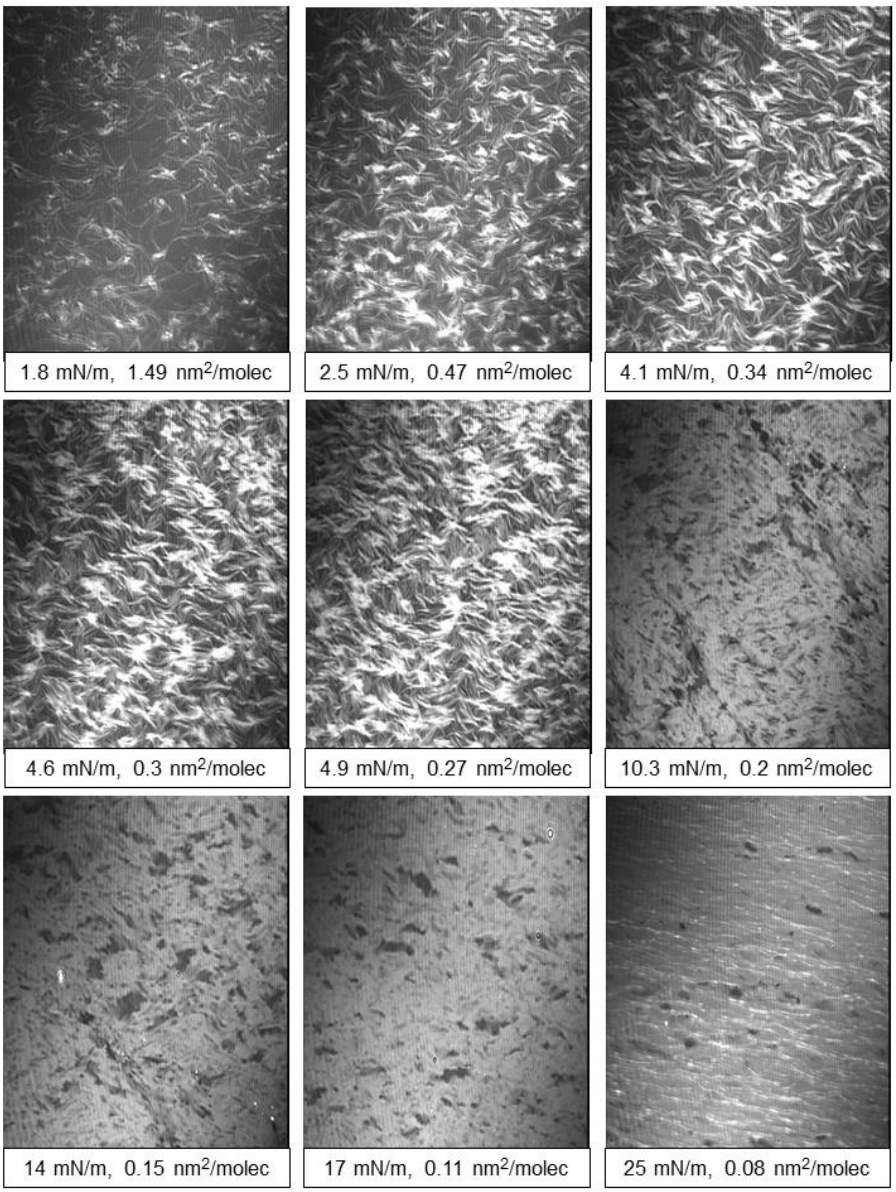

Figure SI9. Brewster angle microscopy pictures for the Fmoc-MF at the air/water interface. The subphase was a HCl solution adjusted to pH = 2. The values of surface pressure and available surface area are included for each picture as inset. The width of each frame corresponds to 215 μm.

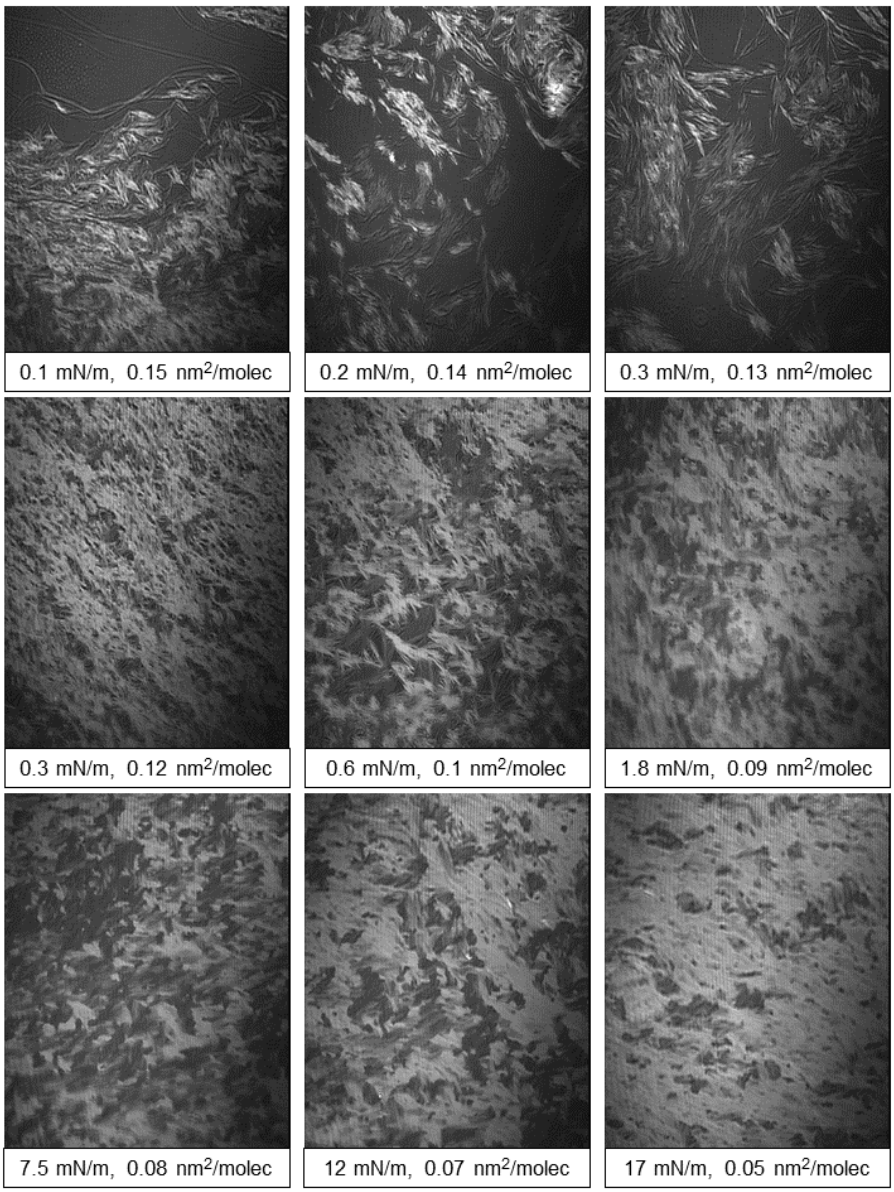

Figure SI10. Brewster angle microscopy pictures for the Fmoc-FF at the air/water interface. The subphase was a HCl solution adjusted to pH = 2. The values of surface pressure and available surface area are included for each picture as inset. The width of each frame corresponds to 215 μm.

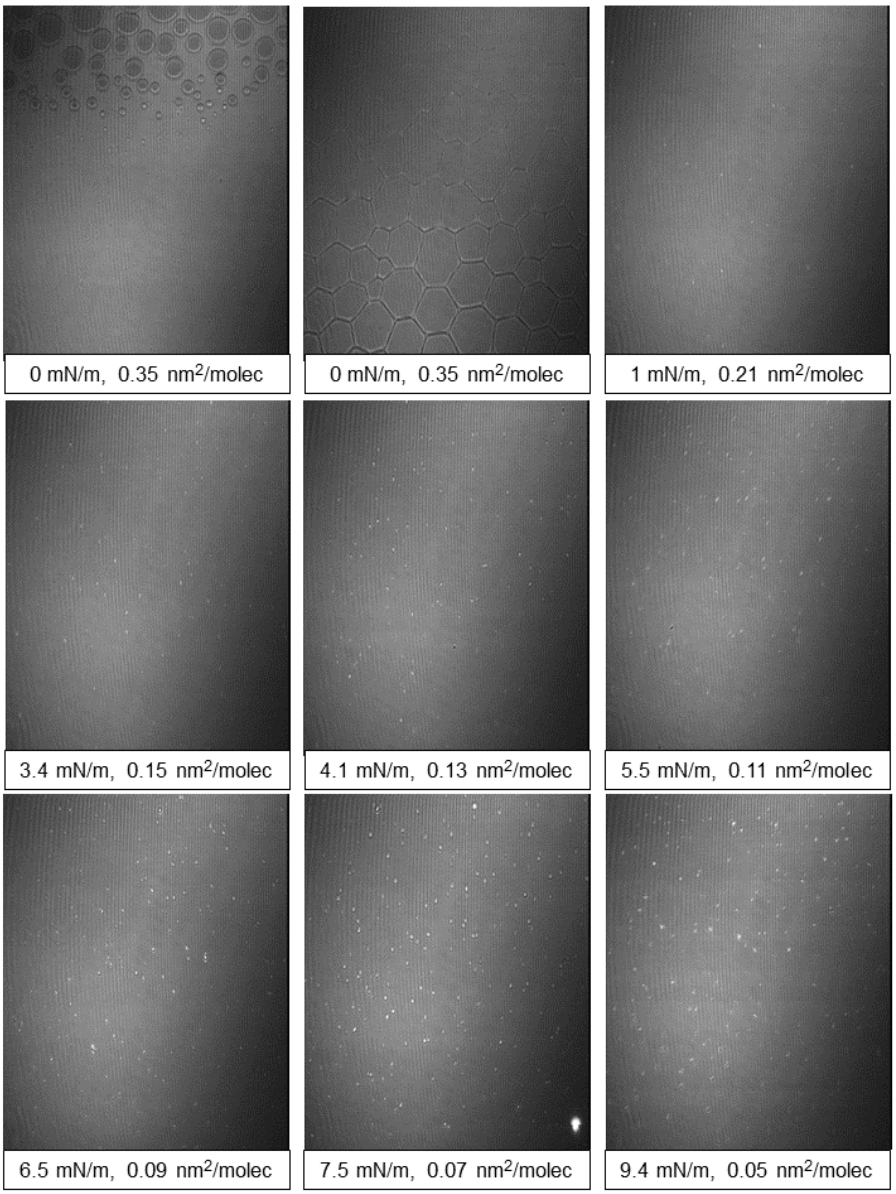

Figure SI11. Brewster angle microscopy pictures for the Fmoc-F at the air/water interface. The subphase was a HCl solution adjusted to pH = 2. The values of surface pressure and available surface area are included for each picture as inset. The width of each frame corresponds to 215 μm.

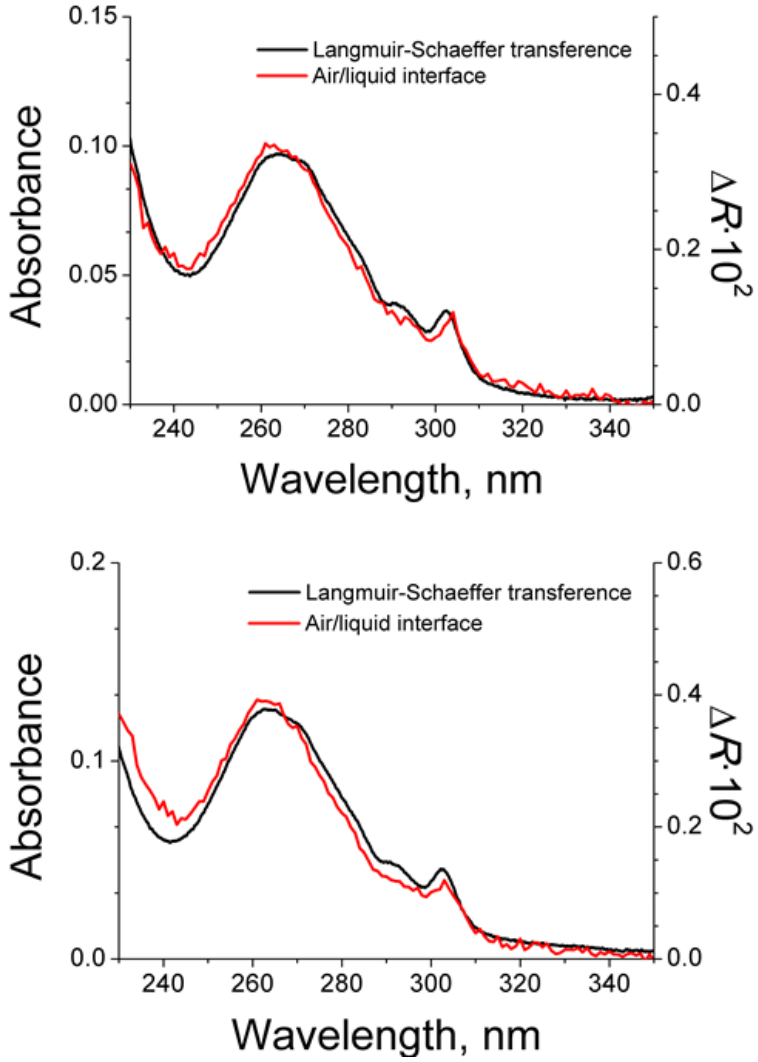

Figure SI12. Top) Bulk transmission UV-vis spectrum of Fmoc-FF transferred onto a quartz support (15 layers, π_{transf} = 8 mN/m, black line) and UV-vis reflection spectra (0.45 nm^2 per molecule, red line). Bottom) Bulk transmission UV-vis spectrum of Fmoc-MF transferred onto a quartz support (10 layers, π_{transf} = 20 mN/m, black line) and UV-vis reflection spectra (0.1 nm^2 per molecule, red line).

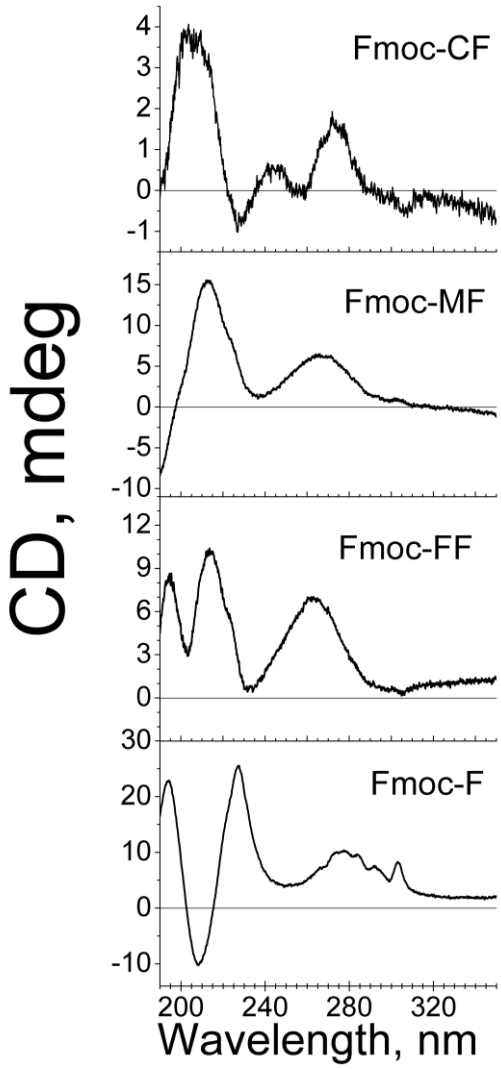

Figure SI13. Circular dichroism spectra for Langmuir-Schaeffer transferred Fmoc-dipeptides from the air/water interface onto quartz support. The transferred films are formed by the following Fmopc-dipeptides from top to bottom: Fmoc-CF (10 layers, π_{transf} = 30 mN/m), Fmoc-MF (10 layers, π_{transf} = 20 mN/m), Fmoc-FF (15 layers, π_{transf} = 8 mN/m), Fmoc-F (15 layers, π_{transf} = 8 mN/m).

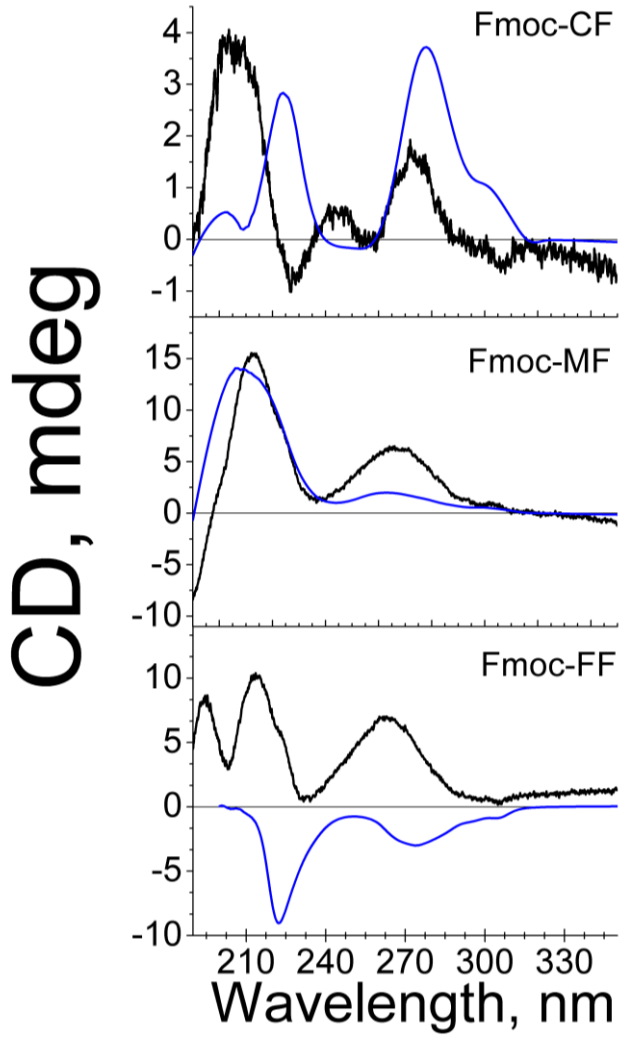

Figure SI14. Comparison of the circular dichroism spectra for Langmuir-Schaeffer transferred Fmoc-dipeptides from the air/water interface onto quartz support (black line) and bulk conditions forming hydrogel in solution (blue line). From top to bottom: Fmoc-CF, Fmoc-MF, Fmoc-FF.

Section SI15. Assessment of the UV-vis bands of the Fmoc group and the Fmoc-dipeptides in bulk solution.

The 9-fluorenylmethyloxycarbonyl (Fmoc) molecule shows three groups of bands in the UV-vis absorbance spectrum, see Figure SI15.1. Moderately intense bands are found at *ca.* 300 and 290 nm. A more complex region formed by the addition of several bands is found in the interval from 280 to 250 nm. A set of large signals are found at shorter wavelengths than 230 nm. The latter group is not relevant for the current discussion. The weak band observed at *ca.* 270 nm corresponds to the A_1 transition, polarized along the short axis of the Fmoc molecule. The other bands are ascribed to the B_2 transition, which are polarized along the long axis of the Fmoc molecule.[2] All the bands in the UV-vis transmission spectra of the Fmoc-dipeptides arise from the Fmoc group, as clearly seen in Figure SI13.1 and previously described for Fmoc-tetrapeptides.[3]

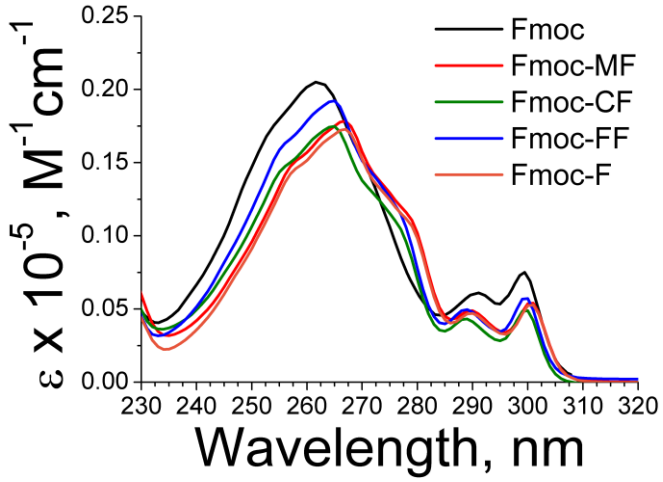

Figure SI15.1. UV-vis transmission spectra of the Fmoc group and Fmoc-dipeptides in bulk solution. The different derivatives of the Fmoc-dipeptides are noted in the inset.

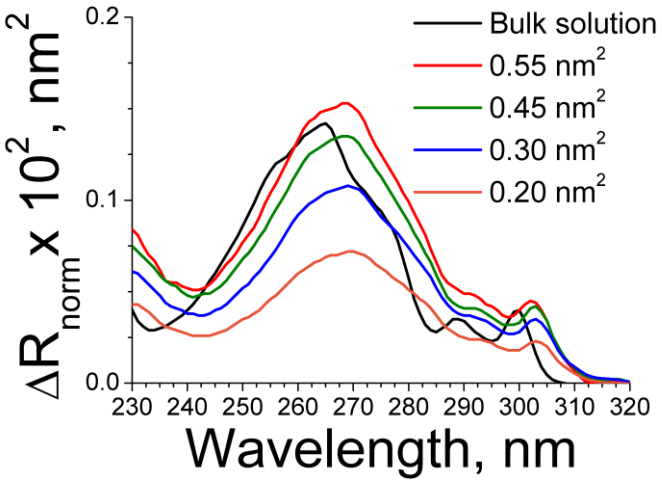

Figure SI15.2. UV-vis reflection spectra of the Fmoc-CF at the air/water interface. Surface area per Fmoc-CF molecule is noted in the inset. The UV-vis spectrum recorded in bulk solution is included as black line for comparison.

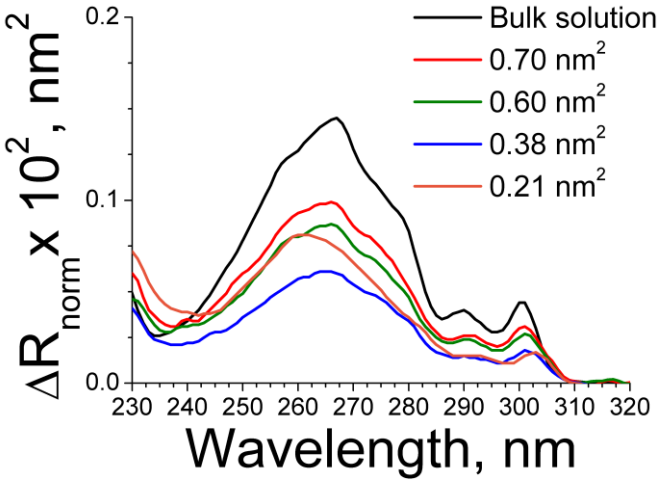

Figure SI15.3. UV-vis reflection spectra of the Fmoc-MF at the air/water interface. Surface area per Fmoc-MF molecule is noted in the inset. The intensity UV-vis reflection spectrum recorded at 0.21 nm^2 per Fmoc-dipeptide molecule has been increased by 1.5 for improving the clarity. The UV-vis spectrum recorded in bulk solution is included as black line for comparison.

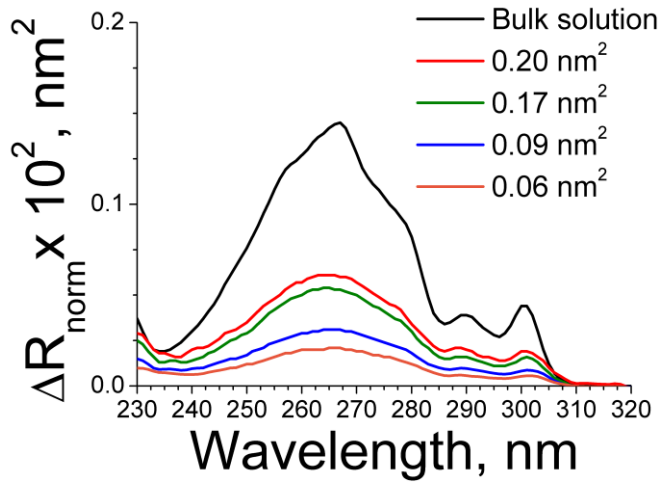

Figure SI15.4. UV-vis reflection spectra of the Fmoc-F at the air/water interface. Surface area per Fmoc-F molecule is noted in the inset. The UV-vis spectrum recorded in bulk solution is included as black line for comparison.

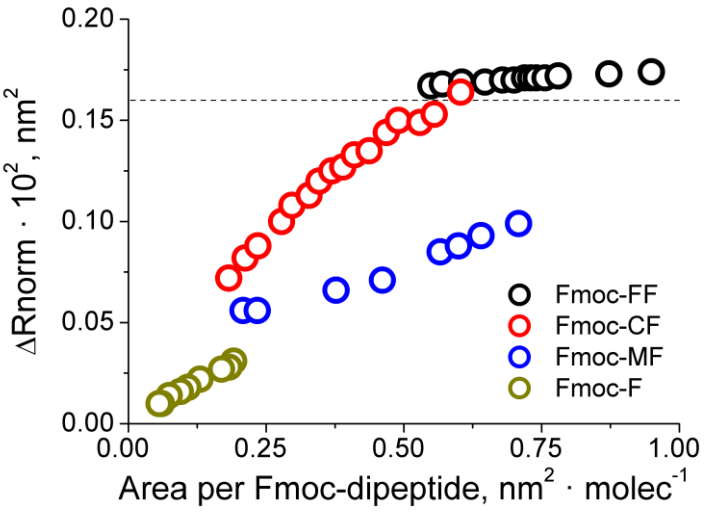

Figure SI15.5. Intensity values of the UV-vis reflection bands at 263-270 nm upon decrease of the available surface area for the supramolecular structures formed by the Fmoc-dipeptides. The different derivatives of the Fmoc-dipeptides are noted in the inset. The calculated maximum value of normalized UV-vis reflection is included as black line. ΔR_{norm} is *ca.* 0.16×10^{-2} nm^2 using $\varepsilon = 2\times 10^4$ mol·L^{-1}·cm^{-1} and $f_0 = 1.5$.

Section SI16. Molecular Dynamics Simulations of self-assembled supramolecular structures of Fmoc-FF at the air/water interface.

The self-assembly of Fmoc-dipeptides onto supramolecular structures is greatly affected by the pH. An antiparallel β sheet conformation as well as an antiparallel arrangement of the Fmoc groups is usually proposed as supramolecular structure of the Fmoc-dipeptides.[4,5] Nanostructured gels in bulk water can be obtained using Fmoc-Ala-Lac. Remarkably, Fmoc-Ala-Lac is not able to interact with other Fmoc-Ala-Lac molecules via β-sheet-like and amide-amide hydrogen bonding. Therefore, the formation of β-sheet-type supramolecular structures through H-bonding is not required to form supramolecular structures from short Fmoc-peptides. Instead, self-assembly driven by hydrophobic and aromatic interactions can form and stabilize self-assembled nanostructures of Fmoc-dipeptides.[6]

Molecular dynamics simulations were performed to attain insights on the supramolecular structure of the Fmoc-FF supramolecular structures self-assembled at the interface. Note that in view of the CD results the supramolecular arrangement might be different in supramolecular structures assembled at the air/water interface with respect to in bulk solution. The molecular dynamics simulations are aimed at modelling the initial stages of self-assembling of Fmoc-FF onto supramolecular structures rather than the compression stages of already formed supramolecular structures. The starting structure comprises an antiparallel β sheet conformation of the amide bonds and an antiparallel arrangement of the Fmoc groups. The longitudinal and transversal axes of the Fmoc group are placed parallel and slightly tilted with respect to the air/water interface, see Figure SI16.1.

A periodic box with the following dimension values was built: x = 40 Å, y = 45 Å, z = 110 Å, see Figure SI16.2. 2658 water molecules were placed in the central region of the box, *i. e.*, z-axis values between 35 and 75 Å. Density of bulk water is then close to 1 g/L. 16 Fmoc-FF molecules were placed in each water surface, thus amounting to a total of 32 Fmoc-FF molecules in the simulations. Two vacuum regions are included between the two monolayers of Fmoc-FF to prevent interactions

between the opposite monolayers, at z = 0-25 Å and z = 85-110 Å. This configuration allows simultaneously simulating two air/water interfaces. An average value of 1.12 nm^2 per Fmoc-FF dipeptide molecule is set. Such value of available surface area is intermediate between the two values of minimum surface area on the interface, *i. e.*, 1.48 and 0.86 nm^2.[7]

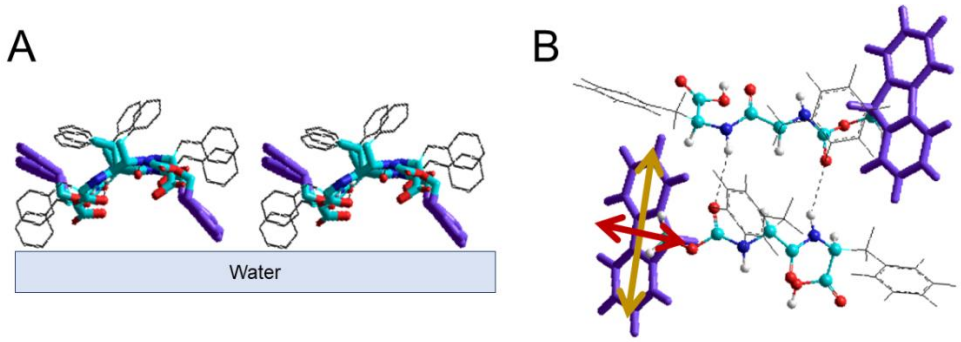

Figure SI16.1. Molecular sketch of the starting configuration for interacting Fmoc-FF molecules. A) side view and B) front view. The Fmoc groups are shown in purple for clarity. The yellow arrow indicates the longitudinal axis of the Fmoc group. The red arrow indicates the transversal axis of the Fmoc group.

The geometry of the simulated box was optimized using the Universal Forcefield, assigning the charge values following the procedure described by Gasteiger and Marsili.[8,9] The following procedure was applied for four complete cycles: 1) Molecular Dynamics simulations with a NPT ensemble (T = 300 K, P = 1 atm) was applied for a total simulation time of 2 nanoseconds. 2) Geometry optimization of the complete simulation box. The resulting supramolecular structure was then analysed, see Figure SI16.2.

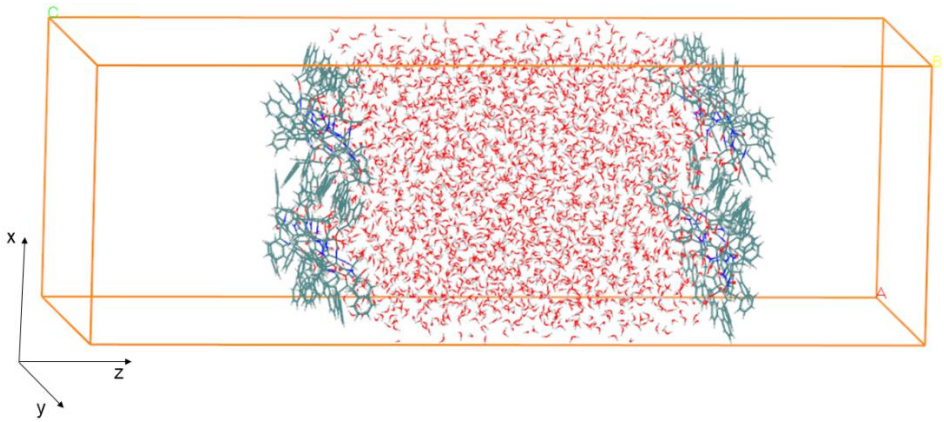

Figure SI16.2. Simulation box for the molecular dynamics simulations. Water molecules are depicted in red. Fmoc-FF molecules are depicted in blue and green. XYZ axes are included.

The density distribution of the different atoms is displayed in Figure SI16.3.

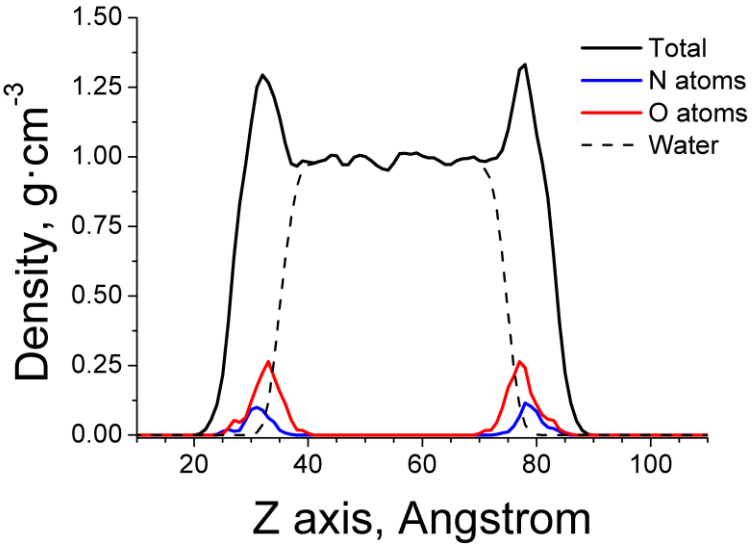

Figure SI16.3. Atomic density distribution of different atom groups as noted in the inset along the z axis. O atoms refer exclusively to those atoms from Fmoc-FF.

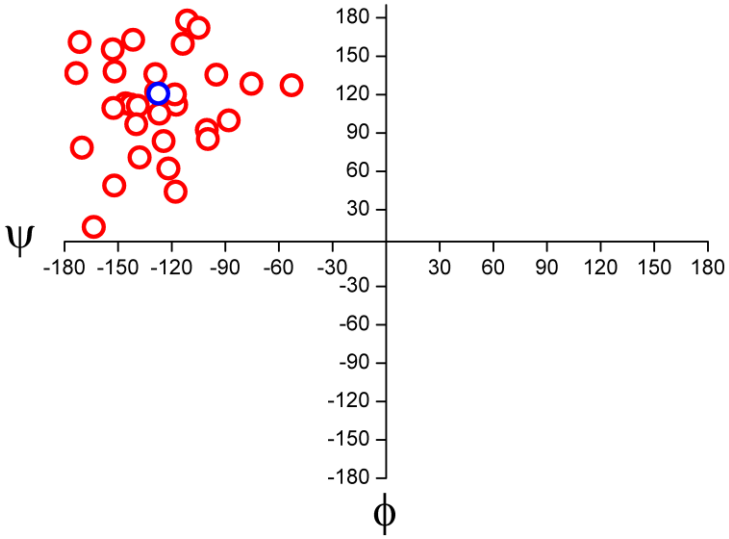

Figure SI16.4. Ramachandran plot for the Fmoc-FF molecules. Red circles: individual measurements for the Fmoc-FF molecules. Blue circle: Average values of the Fmoc-FF molecules for the complete simulation box.

The presence of β-sheet and polyproline II-like features has been obtained in the Ramachandran plot, see Figure SI16.4.10 The polyproline II-like conformation is obtained from the values of ϕ,ψ angles in the range ϕ,ψ = (-100° to 0°, 100° to 180°). The β-sheet conformation is obtained from values of ϕ,ψ angles in the range ϕ,ψ = (-180° to -100°, 100° to 180°). The approximate relative contribution of each structure is *ca.* 55% of β-sheet conformation and *ca.* 10% of polyproline II-like conformation. The following criterion was applied to assess the formation and number of H-bonds: The number of hydrogen bonds was determined with a donor-acceptor distance equal or lower than 3.5 Å and an interaction angle equal or lower than 30°.[10] The number of H-bonds between the peptide bonds is 30 for the complete simulated box, including 32 Fmoc-FF molecules. Note that the carbonyl oxygens, as well as the oxygen atoms from the carbamate group are also able to form H-bonds. Thus, the total amount of H-bonds in the simulated box is 60 H-bonds. An average contribution of two H-bonds per Fmoc-FF molecule with neighbour Fmoc-FF

molecules is then obtained. Additionally, the total number of H-bonds formed by Fmoc-FF with water molecules is 215. An average of 6.7 H-bonds per Fmoc-FF molecule has been obtained.

Section SI17. Application of the Extended Dipole Model for assessment of the UV-vis reflection spectra.

The UV-vis absorption spectrum of the Fmoc-FF dipeptide recorded in bulk solution has been deconvoluted onto Gaussian peaks, see Figure SI17.1. The UV-vis reflection spectrum is included for comparison. Please note that alternative deconvolution of the UV-vis band might be used. Therefore, the conclusions of this section should be taken as qualitative.

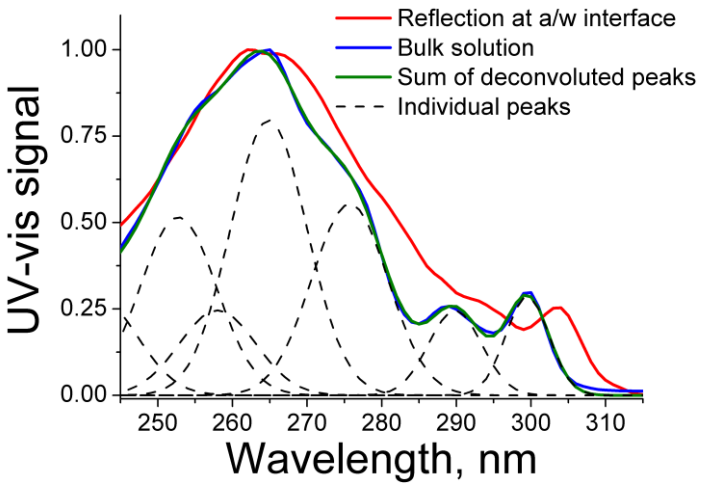

Figure SI17.1. UV-vis reflection spectra of Fmoc-FF molecule, recorded at 0.55 nm^2 per Fmoc-FF molecule (red line). UV-vis absorption spectrum of Fmoc-FF molecule recorded in bulk solution (blue line). Deconvolution of the spectrum onto individual peaks (dashed line) and the sum of the individual peaks (green line).

The UV-vis bands for $\lambda > 235$ nm might be deconvoluted onto 7 absorption modes, see Figure SI17.1. The 7 absorption modes arise from the absorption of the

Fmoc group. However, the vertical transitions obtained with standard TD-DFT calculations did not lead to a general agreement with the observed spectral features for the Fmoc group.[2] The quantum calculations using TD-B3LYP/6-31+G(d,p) render only three transitions. Such transitions are: 276 nm (B_2 symmetry and oscillator strength f = 0.17), 265 nm (B_2 symmetry and oscillator strength f = 0.29) and 256 nm (A_1 symmetry and oscillator strength f = 0.01). These three transitions are related to the following peaks: 276 nm, 265 nm and 258 nm, see Figure SI17.1. The peaks observed at a 253 nm and 242 nm with B_2 symmetry might be related with the excited vibrational modes at 276 and 265 nm. The bands at 299 nm and 290 nm cannot be clearly ascribed to a set of transitions. These peaks have been related with the excited state geometry rearrangements, leading to substantial differences between vertical and adiabatic transitions energies, as well as vibronic coupling phenomena, indicating partial breakdown of the Born–Oppenheimer approximation. These peaks also display B_2 symmetry.[11]

The shift of the UV-vis reflection spectra when compared to the UV-vis absorption spectrum in bulk solution towards longer wavelength values might be quantitatively assessed by applying the extended dipole model.[12–14] In the frame of the extended dipole model, all absorption modes in the Fmoc group are replaced by their transition dipoles, $\mu_i = \ell_i \times q_i$, with fixed dipole length (ℓ_i) and charge (q_i). Given a Fmoc group as a reference molecule and an absorption mode *i*, the interaction of the Fmoc reference molecule with all the dipoles j form the neighbour Fmoc molecules might be considered for obtaining the exciton interaction from the aggregation of the Fmoc molecules. As a common assumption, the interaction of the *i* component with the *i* component of the neighbour Fmoc molecule (Fmoc number 2) is exclusively considered. This assumption is valid unless the difference between the energy values for the absorption transitions between the modes *i* and *j* is not significant compared with the energy of interaction between the dipoles.15

Given a Fmoc reference molecule (Fmoc number *1*), the average excitation energy of this reference molecule, at the *i* absorption mode selected and due to the

aggregation with N neighbor molecules can be expressed as:

$$\Delta E_{1,N} = \Delta E_{mon} + 2\sum_{k=2}^{N} J_{1,k}\frac{2(N+1-k)}{N}$$

ΔE_{mon} is the excitation energy of the monomer, *N* is the aggregation number, being *k* = 2, 3, … N, and $J_{1,k}$ is the interaction energy between the dipoles of the *1* and *k* molecules, corresponding at the *i* absorption mode selected, which can be expressed in an approximately way by:

$$J_{1,k} = \frac{q_i^2}{D}\left[\frac{1}{ac_{1,k}} + \frac{1}{bd_{1,k}} - \frac{1}{ad_{1,k}} - \frac{1}{bc_{1,k}}\right]$$

with *D* of *ca.* 2.7 is the dielectric constant, and *ac*, *bd*, *ad* and *bc* are the distances between ends of the dipoles positive–positive, negative–negative, positive–negative and negative–positive, respectively. Thus, the maximum wavelength of the aggregate at the *i* absortion mode λ_N, is:

$$\lambda_{i,N} = \frac{\lambda_{mon}\, hc10^7}{hc10^7 + 4\lambda_{mon}\sum_{j=k}^{N} J_{1,k}\,\frac{(N+1-k)}{N}}$$

The transition dipole components (μ_i) could be calculated from the band decomposition, but the dipole length (ℓ_i) cannot be obtained from the experimental data. The dipole length value is approximately 66% of the extent of the π conjugate system. A dipole length of $\ell_L \approx 4$ Å is used for all the B_2 symmetry components (long axis transition dipoles), while for the A_1 symmetry component (short axis transition dipoles), a dipole length $\ell_S \approx 2$ Å is used, see Figure SI17.2.[16]

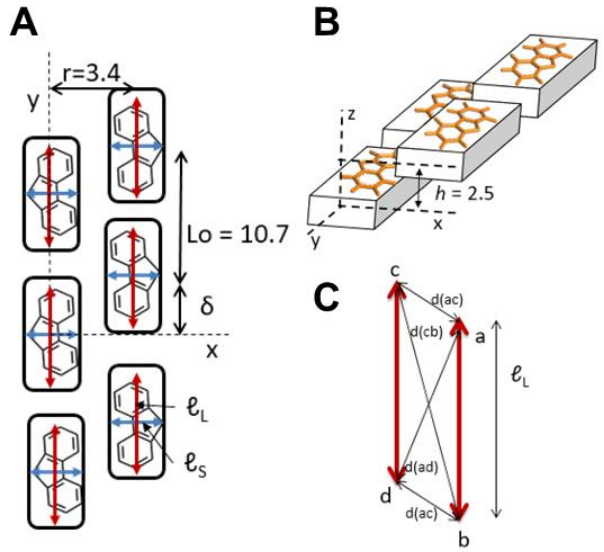

Figure SI17.2. Molecular sketches for the application of the Extended Dipole Model to the Fmoc-FF supramolecular structure.

Lineal aggregates with infinite length of Fmoc-FF molecules are assumed to be formed at the air/water interface (N = ∞). The relative arrangement of two consecutive molecules is set from the final snapshot of the molecular dynamics simulations. Neighbour Fmoc-FF molecules are assumed to be distributed among approximately two parallel rows with a relative displacement δ, see Figure SI17.2A. Such rows are distributed along the *y* axis, being L_0 the separation between molecules of the same row, *r*, the distance between rows along the *x* axis, and *h*, the displacement between the rows along the *z* axis, see FigureSI17.2.

Three absorption components of the Fmoc-FF molecule are analysed using the extended dipole model as displayed in Figure SI17.3. The values of shift of wavelength for the absorption modes at 265 nm and 299 nm (B_2 symmetry) and the absorption mode at 258 nm (A_1 symmetry) are shown in Figure SI15.3. The bands with B_2 symmetry are shifted towards longer wavelength, corresponding to the formation of J-aggregates. The absolute value of the shift of the spectrum is a

function of the maximum value of wavelength of the band and the value of the transition dipole. Using 2.5 D and 1.75 D for the dipole transition for the bands at 265 nm and 299 nm, the shift of the band shows a slight dependence with the relative displacement (δ) up to 6 nm and 4 nm, respectively.

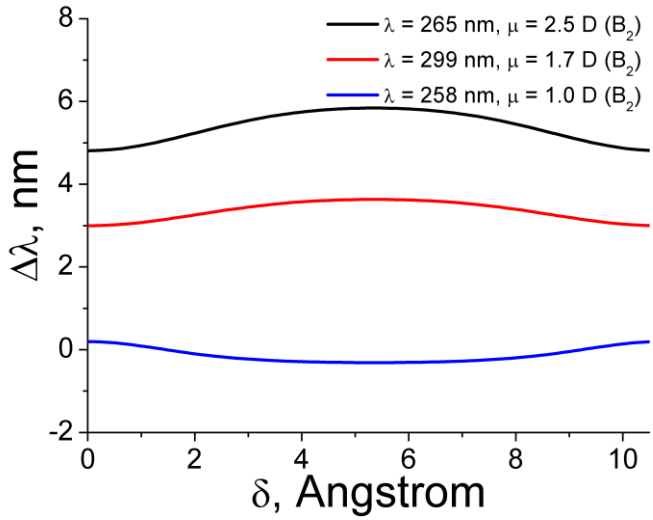

Figure SI17.3. Calculated values for shift of wavelength for the three absorption modes of Fmoc-FF dipeptide as a function of relative molecular displacement (δ).

The band with A_1 symmetry might be shifted towards shorter or longer wavelength depending on the relative molecular displacement (δ). Note that in all cases such shift on the wavelength is rather reduced, smaller than 1 nm. A dipole transition of 1 D is used, obtained from the value of the oscillator strength f = 0.01.[2] The modification of the morphology of the bands when comparing the UV-vis reflection spectra at the air/water interface with the UV-vis absorbance spectrum in bulk solution for the Fmoc-FF dipeptide is related with the different shift of peaks with B_2 and A_1 symmetry. The peaks with B_2 symmetry exhibit a shift towards longer wavelength from 4 to 6 nm, whereas no significant shift is observed for the peaks with A_1 symmetry.

This significant difference on the interaction between UV-vis bands as a function of their symmetry is checked by introducing a shift of 4 to 7 nm to the bands with B_2 symmetry, whereas the A_1 peak at 262 nm is not shifted. The height of the peaks might be slightly modified, although the area of the peaks is kept constant in all cases, see Figure SI17.4.

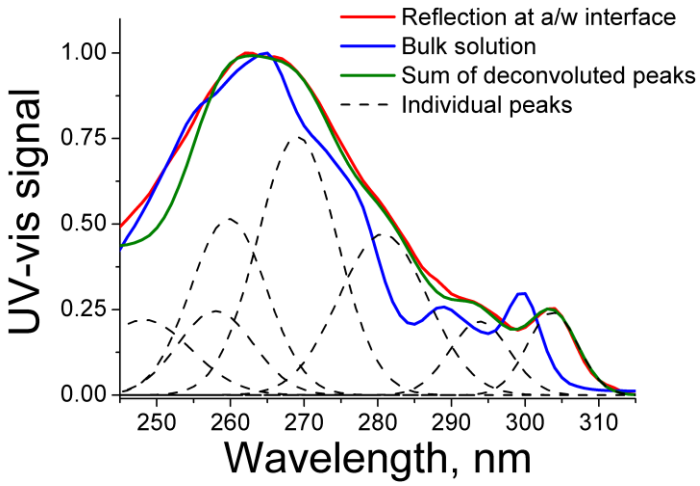

Figure SI17.4. UV-vis reflection spectra of Fmoc-FF molecule, recorded at 0.55 nm^2 per Fmoc-FF molecule (red line). UV-vis absorption spectrum of Fmoc-FF recorded in bulk solution (blue line). Deconvolution of the spectrum onto individual peaks (dashed line) and the sum of the individual peaks (green line). A shift of 4-7 nm is included for the bands with B_2 symmetry.

Remarkably, the sum of the deconvoluted peaks is almost coincident with UV-vis reflection spectrum of the Fmoc-FF at the air/water interface. Additionally, the maximum of the band is shifted towards shorter wavelength, despite the opposite shift of the B_2 bands towards longer wavelength. The A_1 band and the band at 254 nm (bulk solution) that is shifted 7 nm (air/water interface) are placed at the same wavelength, then placing the maximum at 262 nm. This behaviour might explain the experimentally observed shifts in the UV-vis spectra.

The Fmoc-CF shows no modification of the morphology of the bands, instead displaying a net shift of all the peaks towards shorter wavelength. This phenomenon might be ascribed to different values of the orientation factor f. As example values, f lower than 1 for the A_1 bands and f = 1.5 for the B_2 bands would render to the observed shift of the entire UV-vis spectrum for the Fmoc-CF. Note that the circular dichroism spectra in the region of 260 nm of Fmoc-CF shows significant differences with respect to the Fmoc-FF, thus pointing to conformational changes that would support the mentioned variation in the orientation factor values.

References

1. Kaiser, E.; Colescott, R. L.; Bossinger, C. D.; Cook, P. I. *Anal. Biochem*. **1970**, 34 (2), 595.
2. Nguyen, D. D.; Trunk, J.; Nakhimovsky, L.; Spanget-Larsen, J. *J. Mol. Spectrosc.* **2010**, 264 (1), 19.
3. Zou, Y.; Razmkhah, K.; Chmel, N. P.; Hamley, I. W.; Rodger, A. *RSC Adv*. **2013**, 3 (27), 10854.
4. Zhang, Y.; Gu, H.; Yang, Z.; Xu, B. *J. Am. Chem. Soc*. **2003**, 125 (45), 13680.
5. Smith, A. M.; Williams, R. J.; Tang, C.; Coppo, P.; Collins, R. F.; Turner, M. L.; Saiani, A.; Ulijn, R. V. *Adv. Mater*. **2008**, 20 (1), 37.
6. Eckes, K. M.; Mu, X.; Ruehle, M. A.; Ren, P.; Suggs, L. J. *Langmuir* **2014**, 30 (18), 5287.
7. Chemicalize https://chemicalize.com/ (accessed Sept 10, 2018).
8. Rappe, A. K.; Casewit, C. J.; Colwell, K. S.; Goddard, W. A.; Skiff, W. M. *J. Am. Chem. Soc.* **1992**, 114 (25), 10024.
9. Gasteiger, J.; Marsili, M. *Tetrahedron* **1980**, 36 (22), 3219.
10. Mu, X.; Eckes, K. M.; Nguyen, M. M.; Suggs, L. J.; Ren, P. *Biomacromolecules* **2012**, 13 (11), 3562.
11. Bree, A.; Zwarich, R. *J. Chem. Phys*. **1969**, 51 (3), 903.
12. Czikkely, V.; Försterling, H. D.; Kuhn, H. *Chem. Phys. Lett*. **1970**, 6 (1), 11.
13. Czikklely, V.; Forsterling, H. D.; Kuhn, H. *Chem. Phys. Lett*. **1970**, 6 (3), 207.
14. Giner-Casares, J. J.; De Miguel, G.; Pérez-Morales, M.; Martín-Romero, M. T. M. T.; Camacho, L.; Muñoz, E. *J. Phys. Chem. C* **2009**, 113 (14), 5711.
15. Parson, W. W. Springer-Verlag: Berlin, **2007**.
16. Kuhn, H.; Kuhn, C. In J-Aggregates; Kobayasho, T., Ed.; World Scientific: Singapore, **1996**.

THE JOURNAL OF PHYSICAL CHEMISTRY B

Published on 5 April 2019

DOI: 10.1021/acs.jpcb.9b01132

Optimization of Aminoacid Sequence of Fmoc-Dipeptides for Interaction with Lipid Membranes

Pablo G. Argudo,[a] Rafael Contreras-Montoya,[b] Luis Álvarez de Cienfuegos,[b] María T. Martín-Romero,[a] Luis Camacho,[a] Juan J. Giner-Casares[a]

a. Departamento de Química Física y T. Aplicada, Instituto Universitario de Investigación en Química Fina y Nanoquímica IUIQFN, Facultad de Ciencias, Universidad de Córdoba, Campus de Rabanales, Ed. Marie Curie, E-14071 Córdoba, Spain.

b. Departamento de Química Orgánica, Facultad de Ciencias, Universidad de Granada, (UGR), C. U. Fuentenueva, E-18071 Granada, Spain.

Fmoc-dipeptides appear as a highly relevant building block in smart hydrogels and nanovehicles for biological applications. The interactions of the Fmoc-dipeptides with the cell membrane determine the efficiency of the nanomaterials based on the Fmoc-dipeptides, as the internalization of nanovehicles for drug delivery. Here we aim at the understanding of the interplay of the interactions between the Fmoc-dipeptides and a phospholipid surface as a function of the aminoacid sequence. The DMPA (1,2-dimyristoyl-sn-glycero-3-phosphate) phospholipid in Langmuir monolayers was used as a model cell surface. A set of seven derivatives of Fmoc-dipeptides with a broad range of hydrophobicity were included. Mixed monolayers composed by DMPA:Fmoc-dipeptide in equimolar ratio were built and characterized in situ at the air/water interface. Surface pressure-molecular area isotherms (π–A), Brewster Angle Microscopy (BAM) and UV-vis reflection spectroscopy (ΔR) were combined to provide a holistic picture on the interactions of the Fmoc-dipeptide with the phospholipid

molecules. An increase in the hydrophobicity led to an enhanced interaction of the Fmoc-dipeptide and DMPA molecules.
The compression of the mixed monolayer could displace a significant fraction of the Fmoc-dipeptide from the monolayer. A high hydrophobicity promoted self-assembly of the Fmoc-dipeptides over interaction with the phospholipid surface. The interplay of these two phenomena was analyzed as a function of the aminoacid sequence of the Fmoc-dipeptides. The toxicity effect of Fmoc-FF could be observed and detailed at the molecular level. This study suggests that the adjustment of the hydrophobicity of the Fmoc-dipeptides within a defined range might optimize their efficiency for the interaction with the lipid membranes. A semiquantitative guide for the chemical design of Fmoc-dipeptides for biological applications is proposed herein.

Introduction

Dipeptides can self-assemble as single building blocks and in combination with biologically active molecules, *e.g.*, photosensitizers for nanomedicine.[1] The dipeptide structure is highly interesting as a self-assembling moiety when included in bioconjugates for drug delivery.[2–4] Bioinspired materials including dipeptides have been shown to assemble into intriguing nanostructures.[5–8] The Fmoc (9-fluorenylmethyloxycarbonyl) group confers relevant self-assembly and amphiphilic properties to the dipeptides.[9–12] Fmoc-dipeptides display antibacterial activity and can be used to prevent biofilm formation.[13] Self-assembled nanostructures of Fmoc-dipeptides and related building blocks have been proposed for cancer therapy.[14] The aminoacid residues might play a role as well in the assembly process, as shown for complementary peptide nucleic acids.[15–17]

Dipeptides can efficiently affect cell membranes, as demonstrated by the diphenylalanine dipeptide in combination with liposomes to render cytoskeleton-like structures. Such phenomenon is highly relevant when considering dipeptides for drug delivery, taking into account the fusion mechanism between the delivery vehicle and the cell membrane as shown by Li *et al.*[18] Permeation of dipeptides

through the phospholipid membrane has been studied by computer simulations, pointing at the hydrophobicity/hydrophilicity balance and interfacial activity as the key parameters for permeation.[19,20] Given the relevance and interest of Fmoc-dipeptides for biological applications, the ability to tune the interaction and impact of such dipeptides over the cell membrane is key in the rational chemical design of the Fmoc-dipeptides. Indeed, a programmed increase of the hydrophobicity in pH-responsive nanogels for drug delivery allowed Yang *et al*. an enhanced tumor accumulation through an efficient internalization into bulk tumor cells.[21] The significant role of hydrophobic interactions in the self-assembly of dipeptide derivatives for biomedical application on biosurfaces has been highlighted by Adams and Zelzer.[22]

The surface activity of the Fmoc-dipeptides determines the gel-forming properties, with the partition coefficient as key parameter.[23] We have recently related the partition coefficient with the capability of the Fmoc-dipeptides to self-assemble onto microstructures at the air/liquid interface.[24] The Langmuir technique appears as a highly suitable platform for studying the interaction of Fmoc-dipeptides with phospholipid monolayers as model membranes: the available area per phospholipid molecule can be finely tuned and the events at the phospholipid interface can be conveniently studied.[25–29] Pyrene-pentapeptide derivatives have been studied using the Langmuir technique, leading to intriguing mesostructures with prospect applications as bioactive coatings.[30] Hydrophobic dipeptides can form Langmuir monolayers under suitable experimental conditions, including acidic pH of the aqueous subphase.[31] The interactions of a set of Fmoc-dipeptide derivatives with Langmuir monolayers of the 1,2-dimyristoyl-sn-glycero-3-phosphate (DMPA) phospholipid as model lipid for the cell membrane have been studied herein. In situ Brewster Angle Microscopy and UV-vis reflection spectroscopy have offered detailed insights into the interaction between the Fmoc-dipeptides and the phospholipid monolayer as a function of the aminoacid sequence at the air/water interface. A similar procedure for applying surface pressure, *i. e.*, compression at a constant rate, have been applied for all DMPA:Fmoc-dipeptide monolayers.

Drastically different effects on the DMPA monolayer have been obtained as a function of the Fmoc-dipeptide derivative. The relevance of the extent and type of interactions between the DMPA and each Fmoc-dipeptide derivative has been assessed. This study aims to design of a set of general rules for the molecular design of Fmoc-dipeptide derivatives for biological applications.

Materials and Methods

Materials. Fmoc-LG, Fmoc-AA, Fmoc-GG and Fmoc-FF were purchased from Bachem Co. Fmoc-MF, Fmoc-RF and Fmoc-CF were synthesized as described elsewhere.[24] DMPA was purchased from Avanti Lipids and used as received. Solvents were used without further purification and purchased from Aldrich (Germany). Hydrochloric acid 37% was PRS-Codex purchased from Panreac and used as received. The initial 1 mM solutions of Fmoc-RF, Fmoc-CF, Fmoc-MF and Fmoc-FF dipeptides were prepared in dichloromethane. The initial 1 mM solutions of Fmoc-GG, Fmoc-AA and Fmoc-LG were in methanol. A mixture of chloroform:methanol (3:1 in volume), was used for dissolving DMPA at a concentration of 1 mM. The Fmoc-dipeptides and the DMPA were co-spread in molar ratio DMPA:Fmoc-dipeptide 1:1. Ultrapure water produced by a Millipore Milli-Q unit and pre-treated by a Millipore reverse osmosis system (>18.2 MΩ cm) was used to prepare the acid solution for subphase. The subphase temperature was 21 ºC with pH 2. All experiments were performed on tables with vibration isolation (antivibration system MOD-2 S, Accurion, Göttingen, Germany) in a large class 100 clean room.

Surface pressure–area (π—A) isotherms. Two different models of Nima troughs (Nima Technology, Coventry, England) were used, both provided with a Wilhelmy type dynamometric system using a strip of filter paper: a NIMA 611D with one moving barrier for the measurement of the reflection spectra, and a NIMA 601, equipped with two symmetrical barriers to record BAM images. The monolayers were compressed at a speed of 0.03 nm^2 min^{-1} $molecule^{-1}$. Assuming a complete loss of the spread Fmoc-dipeptide molecules from the air/liquid interface to the bulk

subphase, a maximum concentration of 10^{-7} M would be achieved. A bulk concentration of *ca*. 10^{-3} M was required to record a significant change in the surface tension of water according to the Polavarapu *et al*.[32]. We therefore assume the surface tension for the subphase is not modified by the effect of mass transfer of a given fraction of the Fmoc-dipeptide molecules from the mixed monolayers to the bulk subphase. The compression speed allowed a detailed study of the DMPA:Fmoc-dipeptide mixed monolayers and assured that the recorded isotherms were not affected by kinetic effects.

UV-vis reflection spectroscopy. UV–visible reflection spectra at normal incidence as the difference in reflectivity (ΔR) of the film-covered water surface and the bare surface were obtained with a Nanofilm Surface Analysis Spectrometer (Ref SPEC^2, supplied by Accurion GmbH, Göttingen, Germany).

Brewster angle microscopy (BAM). Images of the film morphology were obtained by Brewster angle microscopy (BAM) with a I-Elli2000 (Accurion GmbH) using a Nd:YAG diode laser with wavelength 532 nm and 50 mW, which can be recorded with a lateral resolution of 2 μm. The image processing procedure included a geometrical correction of the image, as well as a filtering operation to reduce interference fringes and noise.

Results and Discussion

A set of seven Fmoc-dipeptides was included in this study, see Figure 1 for the general molecular structure and Table 1 for the detailed aminoacid sequence for each derivative of Fmoc-dipeptide. The Fmoc-dipeptide molecules tend to solubilize in bulk water at neutral pH, forming micelles and other aggregates.[33] Therefore, a diluted solution of HCl with pH = 2 was used as a subphase according to the study on hydrophobic dipeptides by Clegg and Adams.[31] The carboxylic acid of the Fmoc-dipeptides was protonated.[34] The outer cell membrane was modelled as a Langmuir monolayer of the phospholipid Dimyristoylphosphatidic acid (DMPA), showing no net charge at acid pH.[35,36] Note that the commonly used Phosphatidylcholine (PC) phospholipids will be positively charged at such pH conditions and therefore would

not be a suitable phospholipid molecule for mimicking the eukaryotic membrane.[37,38]

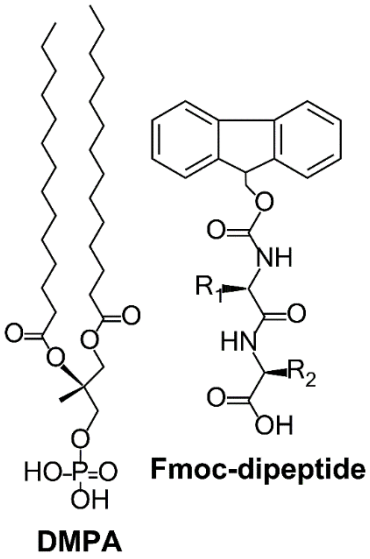

Figure 1. Molecular structures for the DMPA phospholipid and the Fmoc-dipeptide derivatives.

The Fmoc-dipeptide derivatives were co-spread with the DMPA phospholipid in molar ratio 1:1, achieving an initial situation of a mixed monolayer DMPA:Fmoc-dipeptide. This experimental procedure assured the interaction between the components of the Langmuir monolayer, at least prior to compression of the mixed monolayer.[39] The surface pressure-molecular area isotherms for the DMPA:Fmoc-dipeptide and the pure DMPA monolayers are shown in Figure 2. The isotherms for the mixed monolayers DMPA:Fmoc-GG, DMPA:Fmoc-AA, and DMPA:Fmoc-LG overlap to a large extent with the isotherm for the pure DMPA, thus showing a reduced occupancy of the Fmoc-GG, Fmoc-AA and Fmoc-LG molecules at the DMPA monolayer. Note these Fmoc-dipeptides show the lowest values of hydrophobicity, see Table 2. The partition coefficient (P) is the ratio of the concentration of a given compound in the organic phase to that in the water phase at infinite dilution, normally reported as – log P, and was calculated according to

Robins *et al.*[40] The LE expanded phase was suppressed for the isotherms of the DMPA:Fmoc-GG, DMPA:Fmoc-AA, and DMPA:Fmoc-LG mixed monolayers. A relatively small amount of the Fmoc-dipeptide molecules might be present at the mixed monolayers from the expanded state to *ca.* 0.5 nm^2 per DMPA molecule, causing a modification in the physical state of the alkyl chains of the DMPA molecules. While the solid phase of the isotherm was not modified, the region from *ca.* 0.8 to 0.5 nm^2 per DMPA molecule did not display the typical LE phase. The amount of Fmoc-dipeptide molecules at the DMPA monolayer was modest in the three mixed monolayers, as confirmed by UV-vis reflection spectroscopy, see below. Only Fmoc-LG displayed a comparatively higher UV-vis reflection signal, probably corresponding to Fmoc-LG adsorbed beneath the DMPA monolayer. Further compression of the monolayers led to a loss of the Fmoc-dipeptides onto the aqueous subphase, probably as micelle-like aggregates.[41]

Table 1. Abbreviation and chemical groups for each derivative of Fmoc-dipeptide.

Abbreviation	**R_1**	**R_2**
Fmoc-GG	-H	-H
Fmoc-AA	$-CH_3$	$-CH_3$
Fmoc-LG	$-CH_2-CH-(CH_3)_2$	-H
Fmoc-RF	$-(CH_2)_3-NH-C(NH)-NH_2$	$-CH_2$-Phe
Fmoc-CF	$-CH_2-SH$	$-CH_2$-Phe
Fmoc-MF	$-(CH_2)_2-SCH_3$	$-CH_2$-Phe
Fmoc-FF	$-CH_2$-Phe	$-CH_2$-Phe

The surface pressure-molecular area isotherms of the DMPA:Fmoc-dipeptides including a phenyl (F) group show a different behavior to the F-free dipeptides, see Figure 2. Note that the F-containing Fmoc-RF, Fmoc-CF, Fmoc-MF, and Fmoc-FF show a higher hydrophobicity.

Table 2. Values for partition coefficient (– log P) of the Fmoc-dipeptide derivatives.

Fmoc-dipeptide	**– log *P***
FmocGG	1.37
FmocAA	2.51
FmocLG	3.19
FmocRF	3.91
FmocCF	4.21
FmocMF	4.81
FmocFF	5.82

A shift towards larger values of molecular area was obtained for the four F-containing Fmoc-dipeptides in the mixed monolayers at the expanded state. The Fmoc-dipeptide molecules were located at the monolayer for the DMPA:Fmoc-RF, DMPA:Fmoc-CF, and DMPA:Fmoc-MF mixed monolayers as evidenced by the significant lift-off of the surface pressure during the LE-LC transition to values of surface pressure from *ca.* 18 to 22 mN/m. Further compression of these mixed monolayers above 25 mN/m led to desorption of the Fmoc-dipeptide molecules onto the subphase. Note that according to the UV-vis reflection spectra (see below), a significant fraction of the Fmoc-dipeptide molecules remained adsorbed underneath the DMPA phospholipid monolayer. Particularly, the DMPA:Fmoc-RF and DMPA:Fmoc-CF monolayers display a significant expansion of their isotherms with respect to the isotherm of pure DMPA for a large interval of the values of surface pressure. Note there are three points of intercrossing between the isotherms of DMPA:Fmoc-RF and DMPA:Fmoc-CF: 0.95 nm^2 per DMPA molecule (12.1 mN/m); 0.60 nm^2 per DMPA molecule (21.9 mN/m); and 0.56 nm^2 per DMPA molecule (23.7 mN/m). The intercrossing of the isotherms was ascribed to a similar modification in the phase behavior of the DMPA by the Fmoc-dipeptides in a slightly different extent for both Fmoc-RF and Fmoc-CF.[42] The isotherm for the DMPA:Fmoc-MF monolayer shows an expansion with respect to the isotherm for

the pure DMPA similar to those observed for the DMPA:Fmoc-RF and DMPA:Fmoc-CF monolayers indicating the presence of the Fmoc-MF at the DMPA monolayer.[43] Remarkably, the isotherms for DMPA:Fmoc-LG, DMPA:Fmoc-RF, and DMPA:Fmoc-CF converge with isotherm for pure DMPA for surface pressure greater than 25 mN/m. The convergence at high values of surface pressure was related to the expelling of a fraction of the Fmoc-dipeptides from the mixed monolayer onto the subphase.[44] However, the isotherm for the DMPA:Fmoc-FF monolayer shows the largest deviation with respect to the pure DMPA monolayer.

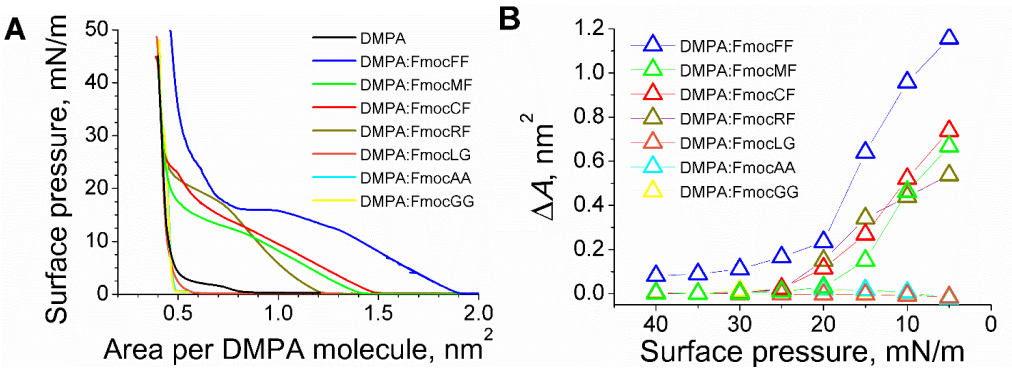

Figure 2. A) Surface pressure-molecular area isotherms for the pure DMPA and the DMPA:Fmoc-dipeptide mixed monolayers. B) Increment of the molecular area per DMPA molecule of the isotherms for the mixed monolayers DMPA:Fmoc-dipeptide with respect to the isotherm for the pure DMPA monolayer.

The DMPA:Fmoc-FF monolayer was the only case for a persistent shift of the isotherm even at high values of surface pressure. Note that the Fmoc-FF dipeptide is the most hydrophobic Fmoc-dipeptide derivative included in this study. The relative amount of Fmoc-FF molecules could be estimated by considering the shift of the isotherm at high values of surface pressure and an approximate value of the area occupied by a Fmoc-FF molecule in a completely upright arrangement. A value of *ca.* 0.23 nm^2 per Fmoc-FF molecule was obtained using the HyperChem molecular modelling program.[45] The expansion values of the DMPA:Fmoc-FF isotherm with

respect to the pure DMPA isotherm at surface pressure of 20, 30, and 40 mN/m were 0.24, 0.12, and 0.08 nm^2 per DMPA molecule, respectively. These values of shift in the molecular area of the isotherms pointed to an approximate composition of the mixed monolayer DMPA:Fmoc-FF of 1:1, 2:1, and 3:1 for surface pressure values of 20, 30, and 40 mN/m, respectively. Therefore, the transfer of Fmoc-FF molecules from the mixed monolayer to the subphase led to an enrichment of DMPA in the mixed monolayer up to three-fold at the most compressed state. Remarkably, the amount of Fmoc-FF molecules at the interface increased steadily with the compression of the DMPA:Fmoc-FF mixed monolayer as revealed by UV-vis reflection spectroscopy. Therefore, the interactions between the Fmoc-FF molecules and the DMPA molecules at the phospholipid monolayer were largely favored.

The influence of the Fmoc-dipeptide molecules on the morphology of the DMPA monolayer at the micrometric level was revealed by in situ Brewster Angle Microscopy (BAM).[46–48] The DMPA:Fmoc-GG, DMPA:Fmoc-AA, and DMPA:Fmoc-LG monolayers showed a similar behavior, see Figure 3. A rather dense and reflective gas-condensed phase transition plateau was found at the expanded state, indicating the presence of Fmoc-dipeptide molecules interacting with the DMPA at early stages of compression of the mixed monolayers. A fluid phase appeared with a slight increase of surface pressure to 0.5 to 3 mN/m. Such phase was more reflective and dense than the previous gas-condensed phase transition plateau, showing small holes that might correspond to fluid domains of the mixed monolayers. Note that the commonly observed domains of DMPA and related phospholipids were not observed, suggesting the disruption of the liquid expanded-liquid condensed (LE-LC) phase transition of DMPA.[49] A solid and homogenous phase was formed upon compression of the monolayer. There was a significant effect of the Fmoc-dipeptide molecules at intermediate values of surface pressure, suppressing the LE-LC phase transition. A certain fraction of the Fmoc-GG, Fmoc-AA, and more significantly Fmoc-LG molecules might remain at the DMPA even at high values of surface pressure. No area was occupied as noted by the isotherms, indicating that the Fmoc-LG molecules were adsorbed underneath the DMPA

monolayer as verified by UV-vis reflection spectroscopy, see below.

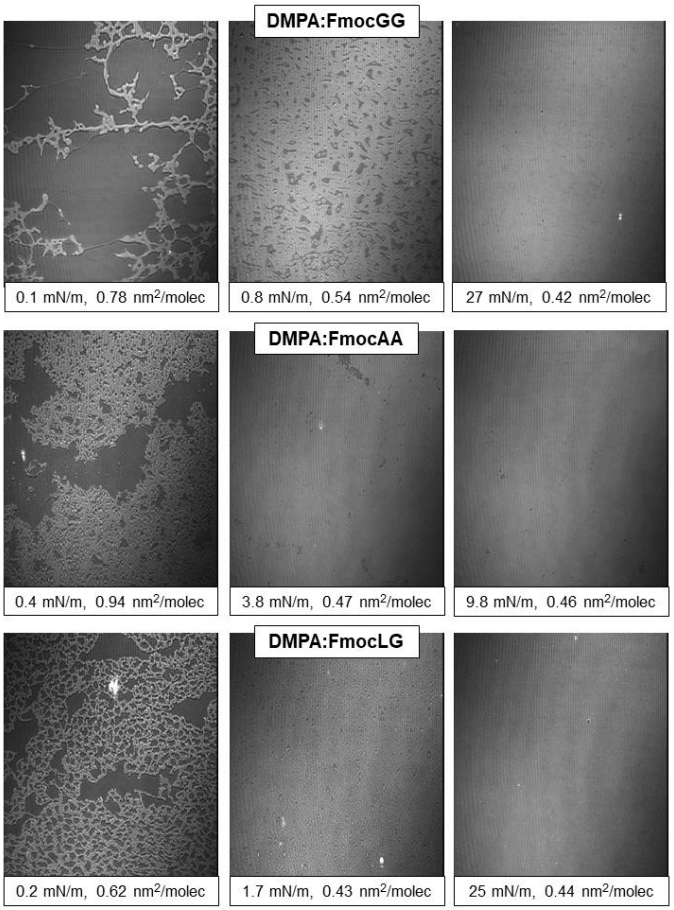

Figure 3. Brewster Angle Microscopy images for the DMPA:Fmoc-GG (top), DMPA:Fmoc-AA (middle), and DMPA:Fmoc-LG (bottom) monolayers. The values of surface pressure and available surface area per DMPA molecule are included at the bottom of each picture. The width of each frame corresponds to 215 μm.

The DMPA:Fmoc-RF monolayer at highly expanded state displayed a gas-condensed phase transition plateau with some aggregates, see Figure 4. Rounded bright domains during the LE-LC transition were also observed with compression of the monolayer. The domains retained the typical shape for pure DMPA domains, however with higher polydispersity of the size of the domains. The large domains might be composed by pure DMPA in LC state in combination with DMPA and

Fmoc-RF. The bright domains reached a more homogeneous size with further compression of the monolayer to *ca.* 43 mN/m, see Figure 4. Note that the background became highly reflective as well, probably related with the presence of the Fmoc-RF molecules.

The DMPA:Fmoc-CF monolayer showed an atypical behavior that was already suggested by the slightly larger shift in the isotherm with respect to DMPA:Fmoc-MF as expected from the lower value of – log P of Fmoc-CF. A comparatively more reflective gas-condensed phase transition plateau with some defects appearing as rounded dark domains was obtained, see Figure 4. Rounded bright domains for the LE-LC transition were observed, similarly to the DMPA:Fmoc-CF monolayer. A small fraction of elongated microstructures analogous to those formed by pure Fmoc-CF at the air/water interface were also found, with no coalescence with the domains.[24] An inversion in the phase contrast was obtained upon further compression of the monolayer to a highly compressed state. The more fluid phase surrounding the domains turned brighter than the mentioned domains. Such inversion in the phase contrast was ascribed to an enrichment of the more fluid phase with Fmoc-CF molecules.[50] This enrichment was promoted by specific interaction between Fmoc-CF molecules: complexation of the cysteine group with neighbor Fmoc groups via –SH::: π electrons in the aromatic rings, with a significant binding energy.[51] The –SH group acted as the H-bond donor. This preferential interaction led to the segregation of the more reflective Fmoc-CF molecules out of the DMPA phospholipid domains and therefore to the inversion of the contrast. Thin and elongated structures were found in the gas-condensed phase transition plateau for the DMPA:Fmoc-MF monolayer, see Figure 4. Bright and regular domains were found during the LE-LC transition at *ca.* 13 mN/m, analogous to a pure DMPA monolayer. The DMPA domains persisted even at the solid state of the DMPA:Fmoc-MF monolayer, where additional small and highly reflective spots appeared, indicating aggregates of Fmoc-MF, see Figure 4. The inversion in phase contrast was not observed in this case, given the methionine group was not able to present the mentioned H-bonding due to the methylene group substituting the hydrogen atom present in the cysteine residue.

The presence of Fmoc-CF and Fmoc-MF in the mixed monolayers at high values of surface pressure was further confirmed by UV-vis reflection spectroscopy, see below. BAM informed on the different morphology of the mixed monolayers, disclosing self-aggregated Fmoc-MF and more distributed Fmoc-CF at the mixed monolayers. Note the higher hydrophobicity of Fmoc-MF with respect to Fmoc-CF, leading to superior interaction with the phospholipid monolayer.

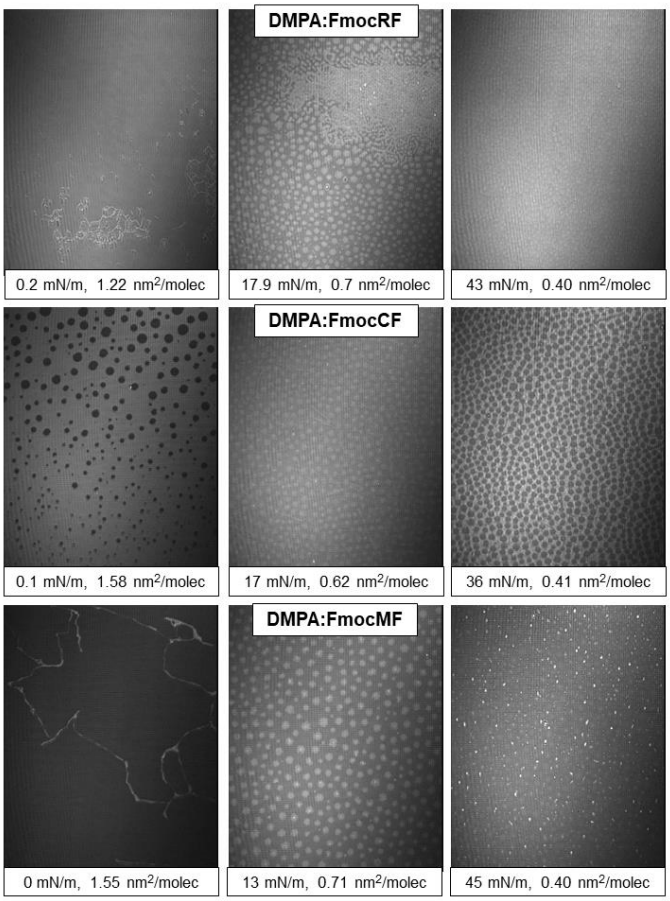

Figure 4. Brewster Angle Microscopy images for the DMPA:Fmoc-RF (top), DMPA:Fmoc-CF (middle), and DMPA:Fmoc-MF (bottom) monolayers. The values of surface pressure and available surface area per DMPA molecule are included at the bottom of each picture. The width of each frame corresponds to 215 μm.

The π–A isotherms converge with the pure DMPA isotherm in spite of the significant modification of the morphology observed by BAM. The Fmoc-dipeptide molecules were adsorbed underneath the DMPA monolayer, thus occupying no net area and rendering a significant effect on the BAM images and UV-vis reflection signal. This significant interaction of the mentioned Fmoc-dipeptide derivatives with the DMPA monolayer, already shown in a minor extent by the DMPA:Fmoc-LG monolayer, indicated the suitability of the Fmoc-RF, Fmoc-CF, Fmoc-MF for effective interaction with a phospholipid surface.

The DMPA:Fmoc-FF monolayer displayed a quite different morphology to the mentioned mixed monolayers, see Figure 5. Small aggregates with rounded and elongated shapes were found for the gas-condensed phase transition plateau of the DMPA:Fmoc-FF monolayer. The elongated aggregates persisted along the complete isotherm of the DMPA:Fmoc-FF monolayer, with a significant increase in number and size with compression of the mixed monolayer. These elongated structures are remarkably similar to those obtained for the pure Fmoc-FF spread at the air/water interface.[24] Note that the number of rounded domains decreased simultaneously to the increase of elongated structures, pointing at a mass transfer of the Fmoc-FF molecules from those domains to the elongated structures. The DMPA domains were not observed for the DMPA:Fmoc-FF monolayer at intermediate values of surface pressure, pointing to a significant distortion of the physical state of the DMPA molecules in the mixed monolayers caused by the Fmoc-FF molecules. Further compression to high values of surface pressure led to aggregation of the elongated structures onto heterogeneous and highly reflective assemblies. The high reflectivity observed by BAM was related with a large surface concentration of Fmoc-FF. This observation was consistent with the UV-vis reflection spectroscopy results, see below.

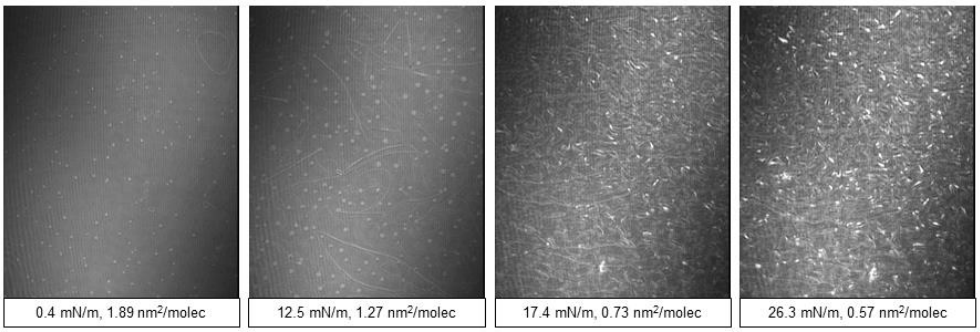

Figure 5. Brewster Angle Microscopy images for the DMPA:Fmoc-FF monolayer. The values of surface pressure and available surface area per DMPA molecule are included at the bottom of each picture. The width of each frame corresponds to 215 μm.

To gain further insight into the surface concentration of the Fmoc-dipeptide derivatives at the air/water interface, in situ UV-vis reflection spectroscopy was applied.[52] The UV-vis reflection signal neglects any contribution from the bulk solution, instead arising exclusively from the enhancement of reflection of the incoming radiation by absorbance of molecules located at the air/water interface according to the equation (1):

$$\Delta R \simeq 2.303 \cdot 10^3 f_0 \varepsilon \sqrt{R_S} \Gamma \qquad (1)$$

where ΔR is the increase of reflection under normal incidence, ε is the molar absorption coefficient ($M^{-1} \cdot cm^{-1}$), R_S is the reflectivity of the aqueous interface, Γ is the surface concentration ($mol \cdot cm^{-2}$), and f_0 is the orientation factor.

The Fmoc group displays a significant UV-vis signal. The UV-vis reflection spectra of the DMPA:Fmoc-CF and DMPA:Fmoc-FF as representative examples for the mixed monolayers at different values of molecular area are shown in Figure 6. The UV-vis reflection spectra for the DMPA:Fmoc-CF mixed monolayer showed 4 peaks located at 258, 262, 268, and 283 nm overlapped into a broad band. Similar spectra were achieved for the DMPA:Fmoc-FF mixed monolayer, showing four bands centred at 257, 262, 270, and 283 nm with a high extent of overlapping as well. The positions of the bands are similar to those found in self-assembled

structures of pure Fmoc-FF at the air/liquid interface.[24] Therefore, segregation of the Fmoc-dipeptide and DMPA molecules at the mixed monolayers is expected. This segregation was in agreement with the BAM pictures, in which DMPA domains and elongated reflective structures for the DMPA:Fmoc-CF and DMPA:Fmoc-FF mixed monolayers, respectively. The Fmoc-dipeptide molecules were located at the mixed monolayers with the Fmoc groups self-arranged in a zipper-like manner.

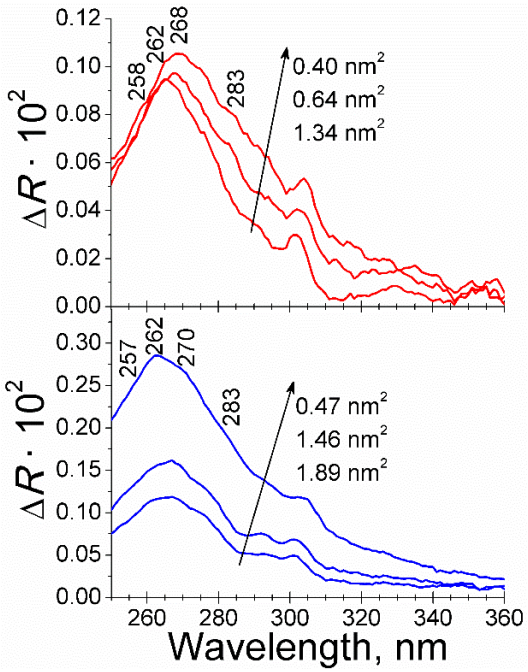

Figure 6. UV-vis reflection for the DMPA:Fmoc-CF (top, red line) and DMPA:Fmoc-FF (bottom, blue line) monolayers. The values of available surface area per DMPA molecule are indicated in the inset. Maximum values of wavelength for each band are indicated in the inset.

The UV-vis reflection spectra for the DMPA:Fmoc-CF monolayer lower signal than those for the DMPA:Fmoc-FF monolayer. The absolute value of the UV-vis signal is *ca.* two-fold greater for the DMPA:Fmoc-FF. Therefore, a higher amount of Fmoc-FF than Fmoc-CF molecules are present at the mixed monolayers, as anticipated from the high reflectivity of the DMPA:Fmoc-FF monolayer observed by BAM, see above. Remarkably, the UV-vis signal did not show a large variation

with compression for the DMPA:Fmoc-CF monolayer. A modest variation of the amount of Fmoc-CF molecules with compression was obtained, indicating an expelling of those Fmoc-CF molecules from the mixed monolayer under compression when a steady surface concentration was reached. On the other hand, the UV-vis signal corresponding to the Fmoc-FF molecules increased with compression of the monolayer, indicating a significant increase in the surface concentration and the residence of Fmoc-FF molecules at the phospholipid surface.

The absolute amount of Fmoc-dipeptide molecules at the air/water interface could be monitored by the UV-vis reflection spectra for the DMPA:Fmoc-dipeptide mixed monolayers. Considering the Fmoc group was responsible for the UV-vis signal and all Fmoc-dipeptide derivatives include one Fmoc group per dipeptide molecule, the integrated value of the UV-vis spectra can be directly compared. The integral values of the UV-vis spectra are shown in Figure 7. Considering the high values of available surface area per DMPA molecule, *i. e.*, the expanded state of the monolayers, three groups of DMPA:Fmoc-dipeptide monolayers could be considered. The mixed monolayers containing Fmoc-GG, Fmoc-AA, and Fmoc-LG showed no significant UV-vis signal, pointing to a reduced presence of the Fmoc-dipeptide at the mixed monolayer. This group is formed by the less hydrophobic Fmoc-dipeptide derivatives, see Table 2. A second group comprising Fmoc-RF, Fmoc-CF and Fmoc-CF where a significant UV-vis signal was already present even prior to the compression of the mixed monolayers could be defined. A third group was observed solely for the DMPA:Fmoc-FF monolayer, in which the UV-vis signal was *ca.* two-fold the observed signal or the previous group, thus indicating a comparatively higher content of Fmoc-FF molecules in the mixed monolayer.

Different trends were observed with compression of the mixed monolayers. Concerning the first group of hydrophilic dipeptides, no signal was attained from the mixed monolayers containing Fmoc-GG and Fmoc-AA. This result was in agreement with the expected solubilization of the Fmoc-dipeptide molecules onto the aqueous subphase. However, a significant increase of the UV-vis signal is obtained for the Fmoc-LG in contact with a highly compressed DMPA monolayer,

indicating the partition of the Fmoc-LG molecules from the aqueous subphase to the DMPA monolayer when the phospholipid molecules provide enough surface to interact.

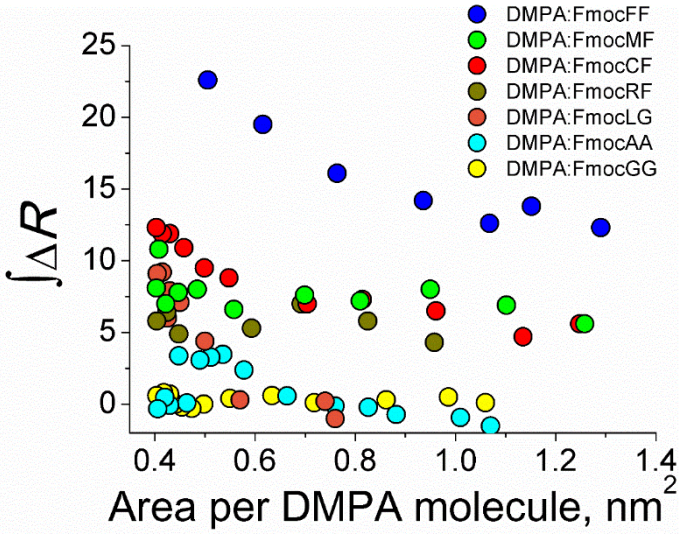

Figure 7. Integral value of the UV-vis spectra for the DMPA:Fmoc dipeptide derivatives at different values of available surface area per DMPA molecule. Composition of the mixed monolayers as noted in the inset.

A constant value for the UV-vis reflection signal was obtained for the mixed monolayers of the more hydrophobic second group of Fmoc-dipeptides, with a modest increase at the highly compressed state of the mixed monolayer. Despite this increase of surface concentration of Fmoc-dipeptide molecules at the highest surface pressure, the intensity of the UV-vis signal remained almost constant for most of the isotherm. The relative fraction of the Fmoc-RF, Fmoc-CF, and Fmoc-MF molecules was in a steady state along compression, in which the accumulation of Fmoc-dipeptide molecules by compression of the monolayer is compensated by a certain solubilization onto the aqueous subphase.

An increase of the UV-vis reflection signal with the compression of the DMPA:Fmoc-FF monolayer was registered, pointing to a steady enrichment in

Fmoc-FF molecules. This enrichment was related to the decrease in the available surface area with reduced or no solubilization of the Fmoc-FF molecules into the aqueous subphase. The residence of the Fmoc-FF molecules at the DMPA:Fmoc-FF mixed monolayers was therefore superior to the other Fmoc-dipeptide derivatives, as expected from the highest value of – log P. This increase of amount of Fmoc-FF molecules interacting with the DMPA molecules with a relative increase of the hydrophobicity was in agreement with the study on oligopeptides with phospholipid mono- and bi-layers by Blume *et al*.[53]

The evolution of the surface concentration of the Fmoc-dipeptide molecules with the compression of the mixed monolayers could be elucidated following the UV-vis reflection signal normalized by the DMPA surface area, as described by equation (2) considering A_{DMPA} the available surface area per DMPA molecule and N_A as the Avogadro number:

$$\Delta R_{norm} = A_{DMPA} \times \Delta R = \frac{2.303 \times 10^{17} f_0 \varepsilon}{N_A} \sqrt{R_S} = 5.41 \times 10^{-8} f_0 \varepsilon \qquad (2)$$

The integrated values of the normalized UV-vis signal for the mixed monolayers containing the Fmoc-CF, Fmoc-MF, and Fmoc-FF are shown in Figure 8.

The DMPA:Fmoc-CF and DMPA:Fmoc-MF monolayers showed a similar behavior, with a *ca.* 25% of the UV-vis reflection intensity remaining from the initial UV-vis reflection intensity after complete compression of the mixed monolayers. This observation agrees with the previous finding on the Fmoc-CF and Fmoc-MF molecules being expelled to the aqueous subphase in a certain fraction with compression of the mixed monolayers. On the other hand, a *ca.* 80% of the UV-vis reflection intensity remained from the initial UV-vis reflection intensity after compression from 1.25 nm^2 to 0.7 nm^2 per DMPA molecule. Note that the surface concentration of Fmoc-FF appeared as almost constant for the final interval of the isotherm from 0.7 nm^2 to 0.5 nm^2 per DMPA molecule. The discrepancy with the surface pressure-molecular area isotherm was ascribed to a phase transition in the mixed monolayer for the large area range considered. The persistence of the Fmoc-FF molecules even in a highly compressed monolayer was therefore confirmed. This

observation is also in agreement with the observed increase of DMPA molecular area in the surface pressure-molecular area isotherm at high values of surface pressure. From these data we could conclude that high hydrophobicity led to a strong interfacial self-assembly of the Fmoc-FF molecules prevailing over the interactions with the DMPA molecules. The persistent presence of these self-assembled structures was able to significantly distort the DMPA phospholipid layer. Indeed, Laverty *et al.* proposed that the hydrophobic interactions promoted by aromatic groups in Fmoc-FF with phospholipids composing the membrane of erythrocytes could lead to a significant toxicity shown in significant hemolysis during in vitro experiments.[54]

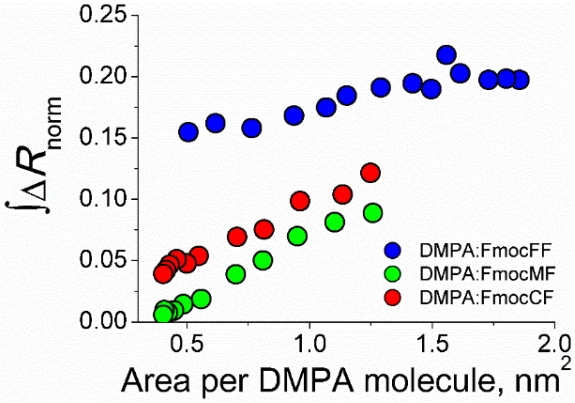

Figure 8. Integral value of the normalized UV-vis spectra at different values of available surface area per DMPA molecule for the DMPA:FmocFF, DMPA:FmocMF, and DMPA:FmocCF as noted in the inset.

Therefore, the aminoacid sequence determines the hydrophobicity/hydrophilic balance in Fmoc-dipeptide derivatives, which in turn controls the interaction with the phospholipid surface. By adjusting the hydrophobicity of the Fmoc-dipeptide derivatives, the tuning of the interactions of the Fmoc-dipeptide molecules with the DMPA phospholipid surface has been demonstrated here. There was no linear or easily predicted trend of the extent of interaction of the Fmoc-dipeptide molecules with the phospholipid monolayer with the values of – log P. Instead, three types of behavior could be found, see Table 3.

Table 3. Summary of the interactions of the Fmoc-dipeptide derivatives with a model membrane as a function of – log P.

– log ***P***	**Amino acid sequence for the Fmoc-dipeptide**	**Effect on a model cell surface**	**Expected biological activity**
1.37 to 3.19	Fmoc-GG, Fmoc-AA, Fmoc-LG	Low or no adsorption along the isotherm	Reduced or no interaction with living cells
3.91 to 4.81	Fmoc-RF, Fmoc-CF, Fmoc-MF	Significant interactions at low values of surface pressure and adsorption at high values of surface pressure	Significant interactions with living cells with no disruption of the membrane, "safety zone"
5.82	Fmoc-FF	Persistent presence of the Fmoc-dipeptide and significant disruption of the lipid monolayer at all values of surface pressure	Disruption of cell membrane

While hydrophilic Fmoc-dipeptides did not show significant interaction with the DMPA phospholipid monolayer, an excess of hydrophobicity might lead to predominance of self-assembly of Fmoc-dipeptides at the phospholipid monolayer, ultimately showing toxicity. A "safety zone" for Fmoc-dipeptide derivatives that present efficient interaction with the phospholipid surface while avoiding toxicity has been defined in the interval of – log P from *ca.* 4 to 5. The interval corresponded to the Fmoc-RF, Fmoc-CF, and Fmoc-MF from this set of Fmoc-dipeptides. This study aimed to provide a semiquantitative guide on the hydrophobicity/hydrophilicity balance that might allow an efficient interaction with the phospholipid surface at cell membranes and therefore an optimal performance for biological applications.

Conclusions

The interactions between a set of Fmoc-dipeptide derivatives with a broad range of hydrophobicity with a DMPA phospholipid surface as model of cell membrane have been assessed. Less hydrophobic Fmoc-dipeptide molecules are expelled from the model surface, instead occupying the bulk aqueous phase. With the gradual increase of hydrophobicity, the interactions between the Fmoc-dipeptides and the DMPA molecules are enhanced, leading to an improved residence of the Fmoc-dipeptide molecules at the mixed monolayers. Comparatively hydrophilic Fmoc-dipeptide suppressed the LE expanded phase of the DMPA phospholipid. A greater modification of the physical state of the DMPA phospholipid molecules at the mixed monolayer with hydrophobic Fmoc-dipeptide derivatives was also observed. A significant fraction of the Fmoc-dipeptide molecules remained adsorbed underneath the DMPA phospholipid monolayer. However, a severe alteration of the DMPA phospholipid molecules has been observed for the DMPA:Fmoc-FF mixed monolayer, thus pointing to the toxic effect of the highly hydrophobic Fmoc-FF as a result of such interactions. The shift in the molecular area of the isotherms pointed to an approximate composition of the mixed monolayer DMPA:Fmoc-FF from 1:1 to 3:1 for surface pressure from 20 to 40 mN/m. Besides additional suitable chemical modifications, the phenyl group in the aminoacid residues appeared as a relevant chemical group for tuning the hydrophobic/hydrophilic balance. This study provides insights for a semiquantitative range of hydrophobicity in the chemical design of Fmoc-dipeptides for biologically related applications.

Author Information

Corresponding Author

lac@ugr.es (L. A.-C.), jjginer@uco.es (J. J. G.-C.)

Author Contributions

The manuscript was written through contributions of all authors. All authors have given approval to the final version of the manuscript.

Acknowledgment

Support from the Ministry of Economy and Competitiveness of Spain through the MANA project CTQ2017-83961-R is acknowledged. FIS2017-85954-R (Agencia Estatal de Investigación, AEI, Spain, co-funded by Fondo Europeo de Desarrollo Regional, ERDF, European Union). J.J.G.-C. acknowledges the Ministry of Economy and Competitiveness for a "Ramon y Cajal" contract (RyC-2014-14956).

References

(1) Li, S.; Zou, Q.; Li, Y.; Yuan, C.; Xing, R.; Yan, X. Smart Peptide-Based Supramolecular Photodynamic Metallo-Nanodrugs Designed by Multicomponent Coordination Self-Assembly. *J. Am. Chem. Soc.* **2018**, *140* (34), 10794–10802.

(2) Anami, Y.; Yamazaki, C. M.; Xiong, W.; Gui, X.; Zhang, N.; An, Z.; Tsuchikama, K. Glutamic Acid–valine–citrulline Linkers Ensure Stability and Efficacy of Antibody–drug Conjugates in Mice. *Nat. Commun.* **2018**, *9* (1), 2512.

(3) Baral, A.; Roy, S.; Dehsorkhi, A.; Hamley, I. W.; Mohapatra, S.; Ghosh, S.; Banerjee, A. Assembly of an Injectable Noncytotoxic Peptide-Based Hydrogelator for Sustained Release of Drugs. *Langmuir* **2014**, *30* (3), 929–936.

(4) Feng, Z.; Wang, H.; Xu, B. Instructed Assembly of Peptides for Intracellular Enzyme Sequestration. *J. Am. Chem. Soc.* **2018**, *140* (48), 16433–16437.

(5) Katsoulidis, A. P.; Antypov, D.; Whitehead, G. F. S.; Carrington, E. J.; Adams, D. J.; Berry, N. G.; Darling, G. R.; Dyer, M. S.; Rosseinsky, M. J. Chemical Control of Structure and Guest Uptake by a Conformationally Mobile Porous Material. *Nature* **2019**, *565* (7738), 213–217.

(6) Paramonov, S. E.; Jun, H.-W.; Hartgerink, J. D. Self-Assembly of Peptide−Amphiphile Nanofibers: The Roles of Hydrogen Bonding and Amphiphilic Packing. *J. Am. Chem. Soc.* **2006**, *128* (22), 7291–7298.

(7) Mozhdehi, D.; Luginbuhl, K. M.; Simon, J. R.; Dzuricky, M.; Berger, R.; Varol, H. S.; Huang, F. C.; Buehne, K. L.; Mayne, N. R.; Weitzhandler, I.; *et al*. Genetically Encoded Lipid–polypeptide Hybrid Biomaterials That Exhibit Temperature-Triggered Hierarchical Self-Assembly. *Nat. Chem.* **2018**, *10* (5), 496–505.

(8) Sánchez-Ferrer, A.; Adamcik, J.; Handschin, S.; Hiew, S. H.; Miserez, A.; Mezzenga, R. Controlling Supramolecular Chiral Nanostructures by Self-Assembly of a Biomimetic β-Sheet-Rich Amyloidogenic Peptide. *ACS Nano* **2018**, *12* (9), 9152–9161.

(9) Fleming, S.; Debnath, S.; Frederix, P. W. J. M.; Tuttle, T.; Ulijn, R. V. Aromatic Peptide Amphiphiles: Significance of the Fmoc Moiety. *Chem. Commun.*

2013, *49* (90), 10587.

(10) Yang, D.; Duan, P.; Zhang, L.; Liu, M. Chirality and Energy Transfer Amplified Circularly Polarized Luminescence in Composite Nanohelix. *Nat. Commun.* **2017**, *8*, 15727.

(11) Mansbach, R. A.; Ferguson, A. L. Patchy Particle Model of the Hierarchical Self-Assembly of π-Conjugated Optoelectronic Peptides. *J. Phys. Chem. B* **2018**, *122* (44), 10219–10236.

(12) McDougall, L.; Draper, E. R.; Beadle, J. D.; Shipman, M.; Raubo, P.; Jamieson, A. G.; Adams, D. J. Enzymatically-Stable Oxetane-Based Dipeptide Hydrogels. *Chem. Commun.* **2018**, *54* (14), 1793–1796.

(13) Debnath, S.; Shome, A.; Das, D.; Das, P. K. Hydrogelation Through Self-Assembly of Fmoc-Peptide Functionalized Cationic Amphiphiles: Potent Antibacterial Agent. *J. Phys. Chem. B* **2010**, *114* (13), 4407–4415.

(14) Wang, H.; Feng, Z.; Xu, B. D-Amino Acid-Containing Supramolecular Nanofibers for Potential Cancer Therapeutics. *Adv. Drug Deliv. Rev.* **2017**, *110–111*, 102–111.

(15) Avitabile, C.; Diaferia, C.; Della Ventura, B.; Mercurio, F. A.; Leone, M.; Roviello, V.; Saviano, M.; Velotta, R.; Morelli, G.; Accardo, A.; *et al*. Self-Assembling of Fmoc-GC Peptide Nucleic Acid Dimers into Highly Fluorescent Aggregates. *Chem. Eur. J.* **2018**, *24* (18), 4729–4735.

(16) Kulkarni, K.; Hung, J.; Fulcher, A. J.; Chan, A. H. P.; Hong, A.; Forsythe, J. S.; Aguilar, M.-I.; Wise, S. G.; Del Borgo, M. P. β3-Tripeptides Coassemble into Fluorescent Hydrogels for Serial Monitoring in Vivo. *ACS Biomater. Sci. Eng.* **2018**, *4* (11), 3843–3847.

(17) González-Díaz, N. E.; López-Rendón, R.; Ireta, J. Insight Into the Dipeptide Self-Assembly Process Using Density Functional Theory. *J. Phys. Chem. C* **2019**, *123* (4), 2526–2532.

(18) Fu, M.; Li, Q.; Sun, B.; Yang, Y.; Dai, L.; Nylander, T.; Li, J. Disassembly of Dipeptide Single Crystals Can Transform the Lipid Membrane into a Network. *ACS Nano* **2017**, *11* (7), 7349–7354.

(19) Wei, C.; Pohorille, A. Sequence-Dependent Interfacial Adsorption and Permeation of Dipeptides across Phospholipid Membranes. *J. Phys. Chem. B* **2017**, *121* (42), 9859–9867.

(20) Uyaver, S.; Hernandez, H. W.; Habiboglu, M. G. Self-Assembly of Aromatic Amino Acids: A Molecular Dynamics Study. *Phys. Chem. Chem. Phys.* **2018**, *20* (48), 30525–30536.

(21) Yang, H.; Wang, Q.; Li, Z.; Li, F.; Wu, D.; Fan, M.; Zheng, A.; Huang, B.; Gan, L.; Zhao, Y.; *et al.* Hydrophobicity-Adaptive Nanogels for Programmed Anticancer Drug Delivery. *Nano Lett.* **2018**, *18* (12), 7909–7918.

(22) Yang, B.; Adams, D. J.; Marlow, M.; Zelzer, M. Surface-Mediated Supramolecular Self-Assembly of Protein, Peptide, and Nucleoside Derivatives: From Surface Design to the Underlying Mechanism and Tailored Functions. *Langmuir* **2018**, *34* (50), 15109–15125.

(23) Adams, D. J.; Mullen, L. M.; Berta, M.; Chen, L.; Frith, W. J. Relationship between Molecular Structure, Gelation Behaviour and Gel Properties of Fmoc-Dipeptides. *Soft Matter* **2010**, *6* (9), 1971.

(24) Argudo, P. G.; Contreras-Montoya, R.; Álvarez de Cienfuegos, L.; Cuerva, J. M.; Cano, M.; Alba-Molina, D.; Martín-Romero, M. T.; Camacho, L.; Giner-Casares, J. J. Unravelling the 2D Self-Assembly of Fmoc-Dipeptides at Fluid Interfaces. *Soft Matter* **2018**, *14* (46), 9343–9350.

(25) Giner-Casares, J. J.; Brezesinski, G.; Möhwald, H. Langmuir Monolayers as Unique Physical Models. *Curr. Opin. Colloid Interface Sci.* **2014**, *19* (3), 176–182.

(26) Benedini, L. A.; Sequeira, M. A.; Fanani, M. L.; Maggio, B.; Dodero, V. I. Development of a Nonionic Azobenzene Amphiphile for Remote Photocontrol of a Model Biomembrane. *J. Phys. Chem. B* **2016**, *120* (17), 4053–4063.

(27) Lopes, D.; Nunes, C.; Fontaine, P.; Sarmento, B.; Reis, S. Proof of Pore Formation and Biophysical Perturbations through a 2D Amoxicillin-Lipid Membrane Interaction Approach. *Biochim. Biophys. Acta, Biomembr.* **2017**, *1859* (5), 803–812.

(28) Cruz Gomes da Silva, R. L.; Oliveira da Silva, H. F.; da Silva Gasparotto,

L. H.; Caseli, L. How the Interaction of PVP-Stabilized Ag Nanoparticles with Models of Cellular Membranes at the Air-Water Interface Is Modulated by the Monolayer Composition. *J. Colloid Interface Sci.* **2018**, *512*, 792–800.

(29) Bettini, S.; Pagano, R.; Borovkov, V.; Giancane, G.; Valli, L. The Role of the Central Metal Ion of Ethane-Bridged Bis-Porphyrins in Histidine Sensing. *J. Colloid Interface Sci.* **2019**, *533*, 762–770.

(30) De Zotti, M.; Muzzi, B.; Gatto, E.; Di Napoli, B.; Mazzuca, C.; Palleschi, A.; Placidi, E.; Formaggio, F.; Toniolo, C.; Venanzi, M. Tuning the Morphology of Nanostructured Peptide Films by the Introduction of a Secondary Structure Conformational Constraint: A Case Study of Hierarchical Self-Assembly. *J. Phys. Chem. B* **2018**, *122* (24), 6305–6313.

(31) Li, T.; Kalloudis, M.; Cardoso, A. Z.; Adams, D. J.; Clegg, P. S. Drop-Casting Hydrogels at a Liquid Interface: The Case of Hydrophobic Dipeptides. *Langmuir* **2014**, *30* (46), 13854–13860.

(32) Vijay, R.; Polavarapu, P. L. Fmoc-Amino Acid Surfactants: Discovery, Characterization and Chiroptical Spectroscopy. *J. Phys. Chem. A* **2012**, *116* (44), 10759–10769.

(33) Teixeira, R.; Andrade, S. M.; Vaz Serra, V.; Paulo, P. M. R.; Sánchez-Coronilla, A.; Neves, M. G. P. M. S.; Cavaleiro, J. A. S.; Costa, S. M. B. Reorganization of Self-Assembled Dipeptide Porphyrin J-Aggregates in Water–Ethanol Mixtures. *J. Phys. Chem. B* **2012**, *116* (8), 2396–2404.

(34) Tao, K.; Levin, A.; Adler-Abramovich, L.; Gazit, E. Fmoc-Modified Amino Acids and Short Peptides: Simple Bio-Inspired Building Blocks for the Fabrication of Functional Materials. *Chem. Soc. Rev.* **2016**, *45* (14), 3935–3953.

(35) Pott, T.; Maillet, J. C.; Dufourc, E. J. Effects of PH and Cholesterol on DMPA Membranes: A Solid State 2H- and 31P-NMR Study. *Biophys. J.* **1995**, *69* (5), 1897–1908.

(36) Zhang, T.; Brantley, S. L.; Verreault, D.; Dhankani, R.; Corcelli, S. A.; Allen, H. C. Effect of PH and Salt on Surface p K a of Phosphatidic Acid Monolayers. *Langmuir* **2018**, *34* (1), 530–539.

(37) Goto, T. E.; Lopes, C. C.; Nader, H. B.; Silva, A. C. A.; Dantas, N. O.; Siqueira, J. R.; Caseli, L. CdSe Magic-Sized Quantum Dots Incorporated in Biomembrane Models at the Air–water Interface Composed of Components of Tumorigenic and Non-Tumorigenic Cells. *Biochim. Biophys. Acta, Biomembr.* **2016**, *1858* (7), 1533–1540.

(38) Griffith, E. C.; Perkins, R. J.; Telesford, D.-M.; Adams, E. M.; Cwiklik, L.; Allen, H. C.; Roeselová, M.; Vaida, V. Interaction of *l*-Phenylalanine with a Phospholipid Monolayer at the Water–Air Interface. *J. Phys. Chem. B* **2015**, *119* (29), 9038–9048.

(39) Hädicke, A.; Schwieger, C.; Blume, A. Cospreading of Anionic Phospholipids with Peptides of the Structure (KX) 4 K at the Air–Water Interface: Influence of Lipid Headgroup Structure and Hydrophobicity of the Peptide on Monolayer Behavior. *Langmuir* **2017**, *33* (43), 12204–12217.

(40) Viswanadhan, V. N.; Ghose, A. K.; Revankar, G. R.; Robins, R. K. Atomic Physicochemical Parameters for Three Dimensional Structure Directed Quantitative Structure-Activity Relationships. 4. Additional Parameters for Hydrophobic and Dispersive Interactions and Their Application for an Automated Superposition of Certain. *J. Chem. Inf. Model.* **1989**, *29* (3), 163–172.

(41) Draper, E. R.; Su, H.; Brasnett, C.; Poole, R. J.; Rogers, S.; Cui, H.; Seddon, A.; Adams, D. J. Opening a Can of Worm(-like Micelle)s: The Effect of Temperature of Solutions of Functionalized Dipeptides. *Angew. Chem. Int. Ed.* **2017**, *129* (35), 10603–10606.

(42) Fidalgo Rodríguez, J. L.; Dynarowicz-Latka, P.; Miñones Conde, J. Effects of Saturated and Polyunsaturated Fatty Acids on Interactions with Cholesterol versus 7-Ketocholesterol in Langmuir Monolayers and Their Potential Biological Implications. *Colloids Surf., B* **2018**, *174*, 189–198.

(43) Nunes, C.; Brezesinski, G.; Lopes, D.; Lima, J. L. F. C.; Reis, S.; Lúcio, M. Lipid–Drug Interaction: Biophysical Effects of Tolmetin on Membrane Mimetic Systems of Different Dimensionality. *J. Phys. Chem. B* **2011**, *115* (43), 12615–12623.

(44) Tuccitto, N.; Amato, T.; Gangemi, C. M. A.; Trusso Sfrazzetto, G.; Puglisi, R.; Pappalardo, A.; Ballistreri, F. P.; Messina, G. M. L.; Li-Destri, G.; Marletta, G. Driving Coordination Polymer Monolayer Formation by Competitive Reactions at the Air/Water Interface. *Langmuir* **2018**, *34* (39), 11706–11713.

(45) HyperChem 7.5. Hypercube (2003).

(46) Fanani, M. L.; Busto, J. V.; Sot, J.; Abad, J. L.; Fabrías, G.; Saiz, L.; Vilar, J. M. G.; Goñi, F. M.; Maggio, B.; Alonso, A. Clearly Detectable, Kinetically Restricted Solid–Solid Phase Transition in Cis -Ceramide Monolayers. *Langmuir* **2018**, *34* (39), 11749–11758.

(47) Alves, A. C.; Nunes, C.; Lima, J.; Reis, S. Daunorubicin and Doxorubicin Molecular Interplay with 2D Membrane Models. *Colloids Surf., B* **2017**, *160*, 610–618.

(48) Wojcik, A.; Pawłowski, M.; Wydro, P.; Broniatowski, M. Effects of Polychlorinated Pesticides and Their Metabolites on Phospholipid Organization in Model Microbial Membranes. *J. Phys. Chem. B* **2018**, *122* (50), 12017–12030.

(49) Aroti, A.; Leontidis, E.; Maltseva, E.; Brezesinski, G. Effects of Hofmeister Anions on DPPC Langmuir Monolayers at the Air−Water Interface. *J. Phys. Chem. B* **2004**, *108* (39), 15238–15245.

(50) Roldán-Carmona, C.; Giner-Casares, J. J.; Pérez-Morales, M.; Martín-Romero, M. T.; Camacho, L. Revisiting the Brewster Angle Microscopy: The Relevance of the Polar Headgroup. *Adv. Colloid Interface Sci.* **2012**, *173*, 12–22.

(51) Biswal, H. S.; Wategaonkar, S. Sulfur, Not Too Far Behind O, N, and C: SH···π Hydrogen Bond. *J. Phys. Chem. A* **2009**, *113* (46), 12774–12782.

(52) Rubia-Payá, C.; De Miguel, G.; Martín-Romero, M. T.; Giner-Casares, J. J.; Camacho, L. UV-Vis Reflection-Absorption Spectroscopy at Air-Liquid Interfaces. *Adv. Colloid Interface Sci.* **2015**, *225*, 134–145.

(53) Hädicke, A.; Blume, A. Interaction of Short Pentavalent Cationic Peptides with Negatively Charged DPPG Monolayers and Bilayers: Influence of Peptide Modifications on Binding. *J. Phys. Chem. B* **2018**, *122* (46), 10522–10534.

(54) McCloskey, A. P.; Draper, E. R.; Gilmore, B. F.; Laverty, G. Ultrashort Self-

Assembling Fmoc-Peptide Gelators for Anti-Infective Biomaterial Applications. *J. Pept. Sci*. **2017**, *23* (2), 131–140.

RSC Advances

Under Review

Subtle chemical modification for enrichment of Fmoc-amino acid at phospholipid interface

Pablo G. Argudo,[a] Rafael Contreras-Montoya,[b] Luis Álvarez de Cienfuegos,[b] María T. Martín-Romero,[a] Luis Camacho,[a] Juan J. Giner-Casares[a]

a. Departamento de Química Física y T. Aplicada, Instituto Universitario de Investigación en Química Fina y Nanoquímica IUIQFN, Facultad de Ciencias, Universidad de Córdoba, Campus de Rabanales, Ed. Marie Curie, E-14071 Córdoba, Spain.

b. Departamento de Química Orgánica, Facultad de Ciencias, Universidad de Granada, (UGR), C. U. Fuentenueva, E-18071 Granada, Spain.

Amino acids including the Fmoc group (9-fluorenylmethyloxycarbonyl) are bioinspired molecules that display intriguing features in self-assembly and biological applications. The influence of a delicate chemical modification between Fmoc-F and Fmoc-Y on the interaction with a phospholipid surface was analyzed. Langmuir monolayers of the 1,2-dimyristoyl-sn-glycero-3-phosphate (DMPA) phospholipid were used to mimic the eukaryotic cell membrane. *In situ* Brewster Angle Microscopy and UV-vis reflection spectroscopy provided insights on the effect of the Fmoc-amino acid derivatives on the DMPA phospholipid. The formation of H-bonds between the Fmoc-Y and the DMPA molecules was assessed, demonstrating the crucial role of the hydroxyl group of Fmoc-Y in enhancing the interaction with biosurfaces.

Introduction

Fmoc-amino acids are highly valuable elements in nanoscience as recently shown by Yan *et al.*, demonstrating co-assembly of Fmoc-His with phthalocyanine into nanovesicles as catalysts.[1] Fmoc-amino acids are excellent hydrogelators as well.[2–4] Fmoc-amino acids have been successfully included in nanocomposite structures for drug delivery.[5,6] Additional biological applications of the Fmoc-amino acids included their use as effective antibacterial agents.[7] The versatility of Fmoc-amino acids for combining with other inorganic and organic nanoparticles led to interesting hybrid materials including graphene oxide.[8] Partition coefficient (P) was proven a key parameter for Fmoc-dipeptides in interfacial self-assembly and interaction with lipid monolayers.[9,10] The surface activity of the Fmoc-amino acids played a significant role in the capability for self-assembly.[11] The hydrophobicity of the Fmoc-Met has been related with the formation of amyloid fibrils.[12] Gazit *et al.* reported on the complementary self-assembly of amino acids for tuning the intermolecular interactions, confirming the hypothesis that slight chemical modifications might have a large impact in the obtained supramolecular structures.[13]

Motivated by the relevance of the Fmoc-amino acids in biological applications, the interaction of two related Fmoc-amino acids with a model eukaryotic cell membrane has been explored. A Langmuir monolayer of the 1,2-dimyristoyl-sn-glycero-3-phosphate (DMPA) phospholipid provided a convenient model for the eukaryotic cell surface. The Langmuir technique allows a fine adjustment of the area per phospholipid molecule. Experimental *in situ* characterization of the effect of the Fmoc-amino acids on the phospholipid monolayer was performed.[14,15] Brewster Angle Microscopy (BAM) was used to examine the morphology of the phospholipid monolayer, attaining relevant information on the lipid domains.[16,17] UV-vis reflection spectroscopy allowed to monitor the presence of the Fmoc-amino acids at the phospholipid interface by the characteristic UV-vis signal from the Fmoc group.[18,19] We also examined the specific intermolecular interactions of DMPA with the Fmoc-amino acids and found that Fmoc-Y showed superior performance

when interacting with the phospholipid surface by Molecular mechanics computational simulations.

Materials and Methods

Materials. Fmoc-Phenylalanine (Fmoc-F) and Fmoc-Tyrosine (Fmoc-Y) were purchased from Sigma-Aldrich. 1,2-dimyristoyl-sn-glycero-3-phosphate (DMPA) phospholipid was purchased from Avanti Lipids and used as received. Solvents were used without further purification and purchased from Aldrich (Germany). Hydrochloric acid 37% was PRS-Codex purchased from Panreac and used as received. The initial 1 mM solutions of Fmoc-F and Fmoc-Y were prepared in dichloromethane. A mixture of chloroform:methanol (3:1 in volume) was used for dissolving DMPA at a concentration of 1 mM. The Fmoc-amino acids and the DMPA were co-spread in molar ratio DMPA:Fmoc amino acid 1:1. The choice of different solvents for the Fmoc-amino acid derivatives and the phospholipid was motivated to minimize any solubility problems. Considering the high miscibility of the solvents, no phase segregation was expected. Ultrapure water produced by a Millipore Milli-Q unit and pre-treated by a Millipore reverse osmosis system (>18.2 MΩ/cm) was used to prepare the acid solution for subphase. The subphase temperature was 21 ºC with pH 2. All experiments were performed on tables with vibration isolation using the antivibration system MOD-2 S (Accurion, Göttingen, Germany) in a large class 100 clean room.

Surface pressure–area (π—A) isotherms. Two different models of Nima troughs (Nima Technology, Coventry, England) were used, both provided with a Wilhelmy type dynamometric system using a strip of filter paper: a NIMA 611D with one moving barrier for the measurement of the reflection spectra, and a NIMA 601, equipped with two symmetrical barriers to record BAM images. The monolayers were compressed at a speed of 0.03 $nm^2\ min^{-1}\ molecule^{-1}$. The measurements for the surface pressure-molecular area isotherms were performed at least three times each, obtaining no significant differences.

Brewster angle microscopy (BAM). Images of the film morphology were

obtained by Brewster angle microscopy (BAM) with a I-Elli2000 (Accurion GmbH) using a Nd:YAG diode laser with wavelength 532 nm and 50 mW with a lateral resolution of 2 μm. The image processing procedure included a geometrical correction of the image, as well as a filtering operation to reduce interference fringes and noise.

UV-vis reflection spectroscopy. UV–visible reflection spectra at normal incidence as the difference in reflectivity *(ΔR)* of the film-covered water surface and the bare surface were obtained with a Nanofilm Surface Analysis Spectrometer Ref SPEC^2 (Accurion, Göttingen, Germany).

Computer simulations. All the simulations were performed using HyperChem 7.51.[20] Note that the computational results presented herein offer a qualitative picture of the interactions between DMPA and Fmoc-Y. The simulations were performed *in vacuo* to avoid the large computational cost of simulating the solvent molecules. The molecular structures of the DMPA and Fmoc-Y molecules were optimized by the semiempirical method AM1. After optimization, the DMPA and Fmoc-Y molecules were set with their polar heads pointing to each other. One 5 nanoseconds run of molecular dynamics at a temperature of 500 K was performed to avoid any initial constraint on the configuration of the system. No hydrogen bonds were detected after the run of 2 nanoseconds. Molecular mechanics was applied for finding an optimal configuration, using 300 K and a total run time of 5 nanoseconds. The formation of hydrogen bonds within the C5 molecule was detected during the optimization run.

Results and Discussion

A Langmuir monolayer of the DMPA phospholipid was used as model for the eukaryotic cell surface, see Figure 1 for the molecular structures. Two Fmoc-amino acid derivatives were studied, Fmoc-F and Fmoc-Y. Both Fmoc-amino acid derivatives share the same molecular structure, with an additional hydroxyl terminal group for the latter, see Figure 1.

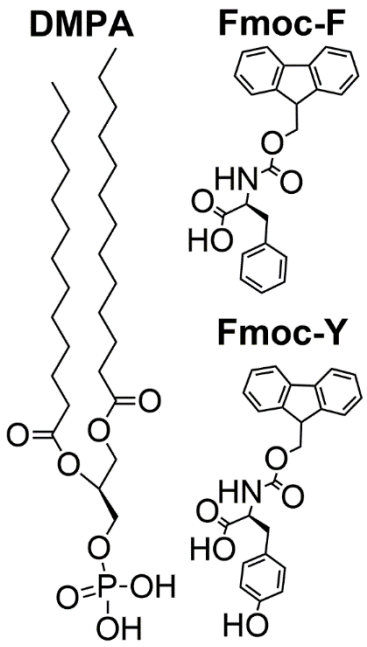

Figure 1. Molecular structure of the 1,2-dimyristoyl-sn-glycero-3-phosphate (DMPA) phospholipid, Fmoc-Phenylalanine (Fmoc-F) and Fmoc-Tyrosine (Fmoc-Y).

The Fmoc-amino acid derivatives displayed a great tendency to be solved into the bulk subphase, therefore avoiding the possibility of studying the effect of the Fmoc-amino acids on the phospholipid monolayer. We followed the strategy described by Adams and Clegg, where the authors demonstrated that an acid value of the pH of the subphase was required for avoiding the complete solving of the Fmoc-amino acids spread at the air/water interface.[21] This procedure included the pH = 2 value with a diluted HCl solution. The Fmoc-amino acid derivatives were expected to be fully protonated.[22,23] This study aims at providing a detailed description of the molecular interactions between the Fmoc-amino acid derivatives and the DMPA phospholipid monolayer as a simplified model of the highly complex surface of a eukaryotic cell membrane. While phosphatidylcholine (PC) lipids constitute the largest fraction of phospholipids in a eukaryotic cell membrane, the PC lipids display no net charge at physiological pH. Unfortunately, the polar head group of PC lipids

displays a net positive charge under the described acidic conditions. Given that the pH = 2 value of the bulk subphase was required to allow the residence of the Fmoc-amino acid derivatives at the air/liquid interface, we replaced the commonly used PC lipid by DMPA. DMPA phospholipid is protonated at pH = 2, displaying no net charge and being therefore closer to the biological scenario than the PC lipids.[24]

Herein mixed monolayers of DMPA:Fmoc-amino acid 1:1 have been prepared. The surface pressure-molecular area isotherms for the mixed monolayers DMPA:Fmoc-F and DMPA:Fmoc-Y are shown in Figure 2. An expansion of the isotherms for both DMPA:Fmoc-F and DMPA:Fmoc-Y monolayers comparing to the pure DMPA isotherm was observed. However, the expansion of the isotherm was significantly higher for Fmoc-F than for Fmoc-Y. This observation pointed to a comparatively reduced occupancy of the Fmoc-Y molecules at the DMPA monolayer. The difference between the isotherms for DMPA:Fmoc-F and DMPA:Fmoc-Y was more noticeable at low values of surface pressure, corresponding to an expanded state of the monolayer. The lift-off of the surface pressure took place at *ca.* 1.3 nm^2 per DMPA molecule for the DMPA:Fmoc-F monolayer, whereas surface pressure remains zero until *ca.* 0.7 nm^2 per DMPA molecule was reached in the DMPA:Fmoc-Y monolayer. The expansion of the DMPA:Fmoc-F with respect to the DMPA:Fmoc-Y isotherm from 0 to 5 mN/m was ca. 0.6 nm^2 per DMPA molecule. Assuming a surface area of 0.21 nm^2 per Fmoc-F molecule, the expansion in this region of the isotherm indicated an approximate number of three Fmoc-F molecules at the monolayer per molecule of DMPA. This is an approximation exclusively based on the surface area per Fmoc-F molecule assuming a completely upright arrangement. Miscibility experiments using mixed Langmuir monolayers of DMPA:Fmoc-F in different molar ratios would be relevant to attain insights on the molar ratio at the interface. Unfortunately, the significant tendency of the Fmoc-F molecules to be transferred to the bulk subphase with compression of the monolayer hindered the consistency of such experiment.[25] Thus, Fmoc-F showed a greater tendency to accommodate in an expanded monolayer, probably interacting *via* hydrophobic interactions between the Fmoc

groups with the alkyl chains of the DMPA molecules. Note that these interactions were not able to sustain the Fmoc-F molecules when the mixed monolayer was subjected to compression. Instead, a constant loss of the Fmoc-F molecules to the bulk subphase was obtained, as demonstrated below by UV-vis reflection spectroscopy.

A region of reduced increase of surface pressure with compression of the monolayer similar to a plateau was observed from *ca.* 0.9 to 0.6 nm^2 per DMPA molecule for the DMPA:Fmoc-F mixed monolayer. This region might be connected with the liquid expanded-liquid condensed (LE-LC) transition and the transfer of Fmoc-F molecules from the mixed monolayer to the bulk subphase. Although the effect of these two processes could not be distinguished exclusively from the isotherm, the UV-vis reflection spectra informed on a significant transfer of Fmoc-F to the bulk subphase, continuing the trend observed before. The isotherm for DMPA:Fmoc-Y showed a modest expansion and a similar shape to the isotherm for pure DMPA. This expansion was almost constant up to 10 mN/m and reached a value of *ca.* 0.03 nm^2 per DMPA molecule, *i. e.*, less than one Fmoc-Y molecule per twelve DMPA molecules. However, according to the UV-vis reflection spectra, the amount of Fmoc-amino acid was equal for both DMPA:Fmoc-F and DMPA:Fmoc-Y monolayers at *ca.* 0.7 nm^2 per DMPA molecule. Therefore, the Fmoc-Y molecules were adsorbed to the DMPA monolayer, residing at the phospholipid interface but occupying no space in the phospholipid region.

For both DMPA:Fmoc-F and DMPA:Fmoc-Y mixed monolayers a convergence with the isotherm for the pure DMPA at *ca.* 25 mN/m was obtained. This overlapping between the three isotherms indicated that both Fmoc-amino acids did not penetrate into the phospholipid monolayer at 30 mN/m. The phospholipid monolayer is equivalent to a bilayer at a surface pressure of 30 mN/m.[26] From purely thermodynamical arguments, the absence of any variation in the surface pressure – molecular area isotherm at 30 mN/m indicated no disruption of the phospholipid layer, thus pointing to a high biocompatibility concerning the rupture and modification of the cell surface.

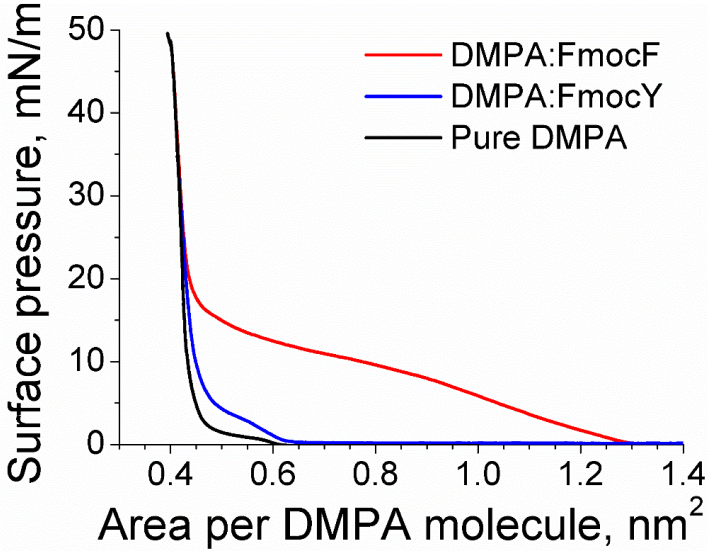

Figure 2. Surface pressure-molecular area isotherms for the DMPA:Fmoc-F mixed monolayer (red line), DMPA:Fmoc-Y mixed monolayer (blue line),and pure DMPA monolayer (black line).

The Fmoc-amino acids are soluble in water, showing a great tendency to form micelle-like aggregates. The Fmoc-amino acids can be solved in water up to 0.4 M, according to Polavarapu *et al.*[11] Assuming a complete loss of the spread Fmoc-amino acid molecules from the air/liquid interface to the bulk subphase, a maximum concentration of 10^{-7} M would be achieved. Therefore, no influence of the solubility values of the Fmoc-F and Fmoc-Y was expected.

Brewster Angle Microscopy (BAM) provided direct visualization of the DMPA:Fmoc-amino acid mixed monolayers at the air/liquid interface, see Figure 3.[27,28] Bright domains of LC phase appeared already at 0.8 nm^2 per DMPA molecule, with remarkable monodispersity in size and shape. The bright domains increased their size with compression of the DMPA monolayer up to *ca.* 10 mN/m. The domains coalesced into a homogenous solid phase for highly compressed state. [29] The morphology of the DMPA:Fmoc-F mixed monolayer was similar, with small and highly reflective dots appeared at 16 mN/m. Such bright dots were

persistent and remained for the complete isotherm, and might be formed by a mixture of aggregated DMPA lipid molecules and a small fraction of Fmoc-F molecules.[30,31] Given the almost zero UV-vis reflection signal obtained for the DMPA:Fmoc-F mixed monolayer at 30 mN/m and the complete overlap of the isotherm with that of pure DMPA, the amount of Fmoc-F molecules was assumed to be close to zero. Thus, the bright dots might correspond to small aggregates of phospholipid formed by nucleation with the Fmoc-F molecules promoted by the hydrophobic interactions of the alkyl chains with the Fmoc group.

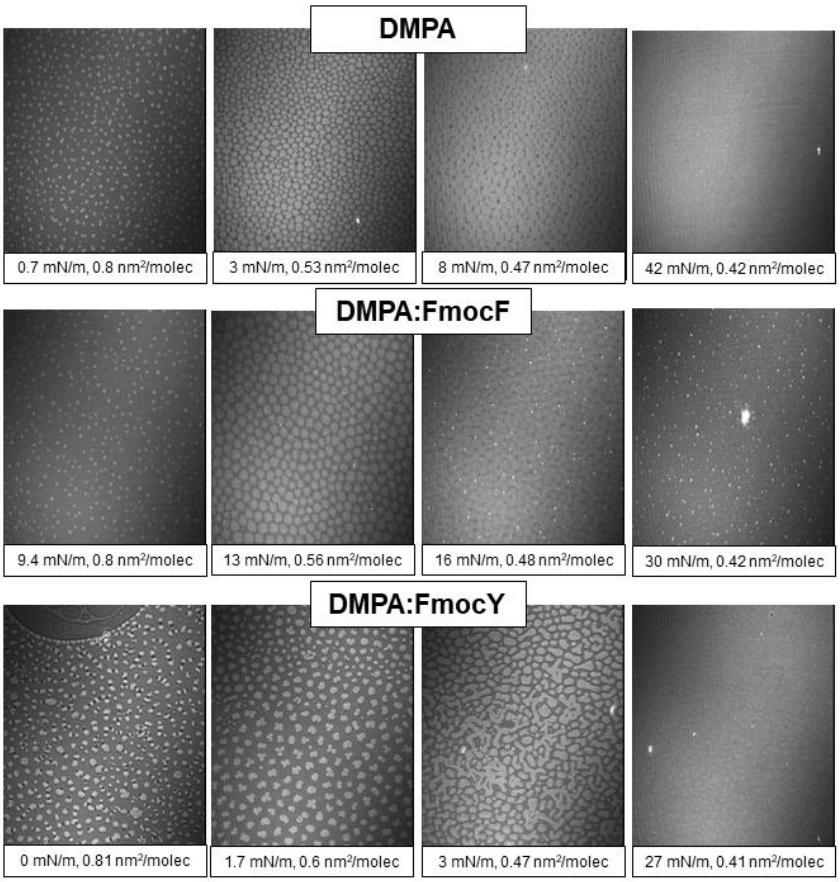

Figure 3. Brewster Angle Microscopy images for the DMPA (top), DMPA:Fmoc-F (middle) and DMPA:Fmoc-Y (bottom) monolayers. The values of surface pressure and available surface area per DMPA molecule are included at the bottom of each picture. The width of each frame corresponds to 215 μm.

On the other hand, a significant modification of the morphology of the lipid domains was obtained for the DMPA:Fmoc-Y monolayer, probably caused by the interaction of the Fmoc-Y molecules with the polar head groups of the DMPA phospholipid that modified the line tension-electrostatic repulsion balance.[32] Not discrete but polidisperse domains that were connected to each other were obtained from 3 mN/m to further compressed state of the monolayer. A highly reflective and almost homogeneous morphology was obtained for the solid state of the monolayer, with no complete coalescence. An almost homogenous monolayer was obtained after compression of the monolayer to high values of surface pressure, indicating the expulsion of the Fmoc-Y molecules from the lipid monolayer to the adsorption region underneath the phospholipid head groups as confirmed by UV-vis reflection spectroscopy.

The presence of Fmoc-amino acid molecules in contact with the DMPA phospholipid monolayer was verified by UV-vis reflection spectroscopy, see Figure 4. Note the UV-vis reflection signal for the pure DMPA monolayer was not significant along the complete isotherm of the DMPA. A small increase of the UV-vis reflection signal was found at the most compressed state of the DMPA monolayer, *i. e.*, 0.4 nm^2 per DMPA molecule. The UV-vis reflection signal was increased to a maximum value of 0.02 from 240 to 280 nm. On the other hand, the UV-vis reflection signal for the DMPA:Fmoc-Y mixed monolayer displayed a maximum intensity of *ca.* 0.09, showing a broad band from 240 to *ca.* 360 nm. Therefore, the contribution of the increase of reflection signal induced by the DMPA molecules was considered not significant for the UV-vis reflection spectra of the DMPA:Fmoc-F and DMPA:Fmoc-Y monolayers.

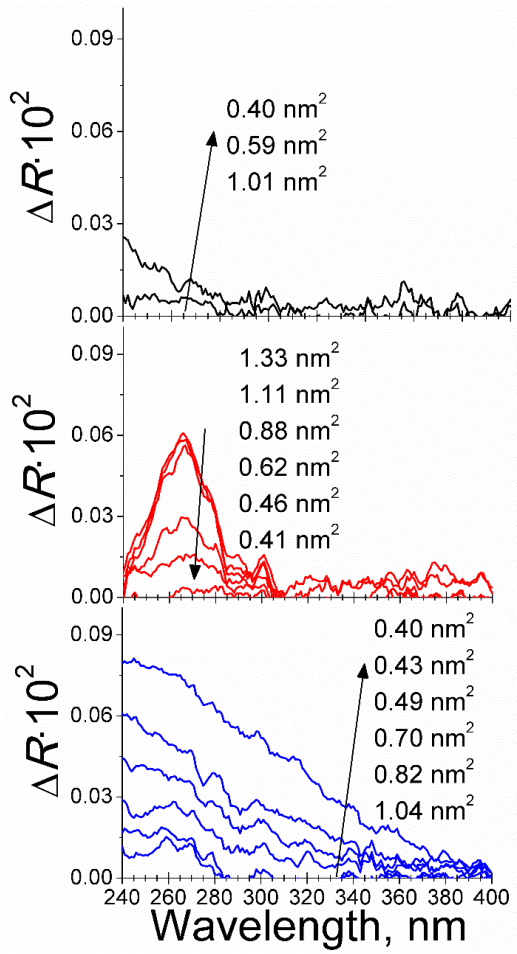

Figure 4. UV-vis reflection for the pure DMPA (top, black line) DMPA:Fmoc-F (middle, red line) and DMPA:Fmoc-Y (bottom, blue line) monolayers. The values of available surface area per DMPA molecule are indicated in the inset.

The bulk spectrum of Fmoc-F in bulk solution was formed by five components at 257, 266, 276, 290 and 300 nm, with the most intense component at 266 nm, see Figure S1. The UV-vis reflection spectra of the DMPA:Fmoc-F mixed monolayer were formed by five components at 257, 266, 276, 290 and 301 nm, with the most intense component at 266 nm. The aggregation of the Fmoc-F molecules in contact with the DMPA molecules was therefore not significant. This finding was in agreement with the proposed model of the absence of a specific interaction between

DMPA and Fmoc-F molecule at the air/liquid interface. The bulk spectrum of Fmoc-Y in bulk solution was formed by five components at 256, 266, 277, 290 and 300 nm, with the most intense component at 266 nm, see Figure S1. However, the UV-vis reflection spectra appeared as a broad band with no defined peaks from 240 to *ca.* 360 nm in the case of the DMPA:Fmoc-Y mixed monolayer, indicating a significant aggregation of the Fmoc-Y molecules. Note the intensity of the UV-vis reflection band displayed an intensity value more than four-fold higher than that of the pure DMPA monolayer at the most compressed state.

A significant amount of Fmoc-F molecules was already present at the expanded state of the DMPA:Fmoc-F mixed monolayer. The initial compression of the monolayer already decreased the surface concentration of Fmoc-F despite the significant expansion of the isotherm, as discussed above. A significant loss of Fmoc-F molecules was observed with further compression from *ca.* 1.1 to 0.5 nm^2 per DMPA molecule, concurrent with the plateau observed in the isotherm. Thus, the expulsion of the Fmoc-F molecules from the mixed monolayer also contributed to the observed plateau in the isotherm, see Figure 2. Remarkably, the Fmoc-F molecules were almost completely expelled from the air/liquid interface to the bulk subphase at the complete compression of the monolayer, with no UV-vis reflection signal obtained, see Figure 5.

The DMPA:Fmoc-Y mixed monolayer displayed an opposite behavior to the DMPA:Fmoc-F monolayer. While no significant presence of the Fmoc-Y molecules was observed for the highly expanded state of the mixed monolayer, a steady enrichment of the Fmoc-Y molecules at the mixed monolayer with compression of the monolayer from *ca.* 0.8 nm^2 per DMPA molecule was obtained. The slight modification of the surface pressure-molecular area isotherm of the DMPA:Fmoc-Y mixed monolayer with respect to the isotherm of pure DMPA for low values of surface pressure and the complete overlap of both isotherms for values of surface pressure higher than 20 mN/m indicated the adsorption of Fmoc-Y molecules underneath the DMPA lipid monolayer.

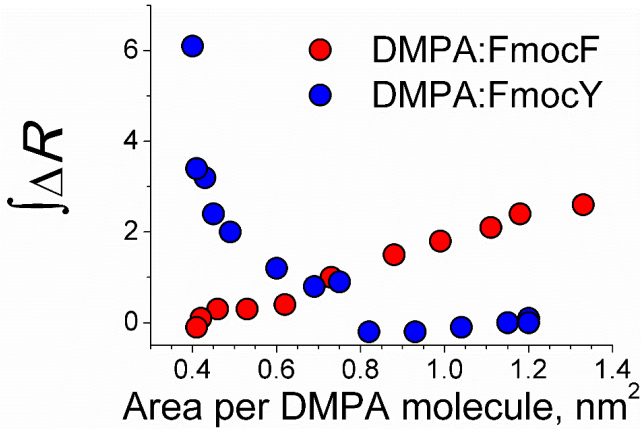

Figure 5. Integral values of the UV-vis spectra for the DMPA:Fmoc amino acid derivatives at different values of available surface area per DMPA molecule. Composition of the mixed monolayers as noted in the inset.

Given that the Fmoc group was the source of the UV-vis reflection signal, the amount of the Fmoc-Y and Fmoc-F molecules at the mixed monolayer could be directly compared.[33] An intercrossing in the integral value of the UV-vis reflection spectra for the DMPA:Fmoc-F and DMPA:Fmoc-Y monolayers was found at *ca.* 0.7 nm^2 per DMPA molecule. The intercrossing was coincident with the plateau in the isotherm of the DMPA:Fmoc-F monolayer and values of surface pressure of 11 and 0 mN/m for the DMPA:Fmoc-F and DMPA:Fmoc-Y monolayers, respectively. Remarkably, the enrichment of Fmoc-Y with compression of the mixed monolayer led to a final surface concentration of Fmoc-Y being *ca.* two-fold higher than the initial surface concentration of Fmoc-F prior to compression of the monolayer, suggesting a superior capability of Fmoc-Y in interacting with the DMPA monolayer. Although the Fmoc-Y molecules did not occupy the phospholipid region, the interaction with the DMPA monolayer was more efficient than that of Fmoc-F, as noted by the significant enrichment in Fmoc-Y molecules. The location of the Fmoc-Y molecules underneath the DMPA monolayer might be the origin of the broadening and noise in the UV-vis reflection spectra, see Figure 4.

An opposite trend was found for the DMPA:Fmoc-F mixed monolayers. While

Fmoc-F molecules showed a higher occupancy at the monolayer at the expanded state, the Fmoc-Y molecules were not present at such state, as evidenced by the shift in the surface pressure-molecular area isotherms and confirmed by the UV-vis reflection spectra. Hydrophobic interactions between the Fmoc group and the alkyl chains of the DMPA molecules might be responsible for this effect at the expanded state of the monolayer. A striking inversion of the effect of the Fmoc-amino acid molecules in the DMPA monolayer was observed with compression of the mixed monolayers. While the Fmoc-F molecules were gradually detached from the mixed monolayer, an enrichment of the mixed monolayer with Fmoc-Y molecules was detected. The intercrossing in the amount of Fmoc-amino acid took place during the plateau in the DMPA:Fmoc-F monolayer, with this region probably displaying simultaneously the phase transition of the phospholipid and the expelling of the Fmoc-F molecules. This observation was consistent with the modification of the shape of the DMPA domains observed by BAM. Further compression of the mixed monolayers led to a complete removal of the Fmoc-F molecules from the mixed monolayers with no significant amount of Fmoc-F molecules adsorbed to the DMPA monolayer, as evidenced by the UV-vis reflection spectra. In contrast, the amount of Fmoc-Y molecules present at the phospholipid interface increased steadily to a maximum value at the highest value of surface pressure that was two-fold higher than the amount of the Fmoc-F molecules. Note the Fmoc-Y molecules were adsorbed underneath the DMPA monolayer, as confirmed by the overlap of the surface pressure-molecular area isotherms for DMPA, DMPA:Fmoc-F and DMPA:Fmoc-Y.

As commented above, we have used pH = 2 in the subphase to promote the residence of both Fmoc-F and Fmoc-Y. However, such experimental condition could not assure completely the presence of both Fmoc-amino acid derivatives at the air/water interface at all compression state of the DMPA monolayer. Instead, the residence of the Fmoc-amino acid derivatives at the mixed monolayers showed a great dependency on the compression state and the interactions with the DMPA phospholipid molecules.

The Fmoc-F molecule is slightly more hydrophobic than the Fmoc-Y molecules, with values of – log *P* of 4.7 and 4.4, respectively. This minor difference in hydrophobicity could not account for the radically different behavior of Fmoc-F and Fmoc-Y. To gain further insights into the specific intermolecular interactions between Fmoc-Y and DMPA, the formation of a complex was studied in more depth. Formation of H-bonds formed between the terminal hydroxyl group of Fmoc-Y and the polar head group of DMPA was expected. Molecular mechanics computational simulations were performed to examine the feasibility of the formation of H-bonds between the DMPA and Fmoc-Y molecules.[34] Three H-bonds were detected using *in vacuo* simulations, see Figure 6. The terminal hydroxyl group of a single molecule of Fmoc-Y was able to form up to three H-bonds with a DMPA molecule. Two of the H-bonds were formed with the oxygen atoms from the phosphate group of the DMPA. Remarkably, the hydroxyl group of Fmoc-Y could also from a H-bond with the phosphorous atom from the phosphate group of DMPA, as recently described by Kjaergaard *et al.*[35]

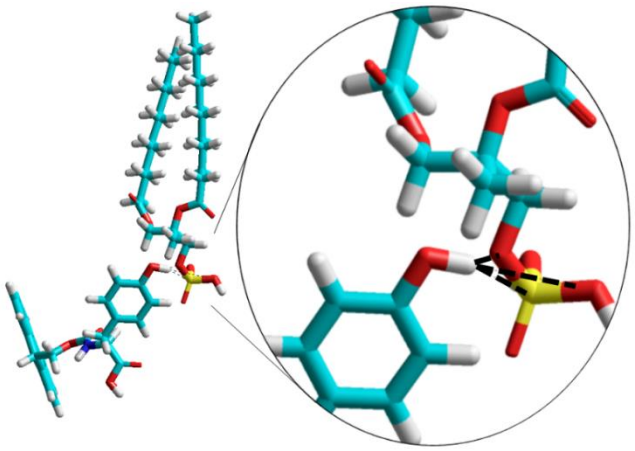

Figure 6. Snapshot of the simulation of the DMPA:Fmoc-Y mixed monolayer. The intermolecular H-bonds are displayed as dashed black lines. Key color for atom type: light blue (carbon), red (oxygen) yellow (phosphorus) and deep blue (nitrogen).

Conclusions

The interactions between Fmoc-F and Fmoc-Y with a DMPA Langmuir monolayer as model eukaryotic cell surface were analyzed. Despite the hydroxyl group at the Fmoc-Y molecule as the unique chemical difference to Fmoc-F, an opposite behavior between the two Fmoc-amino acids was found. While Fmoc-F was present in the DMPA monolayer at the expanded state and was expelled with compression, Fmoc-Y was not in contact with the DMPA monolayer at the expanded state. A significant enrichment of the phospholipid interface with Fmoc-Y molecules was demonstrated by UV-vis reflection spectroscopy. At the biologically relevant surface pressure of 30 mN/m, Fmoc-Y was found in higher surface concentration, indicating the superior interaction of Fmoc-Y with the phospholipid surface in contrast to the more hydrophobic Fmoc-F that was completely expelled to the bulk subphase. The origin of this enhanced interaction was the H-bonds formed by the hydroxyl group of Fmoc-Y with the phosphate group of DMPA. Therefore, purely thermodynamical considerations as given by the partition coefficient did not account for the experimental behavior of the Fmoc-amino acid derivatives. The subtle chemical modification of including a single hydroxyl group in the terminal side of the Fmoc-amino acid derivative could promote specific intermolecular interactions between the Fmoc-Y and the phospholipid surface, in this case H-bonds. Infrared reflection spectroscopy and neutron reflectivity measurements would be highly informative as well in detailing these interactions. This work suggest that the inclusion of hydroxyl groups that are capable of forming directed H-bonds is a straightforward strategy to improve the biological application of assemblies based on Fmoc-amino acids.

Author Information

Corresponding Author

lac@ugr.es (L. A.-C.), jjginer@uco.es (J. J. G.-C.)

Acknowledgment

Support from the Ministry of Science, Innovation and Universities of Spain through the MANA project (CTQ2017-83961-R) is acknowledged. FIS2017-85954-R (Agencia Estatal de Investigación, AEI, Spain, co-funded by Fondo Europeo de Desarrollo Regional, ERDF, European Union) is acknowledged. J.J.G.-C. acknowledges the Ministry of Science, Innovation and Universities for a "Ramon y Cajal" contract (RyC-2014-14956).

References

1. B. Franklin. Of the stilling of Waves by means of Oil. *Philos. Trans.* **64**, 445 (1774).
2. Pockels, A. Surface Tension. *Nature* (1891).
3. Lord Rayleigh. Investigations in Capillarity:—The size of drops.—The liberation of gas from supersaturated solutions.—Colliding jets.—The tension of contaminated water-surfaces. *London, Edinburgh, Dublin Philos. Mag. J. Sci.* **48**, 321–337 (1899).
4. Langmuir, I. The constitution and fundamental properties of solids and liquids. II. Liquids. *J. Am. Chem. Soc.* **39**, 1848–1906 (1917).
5. Langmuir, I. Vapor pressures, evaporation, condensation and adsorption. *J. Am. Chem. Soc.* **54**, 2798–2832 (1932).
6. Langmuir, I. Oil lenses on water and the nature of monomolecular expanded films. *J. Chem. Phys.* **1**, 756–776 (1933).
7. Blodgett, K. B. Monomolecular films of fatty acids on glass. *J. Am. Chem. Soc.* **56**, 495 (1934).
8. Blodgett, K. B. Films Built by Depositing Successive Monomolecular Layers on a Solid Surface. *J. Am. Chem. Soc.* **57**, 1007–1022 (1935).
9. Blodgett, K. B. A method of extinguising the reflection of light from glass. *Science (80-.).* **89**, 60–61 (1939).
10. Hussain, S. A., Dey, B., Bhattacharjee, D. & Mehta, N. Unique supramolecular assembly through Langmuir – Blodgett (LB) technique. *Heliyon* **4**, e01038 (2018).
11. Langmuir, I. & Schaefer, V. J. Activities of Urease and Pepsin Monolayers. *J. Am. Chem. Soc.* **60**, 1351–1360 (1938).
12. Gaines, G. L. *Insoluble monolayers at Liquid-Gas Interfaces*. (Wiley-Interscience, 1966).
13. Adamson, A. W. *Physical Chemistry of Surfaces*. (Interscience, 1967).
14. Tasman Davies, J. & Keightley Rideal, S. E. *Interfacial Phenomena*. (Academic Press, 1963).

15. Gericke, A., Simon-Kutscher, J. & Hühnerfuss, H. Influence of the Spreading Solvent on the Properties of Monolayers at the Air/Water Interface. *Langmuir* **9**, 2119–2127 (1993).
16. Kuhn, H., Möbius, D. & Bücher, H. *Physical Methods of Chemistry*. (Wiley-Interscience, 1972).
17. Chechel, O. V. & Nikolaev, E. N. Devices for production of Langmuir-Blodgett Films. *Instruments Exp. Tech.* **34**, 750–762 (1991).
18. Barnes, G. T. & Gentle, I. R. *Interfacial Science: an introduction*. (Oxford, 2005).
19. Knobler, C. M. Condensed monolayer phases at the air/water interface: Phase transitions and structures. *J. Phys. Condens. Matter* **3**, S17–S22 (1991).
20. Dynarowicz-Latka, P., Dhanabalan, A. & Oliveira, O. N. J. Modern physicochemical research on Langmuir monolayers. *Adv. Colloid Interface Sci.* **91**, 221–293 (2001).
21. Zhao, L. & Lin, Z. Self-assembly of non-linear polymers at the air/water interface: The effect of molecular architecture. *Soft Matter* **7**, 10520–10535 (2011).
22. Miller, R. *et al.* Dynamics of protein and mixed protein/surfactant adsorption layers at the water/fluid interface. *Adv. Colloid Interface Sci.* **86**, 39–82 (2000).
23. Kasprzyk-Hordern, B. Chemistry of alumina, reactions in aqueous solution and its application in water treatment. *Adv. Colloid Interface Sci.* **110**, 19–48 (2004).
24. Holmberg, M. *et al.* Surface Force Studies of Langmuir – Blodgett Cellulose Films. *J. Colloid Interface Sci.* **186**, 369–381 (1997).
25. Valluzzi, R., Gido, S. P., Muller, W. & Kaplan, D. L. Orientation of silk III at the air-water interface. *Int. J. Biol. Macromol.* **24**, 237–242 (1999).
26. Chen, Z., Shen, Y. R. & Somorjai, G. A. Studies of Polymer Surfaces By Sum Frequency Generation Vibrational Spectroscopy. *Annu. Rev. Phys. Chem.* **53**, 437–465 (2002).

27. Aguilar, M. R. & Román, J. S. *Smart Polymers and their Applications*. *Woodhead Publishing* (Woodhead Publishing, 2014).
28. Sánchez, A. & Vázquez, A. Bioactive peptides: A review. *Food Qual. Saf.* **1**, 29–46 (2017).
29. Fischer, E. & Fourneau, E. Ueber einige Derivate des Glukocolls. *Ber Dtsch Chem Bunenges* **34**, 2868–2877 (1901).
30. Goodman, M., Cai, W. & Smith, N. C. The bold legacy of Emil Fischer. *J. Pept. Sci.* **9**, 594–603 (2003).
31. Curtius, T. Verkettung von Amidosäuren I. Abhandlung. *J. für Prakt. Chemie* **70**, 57–72 (1904).
32. Curtius, T. Synthetische Versuche mit Hippurazid. *Berichte der Dtsch. Chem. Gesellschaft* **35**, 3226–3228 (1902).
33. Curtius, T. & Gumlich, O. Verkettung von Amidosäuren. VII. Abhandlung. Kettenbildung zwischen Hippurazid und β-Amino-α -oxypropionsäure und β-Aminobuttersäure. *J. für Prakt. Chemie* **70**, 195–223 (1904).
34. Curtius, T. & Müller, E. Über Hippuryl-y-aminobuttersäure und Hippuryl-b-phenyl-a-alanin. *J. für Prakt. Chemie* **70**, 223–229 (1904).
35. Bergmann, M. & Zervas, L. Über ein allgemeines Verfahren der peptid-synthese. *Ber Dtsch Chem Ges* **65**, 1192–1201 (1932).
36. Akabori, S., Ikenaka, T. & Matsumoto, K. Asymmetric synthesis of amino acids. *Proc Jpn Acad* **27**, 7–9 (1951).
37. Izumi, Y., Tasumi, S., Imaida, M., Fukuda, Y. & Akabori, S. The Preparation of Optically Active a-C-Substituted Glutamic Acid. *Bull. Chem. Soc. Jpn.* **38**, 1338–1340 (1965).
38. Zhang, Z., Zhu, W. & Kodadek, T. Selection and application of peptide-binding peptides. *Nat. Biotechnol.* **18**, 71–74 (2000).
39. Hajfathalian, M., Ghelichi, S., García-Moreno, P. J., Moltke Sørensen, A. D. & Jacobsen, C. Peptides: Production, bioactivity, functionality, and applications. *Crit. Rev. Food Sci. Nutr.* **58**, 3097–3129 (2018).
40. Hamley, I. W. Small Bioactive Peptides for Biomaterials Design and

Therapeutics. *Chem. Rev.* **117**, 14015–14041 (2017).

41. Keymanesh, K., Soltani, S. & Sardari, S. Application of antimicrobial peptides in agriculture and food industry. *World J. Microbiol. Biotechnol.* **25**, 933–944 (2009).
42. Lupo, M. P. & Cole, A. L. Cosmeceutical peptides. *Dermatol. Ther.* **20**, 343–349 (2007).
43. Pugliese, R. & Gelain, F. Peptidic Biomaterials: From Self-Assembling to Regenerative Medicine. *Trends Biotechnol.* **35**, 145–158 (2017).
44. Agarwal, R. *et al.* Delivery and tracking of quantum dot peptide bioconjugates in an intact developing avian brain. *ACS Chem. Neurosci.* **6**, 494–504 (2015).
45. Moldaver, D. & Larché, M. Immunotherapy with peptides. *Allergy Eur. J. Allergy Clin. Immunol.* **66**, 784–791 (2011).
46. di Luca, M., Maccari, G. & Nifosí, R. Treatment of microbial biofilms in the post-antibiotic era: Prophylactic and therapeutic use of antimicrobial peptides and their design by bioinformatics tools. *Pathog. Dis.* **70**, 257–270 (2014).
47. Skalickova, S. *et al.* Perspective of use of antiviral peptides against influenza virus. *Viruses* **7**, 5428–5442 (2015).
48. Yagasaki, M. & Hashimoto, S. I. Synthesis and application of dipeptides; Current status and perspectives. *Appl. Microbiol. Biotechnol.* **81**, 13–22 (2008).
49. González-Díaz, N. E., López-Rendón, R. & Ireta, J. Insight into the Dipeptide Self-Assembly Process Using Density Functional Theory. *J. Phys. Chem. C* **123**, 2526–2532 (2019).
50. Wang, J. *et al.* Trace Solvent as a Predominant Factor to Tune Dipeptide Self-Assembly. *ACS Nano* **10**, 2138–2143 (2016).
51. Ryan, D. M. & Nilsson, B. L. Self-assembled amino acids and dipeptides as noncovalent hydrogels for tissue engineering. *Polym. Chem.* **3**, 18–33 (2012).
52. Schnaider, L. *et al.* Self-assembling dipeptide antibacterial nanostructures with membrane disrupting activity. *Nat. Commun.* **8**, (2017).

53. Fichman, G. & Gazit, E. Self-assembly of short peptides to form hydrogels: Design of building blocks, physical properties and technological applications. *Acta Biomater.* **10**, 1671–1682 (2014).

54. Drury, J. L. & Mooney, D. J. Hydrogels for tissue engineering: Scaffold design variables and applications. *Biomaterials* **24**, 4337–4351 (2003).

55. Van Vlierberghe, S., Dubruel, P. & Schacht, E. Biopolymer-based hydrogels as scaffolds for tissue engineering applications: A review. *Biomacromolecules* **12**, 1387–1408 (2011).

56. Qiu, Y. & Park, K. Environment-sensitive hydrogels for drug delivery. *Adv. Drug Deliv. Rev.* **53**, 321–339 (2001).

57. Tibbitt, M. W. & Anseth, K. S. Hydrogels as extracellular matrix mimics for 3D cell culture. *Biotechnol. Bioeng.* **103**, 655–663 (2009).

58. Bera, D., Qian, L., Tseng, T. K. & Holloway, P. H. Quantum dots and their multimodal applications: A review. *Materials (Basel).* **3**, 2260–2345 (2010).

59. Ji, X., Peng, F., Zhong, Y., Su, Y. & He, Y. Fluorescent quantum dots: Synthesis, biomedical optical imaging, and biosafety assessment. *Colloids Surfaces B Biointerfaces* **124**, 132–139 (2014).

60. Henglein, A. Small-Particle Research: Physicochemical Properties of Extremely Small Colloidal Metal and Semiconductor Particles. *Chem. Rev.* **89**, 1861–1873 (1989).

61. Murphy, C. J. & Coffer, J. L. QuantumDots: A Primer. *Focal point* **56**, 16A-20A (2002).

62. Ekimov, A. I. & Onushchenko, A. A. Quantum size effect on three-dimensional microscopic semiconductor crystals. *Pis'ma v Zhurnal Èksperimental'noi i Teor. Fiz.* **34**, 363–366 (1981).

63. Brus, L. E. Electron-electron and electron-hole interactions in small semiconductor crystallites: The size dependence of the lowest excited electronic state. *J. Chem. Phys.* **80**, 4403–4409 (1984).

64. Murray, C. B., Norris, D. J. & Bawendi, M. G. Synthesis and characterization of nearly monodisperse CdE (E = sulfur, selenium, tellurium) semiconductor

nanocrystallites. *J. Am. Chem. Soc.* **115**, 8706–8715 (1993).

65. Alivisatos, A. . Semiconductor clusters, nanocrystals, and quantum dots. *Science (80-.).* **271**, 933–937 (1996).
66. Wang, Y. & Herron, N. Nanometer-sized semiconductor clusters: Materials synthesis, quantum size effects, and photophysical properties. *J. Phys. Chem.* **95**, 525–532 (1991).
67. Zhu, J.-J., Li, J.-J., Huang, H.-P. & Cheng, F.-F. *Quantum Dots for DNA Biosensing*. *Springer* (2013). doi:10.1007/978-3-642-44910-9
68. Petryayeva, E., Algar, W. R. & Medintz, I. L. Quantum dots in bioanalysis: A review of applications across various platforms for fluorescence spectroscopy and imaging. *Focal Point Rev.* **67**, 215–252 (2013).
69. Barkhouse, D. A. R., Pattantyus-abraham, A. G., Levina, L. & Edward, H. Thiols Passivate Recombination in Colloidal Quantum Dots Leading to Enhanced. *ACSNano* **2**, 2356–2362 (2008).
70. Peng, X., Schlamp, M. C., Kadavanich, A. V. & Alivisatos, A. P. Epitaxial growth of highly luminescent CdSe/CdS core/shell nanocrystals with photostability and electronic accessibility. *J. Am. Chem. Soc.* **119**, 7019–7029 (1997).
71. Reiss, P., Bleuse, J. & Pron, A. Highly Luminescent CdSe/ZnSe Core/Shell Nanocrystals of Low Size Dispersion. *Nano Lett.* **2**, 781–784 (2002).
72. Pathak, Y. & Thassu, D. Semiconducting Quantum Dots for Bioimaging. in *Drug Delivery Nanoparticles Formulation and Characterization* 416 (2016).
73. Yang, H., Holloway, P. H. & Santra, S. Water-soluble silica-overcoated CdS:Mn/ZnS semiconductor quantum dots. *J. Chem. Phys.* **121**, 7421–7426 (2004).
74. Coe-Sullivan, S. Optoelectronics: Quantum dot developments. *Nat. Photonics* **3**, 315–316 (2009).
75. C David, M. *et al.* Multi-colour organic light-emitting displays by solution processing. *Nature* **421**, 829–833 (2003).
76. Guldi, D. M. *et al.* CNT-CdTe versatile donor-acceptor nanohybrids. *J. Am.*

Chem. Soc. **128**, 2315–2323 (2006).

77. Lee, J., Sundar, V. C., Heine, J. R., Bawendi, M. G. & Jensen, K. F. Full Color Emission from II-VI Semiconductor Quantum Dot-Polymer Composites. *Adv. Mater.* **12**, 1102–1105 (2000).
78. Cassidy, P. J. & Radda, G. K. Molecular imaging perspectives. *J. R. Soc. Interface* **2**, 133–144 (2005).
79. Maiti, A. & Bhattacharyya, S. Review : Quantum Dots and Application in Medical Science. *Int. J. Chem. Chem. Eng.* **3**, 37–42 (2013).
80. Chunyan, L., Bohua, D. & Qiangbin, W. Properties of Quantum Dots: A New Nanoprobe for Bioimaging. in *Handbook of Nanomaterials Properties* 1263–1298 (2014).
81. Martynenko, I. V. *et al.* Application of semiconductor quantum dots in bioimaging and biosensing. *J. Mater. Chem. B* **5**, 6701–6727 (2017).
82. Herbst, R. S. & Shin, D. M. Monoclonal antibodies to target epidermal growth factor receptor-positive tumors. *Cancer* **94**, 1593–1611 (2002).
83. Sharma, P., Brown, S., Walter, G., Santra, S. & Moudgil, B. Nanoparticles for bioimaging. *Adv. Colloid Interface Sci.* **123**–**126**, 471–485 (2006).
84. Gambhir, S. S. & Weiss, S. Quantum Dots for Live Cells, in Vivo Imaging, and Diagnostics. *Science (80-.).* **307**, 538–545 (2005).
85. Lakowicz, J. R. *Principles of Fluorescence Spectroscopy*. (2006).
86. Medintz, I. L., Uyeda, H. T., Goldman, E. R. & Mattoussi, H. Quantum dot bioconjugates for imaging, labelling and sensing. *Nat. Mater.* **4**, 435–446 (2005).
87. Hassan, M. & Klaunberg, B. A. Comparative Medicine Overview Biomedical Applications of Fluorescence Imaging In Vivo. *Comp. Med.* **54**, 635–644 (2004).
88. Han, M., Gao, X., Su, J. Z. & Nie, S. Quantum-dot-tagged microbeads for multiplexed optical coding of biomolecules. *Nat. Biotechnol.* **19**, 631–635 (2001).
89. Haldavnekar, R., Venkatakrishnan, K. & Tan, B. Non plasmonic

semiconductor quantum SERS probe as a pathway for in vitro cancer detection. *Nat. Commun.* **9**, 1–18 (2018).

90. Zamborini, F. P., Bao, L. & Dasari, R. Nanoparticles in measurement science. *Anal. Chem.* **84**, 541–576 (2012).
91. Kalangi, S. K. *et al.* Synthesis, Characterization, and Biodistribution of Quantum Dot-Celecoxib Conjugate in Mouse Paw Edema Model. *Oxid. Med. Cell. Longev.* **2018**, 1–8 (2018).
92. Santra, S. *et al.* Synthesis and characterization of fluorescent, radio-opaque, and paramagnetic silica nanoparticles for multimodal bioimaging applications. *Adv. Mater.* **17**, 2165–2169 (2005).
93. Nelson, D. L. & Cox, M. M. *Lehninger Principles of Biochemistry*. (W.H. Freeman and Company, 2017).
94. Miescher, F. Ueber die chemische Zusammensetzung der Eiterzellen. in *Medicinisch-chemische Untersuchungen* 441–460 (1871).
95. Levene, P. A. The Structure of Yeast Nucleic Acid. *J. Biol. Chem* **41**, 19–23 (1919).
96. Ascoli, A., Thymin, D. & Neumann, V. A. K. A. Ueber ein neues Spaltungsprodukt des Hefenucleins. *Zeitschrift für Physiol. Chemie* **31**, 161–164 (1900).
97. Reader, V. The assay of vitamin B(4). *Biochem. J.* **24**, 1827–1831 (1930).
98. Albrecht, K. & Neumann, A. Ueber das Thymin, ein Spaltungsproduct der Nucleïnsäure. *Berichte der Dtsch. Chem. Gesellschaft zu Berlin* **26**, 2753–2756 (1893).
99. Magnus. Ueber das Vorkommen von Xanthicoxyd im Guano. *Ann. der Chemie und Pharm.* **51**, 395–397 (1844).
100. Kossel, A. & Neumann, A. Berichte der Deutschen chemischen Gesellschaft zu Berlin. in *Berichte der Deutschen Chemischen Gesellschaft zu Berlin* **27**, 2215–2222 (1894).
101. Pauling, L. The Nature of the Chemical Bond and the Structure of Molecules and Crystals: An Introduction to Modern Structural Chemistry. *Cornell*

University Press 450 (1960). doi:10.1021/ja01500a088

102. Miao, Z. & Westhof, E. RNA Structure: Advances and Assessment of 3D Structure Prediction. *Annu. Rev. Biophys.* **46**, 483–503 (2017).

103. Sivakova, S. & Rowan, S. J. Nucleobases as supramolecular motifs. *Chem. Soc. Rev.* **34**, 9–21 (2005).

104. Lippert, B. & Martin, R. B. *Multiplicity of metal ion binding patterns to nucleobases*. *Coordination Chemistry Reviews* (Wiley-VCH Weinheim, 2000). doi:10.1016/S0010-8545(00)00260-5

105. Katz, S. The Reversible Reaction of Sodium Thymonucleate and Mercuric Chloride. *J. Am. Chem. Soc.* **74**, 2238–2245 (1952).

106. Rosenberg, B., VanCamp, L., Trosko, J. E. & Mansour, V. H. Patinum Compounds: a New Class of Potent Antitumour Agents. *Nature* **222**, 385–386 (1969).

107. Lippert, B. *Cisplatin: Chemistry and Biochemistry of a Leading Anticancer Drug*. *Encyclopedia of Toxicology: Third Edition* (1999). doi:10.1016/B978-0-12-386454-3.00288-8

108. Clarke, M. J., Zhu, F. & Frasca, D. R. Non-Platinum Chemotherapeutic Metallopharmaceuticals. *Chem. Rev.* **99**, 2511–2534 (2002).

109. LaChance-Galang, K. J., Zhao, M. & Clarke, M. J. Disproportionation of [(py)(NH 3)4RuIII] at the N7 of Guanine Nucleosides: Severing the N-Glycosidic Bond. *Inorg. Chem.* **35**, 6021–6026 (2002).

110. Fusch, E. C. & Lippert, B. [Zn3(OH)2(1-MeC-N3)5(1-MeC-O2)3]4+(1-MeC=1-Methylcytosine): Structural Model for DNA Cross-Linking and DNA Rewinding by Zn(II)? *J. Am. Chem. Soc.* **116**, 7204–7209 (1994).

111. Kimura, E. & Shionoya, M. Zinc complexes as targeting agents for nucleic acids. *Met Ions Biol Syst.* **33**, 29–52 (1996).

112. Wang, F., Liu, X. & Willner, I. DNA switches: From principles to applications. *Angew. Chemie - Int. Ed.* **54**, 1098–1129 (2015).

113. Nayak, A. K. & Subudhi, U. Directed self-assembly of genomic sequences into monomeric and polymeric branched DNA structures. *RSC Adv.* **4**,

54506–54511 (2014).

114. Berti, L. & Burley, G. A. Nucleic acid and nucleotide-mediated synthesis of inorganic nanoparticles. *Nat. Nanotechnol.* **3**, 81–87 (2008).

115. Marino, N. *et al.* Homochiral self-assembly of biocoordination polymers: Anion-triggered helicity and absolute configuration inversion. *Chem. Sci.* **6**, 4300–4305 (2015).

116. Shimizu, T., Iwaura, R., Masuda, M., Hanada, T. & Yase, K. Internucleobase-interaction-directed self-assembly of nanofibers from homo- and heteroditopic 1,ω-nucleobase bolaamphiphiles. *J. Am. Chem. Soc.* **123**, 5947–5955 (2001).

117. Thibault, R. J., Hotchkiss, P. J., Gray, M. & Rotello, V. M. Thermally reversible formation of microspheres through non-covalent polymer cross-linking. *J. Am. Chem. Soc.* **125**, 11249–11252 (2003).

118. Thibault, R. J. *et al.* Specific interactions of complementary mono- and multivalent guests with recognition-induced polymersomes. *J. Am. Chem. Soc.* **124**, 15249–15254 (2002).

119. Pu, F., Ren, J. & Qu, X. Nucleobases, nucleosides, and nucleotides: Versatile biomolecules for generating functional nanomaterials. *Chem. Soc. Rev.* **47**, 1285–1306 (2018).

120. Herskovits, T. T. & Harrington, J. P. Solution Studies of the Nucleic Acid Bases and Related Model Compounds. Solubility in Aqueous Alcohol and Glycol Solutions. *Biochemistry* **11**, 4800–4811 (1972).

121. Wong, A., Ida, R., Spindler, L. & Wu, G. Disodium guanosine 5′-monophosphate self-associates into nanoscale cylinders at pH 8: A combined diffusion NMR spectroscopy and dynamic light scattering study. *J. Am. Chem. Soc.* **127**, 6990–6998 (2005).

122. Sessler, J. L., Wang, B. & Harriman, A. Photoinduced Energy Transfer in Associated but Noncovalently Linked Photosynthetic Model Systems. *J. Am. Chem. Soc.* **117**, 704–714 (1995).

123. Nikolova, E. N. *et al.* Transient Hoogsteen base pairs in canonical duplex

DNA. *Nature* **470**, 498–504 (2011).

124. Esguerra, M., Nilsson, L. & Villa, A. Triple helical DNA in a duplex context and base pair opening. *Nucleic Acids Res.* **42**, 11329–11338 (2014).

125. Mertz, E., Mattei, S. & Zimmerman, S. C. Synthesis and duplex DNA recognition studies of oligonucleotides containing a ureido isoindolin-1-one homo-N-nucleoside. A comparison of host-guest and DNA recognition studies. *Bioorganic Med. Chem.* **12**, 1517–1526 (2004).

126. Ariga, K. & Kunitake, T. Molecular Recognition at Air-Water and Related Interfaces: Complementary Hydrogen Bonding and Multisite Interaction. *Acc. Chem. Res.* **31**, 371–378 (1998).

127. Wang, Y., Du, X., Miao, W. & Liang, Y. Molecular recognition of cytosine- and guanine-functionalized nucleolipids in the mixed monolayers at the air-water interface and Langmuir-Blodgett films. *J. Phys. Chem. B* **110**, 4914–4923 (2006).

128. Miao, W., Du, X. & Liang, Y. Molecular recognition of nucleolipid monolayers of 1-(2-octadecyloxycarbonylethyl)cytosine to guanosine at the air-water interface and Langmuir-Blodgett films. *Langmuir* **19**, 5389–5396 (2003).

129. Grüniger, H., Möbius, D. & Meyer, H. Enhanced light reflection by dye monolayers at the air-water interface. *J. Chem. Phys.* **79**, 3701–3710 (1983).

130. David Brewster, L. IX. On the laws which regulate the polarisation of light by reflexion from transparent bodies. *Philos. Trans. R. Soc. London* 125–159 (1815).

131. Hénon, S. & Meunier, J. Microscope at the Brewster angle: Direct observation of first-order phase transitions in monolayers. *Rev. Sci. Instrum.* **62**, 936–939 (1991).

132. Rashed, R. A pioneer in anaclastics: Ibn Sahl on burning mirrors and lenses. *Isis* **81**, 464–491 (1990).

133. Oliveira Jr., O. N. Langmuir-Blodgett Films - Properties and Possible Applicat ions. *Brazilian J. Phys.* **22**, 60–69 (1992).

134. Kato, T. Studies on the fully automatic horizontal lifting deposition of lb films using double gates. *Jpn. J. Appl. Phys.* **27**, L1358–L1360 (1988).

135. Kato, T. Overturn of molecules during the fully automatic horizontal lifting deposition using double gates. *Jpn. J. Appl. Phys.* **27**, L2128–L2130 (1988).

136. Bikerman, J. J. & Schulman, J. H. On the structure of 'built-up' films on metals. *Phys. Rev.* **53**, 909 (1938).

137. N'soukpoé-Kossi, C. N. & Leblanc, R. M. Absorption and photoacoustic spectroscopies of lutein and zeaxanthin Langmuir–Blodgett films in connection with the Haidinger's brushes. *Can. J. Chem.* **66**, 1459–1466 (2011).

138. Bikerman, J. J. On the formation and structure of multilayers. *J. Proc. R. Soc.* **A170**, 130–145 (1939).

139. Honig, E. P., Hengst, J. H. T. & Den Engelsen, D. Langmuir-blodgett deposition ratios. *J. Colloid Interface Sci.* **45**, 92–102 (1973).

140. Skoog, D. A., Holler, F. J. & Crouch, S. R. *Principles of Instrumental Analysis*. *Thomson Brooks/Cole* (2007).

141. Bouguer, P. Essai d'optique sur la gradation de la lumière. *Claude Jombert* 19–22 (1729).

142. Lambert, J. H. Photometria sive de mensura et gradibus luminis, colorum et umbrae. *Eberhardt Klett.* 170 (1760).

143. Beer. Bestimmung der Absorption des rothen Lichts in farbigen Flüssigkeiten. *Ann. Phys.* **86**, 78–88 (1852).

144. G.D. Fasman. *Circular Dichroism and the Conformational Analysis of Biomolecules*. (1996).

145. Scattering, L. L. Laser Light Scattering Systems. *Anal. Chem.* **21**, 145–174 (1970).

146. Amin, S. (Norton) & Rega, C. A. (Bromborough). Dynamic Light Scattering Based Microrheology of Complex Fluids With Improved Single-Scattering Mode Detection. (2013).

147. Berne, B. J. & Pecora, R. *Dynamic Light Scattering with Applications to*

Chemistry, Biology, and Physics (Berne, Bruce J.; Pecora, Robert). *Courier Dover Publications* (1977).

Supporting Information

Subtle chemical modification for enrichment of Fmoc-amino acid at phospholipid interface

Pablo G. Argudo,[1] Rafael Contreras-Montoya,[2] Luis Álvarez de Cienfuegos,[2] María T. Martín-Romero,[1] Luis Camacho,[1] Juan J. Giner-Casares[1]

[1]Departamento de Química Física y T. Aplicada, Instituto Universitario de Investigación en Química Fina y Nanoquímica IUNAN, Facultad de Ciencias, Universidad de Córdoba (UCO), Campus de Rabanales, Ed. Marie Curie, E-14071 Córdoba, Spain

[2]Departamento de Química Orgánica, Facultad de Ciencias, Universidad de Granada, (UGR), C. U. Fuentenueva, E-18071 Granada, Spain.

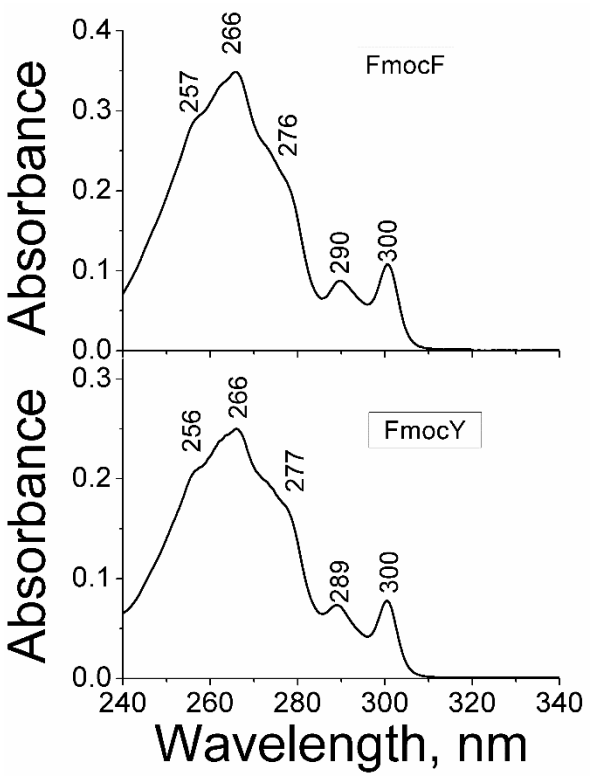

Figure S1. Bulk UV-vis absorption spectra for Fmoc-F (top) and Fmoc-Y (bottom) solutions in dichloromethane.

CHEMISTRY
A European Journal

Published on 26 Sep 2018
DOI: 10.1002/chem.201804704

Surface-active fluorinated quantum dots for enhanced cellular uptake

Pablo G. Argudo,[a] Mónica Carril,[b,c] María T. Martín-Romero,[a] Juan J. Giner-Casares[a] and Carolina Carrillo-Carrión[d,e]

a. Institute of Fine Chemistry and Nanochemistry, Department of Physical Chemistry and Applied Thermodynamics, University of Córdoba, Campus Universitario de Rabanales, Edificio Marie Curie, 14014 Córdoba, Spain.

b. Biofisika Institute (CSIC, UPV/EHU) and Department of Biochemistry and Molecular Biology, University of the Basque Country UPV/EHU, 48940Leioa, Spain.

c. Ikerbasque, Basque Foundation for Science, 48011 Bilbao, Spain

d. CIC biomaGUNE, 20014 San Sebastian, Spain.

e. Center for Research in Biological Chemistry and Molecular Materials (CiQUS), University of Santiago de Compostela, 15782 Santiago de Compostela, Spain.

Fluorescent nanoparticles, such as quantum dots, hold great potential for biomedical applications, mainly sensing and bioimaging. However, the inefficient cell uptake of some nanoparticles hampers their application in clinical practice. Here, the effect of the modification of the quantum dot surface with fluorinated ligands to increase their surface activity and, thus, enhance their cellular uptake was explored.

Introduction

Much effort has been directed towards the understanding of the cellular uptake of nanoparticles (NPs) to design novel nanostructures with improved bioperformance and, consequently, a higher efficiency in biomedical applications, such as bioimaging, intracellular sensing, and drug delivery, among others.[1–4] In this direction, functionalization strategies to optimize cellular uptake and trafficking as well as methodologies to reveal the parameters controlling the nanoparticle–cell interactions are of utmost importance.[5, 6] The first major barrier against the influx of exogenous materials inside a cell is the impermeable phospholipid bilayer of the cellular membrane, the effect of which is often unpredictable. Although the effects of the physicochemical properties of NPs, such as size, shape, stiffness, charge, and surface chemistry, have been widely studied,[7–12] the role of the surface hydrophobic/hydrophilic balance in the cellular uptake of NPs is still not well understood and has gained increasing attention lately.[13–16]

It is generally accepted that hydrophobic and interfacial forces play important roles in the interaction between NPs and cellular membranes. Molecular dynamic simulations have clearly shown that hydrophobic NPs were thermodynamically stable within the hydrophobic core of the cell membrane, whereas semihydrophilic NPs were only found to adsorb onto the membrane.[14, 15] Recently, Shastri and co-workers have described the preparation of polymeric NPs with increased hydrophobicity by copolymerization with lipid components of cell membranes, which resulted in an increased cellular uptake of the most hydrophobic NPs.[16] Similarly, Sung and co-workers, based on both experimental evidence and molecular dynamic simulations, have reported that the cellular uptake of hydrophobically modified chitosan NPs was enhanced when their hydrophobic character was increased.[17]

In addition, the impact of fluorine atoms on the interaction of bioactive molecules with cells is profound, mainly due to its high hydrophobicity. Indeed, it is not a coincidence that fluorine is present in around 20% of current pharmaceutical compounds, and most of the optimization process in drug development is focused on

the modification of active compounds with fluorine atoms.[18–20] In spite of this, the modification of NPs with fluorinated ligands to increase their hydrophobicity and exploit the effect of fluorine on the interactions with cells has been poorly investigated, and little is known about the cellular uptake of fluorinated NPs.[21]

Here, we report the fluorination of NPs as a straightforward strategy to modulate their interactions with cells and subsequent cellular uptake. To gain insight into the mechanism underlying the differential cellular uptake of fluorinated NPs, the interaction of these NPs with a cell membrane model was studied. In particular, we focused on fluorescent quantum dots (QDs) owing to their superior properties as bioimaging probes in comparison to conventional organic fluorophores.[22–24]

Results and Discussion

In this work, fluorinated QDs (referred to as QD_F) were prepared by ligand-exchange of trioctylphosphine oxide (TOPO)-capped ZnCdS/ZnS QDs (referred to as QD_TOPO) with the fluorinated ligand HS-C_{11}-$(EG)_4$-O-$C(CF_3)_3$ (EG=ethylene glycol; Figure 1A, see details in the Supporting Information). The use of this ligand containing a perfluoro-*tert*-butyl group allows for the introduction of a high amount of fluorine atoms on the outer surface of the QDs, whereas the ethylene glycol units enhance the QDs dispersibility. The as-prepared QD_TOPO and QD_F NPs presented an inorganic core diameter of (7.0 ± 0.5) nm, as determined by transmission electron microscopy (TEM; Figure S1, Supporting Information), and maximum emission fluorescence at approximately 435 nm upon excitation at 350 nm (Figure S2, Supporting Information).

The emission spectrum of the QD_F was slightly narrower than that of the QD_TOPO sample, which indicates a narrower particle size distribution. This may be the result of the additional purification steps by centrifugation after the ligand-exchange process, which could lead to the isolation of more homogeneous particles. The same observation was also derived from dynamic light scattering (DLS; Figure S3 in the Supporting Information) measurements because the DLS size distribution of QD_F, compared to that of QD_TOPO, was narrower and associated to a smaller

polydispersity index value. The hydrodynamic diameters, given as number distributions, were (10.5 ± 2.3) nm for QD_TOPO and (16.7 ± 1.7) nm for QD_F. As expected, the hydrodynamic size increased after the ligand exchange owing to the larger length of the fluorinated ligand in comparison to that of TOPO. In both cases, the low polydispersity index values demonstrated the homogeneity of the NPs in terms of size. The presence of the fluorinated ligands on the QD surface after functionalization, along with residual TOPO molecules, was confirmed by ^{1}H and ^{19}F NMR spectroscopy (Figure S4, Supporting Information). The non-fluorinated QD_TOPO were used as a control because they are also hydrophobic but lack fluorine atoms. Interfacial tension measurements performed by using the pendant drop method revealed the hydrophobic character of both QDs and that QD_F are more hydrophobic than QD_TOPO[25] (Figure S5, Supporting Information).

To evaluate the influence of the ligand-exchange process and, thus, the change of the organic shell on the fluorescence emission efficiency of the QD, the quantum yield (QY) before and after the exchange was determined by the method developed by Horiba, which is based on the comparative method work of Williams *et al.*[26] Details of the used procedure and calculations are given in the Supporting Information (section II.3, Figure S6). The determined QY values were 0.82 for QD_TOPO and 0.77 for QD_F, indicating that the exchange process did not affect significantly the fluorescence efficiency.

To first study the potential interaction of both QDs types with cells, Langmuir monolayers of the phospholipid 1,2-dipalmitoyl-*sn*-glycero-3-phosphocholine (DPPC), which is a major constituent of eukaryotic cell membranes, were used as model surfaces. This model allows for the mimicry of the response of the cell membrane against the QDs.[27] For the formation of the monolayers, QDs and DPPC were co-spread in a fixed optimized molar ratio and, thus, the amount of QDs that might be at the DPPC interface is well-defined. A slight excess of DPPC molecules was included for the formation of a close-packed monolayer of QDs (Figure S5, Supporting Information).

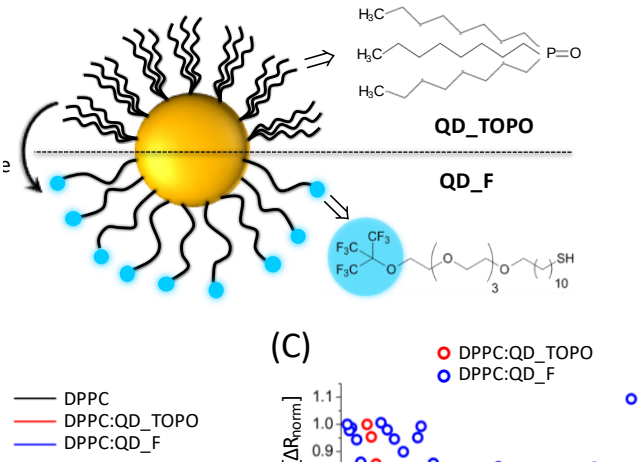

Figure 1. (A) Scheme of the two types of QDs studied, TOPO-capped QDs (QD_TOPO) and fluorinated QDs (QD_F). (B) Surface pressure versus molecular area isotherms of a pure DPPC monolayer (black line), DPPC monolayers with QD_TOPO (red line) and QD_F (blue line). (C) Value of integral of the UV/Vis reflection spectra as a function of area of the monolayer for DPPC:QD_TOPO (red circles) and DPPC:QD_F (blue circles).

Restricting the physical scenario to a simplified model allowed us to discern the different behavior of fluorinated and non-fluorinated NPs (QD_F versus QD_TOPO) exclusively as the result of the changes in the surface activity of the QDs.[28] The possibility of studying *in situ* the DPPC monolayer and the influence of the QDs at different values of molecular area per phospholipid molecule provides a detailed picture of the surface activity of the QDs. Taking into account that the inorganic core of the QDs is the same in both cases, the observed changes in the surface activity are due solely to the presence of different capping ligands on their surface, that is, fluorinated and non-fluorinated ligands.

Surface pressure versus molecular area isotherms of the DPPC monolayers

(Figure 1B) provide information on the surface activity of the QDs and their interaction with the model DPPC surface.[29] The modification of the isotherm induced by QD_F was significantly higher than that induced by QD_TOPO. The values of molecular area corresponding to the increase of the surface pressure for pure water were 0.9, 1.6, and 3.5 nm^2 for DPPC, QD_TOPO and QF_F, respectively. The greater expansion of the isotherm recorded in presence of the QD_F indicates a higher occupancy of the DPPC interface by QD_F, in contrast to QD_TOPO. The shape of the isotherms was also significantly affected by the incorporation of QDs into the monolayer, pointing out a modification of the phase behaviour of the DPPC molecules in contact with the QDs. In particular, the QDs induced a fluidization of the DPPC monolayer by effectively interacting with the phospholipid molecules. Interestingly, such a fluidization was greater for QD_F when compared to QD_TOPO, noted in a quantitative decrease of the compression modulus C_s^{-1} from 200 to 300 mNm^{-1} (liquid condensed and solid monolayer) for pure DPPC and DPPC:QD_TOPO monolayers and from 0 to 50 mNm^{-1} (liquid-expanded monolayer) for DPPC:QD_F monolayers (Figure S6, Supporting Information). This effect arises from a significant interaction between the QD_F and the hydrophobic region of the DPPC monolayer. The available surface area per DPPC molecule was reduced by compression of the monolayer. The 2D clustering of QD_F with subsequent compression of the monolayer enhanced the hydrophobic interaction with the alkyl chains of DPPC molecules. This interaction with the curved surface of QD_F led to an effective removal of DPPC molecules from the monolayer towards the QD_F surface, as observed in the area decrease at almost constant surface pressure of about 25 mNm^{-1} and the intercrossing of the isotherm with that of the pure DPPC monolayer at approximately 41 mNm^{-1} (Figure 1B). This enhancement in the hydrophobic interactions between the QD_F and the phospholipids is key for the superior cell uptake.

Taking advantage of the reflection band of QDs in the range 250–500 nm,[30] the amount of both QDs present at the DPPC interface along the isotherm could be monitored by in situ UV/Vis reflection spectroscopy. For comparison, the UV/Vis

reflection spectra obtained for both DPPC:QD_TOPO and DPPC:QD_F monolayers were integrated and normalized to the maximum value, that is, the absorption at the most compressed state of the monolayer and, therefore, with the highest density of QDs at the interface. As presented in Figure 1C, QD_F were present as at least 80% of the maximum amount over the entire compression range, whereas the QD_TOPO were initially present only as 40% and their amount increased gradually with compression and only reached the maximum amount at a highly compressed state of the monolayer. The observed variation in intensity of the UV/Vis reflection spectra with the decrease in molecular area of the DPPC was due to the enrichment of QD_F at the lipid–water interface. Such an enrichment was connected to the increase of DPPC molecules available to interact with the QD_F, thus, attracting and keeping a larger number of QD_F at the interface. The comparatively higher signal-to-noise ratio of the UV/Vis reflection spectra of QD_F compared to those of QD_TOPO might arise from a larger aggregation at the air–liquid interface, see Figure S8 (Supporting Information). The aggregation of inorganic nanoparticles at the air–liquid interface led to micron-sized domains of nanoparticles, resulting in a higher noise in the spectroscopic signal.[31] Such domains were visualized by microscopy, as reported below.

The change of the DPPC monolayer interfacial structure and organization induced by the QDs was monitored in situ by Brewster angle microscopy (BAM), allowing us to gain insights into the micrometric domains. Interestingly, a contrast inversion took place for both QD types, in which the surrounding phase of the DPPC liquid condensed domains appeared brighter than the domains (Figure 2 and Figure S8 in the Supporting Information). Images were taken at different values of the surface pressure, corresponding to different degrees of compression of the monolayer. These images clearly showed the lack of a significant modification of the morphology of the DPPC monolayer in contact with QD_TOPO at a greater compression state of the DPPC monolayer (Figure 2A), suggesting a comparatively modest occupancy of the interface. In contrast, the DPPC monolayer in contact with QD_F displayed a noticeable modification (Figure 2B), in which the domains were disrupted and bright

solid-like microstructures appeared. The formation of such microstructures can be explained by the accumulation of the surface active QD_F into aggregates at the DPPC interface, as expected from the surface pressure versus molecular area isotherm (see above), further confirming their greater surface activity.

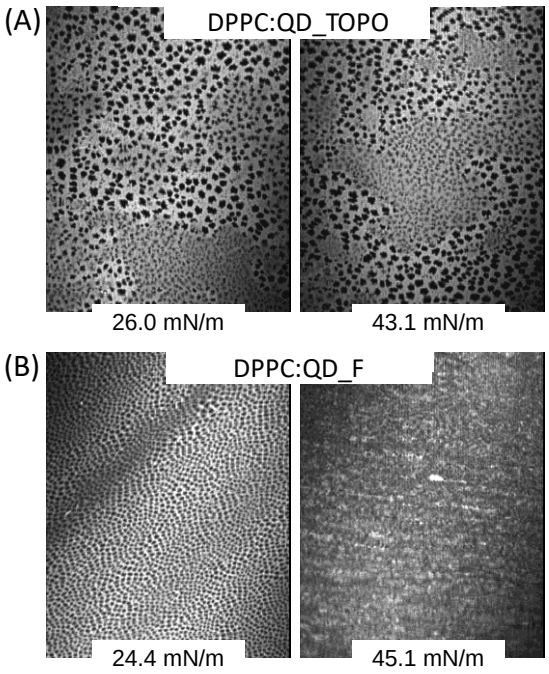

Figure 2. Brewster angle microscopy images of the DPPC monolayer in contact with (A) QD_TOPO, and (B) QD_F. The values of surface pressure for each picture are indicated in the insets. Width equal to 225 μm.

Once the interaction of different QDs with a cell membrane model had been studied, results clearly revealed a higher surface activity of QD_F deriving in an enhanced interaction at the phospholipid interface. Then, cellular uptake studies of the QDs were carried out to investigate whether there is a correlation between the observations with the DPCC membrane model and the truly behavior in cells. To this end, HeLa cells were first incubated with both QD_F and QD_TOPO NPs at a concentration of 5 nM for 24 h. The cytotoxicity was evaluated obtaining that the

cell viability decreased to around 80% as determined by MTT assay (Figure 3A).

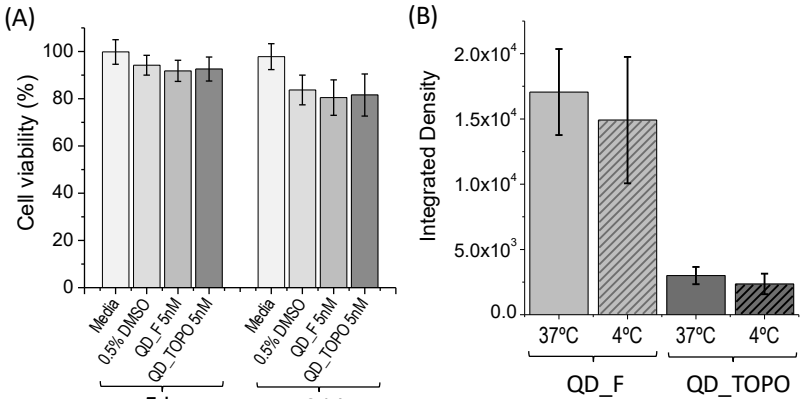

Figure 3. (A) Cell viability obtained by MTT assay of HeLa cells incubated for either 5 or 24 h with QD_TOPO or QD_F (both at 5 nM). NPs were dispersed in a serum-free cell medium containing 0.5% DMSO. (B) Quantification of fluorescence density per cell by analyzing the confocal fluorescence images of HeLa cells incubated for 5 h with either QD_TOPO or QD_F (both at 5 nM) at 37 or 4 ºC. For each case, 50 cells were analyzed with ImageJ. Results are expressed as the mean ± standard deviation (SD).

However, such a decrease may be attributed mainly to the presence of 0.5% of DMSO, which is needed for a good dispersion of the hydrophobic NPs in the cell culture medium. To minimally affect the cell viability (*i.e.*, maintaining viability ≥90%), the treatment of HeLa cells with NPs (5 nM) was reduced to 5 h, which demonstrated to be sufficient for sensitive uptake studies by confocal fluorescence microscopy (Figure 4). Notably, the uptake studies were performed in a serum-free medium to avoid the potential adsorption of proteins around the QDs (*i.e.*, formation of the so-called protein corona),[32, 33] and, therefore, allowing for the direct interaction of the surface coating of the QDs (TOPO or fluorinated ligands) with the cellular membrane. In this way the impact of the presence of fluorine atoms on the QD surface could be truly investigated without being masked by adsorbed proteins.[34] As can be seen in the confocal images (Figure 4), although both QDs types were

efficiently internalized within cells, the extent of the cell uptake was significantly higher for QD_F. To quantify this uptake enhancement, due to the presence of fluorinated ligands on the QD surface, the fluorescence density per cell was determined by analyzing the images with ImageJ (details in the Supporting Information). The fluorescence density within cells can be correlated to the amount of QDs internalized, and as shown in Figure 3B, QD_F were taken up more efficiently by a factor of 5.7 in comparison with the control non-fluorinated QD_TOPO. This enhanced cellular uptake of QD_F is consistent with the observed higher interaction with the cell membrane model, and allows us to conclude that increasing the surface activity of QDs leads to their enhanced internalization by cells.

To further investigate whether the uptake mechanism occurs through active or passive internalization processes, the cells were incubated with QDs (QD_F and QD_TOPO 5 nM) at 4 ºC, knowing that at this low temperature many cellular processes, such as the endocytosis of NPs, are inhibited.[35] The amount of QDs internalized at 4 ºC was only slightly lower than that at 37 ºC (Figure 3B), which indicates that these QDs can directly translocate through the lipid bilayer of the cell membrane by passive diffusion. This observation is in agreement with previous studies on lipid-coated hydrophobic Au NPs of 5 nM, which demonstrated that hydrophobic NPs with diameter $d > 5$ nm translocate through the bilayer, whereas individual NPs with $d \leq 5$ nm are trapped in the bilayer. The only possibility of small hydrophobic NPs for leaving the bilayer is by forming clusters exceeding the threshold size.[36] Based on our previous work, we know that the QD_F form nanoclusters in aqueous media containing only 5% of DMSO.[37] Therefore our hypothesis is that these hydrophobic QDs, both QD_F and QD_TOPO, cross the cell membrane as clusters. The clear advantage of having clusters inside cells instead of single QDs is that the sensitivity in bioimaging applications increases, due the higher signal-to-noise ratio induced by the more intense fluorescence of the clusters. Therefore, this would allow for a better discrimination from the fluorescence background (*i.e.*, cell autofluorescence), which is a common issue that makes it difficult to obtain an accurate and reliable diagnosis in those cases in which the

sensitivity of the imaging probe is not good enough.

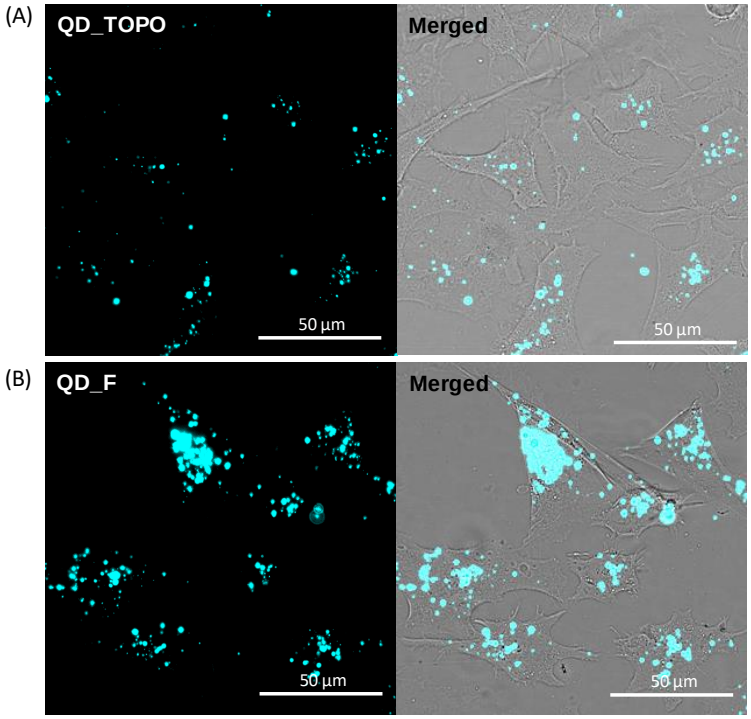

Figure 4. Confocal microscopy images of HeLa cells after incubation for 5 h at 37 ºC with (A) QD_TOPO, or (B) QD_F (both at 5 nM). The incubation was performed in serum-free Dulbecco modified eagle medium (DMEM) cell medium containing 0.5% of DMSO. The fluorescence signal was collected in the range 420–500 nm (λ_{ex} 405 nm). Images obtained from the single fluorescence channel and merged with the transmitted light images are shown. The scale bars correspond to 50 µm.

Conclusions

In summary, fluorination of ZnCdS/ZnS QDs has successfully increased their interaction with a phospholipid interface and, consequently, their surface activity. Such an increase of surface activity is proposed as the key feature for the higher cellular internalization of the fluorinated QDs compared to the non-fluorinated counterparts. Extending our discussion beyond the data obtained for the NPs studied

in the present work, the use of a DPPC phospholipid monolayer as a model for the cell membrane allows for the assessment of differences in the surface activity of NPs. This points out the potential of this membrane model for establishing the relationships between NP surface modification and surface activity, which can be then translated into surface activity–cell uptake correlations. In light of the presented findings, it is suggested that fluorination of NPs can be exploited as a simple and universal strategy to promote NP–cell membrane interactions and, consequently, their efficient cellular uptake. This work opens up new possibilities for the design of NP-based biomedical tools for diagnostics and therapy with improved uptake by cells, which may consequently lead to improved performances.

References and Notes

1. M. Björnmalm, K. J. Thurecht, M. Michael, A. M. Scott, and F. Caruso, *ACS Nano* **2017**, 11, 9594.
2. E. Blanco, H. Shen, and M. Ferrari, *Nat. Biotechnol*., **2015**, 33, 941.
3. R. Thiruppathi, S. Mishra, M. Ganapathy, P. Padmanabhan, and B. Gulyás, *Adv. Sci.* **2017**, 4, 1600279.
4. S. Ahn, E. Seo, K. Kim, S. J. Lee, *Sci. Rep.* **2013**, 3, 1997.
5. E. Polo, M. Collado, B. Pelaz, and P. del Pino, *ACS Nano* **2017**, 11, 2397.
6. M. Reifarth, S. Hoeppener, and U. S. Schubert, *Adv. Mater*. **2018**, 30, 1703704.
7. B. D. Chithrani, A. A. Ghazani, and W. C. Chan, *Nano Lett*. **2016**, 6, 662.
8. M. Zhu, G. Nie, H. Meng, T. Xia, A. Nel, and Y. Zhao, *Acc. Chem. Res*. **2012**, 46, 622.
9. E. C. Cho, L. Au, Q. Zhang, and Y. Xia, *Small* **2010**, 6, 517.
10. S. Salatin, S. MalekiDizaj, and A. YariKhosroushahi, *Cell Biol. Int*. **2015**, 39, 881.
11. Y. Jiang, S. Huo, T. Mizuhara, R. Das, Y. W. Lee, S. Hou, D. F. Moyano, B. Duncan, X. J. Liang, and V. M. Rotello, *ACS Nano* **2015**, 9, 9986.
12. X. Xie, J. Liao, X. Shao, Q. Li, and Y. Lin, *Sci. Rep*. **2017**, 7, 3827.
13. K. Saha, D. F. Moyano, and V. M. Rotello, *Mater. Horiz.* **2014**, 1, 102
14. Y. Li, X. Chen, and N. Gu, *J. Phys. Chem. B* **2008**, 112, 16647.
15. L. Liu, J. Zhang, X. Zhao, Z. Mao, N. Liu, Y. Zhanga, Q. H. Liu, *Phys. Chem. Chem. Phys.* **2016**, 18, 31946.
16. M. SamadiMoghaddam, M. Heiny, and V. P. Shastri, *Chem. Commun.* **2015**, 51, 14605.
17. Y. L. Chiu, Y. C. Ho, Y. M. Chen, S. F. Peng, C. J. Ke, K. J. Chen, F. L. Mi, and H. W. Sung, *J. Control. Release* **2010**, 146, 152.
18. E.P. Gillis, K.J. Eastman, M.D. Hill, D.J. Donnelly, and N.A. Meanwell, *J. Med. Chem.* **2015**, 58, 8315.
19. J. Wang, M. Sánchez-Roselló, J. L. Aceña, C. del Pozo, A. E. Sorochinsky, S. Fustero, V. A. Soloshonok, and H. Liu, *Chem. Rev*. **2013**, 114, 2432.

20.T. Fischer, and R. Riedl, *ChemistryOpen* **2017**, 6, 192.

21.M. Boccalon, P. Franchi, M. Lucarini, J. J. Delgado, F. Sousa, F. Stellacci, I. Zucca, A. Scotti, R. Spreafico, P. Pengo, and L. Pasquato, *Chem.Commun*. **2013**, 49,8794.

22.P. Zrazhevskiy, M. Sena, and X. Gao, *Chem. Soc. Rev*. **2010**, 39, 4326.

23.K. D. Wegner, and N. Hildebrandt, *Chem. Soc. Rev*. **2015**, 44, 4792.

24.X. Yang, K. Zhanghao, H. Wang, Y. Liu, F. Wang, X. Zhang, K. Shi, J. Gao, D. Jin, and P. Xi, *ACS Photonics* **2016**, 3, 1611.

25.C. Carrillo-Carrión, M. Gallego, W. J. Parak, and M. Carril, *Materials* **2018**, 9, 750.

26.A. T. R. Williams, S. A. Winfield, and J. N. Miller, *Analyst* **1983**, 108, 1067.

27.W. J. M. Lokerse, E. C. M. Kneepkens, T. L. M. ten Hagen, A. M. M. Eggermont, H. Grüll and G. A. Koning, *Biomaterials* **2016**, 82, 138.

28.J. Gao, R. S. Ndong, M. B. Shiflett and N. J. Wagner, *ACS Nano* **2015**, 9, 3243.

29.J. J. Giner-Casares, G. Brezesinski and H. Möhwald, *Curr. Opin. Colloid Interface Sci.* **2014**, 19, 176.

30.J. P. Coelho, M. J. Mayoral, L. Camacho, M. T. Martín-Romero, G. Tardajos, I. López-Montero, E. Sanz, D. Ávila-Brande, J. J. Giner- Casares, G. Fernández and A. Guerrero-Martínez, *J. Am. Chem. Soc.* **2017**, 139, 1120.

31.J. J. Giner-Casares, and J. Reguera, *Nanoscale* **2016**, 8, 16589

32.I. Lynch, K. A. Dawson, *Nano Today* **2008**, 3, 40.

33.C. D. Walkey, W. C. W. Chan, *Chem. Soc. Rev.* **2012**, 41, 2780.

34.A. Salvati, A. S. Pitek, M. P. Monopoli, K. Prapainop, F. Baldelli Bombelli, D. R. Hristov, P. M. Kelly, C. Åberg, E. Mahon, K. A. Dawson, *Nat. Nanotechnol.* **2013**, 8, 137.

35.T. Dos Santos, J. Varela, I. Lynch, A. Salvati, K. A. Dawson, PloSone, **2011**, 6, e24438.

36.Y. Guo, E. Terazzi, R. Seemann, J. B. Fleury, and V. A. Baulin, *Sci. Adv*., **2016**, 2, e1600261.

37.C. Carrillo-Carrión, M. Atabakhshi-Kashi, M. Carril, K. Khajeh, and W. J. Parak,

Angew. Chem. Int. Ed., 2018, 57, 5033. *Angew. Chem.* **2018**, 130, 5127.

Supporting Information

Experimental section

Materials. Cadmium oxide (CdO, 99.9%) was purchased from Alfa Aesar. Zinc oxide (ZnO, 99.9%), stearic acid (SA, 99%), sulphur powder (S, 99.98%), octadecene (ODE, 90%), hexyldecylamine (HDA, 90%), trioctylphosphine oxide (TOPO, 90%), trioctylphosphine (TOP, 97%), diethylzinc solution ($ZnEt_2$, 1 M in hexane), bis(trimethylsilyl) sulfide ($(TMS)_2S$, 99%), 1,2- dipalmitoyl-sn-glycero-3-phosphocholine (DPPC, 99%) were purchased from Sigma-Aldrich (Germany). All these chemicals were used as received without further purification. All organic solvents used were of analytical grade. The used fluorinated ligand, $HS\text{-}C_{11}\text{-}(EG)_4\text{-}O\text{-}C(CF_3)_3$ (EG = ethyleneglycol), was synthesized as previously reported.[1] Human cervical cancer cell line (HeLa) was purchased from ATCC-LGC. Dulbecco's modified Eagle's medium (DMEM), fetal bovine serum (FBS), and L-glutamine were purchased from Gibco. Penicillin and streptomycin were purchased from Hyclone. The PBS buffer was purchased in tablets and prepared following manufacturer procedures (Sigma-Aldrich) corresponding to 10 mM phosphate buffer containing 137 mM NaCl and 2.7 mM KCl at pH 7.4. Cell Proliferation kit I based on 3(4,5- Dimethylthiazol-2-yl)-2,5-diphenyltetrazolium bromide (MTT assay) was purchased from Roche. 8-well glass Millicell EZ slide was supplied by Millipore and mounting media by Dako.

Synthesis and fluorination of quantum dots

Synthesis. Hydrophobic trioctylphosphine oxide (TOPO)-capped ZnCdS/ZnS core-shell quantum dots (in the following referred to as QD_TOPO) were synthesized at high temperature in a hot coordinating solvent mixture. ZnCdS cores were synthesized using CdO, ZnO and S as precursors by following a reported protocol.[2] Then the ZnS shell was growth onto the cores using diethylzinc and hexamethyldisilathiane as zinc and sulfur sources, respectively.[3] Briefly, 0.3 mmol of CdO and ZnO was mixed with SA in a three-necked flask and heated to 230 °C under N_2 until getting a clear solution which indicated the formation Cd/Zn-SA precursor. The solution was then allowed to cool down to room temperature (RT)

while the Cd/Zn-SA precursor became a white solid precipitate. 15 mmol of TOPO and 24 mmol of HDA were added into the three-necked flask and stirred under N_2 at RT for 5 min. Then the temperature is increased up to 320 °C to form a transparent solution. Afterwards, the S-ODE precursor (1.5 mmol of S dissolved in 4 mL of ODE) was swiftly injected into the three-neck flask.

The mixture was left to react at 320 °C for 60 min, and then cooled down to 150 °C to stop the reaction. The samples were precipitated with hot anhydrous methanol for purification. Subsequently, 1.5 mL of the Zn/S/TOP stock solution, consisting of 1.75 mL of $ZnEt_2$ and 0.26 mL of $((TMS)_2S$ in 10.25 mL of TOP, was added dropwise to the mixture under vigorous stirring for the formation of the shell. After stirring for 30 min at 150 °C, the temperature was decreased to 90 °C and the mixture was stirred for additional 2 h. After cooling the solution down to RT, the QDs were purified by addition of methanol and centrifugation ($1x10^4$ RCF for 10 min) and washed with methanol twice. The purified nanocrystals were then dispersed in dichloromethane (DCM), and stored in the fridge (4 °C) in darkness.

Fluorination. Fluorinated ZnCdS/ZnS core-shell quantum dots (in the following referred to as QD_F) were prepared by ligand-exchange of QD_TOPO with a fluorinated ligand, $HS\text{-}C_{11}\text{-}(EG)_4\text{-}O\text{-}C(CF_3)_3$ (EG = ethyleneglycol). The fluorinated ligand dissolved in DCM was added to a mixture DCM:MeOH (1:2) in a glass vial. Next, the solution of QD_TOPO was added and the mixture stirred overnight in darkness at 40 °C. With the aim of covering completely the QD surface 20,000 fluorinated ligands per nanoparticle were used. Finally, the QD_F nanoparticles were purified by centrifugation at $1.5x10^5$ RCF for 30 min. The precipitate was redispersed in 0.5 mL of DCM, 3 mL of MeOH was added and the sample was centrifuged again at $1.5x10^5$ RCF for 30 min. Three washes were done and after the last wash the precipitate containing the purified QD_F particles were dispersed in DCM and stored in the fridge (4 °C) in darkness until use.

Characterization techniques for quantum dots

Transmission electron microscopy (TEM). TEM images were acquired with a JEOL JEM 2100F microscope by deposition of the sample on top of a copper grid coated with a layer of carbon. Size measurements based on the TEM images were performed with the free software ImageJ and the analysis of the size distribution and plotting of the histograms were done with the software Origin.

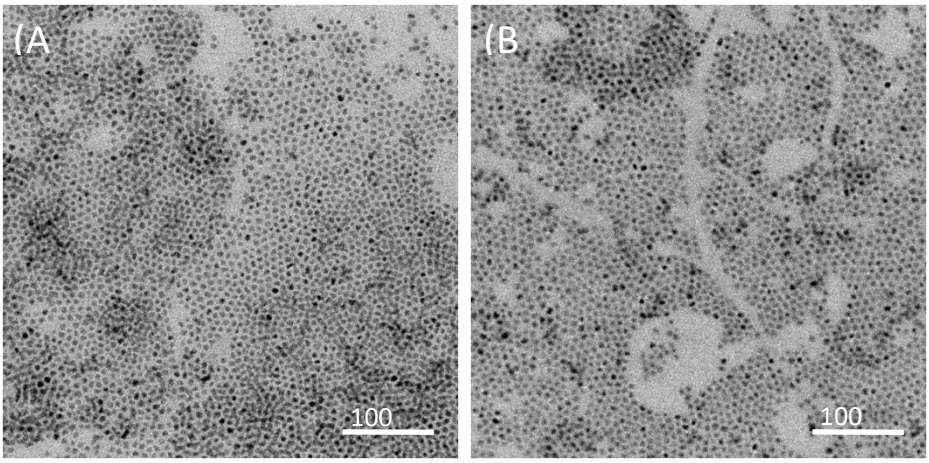

Figure S1. (A) TEM image of QD_TOPO NPs. (B) TEM image of QD_F NPs. The different coating did not affect to the inorganic part of the NPs, and therefore the inorganic core diameter of the QD was the same: d_c = (7.0 ± 0.5) nm.

UV-vis and photoluminescence spectroscopy. UV-vis absorption spectra of the QDs were acquired with a Varian 5000 UV-Vis-NIR spectrophotometer using a 10 mm path length glass cuvette. Fluorescence emission spectra of the QDs were collected using a Fluorolog-3 (model FL3-22, Horiba) fluorescence spectrometer. Measurements were carried out using a 10 mm path length quartz cuvette. Fluorescence spectra were recorded under excitation at λ_{exc}=350 nm, and the integration time was set to 0.1 s per 2 nm increment in wavelength.

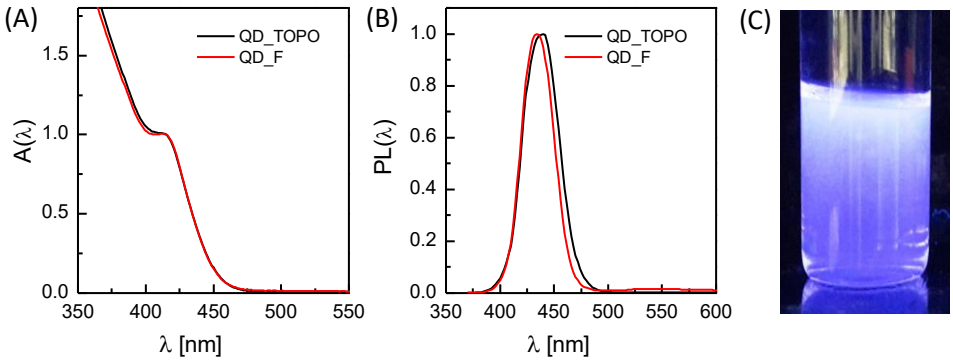

Figure S2. (A) Normalized absorption spectrum A(λ) of QD_TOPO (black line) and QD_F (red line) in DCM showing the first exciton absorption peak at 415 nm. (B) Normalized fluorescence emission spectra PL(λ) of QD_TOPO (black line) and QD_F (red line) in DCM under excitation at 350 nm. The maximum fluorescence emission was located at 440 nm for QD_TOPO NPs and 434 nm for QD_F NPs. (C) Photograph of the QD_F particles dispersed in DCM under UV light.

Dynamic light scattering (DLS). A Malvern Zetasizer (Nano ZS ZEN3600), equipped with a 10 mW He–Ne laser operating at a wavelength of 633 nm and fixed scattering angle of 173˚ was used to measure the hydrodynamic diameter from the number distribution. Measurements were done placing the samples in a glass cuvette and the specific parameters of temperature and refractive index and viscosity of the medium (DCM) were fixed as follows: temperature = 20 ˚C, refractive index: 1.424; viscosity: 0.43 cP. Samples were equilibrated at 20 °C for 10 min to ensure that only Brownian motion was recorded.

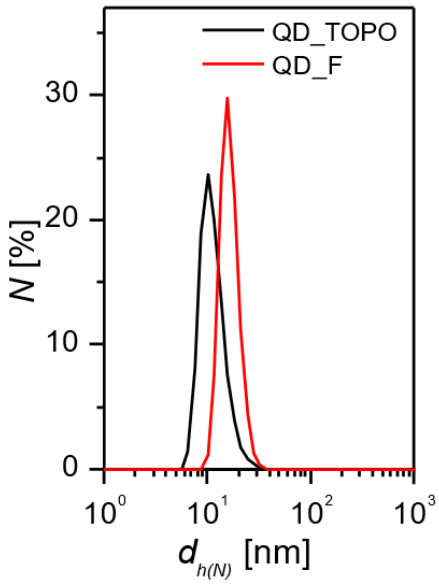

Figure S3. Hydrodynamic diameter d_h given as number distribution N(d_h) of QD_TOPO (black line) and QD_F (red line) in DCM as determined by DLS: d_h = (10.5 ± 2.3) nm and PDI = 0.217 for QD_TOPO, and d_h = (16.7 ± 1.7) nm and PDI = 0.115 for QD_F. Three replicates of each measurement were performed to determine the standard deviation.

Nuclear magnetic resonance (NMR) spectroscopy. ^{1}H and ^{19}F NMR spectra were recorded in CD_2Cl_2 solution (purchased from Cortecnet) in a Bruker 500 MHz spectrometer (500 MHz for ^{1}H and 470 MHz for ^{19}F). Spectra were analyzed with the software MestReNova.

As it can be seen in Figure S4B, QD_F spectrum shows signals coming clearly from the presence of fluorinated ligand on the surface (signals labelled as 3-5) and signals coming clearly from TOPO (signals labelled as 2), and also some signals that come from both ligands (signals labelled as 1 and 6). Also, some impurities from solvents and water can be seen in QD_TOPO and QD_F spectra. The absence of the signal labelled as 7 in QD_F spectrum confirms that the fluorinated ligand is indeed grafted on the QD core and it is not remaining unbound fluorinated ligand.[1]

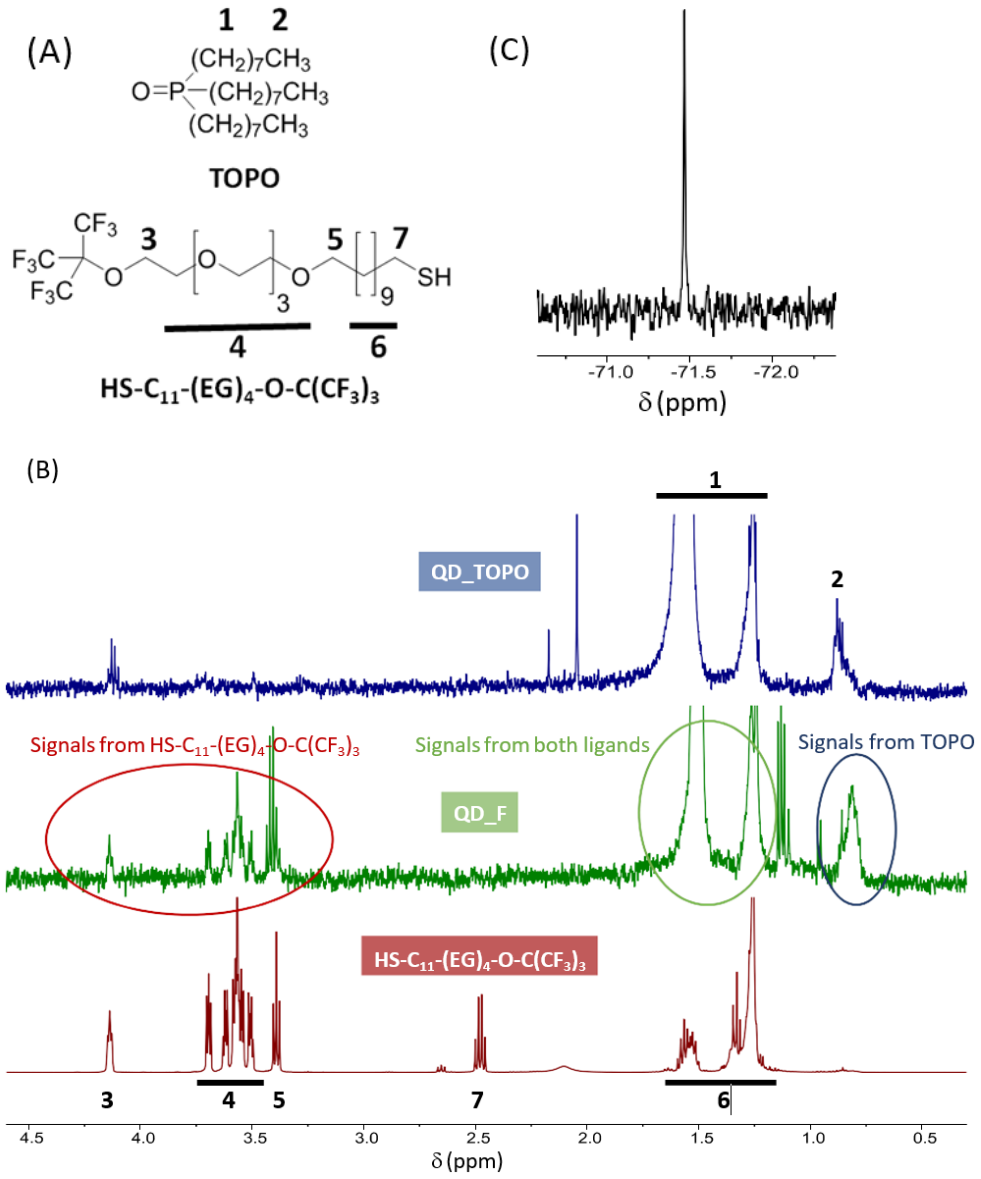

Figure S4. (A) Chemical structures of TOPO and HS-C_{11}-$(EG)_4$-O-$C(CF_3)_3$ with numbers for labelling different groups of protons to facilitate identification on the NMR spectra. (B) ^{1}H NMR spectrum ofHS-C_{11}-$(EG)_4$-O-$C(CF_3)_3$, QD_F and QD_TOPO (from bottom to top). (C) ^{19}F NMR spectrum of QD_F. All spectra were recorded in CD_2Cl_2.

Interfacial tension (IFT) measurements. The dynamic interfacial tension (IFT) of the QD_TOPO and QD_F NPs at the dichoromethane−water interface was measured by the pendant drop technique using a DSA100 measuring instrument (Krüss, Germany). An ultrafast camera (Krüss, Germany) was used to image the time-dependent drop shape changes of a sample droplet of oil (DCM solution) immersed in the aqueous phase.

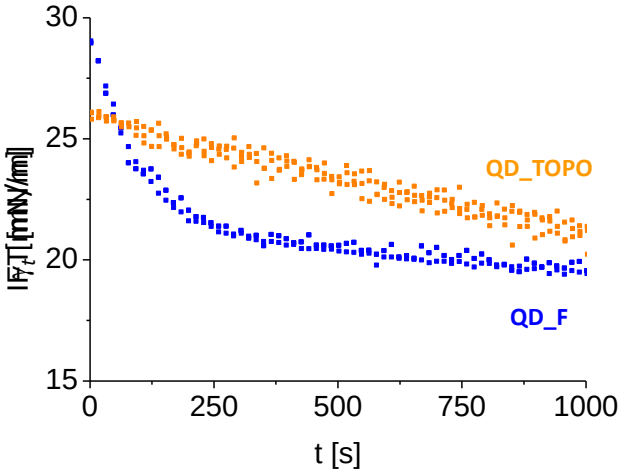

Figure S5. Time dependence of the interfacial tension (IFT) γt for QD_F (100 nM in DCM) and QD_TOPO (100 nM in DCM) immersed in an aqueous buffer solution at pH 5. Measurements were performed in triplicate.

Determination of quantum yield

The quantum yield (QY) of the QD_TOPO NPs (*i.e.* before the ligand exchange) and QD_F NPs (*i.e.* after the ligand exchange) was calculated by the method outlined by Horiba, which compares the absorbance and the emission of the fluorophore to be tested (QD nanoparticles in this case) with those of a standard fluorophore. Fluorescein (F) in NaOH 0.1 M (QYF = 0.79) was used as standard fluorophore. Five solutions at increasing concentrations of fluorescein (F) and the twoNPs (QD_TOPO, QD_F) were prepared and their respective absorbance and fluorescence spectra were recorded by using a cuvette of 10 mm path-length. The concentrations were selected in a way that the higher concentration had an absorbance of *ca.* 0.1, in

order to minimize re-absorption effects and scattering from the NPs. The integrated fluorescence intensity (PL_{int}) was determined by integration of the fluorescence spectrum over the range of wavelength of the fluorescence peak. Then the integrated fluorescence intensity versus the absorbance (A) at the peak was plotted for each set of sample data (Figure S6) and fitted to a straight line with the gradient (grad) as free fit parameter and the intercept set to zero. Absolute values of the QYs of the two NP samples were then calculated using the following equation:

$$QY_X = QY_{ST} \frac{grad_X}{grad_{ST}} \frac{n_X^2}{n_{ST}^2}$$

where the subscripts ST and X denote standard and test sample respectively. QY is the fluorescent quantum yield, grad is the gradient dPL_{int}/dA from the plot of integrated fluorescence intensity I_{int} versus absorbance A, and η corresponds to the refractive index of the solvent (1.333 for water and 1.424 for dichloromethane).

The calculate QY values were 0.82 and 0.77 for QD_TOPO and QD_F, respectively.

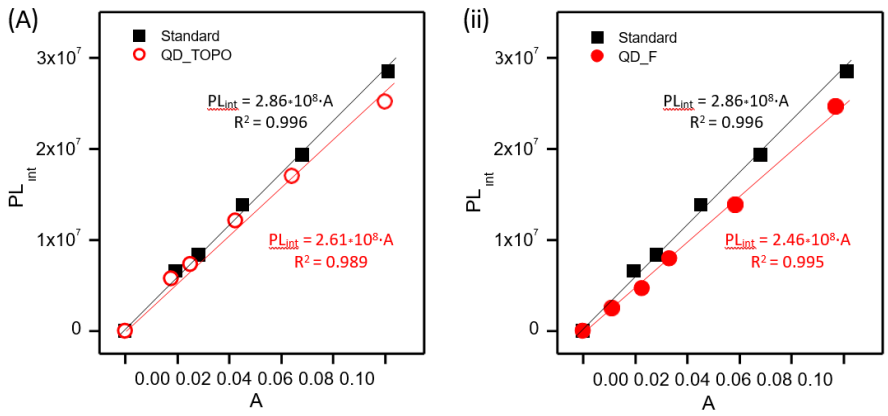

Figure S6. The integrated fluorescence intensity (PLint) plotted as a function of maximum absorbance (A) for (i) QD_TOPO NPs together with the standard fluorophore, and (ii) QD_F NPs together with the standard fluorophore. Data points were fitted with the function $PL_{int}(A) = grad \cdot A$. Thus, the gradient is determined as $grad = dPL_{int}/dA$ as first derivative. R^2 is the coefficient of determination, which indicates the goodness of fit.

Langmuir monolayer studies

Formation of Langmuir monolayers. Chloroform was used as the spreading solvent, and the concentration of chloroform in the spreading was 1 mM. The QDs, either QD_F or QD_TOPO, were included in the spreading solution with DPPC. The molar ratio DPPC:QD in the spreading solution was 120:1 in all cases. This value of molar ratio ensures that *ca.* 20% of the DPPC molecules are in excess with respect to a complete covering of the DPPC monolayer by an underneath monolayer of quantum dots. Ultrapure water, produced by a Millipore Milli-Q unit, pre-treated by a Millipore reverse osmosis system (>18.2 MΩ cm), was used as subphase. The subphase temperature was 21 °C with pH 5.7. All instruments for the study of the Langmuir monolayers at the air/liquid interface were located on tables with vibration isolation (antivibration system MOD-2 S, Accurion, Göttingen, Germany) in a large class 100 clean room.

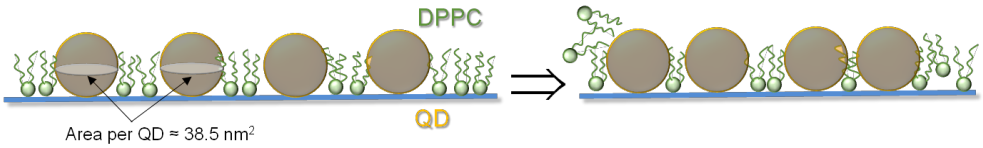

Figure S6. Scheme of the DPPC monolayer in contact with the quantum dots (QDs). After compression of the monolayer the available surface area per DPPC molecule is reduced, and the hydrophobic interaction of the QDs with the alkyl chains of the DPPC molecules leads to an effective removal of some DPPC molecules from the monolayer to the QD surface. The area per QD has been calculated assuming a spherical shape of the QDs and a contact angle of 90° at the interface with the phospholipid molecules.

Characterization techniques for Langmuir monolayers. Surface pressure–area isotherms. Two different models of Nima troughs (Nima Technology, Coventry, England) were used in this work, both provided with a Wilhelmy type dynamometric system using a strip of filter paper: a NIMA 611D with one moving barrier for the measurement of the UV-vis reflection spectra, and a NIMA 601, equipped with two symmetrical barriers to record Brewster angle microscopy images. The monolayers were compressed at a speed of 0.03 nm^2 min^{-1} $molecule^{-1}$.

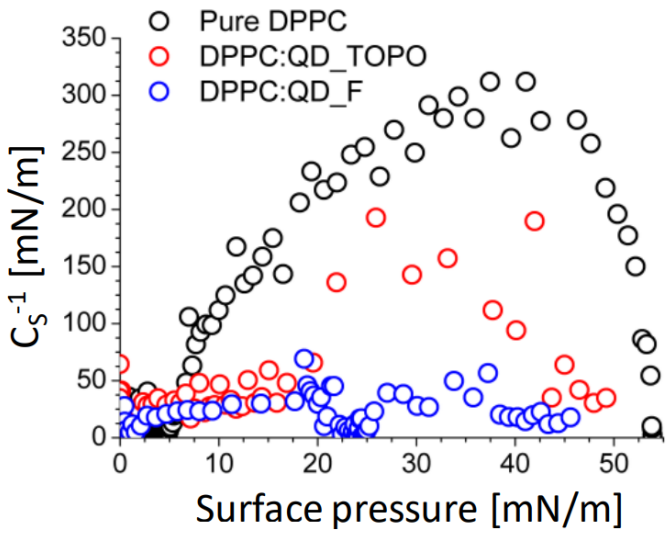

Figure S7. Compressibility modulus-surface pressure plots for the DPPC monolayer on: pure water (black circles), QD_TOPO (red circles) and QD_F (blue circles).

UV-vis reflection spectroscopy. UV–visible reflection spectra at normal incidence as the difference in reflectivity (ΔR) of the film-covered water surface and the bare surface were obtained with a Nanofilm Surface Analysis Spectrometer (Ref SPEC^2, supplied by Accurion GmbH, Göttingen, Germany).

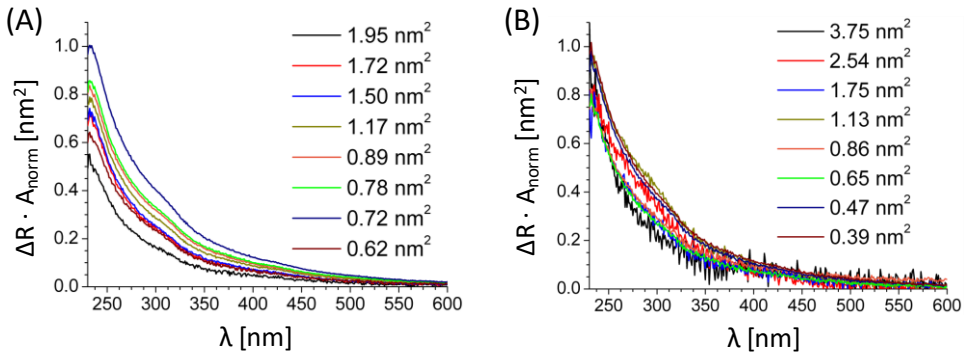

Figure S8. UV-vis reflection spectra normalized to unity for (A) the DPPC:QD_TOPO and (B) the DPPC:QD_F . Values of area per DPPC molecule are indicated in the insets.

Brewster angle microscopy (BAM). Images of the film morphology were obtained by Brewster angle microscopy with a I- Elli2000 (Accurion GmbH) using a Nd:YAG diode laser with wavelength 532 nm and 50 mW, which can be recorded with a lateral resolution of 2 μm. The image processing procedure included a geometrical correction of the image, as well as a filtering operation to reduce interference fringes and noise.

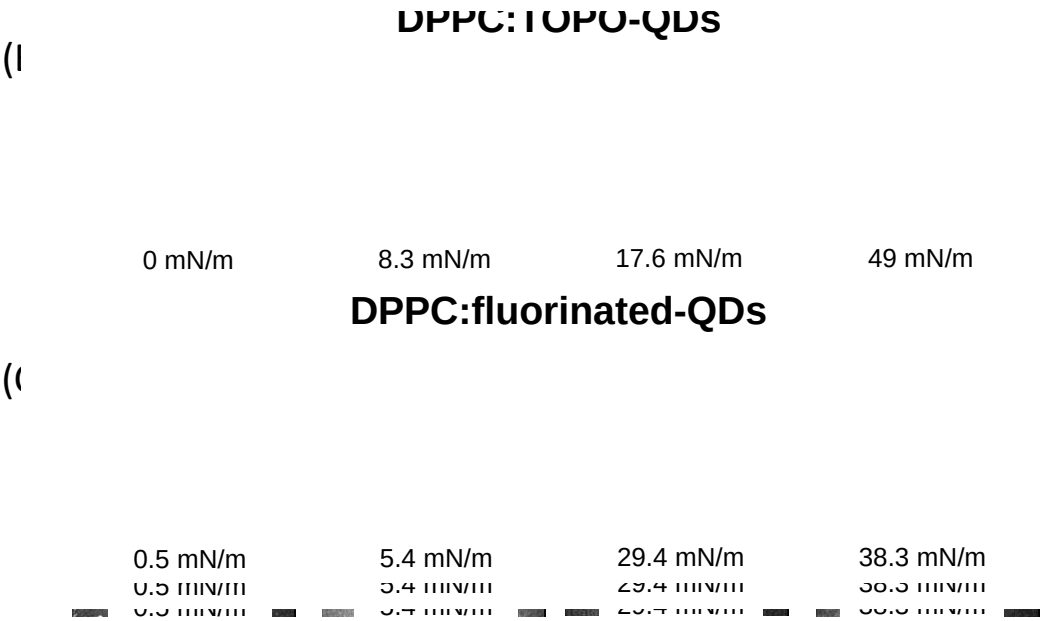

Figure S9. BAM images of the DPPC monolayer in contact with (A) QD_TOPO, and (B) QD_F. Values of surface pressure for each picture are indicated in the insets. Width equals to 225 μm.

Cell culture and NP internalization

Cell culture. HeLa cells (human cervical cancer cell line) were cultured at 37 °C and 5% CO_2 in 75 cm^2 flasks in complete medium, *i.e.* Dulbecco's modified Eagle's medium (DMEM) supplemented with 10 % heat-inactivated fetal bovine serum (FBS), 2 mM L-glutamine, 100 μg/mL streptomycin, and 100 μ/mL penicillin. For cell passage, cells were lifted from the flasks by trypsinization for 5 min at 37 °C, spun at 10^3 RCF for 5 min and the pellet resuspended in 1 mL of media. Cells in the

exponential growth phase were used for experiment. For cell counting, the cell suspension was serially diluted 1:10 in PBS and 1:2 in the exclusion dye Trypan Blue solution (0.4 % Trypan Blue in 0.81 % sodium chloride and 0.06 % potassium phosphate). 10 µL of the diluted cell suspension was counted in a haemocytometer chamber under transmitted light in an inverted microscope (DMIL, Leica).

Uptake. For the uptake studies of nanoparticles (QD_TOPO and QD_F), cells were incubated for 5 h with particles at 5 nM for 5 h at 2 different temperatures (37 ºC and 4 ºC). QDs initially in DCM were changed to DMSO at a concentration of 1 µM, and 10 µL of these stock solutions were added to 1990 µL of serum-free cell media; therefore the final concentrations of particles and DMSO in the media were 5 nM and 0.5 %, respectively. Incubation for 5 h atd 5 nM QD concentration were selected as optimum conditions for obtaining significant fluorescence intensities within cells (*i.e.* for a reliable quantitative analysis) while maintaining a cell viability ≥ 90 %. Serum-free media was used to avoid the adsorption of proteins around the QDs, therefore allowing direct interaction of the surface coating of the QDs (TOPO or fluorinated ligands) with the cellular membrane.

HeLa cells were seeded in 8-well glass Millicell EZ slides at densities of $5x10^4$ cells per well cultured for 24 h in complete medium at 37 ºC and 5 % CO_2. Then, cells were washed twice with 200 µL of serum-free medium and 200 µL of solutions of either QD_TOPO or QD_F (at 5 nM dispersed in serum-free medium) were added. After cell incubation with the nanoparticles for 5 h at either 37 °C or 4 °C, supernatants were removed and cells were washed carefully twice with PBS. Cells were fixed with 200 µL of paraformaldehyde (PF, 4 % in PBS) for 20 min at RT and washed then twice with PBS. Finally a glass slide was fixed with 10 µL of mounting media and left at 4 ºC overnight for hardening before imaging.

Cell viability

Cell viability of HeLa cells was measured with the colorimetric MTT (3-(4,5-dimethylthazolk-2-yl)-2,5-diphenyl tetrazolium bromide) assay. $1x10^5$ cells were seeded in 96-well plates and cultured for 24 h at 37 ºC and 5 % CO_2. Owing to the

fact that the QDs (QD_TOPO and QD_F) were initially dispersed in DMSO and that the final amount of DMSO in the media is 0.5 % this condition was also assayed as control. Cells were incubated with 0.5 % DMSO, 5 nM of QD_TOPO, or 5 nM of QD_F, all of them in serum-free medium for 5 h and 24 h. Cells incubated in serum-free medium but without nanoparticles were used as control (*i.e.* untreated control cells). Afterwards, cells were washed twice with 100 µL of serum-free medium and incubated for 30 min at 37 ºC and 5 % CO_2 with 100 µL of medium containing MTT at the dilution of 1:20. The produced formazan crystals as a result of the dehydrogenase mitochondrial activity of living cells were dissolved in 100 µL DMSO, and the absorbance of MTT product was measured at 550 nm in a microplate reader (Genios Pro, TECAN). Cell viability is expressed as a percentage of absorbance of treated cells related to the untreated control cells and represented as mean of quadruplicates ± standard deviation (SD). Data are shown in Figure 3A.

Confocal microscopy

Imaging. Cells were imaged employing a confocal laser scanning microscope (CLSM 510 Meta) from Zeiss, and using a Plan-Apochromat 63x/1.4 M27 oil immersion objective. QDs (QD_TOPO or QD_F) internalized by cells were excited with a 405 nm laser diode, and their fluorescence emission was collected in the range 420 - 500 nm. Transmission images were also collected.

Quantification fluorescence density. The quantitative evaluation of the QDs (QD_TOPO or QD_F) internalized by cells was performed by measuring the fluorescence density per cell using ImageJ software. A direct comparison was possible since it was previously checked that the intensity of the fluorescence emission of both QD types was almost identical working at the same QD concentration and under the same environment. QDs fluorescent intensity evaluation was performed using ImageJ. All confocal fluorescence images acquired using the same imaging settings were imported into ImageJ, and the area of each cell was outlined and defined as ROI. Then the integrated densities of 50 cells were measured, and expressed as mean ± standard deviation (SD). Note that the integrated density is

the area of the ROI x the mean of the ROI, and thus the different size of the cells does not affect to the calculated fluorescence density value. Data are shown in Figure 3B.

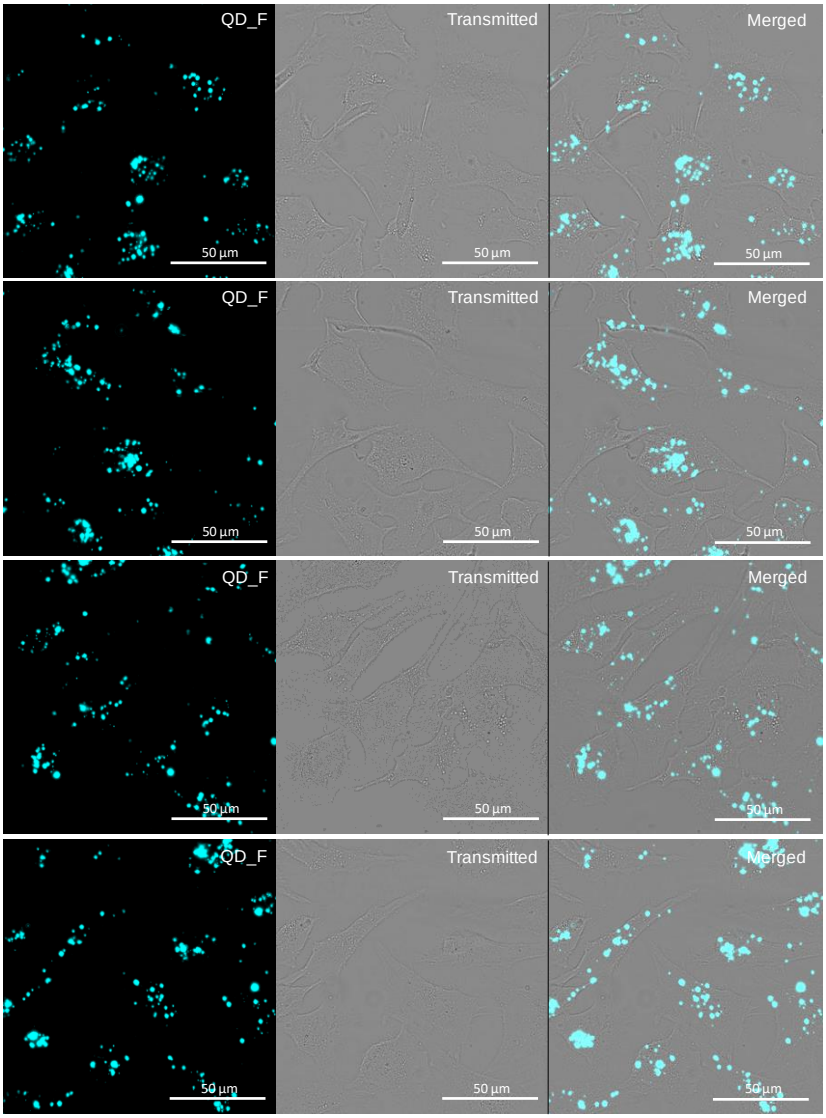

Figure S9. Some representativeconfocal microscopy images of HeLa cells incubated with QD_F (5 nM) for 5 h at 37 °C in serum-free cell media containing 0.5 % of DMSO. Fluorescence channel was collected at 420–500 nm (λ_{ex} 405 nm). Single fluorescence channel transmitted light channel, and the merge of both are shown. The scale bar corresponds to 50 µm.

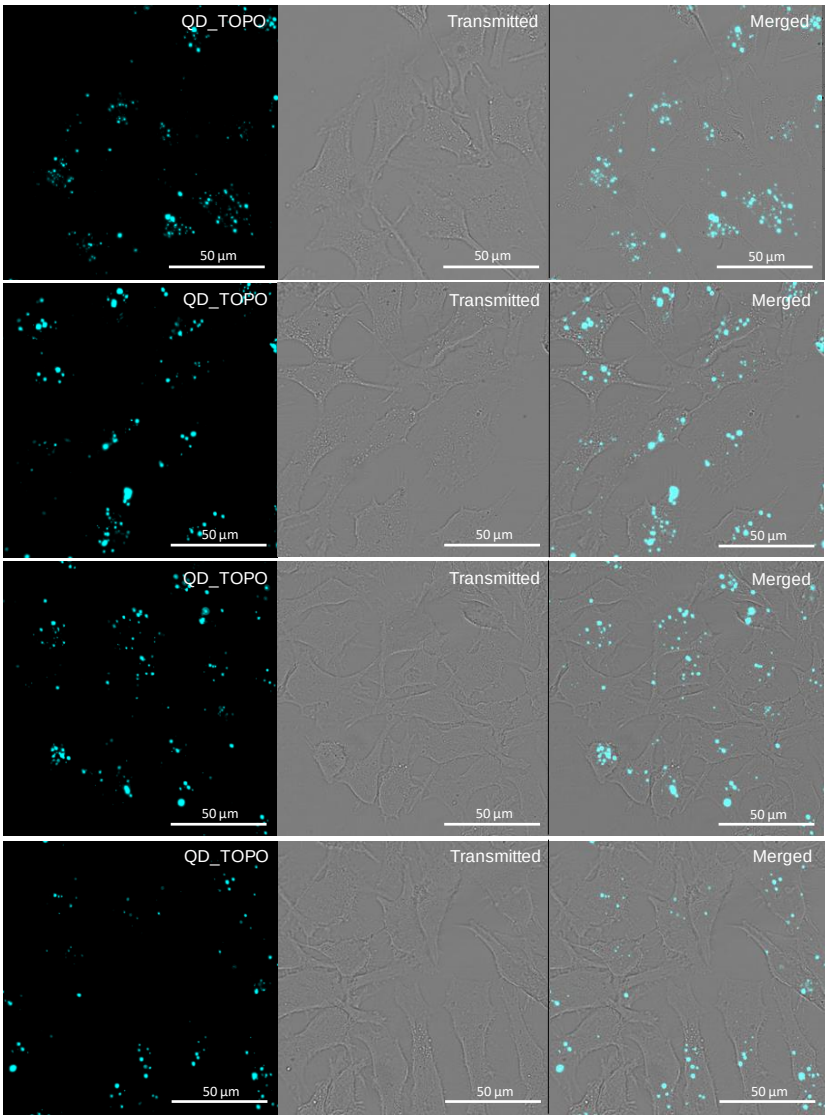

Figure S10. Some representative confocal microscopy images of HeLa cells incubated with QD_TOPO (5 nM) for 5 h at 37 °C in serum-free cell media containing 0.5 % of DMSO. Fluorescence channel was collected at 420–500 nm (λ_{ex} 405nm). Single fluorescence channel transmitted light channel, and the merge of both are shown. The scale bar corresponds to 50 µm.

References

1. O. Michelena, D. Padro, C. Carrillo-Carrión, P. Del Pino, J. Blanco, B. Arnaiz, W. J. Parak, and M. Carril, *Chem. Comm.* **2017**, 53, 2447.
2. H. S. Chen, S. R. Chung, Y. C. Chen, T. Y. Chen, C. Y. Liu, and K. W. Wang, *Cryst. Eng. Comm.* **2015**, 17, 5032.
3. C. Carrillo-Carrión, S. Cárdenas, B. M. Simonet and M. Valcárcel, *Anal. Chem.* **2009**, 81, 4730

An International Journal
COLLOIDS AND SURFACES B

Published on 21 Sep 2018
DOI: 10.1016/j.colsurfb.2018.09.050

Fluorinated CdSe/ZnS quantum dots: Interactions with cell membrane

Pablo G. Argudo[a], María T. Martín-Romero[a], Luis Camacho[a], Mónica Carril[b,c], Carolina Carrillo-Carrión[d,e], Juan J. Giner-Casares[a].

a. Institute of Fine Chemistry and Nanochemistry, Department of Physical Chemistry and Applied Thermodynamics, University of Córdoba, Campus Universitario de Rabanales, Edificio Marie Curie, Córdoba, 14014, Spain

b. Biofisika Institute (CSIC, UPV/EHU) and Department of Biochemistry and Molecular Biology, University of the Basque Country UPV/EHU, Leioa, 48940, Spain

c. Ikerbasque, Basque Foundation for Science, Bilbao, 48011, Spain

d. CIC biomaGUNE, San Sebastian, 20014, Spain

e. Center for Research in Biological Chemistry and Molecular Materials (CiQUS), University of Santiago de Compostela, Santiago de Compostela, 15782, Spain

Fluorescent inorganic quantum dots are highly promising for biomedical applications as sensing and imaging agents. However, the low internalization of the quantum dots, as well as for most of the nanoparticles, by living cells is a critical issue which should be solved for success in translational research. In order to increase the internalization rate of inorganic CdSe/ZnS quantum dots, they were functionalized with a fluorinated organic ligand. The fluorinated quantum dots displayed an enhanced surface activity, leading to a significant cell uptake as demonstrated by in vitro experiments with HeLa cells. We combined the experimental and computational results of Langmuir monolayers of the DPPC phospholipid as a model cell membrane with in vitro experiments for analyzing the mechanism of internalization of the fluorinated CdSe/ZnS

quantum dots. Surface pressure-molecular area isotherms suggested that the physical state of the DPPC molecules was greatly affected by the quantum dots. UV-vis reflection spectroscopy and Brewster Angle Microscopy as in situ experimental techniques further confirmed the significant surface concentration of quantum dots. The disruption of the ordering of the DPPC molecules was assessed. Computer simulations offered detailed insights in the interaction between the quantum dots and the phospholipid, pointing to a significant modification of the physical state of the hydrophobic region of the phospholipid molecules. This phenomenon appeared as the most relevant step in the internalization mechanism of the fluorinated quantum dots by cells. Thus, this work sheds light on the role of fluorine on the surface of inorganic nanoparticles for enhancing their cellular uptake.

Introduction

Colloidal inorganic quantum dots (QDs) are highly valued in optoelectronics,[1] with a growing relevance in the biomedical field as sensing and imaging active agents.[2-4] Yet the inefficient internalization of the QDs by living cells remains as one of the most relevant frontiers for the in vivo clinical application. Such low internalization issue entails the need of using high doses of QDs.[5] Therefore, the interaction of the QDs with the cell membrane appears key for understanding and designing efficient QDs for biomedical applications. Fluorination of the capping ligands of QDs appears as an efficient strategy to improve the internalization by exploiting the change in polarity to render a high surface activity.[6] Herein we studied the effect of a fluorinated CdSe/ZnS QD on a model cell membrane and its uptake by living cells in high detail. Enhanced cell uptake of QDs coated with fluorinated ligands with respect to non-fluorinated QDs has been observed. A detailed view of the intermolecular interaction of the fluorinated QDs at the cell membrane is aimed. Experimental data have been obtained, additionally including molecular dynamics simulations for an atomistic description. The surface of the cell membrane is

modelled as a Langmuir monolayer of the DPPC phospholipid as main constituent of the eukaryotic membranes.[7] The Langmuir technique allows a fine tuning of the available surface area for the phospholipid molecules at the air/water interface. In situ microscopy and UV–vis spectroscopy experiments were performed to monitor the effect of the fluorinated QDs on the phospholipid monolayer.[8] Indeed, Langmuir monolayers of phospholipids have been successfully used by the group of Reis *et al.* to assess the mechanism of action of drugs, quantifying the influence of the drug in the structure on the lipid monolayers, as well as the aggregation state of the drug at the lipid interface.[9,10] Bioactive molecules such as enzymes, have been studied in detail by Caseli *et al.* at the phospholipid interface using monolayers.[11] Monolayers of inorganic nanoparticles might be also formed at the air/liquid interface, provided the capping ligands display enough hydrophobicity.[12,13]

Materials and Methods

Materials. 1,2-dipalmitoyl-sn-glycero-3-phosphocholine (DPPC, ≥99%) and the chloroform (> 99.9%) were purchased from Aldrich (Germany) and used as received. Chloroform was used as the spreading solvent. The concentration of DPPC in chloroform was 1 mM. The quantum dots (QD_F) were included in the spreading solution with DPPC. The molar ratio DPPC:QDs in the spreading solution was 75:1 in all cases. This value of molar ratio ensures that *ca.* 20% of the DPPC molecules are in excess with respect to a complete covering of the DPPC monolayer by an underneath monolayer of quantum dots. Ultrapure water, produced by a Millipore Milli-Q unit, pre-treated by a Millipore reverse osmosis system (> 18.2 MΩ cm^{-1}), was used as subphase. The subphase temperature was 21 °C with pH 5.7. Cadmium oxide (CdO, 99.9%) was purchased from Alfa Aesar. Zinc oxide (ZnO, 99.9%), stearic acid (SA, 99%), sulphur powder (S, 99.98%), octadecene (ODE, 90%), hexyldecylamine (HDA, 90%), trioctylphosphine oxide (TOPO, 90%), trioctylphosphine (TOP, 97%), diethylzinc solution ($ZnEt_2$, 1 M in hexane), bis(trimethylsilyl) sulfide ($(TMS)_2S$, 99%), Dimethyl sulfoxide (DMSO), Dichloromethane (DCM) were purchased from Sigma- Aldrich (Germany). All these

chemicals were used as received without further purification. All organic solvents used were of analytical grade. The used fluorinated ligand, HS-C_{11}-$(EG)_4$-O-$C(CF_3)_3$ (EG = ethyleneglycol), was synthesized as previously reported.[14] Human cervical cancer cell line (HeLa) was purchased from ATCC-LGC. Dulbecco's modified Eagle's medium (DMEM), fetal bovine serum (FBS), and L-glutamine were purchased from Gibco. Penicillin and streptomycin were purchased from Hyclone. The PBS buffer was pur- chased in tablets and prepared following manufacturer procedures (Sigma-Aldrich) corresponding to 10 mM phosphate buffer containing 137 mM NaCl and 2.7 mM KCl at pH 7.4. Cell Proliferation kit I based on 3(4,5-Dimethylthiazol-2-yl)-2,5-diphenyltetrazolium bromide (MTT assay) was purchased from Roche. 8-well glass Millicell EZ slide was supplied by Millipore and mounting media by Dako.

Fluorination. Fluorinated CdSe/ZnS core-shell quantum dots (in the following referred to as QD_F) were prepared as described previously.[6] Briefly, TOPO-capped CdSe/ZnS QDs (in the following referred to as QD_TOPO) were modified with a fluorinated ligand, HS-$C_{11}H_{22}$-$(EG)_4$- O-$C(CF_3)_3$ (EG = ethyleneglycol) via ligand-exchange procedure. The fluorinated ligand and QD_TOPO were reacted in a mixture DCM:MeOH (1:2) and stirred overnight in darkness at 40 °C. 2×10^4 fluorinated ligands per QD were used in order to achieve a maximum coverage of the QD surface. Next day, the QD_F nanoparticles were purified by centrifugation at 1.5×10^5 RCF for 30 min, and washed three times with MeOH. Finally, the purified QD_F particles were dispersed in DCM and stored in the fridge (4 °C) in darkness until use.

Surface pressure–area isotherms. Two different models of Nima troughs (Nima Technology, Coventry, England) were used in this work, both provided with a Wilhelmy type dynamometric system using a strip of filter paper: a NIMA 611D with one moving barrier for the mea- surement of the UV–vis reflection spectra, and a NIMA 601, equipped with two symmetrical barriers to record Brewster angle microscopy images. The monolayers were compressed at a speed of 0.03 nm^2 $min^{-1}molecule^{-1}$.

UV-vis reflection spectroscopy. UV–vis reflection spectra at normal incidence as the difference in reflectivity (ΔR) of the film-covered water surface and the bare surface were obtained with a Nanofilm Surface Analysis Spectrometer (RefSPEC^2, supplied by Accurion GmbH, Göttingen, Germany).

Brewster angle microscopy (BAM). Images of the film morphology were obtained by Brewster angle microscopy with a I-Elli2000 (Accurion GmbH) using a Nd:YAG diode laser with wavelength 532 nm and 50 mW, which can be recorded with a lateral resolution of 2 μm. The image processing procedure included a geometrical correction of the image, as well as a filtering operation to reduce interference fringes and noise.

All instruments for the study of the Langmuir monolayers at the air/ liquid interface were located on tables with vibration isolation (anti-vibration system MOD-2 S, Accurion, Göttingen, Germany) in a large class 100 clean room.

Computer simulations. 36 molecules of the fluorinated ligand were modelled as covalently bound by a S-S bond to the ZnS surface. 0.47 nm^2 was taken as the average value of surface area per fluorinated ligand, corresponding to a dense coating of the QD_F surface. A similar intermolecular distance between the fluorinated ligand molecules was imposed to ensure a homogeneous distribution. The force field CompassII was used for computation of initial atom charge and optimization of the geometry. Molecular dynamics was applied in the NVE ensemble (T = 298 K, 20 ps of total MD time, time step of 0.1 fs). An additional step of geometry optimization was applied subsequently to the Molecular Dynamics. The XYZ dimension values of the computational box were 45.7 × 37.4 × 137.6 Å^3. The computational results and the molecular arrangement were analysed by in-house software using MathCad 14.0.

Cell viability. Cell viability of HeLa cells after exposure to the QD_F nanoparticles was assessed by using the colorimetric MTT (3-(4,5-di-methylthazolk-2-yl)-2,5-diphenyl tetrazolium bromide) assay. 1 × 10^5 cells were seeded in 96-well plates and cultured for 24 h at 37 °C and 5% CO_2 in complete medium. Then, cells were incubated with either 5 nM of QD_F or 0.5% DMSO

(because the QD_F were initially dispersed in DMSO) for 5 h and 24 h in serum-free medium. Untreated cells were used as control. Afterwards, cells were washed twice with 100 μL of serum-free medium and incubated for 30 min at 37 °C and 5% CO_2 with 100 μL of MTT solution (at a dilution 1:20 in medium). The formazan crystals produced by the dehydrogenase mitochondrial activity of living cells were dissolved in 100 μL DMSO, and the absorbance at 550 nm of the MTT product was measured in a microplate reader (Genios Pro, TECAN). Cell viability is expressed as a percentage of absorbance of treated cells related to the untreated control cells and represented as mean of quadruplicates ± standard deviation (SD).

Imaging. Cells were imaged employing a confocal laser scanning microscope (CLSM 510 Meta) from Zeiss, and using a Plan-Apochromat 63x/1.4 M27 oil immersion objective. QD_F internalized by cells were excited with a 405 nm laser diode, and their fluorescence emission was collected in the range 420–500 nm. Transmission images were also collected.

Results and Discussion

The fluorinated-capped CdSe/ZnS QDs will be referred herein as QD_F. The inorganic core of the QD_F has a diameter of 5.5 ± 0.3 nm as measured for Transmission Electron Microscopy (TEM), see Fig. 1A. The molecular structure of the DPPC phospholipid and the fluorinated capping ligand for the QD_F are shown in Fig. 1B. In contrast to either purely hydrophobic or hydrophilic ligands, this fluorinated capping agent was purposefully designed to provide the QD_F with a significant surface activity, aimed at improving the cell uptake. The QD_F was studied in a cospread solution with the DPPC molecules to build a Langmuir monolayer with the DPPC molecules in close contact with the QD_F. The impact of the QD_F at the phospholipid interface on the DPPC molecules was significant, see Fig. 2A. A modification of the surface pressure-molecular area isotherm was observed with respect to the isotherm for the pure DPPC monolayer.[15] Two main regions of the DPPC:QD_F isotherm might be defined. Firstly, an expansion of the DPPC:QD_F isotherm with respect to the pure DPPC could be observed at values of

surface pressure lower than *ca.* 23 mN/m. This expansion of the DPPC isotherm in presence of the QD_F indicated the occupancy of the monolayer by the QD_F similarly to organic molecules as thymol.[16] The interaction between the QD_F and the DPPC molecules occurred mainly at the hydrophobic region of the monolayer. This interaction modified the physical state of the alkyl chains of the DPPC phospholipids, see below.[17] The lateral repulsion between adjacent molecules existing in the supramolecular structure might contribute as well to the expansion of the isotherm. An intercrossing of the isotherms took place at *ca.* 23 mN/m.

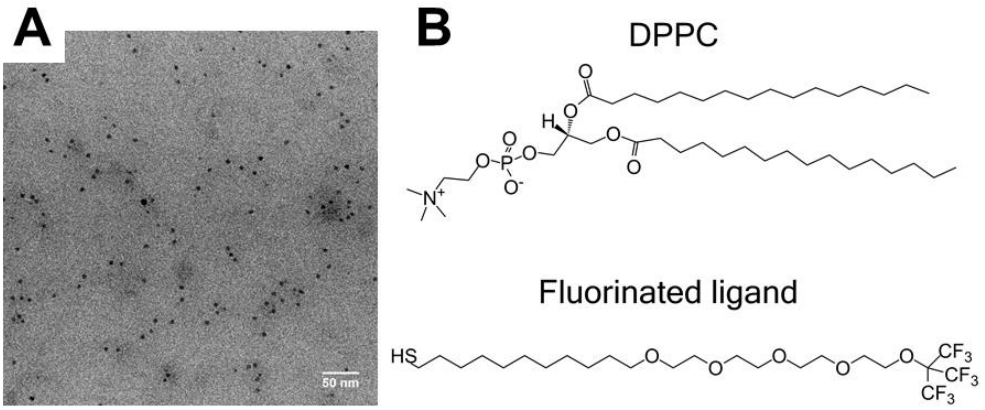

Fig. 1. A) Transmission electron microscopy of fluorinated CdSe/ZnS quantum dots (QD_F). B) Molecular structure of the DPPC phospholipid used herein as model lipid and the fluorinated ligand for capping the CdSe/ZnS quantum dots.

Secondly, a decrease in the molecular area of the DPPC:QD_F isotherm with respect to the DPPC was obtained for values of surface pressure greater than 23 mN/m. This modification of the surface pressure-molecular area isotherm was ascribed to a condensation of the phospholipid monolayer.[18] QD_F could be expelled from the DPPC monolayer upon further compression, sitting on the alkyl chains of the compressed DPPC monolayer. The strong hydrophobicity of the QD_F provoked the removal of DPPC molecules from the air/water interface to the surface of the QD_F. Computer simulations further confirmed the interdigitation of the DPPC

molecules and the fluorinated ligand of the QD_F, see below. A reduction of the effective number of DPPC molecules at the air/water interface was then obtained upon the intercrossing of the surface pressure-molecular area isotherms of DPPC and DPPC:QD_F, see Fig. 2. An early collapse was obtained upon further compression of the DPPC monolayer.

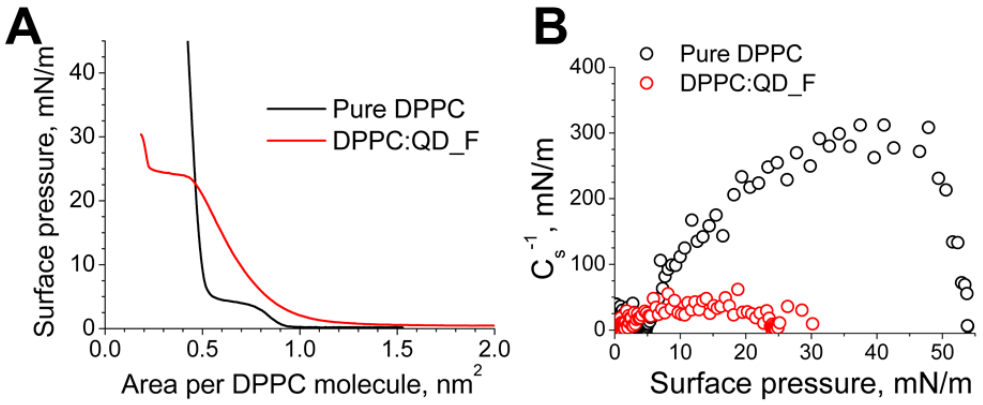

Fig. 2. A) Surface pressure-molecular area isotherms for the DPPC monolayer (black line) and a DPPC monolayer cospread with the QD_F (red line) on pure water as a subphase. B) Compression modulus values versus surface pressure for both isotherms, as noted in the inset. (For interpretation of the references to colour in this figure legend, the reader is referred to the web version of this article.)

Compression modulus is defined as $C_s^{-1} = -(d\pi/dA)$, offering a quantitative indication on the physical state of the DPPC monolayer.[19] Liquid-expanded (LE) state of the monolayers is defined for values of compression modulus in the range from 10 to 50 mN/m, obtained for the DPPC monolayer from the offset of the surface pressure up to *ca.* 10 mN/m. A liquid-condensed (LC) state is expected for values of compression modulus between 100 and 250 mN/m, obtained for the DPPC monolayer in the range of values of surface pressure from *ca.* 10 to 25 mN/m. Further compression of the DPPC monolayer resulted in the so-called solid phase, with values greater than 250 mN/m up to the collapse of the DPPC monolayer. Such

behavior is expected for a pure DPPC monolayer.[15] The interactions between the QD_F and DPPC molecules were significant, as suggested by the isotherms and confirmed by the compression modulus, see Fig. 2B. A significant fluidization of the DPPC monolayer was obtained in the presence of QD_F. The values of the compression modulus were restricted below 50 mN/m along the complete surface pressure-molecular area isotherm. Therefore the ordering of the alkyl chains of the DPPC was highly disrupted by the presence of the QD_F at the phospholipid interface.

Brewster Angle Microscopy (BAM) allows in situ monitoring the formation of different phases and segregation processes at the phospholipid monolayers.[20] The expected domains for the LE/LC phase transition were obtained in the BAM images for the DPPC monolayer, see Fig. 3, top. These domains were similar to those previously pub- lished in the literature.[21] The morphology of the DPPC monolayer was greatly modified by the presence of the QD_F along the complete surface pressure-molecular area isotherm, see Fig. 3, bottom. Bright and small structures with no defined shape were present already at low values of surface pressure, being assigned to aggregates of QD_F. The surface activity of QD_F led to the presence of the bright aggregates together with the DPPC molecules regardless of the surface pressure value. The high brilliance of the aggregates of the QD_F with the DPPC molecules arised from the absorption at 532 nm and high electronic density of the QD_F, causing the enhanced reflection of incoming radiation at the interface.[22] The mixed structures of DPPC and QD_F were relatively ordered at the interface and do not coalesce upon compression of the monolayer. Thus a restricted attractive interaction between the aggregates of DPPC and QD_F was expected, leading to a disordering effect to the DPPC monolayer.[23] The absence of coalescence of the QD_F aggregates was consistent with the adsorption of DPPC molecules onto the surface of the QD_F. Further aggregation and growth of a solid phase of QD_F was then prevented by the surrounding DPPC molecules.

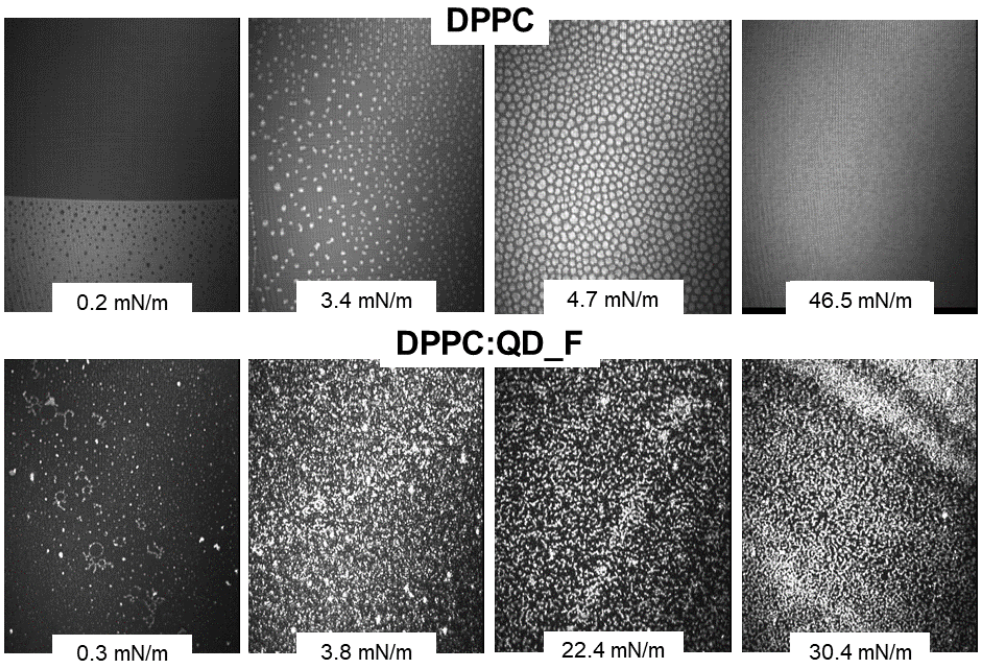

Fig. 3. Brewster Angle Microscopy pictures of the DPPC (top) and a DPPC monolayer cospread with the QD_F (bottom) monolayer on pure water as a subphase. The values of surface pressure for each picture is indicated in the inset. Scale bars equals to 100 μm.

The morphology observed by BAM was consistent with the thermodynamical insights obtained by the surface pressure-molecular area isotherms and compression modulus, see above. The hydrophobic interactions between the alkyl chains of the DPPC monolayers were not able to maintain the monolayer structure of the pure DPPC when the QD_F were present at the interface, due to the significant interactions with the QD_F. The hydrophobic interactions between the QD_F and the QD_F with the DPPC molecules determined the structuring of the DPPC:QD_F monolayer.[24]

The amount of QD_F present at the phospholipid interface could be quantitatively monitored by in situ UV-vis reflection spectroscopy at the air/water interface.[25] The UV-vis band at the air/water interface confirmed the aggregation of the QD_F at the DPPC monolayer when compared to the UV-vis absorption spectrum recorded for a

bulk solution of QD_F, see Fig. 4A. The 2D aggregation of the QD_F at the air/ water interface caused a shift and broadening of the UV–vis bands. An increase of the intensity in the reflection band with compression of the monolayer was recorded, as expected from the increase on the surface concentration of QD_F.[26]

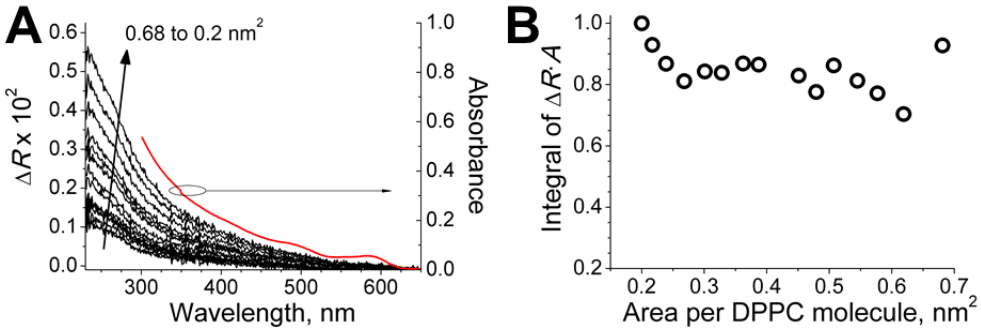

Fig. 4. A) UV–vis reflection spectra of the DPPC monolayer cospread with the QD_F at different values of surface area from 0.68 to 0.2 nm^2 per DPPC molecule, as indicated in the figure (black lines, left axis). UV-vis absorption spectrum of the CdSe/ZnS quantum dots in bulk solution (red line, right axis). B) Values of integrated UV-vis reflection spectra band normalized per surface area as a function of the area per DPPC molecule.

The normalized UV–vis reflection signal (ΔR_{norm}) to the available surface area per DPPC molecule is defined in eq. (1):

$$\Delta R_{norm} = A_{DPPC}\, x\, \Delta R = \frac{2.303 \cdot 10^{17} f_0 \varepsilon}{N_A} \sqrt{R_S} \qquad (1)$$

where ΔR_{norm} represents the normalized UV-vis reflection signal, obtained as the product of the measured absolute UV-vis reflection signal by the available surface area of the DPPC molecules. ε and f_0 denote the absorption coefficient and an orientation factor accounting for a given preferred orientation of the QD_F, respectively. Note that in this case the $f_0 = 1$, given the spherical shape of the QD_F. The integral value of the normalized UV–vis reflection band could be used to

monitor the evolution of the amount of QD_F at the interface with the compression of the DPPC monolayer. This amount of QD_F was expressed relatively to the maximum amount of QD_F at the phospholipid interface, see Fig. 4B. ΔR_{norm} would have a value of unity along the isotherm in case of a constant amount of QD_F at the interface per DPPC molecule, which was not the experimental result. Upon compression of the monolayer, the interaction of the QD_F with the phospholipid molecules was increased, achieving the maximum density of QD_F for a highly compressed DPPC monolayer. The DPPC monolayer in such solid state offered a highly dense surface of hydrophobic chains to interact with the QD_F. Note that at least 80% of the QD_F were present at the phospholipid interface along the complete surface pressure-molecular area, confirming a significant surface activity of the QD_F. The remaining fraction of added QD_F were assumed to be present in the subphase as assemblies.[6] Two minima in the ΔR_{norm} values were observed at *ca.* 0.48 and 0.27 nm^2 per DPPC molecule. These ΔR_{norm} minima appeared at the initial and final points of almost constant surface pressure with reduction of the molecular area in the DPPC:QD_F isotherm, see above. Thus, a rearrangement of the DPPC molecules in this region was expected, probably corresponding to the mentioned adsorption of DPPC molecules onto the QD_F. Note that with the compression of the DPPC monolayer, QD_F diffused towards the monolayer, effectively interacting with the DPPC molecules. Due to the fluidization of the DPPC monolayer provoked by the QD_F, the maximum surface density of QD_F was achieved for values of surface pressure close to 30 mN/m, taken as the equivalent pressure for a monolayer to a biological membrane.[27,28] The QD_F were therefore able to effectively exert a significant fluidization of the DPPC monolayer. The maximum surface density of QD_F in contact with the DPPC monolayer was achieved for values of surface pressure close to 30 mN/ m as suggested by the BAM pictures and further confirmed by the UV-vis reflection spectra.

Molecular dynamics simulations were performed to attain atomistic insights into the interaction of the fluorinated ligand of the QD_F with the DPPC phospholipid molecules.[29] The computational box is shown in Fig. 5A, displaying the fluorinated

ligand molecules in contact with a DPPC molecule. Surprisingly, the interaction of the fluorinated ligands with the hydrophobic tails of the DPPC molecules resulted in the inclusion of the alkyl chains into the layer of the fluorinated ligand. The polar headgroup of the DPPC molecule remained in contact with the water layer. The tilting angle of the polar headgroup is the vector defined by the P–N atoms with respect to the alkyl chains, reaching a value of 73.1°, see Fig. 5B. A significant modification with respect to the expected value of *ca.* 90° was therefore found.[30] The distribution of the fluorine atoms along the Z axis showed a maximum peak toward the outer region of the coating ligands as expected, see Fig. 5C. The average position of the O atoms of the fluorinated ligand showed an almost constant interatomic distance. Remarkably, a significant hydration of the O atoms of the fluorinated ligand was found. The number of H-bonds formed by the O atoms and water molecules from the inner to outer O atoms were 2.2, 1.8, 1.9, 1.4 and 0.4, respectively. The relatively hydrophilic region formed by the hydrated atoms O of the fluorinated ligand was able to accommodate the polar layer of the DPPC molecule including the carbonyl and ester oxygen. The repulsion of the polar headgroup of the DPPC molecule and the F atoms of the capping ligand led to the observed modification of the P–N tilting angle, as commented above. The sum of hydrophobic and polar interactions between the fluorinated ligand and the DPPC molecules resulted in the experimentally observed modification of the DPPC monolayer by the QD_F. The inclusion of the DPPC molecules onto the coating layer of the QD_F could result in the effective removal of DPPC molecules from the monolayer for a compression of the monolayer beyond surface pressure values of *ca.* 23 mN/m, as indicated by the surface pressure-molecular area isotherms.

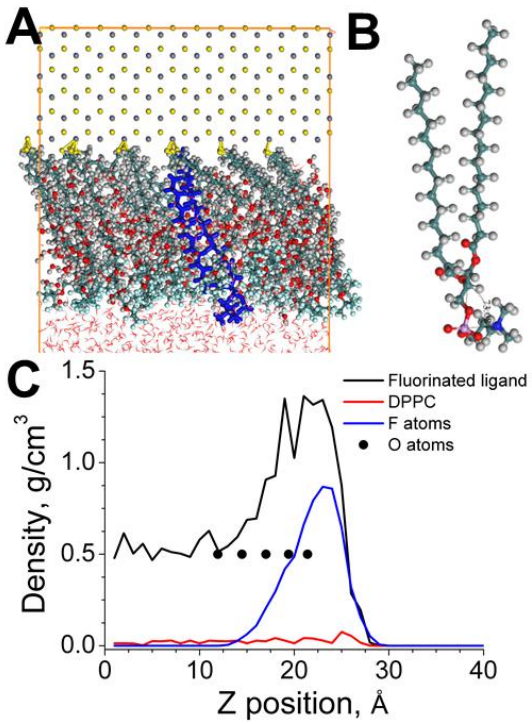

Fig. 5. A) Snapshot of the DPPC molecule in contact with the surface of the QD_F. Top region depicts the inorganic surface. The fluorinated ligands are displayed in green (C atoms), red (O atoms) and light blue (F atoms). The DPPC molecule is highlighted in blue for clarity. Bottom region shows the water molecules. B) Snapshot of the DPPC molecule displaying a tilting angle of the headgroup of 73.1°. C) Distribution of the fluorinated ligand, DPPC, and average position of the oxygen and fluorine atoms along the axis perpendicular to the DPPC monolayer. Zero was placed in the surface of the QD_F.

In vitro cell uptake and imaging experiments were conducted to obtain insights on the interaction of the QD_F with living cells, using HeLa cells as model cell line.[31] The cell viability was decreased to *ca.* 85% after 5 h of incubation with QD_F. A further decrease to *ca.* 75% was obtained after 24 h of incubation, see Fig. 6. DMSO was required to disperse QD_F and perform the cell studies. The contribution by the DMSO solvent to the reduction in cell viability was rather low. Incubation time for imaging experiments was 5 h, rendering a significant uptake of QD_F by the HeLa cells. Confocal fluorescence microscopy showed a significant uptake of QD_F by

the HeLa cells, see Fig. 6.[32]

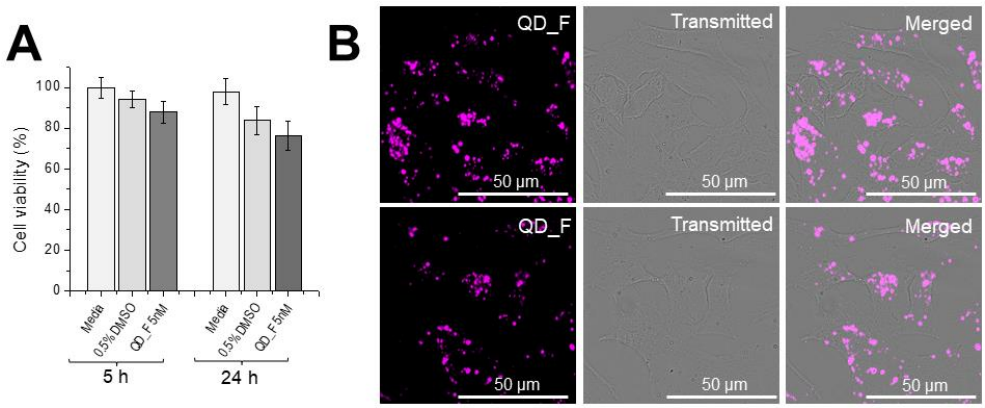

Fig. 6. A) Cell viability obtained by MTT assay of HeLa cells incubated for either 5 h or 24 h with 0.5% DMSO or QD_F at 5 nM. QD_F were dispersed in serum-free cell medium containing 0.5% DMSO. B) Confocal microscopy images of HeLa cells after incubation for 5 h at 37 °C with 5 nM of QD_F NPs. Incubation was performed in serum-free DMEM cell media containing 0.5% of DMSO. Fluorescence channel was collected at 420–500 nm (λ_{exc} 405 nm). Single fluorescence channel and merged with the transmitted light channel are shown.

Conclusions

The interaction of the fluorinated CdSe/ZnS quantum dot (QD_F) with model cell membranes has been characterized in large detail by using a model DPPC phospholipid Langmuir monolayer. The surface pressure-molecular area isotherms point to a fluidization of the DPPC molecules induced by the presence and effective interaction of the QD_F at the DPPC phospholipid monolayer. In situ UV-vis reflection spectroscopy and Brewster Angle Microscopy could confirm the occupancy of the DPPC monolayer by the QD_F and the removal of DPPC molecules to the surface of the QD_F. Molecular dynamics simulations have demonstrated the inclusion of the alkyl chains of the DPPC in the defects of the capped surface of the QD_F. In vitro experiments with living cells showed excellent uptake of the QD_F. As a result of the fluidization of the alkyl chains due to the

significant interaction of the QD_F with the phospholipid molecules, the mechanism of uptake is proposed as passage of the QD_F through the membrane promoted by hydrophobic interactions. This work suggests that fluorination of the capping ligands of inorganic quantum dots may be a suitable and universal route for enhancing their cell uptake, potentially increasing the biological and clinical application of inorganic quantum dots.

References and Notes

1. M. Liu, O. Voznyy, R. Sabatini, F.P. García de Arquer, R. Munir, A.H. Balawi, X. Lan, F. Fan, G. Walters, A.R. Kirmani, S. Hoogland, F. Laquai, A. Amassian, E.H. Sargent, *Nat. Mater*. **2017**, 16, 258–263.
2. J. Owen, L. Brus, *J. Am. Chem. Soc*. **2017**, 139, 10939–10943.
3. B. Yang, B. Chen, M. He, B. Hu, *Anal. Chem*. **2017**, 89, 1879–1886.
4. H.Y. Yang, Y. Fu, M.-S. Jang, Y. Li, W.P. Yin, T.K. Ahn, J.H. Lee, H. Chae, D.S. Lee, *Colloids Surf., B* **2017**, 155,497–506.
5. Giner-Casares, M. Henriksen-Lacey, M. Coronado-Puchau, L.M. Liz-Marzán, *Mater. Today* **2016**, 19, 19–28.
6. C. Carrillo-Carrión, M. Atabakhshi-Kashi, M.M. Carril, K. Khajeh, W.J. Parak, *Angew. Chem. Int. Ed*. **2018**, 57, 5033–5036.
7. K.D. de Souza, K.R. Perez, N. Durán, G.Z. Justo, L. Caseli, *Colloids Surf., B* **2017**, 160, 247–253.
8. J.J. Giner-Casares, G. Brezesinski, H. Möhwald, *Curr. Opin. Colloid Interface Sci*. **2014**, 19, 176–182.
9. A.C. Alves, C. Nunes, J. Lima, S. Reis, *Colloids Surf., B* **2017**, 160, 610–618.
10. D. Lopes, C. Nunes, P. Fontaine, B. Sarmento, S. Reis, *Biochim. Biophys. Acta - Biomembr*. **2017**, 1859, 803–812.
11. Fábio de Paula Ayoub, L. Caseli, *Colloids Surf., B* **2017**, 150, 8–14.
12. S.M. Bradford, E.A. Fisher, M.-V. Meli, *Langmuir* **2016**, 32, 9790–9796.
13. A. Raveendran, C. DeWolf, W. Bu, S. McWhirter, M. Meron, B. Lin, M.-V. Meli, *J. Phys. Chem. C* **2018**, 122, 2975–2982.
14. O. Michelena, D. Padro, C. Carrillo-Carrión, P. del Pino, J. Blanco, B. Arnaiz, W.J. Parak, M. Carril, *Chem. Commun*. **2017**, 53, 2447–2450.
15. A. Aroti, E. Leontidis, E. Maltseva, G. Brezesinski, *J. Phys. Chem. B* **2004**, 108, 15238–15245.
16. J.V.N. Ferreira, T.M. Capello, L.J.A. Siqueira, J.H.G. Lago, L. Caseli, *Langmuir* **2016**, 32 (13), 3234–3241

Journal of COLLOID AND INTERFACE SCIENCE

Published on 16 Nov 2018

DOI: 10.1016/j.jcis.2018.11.036

Folding of cytosine-based nucleolipid monolayer by guanine recognition at the air-water interface

Pablo G. Argudo, Eulogia Muñoz, Juan José Giner-Casares, María Teresa Martín-Romero*, Luis Camacho

Institute of Fine Chemistry and Nanochemistry, Department of Physical Chemistry and Applied Thermodynamics, University of Córdoba, Campus Universitario de Rabanales, Edificio Marie Curie, Córdoba, 14014, Spain

Monolayers of a cytosine-based nucleolipid (1,2-dipalmitoyl-sn-glycero-3-(cytidine diphosphate) (ammonium salt), CDP-DG) at basic subphase have been prepared at the air-water interface both in absence and presence of guanine. The formation of the complementary base pairing is demonstrated by combining surface experimental techniques, *i.e.*, surface pressure (p)–area (A), Brewster angle microscopy (BAM), infrared spectroscopy (PM-IRRAS) and computer simulations. A folding of the cytosinebased nucleolipid molecules forming monolayer at the air-water interface occurs during the guanine recognition as absorbate host and is kept during several compression-expansion processes under set experimental conditions. The specificity between nitrogenous bases has been also registered. Finally, mixed monolayers of CDP-DG and a phospholipid (1,2-dimyristoyl-sn-glycero-3-phosphate (sodium salt), DMPA has been studied and a molecular segregation of the DMPA) molecules has been inferred by the additivity rule.

Introduction

Biorecognition of nucleic acids is a central process in life. Consequently, in the last decades DNA and RNA nanothecnology has attracted great interest from many researchers working in the design of well-defined nanostructures for potential applications. On this framework, to produce new materials, electronic nanodevices, and biosensors novel strategies have been extensively investigated. Self-assembly of cytosine, thymine, adenine, and uracil has been explored on solid surfaces revealing the formation of 1D and 2D supramolecular nanostructures[1], aggregates highly fluorescent[2], efficient sensors to distinguish the unique pattern of viral nucleic acid/bacterial fragments[3], new nucleic acid-based carrier systems to improve the drug action [4], combination of nucleic acid derivatives with lipids rendering hybrid materials as promising supramolecular materials for biomedical and technological applications[5], fabrication of supramolecular gels formed by nucleic acid-based hydrogels to design particular type of gelators[6], scanning of RNA nano-bio interface by functionalized nanoparticles (NPs) to inquire on the RNA nano-bio interaction[7], or nucleic acids-modified NPs to improve the drug delivery and its efficiency[8].

The performance of most those new nucleic acid-based nanoarchitectures to different applications are ground on the molecular recognition between nucleobases in DNA and RNA. It is a fact that molecular recognition is one of the most significant chemical occurrences not only in supramolecular chemistry[9], but also in biochemical frameworks[10]. Particularly, recognition of nucleobases in DNA and RNA is crucial in genetic transmission and protein expression: DNA makes RNA and RNA makes protein. In such cases, nucleobase pairing occurs because complementary hydrogen bonding. In this context, a stimulus established during the last decades has been the design of artificial recognition systems in solution[11], or interfaces[12]. In the last case, different strategies have been designed to analyse and mimicry of the molecular recognition and differentiation between structurally almost identical molecules as nucleic acids at air-water interface. Thus, quite simple host molecules have been mechanically adapted at the air-water interface and this relatively simple implement has allowed the chiral recognition of amino acids by applying mechanical forces to

host monolayers prepared at the air-water interface[13,14]. Furthermore, mechanical tuning of host structure for optimization of molecular recognition tenders an appropriate methodology in host-guest chemistry[15].

The Langmuir monolayers at the air-water interface afford unique frame for molecular interactions and accordingly molecular recognition[16]. To construct superlattice materials whose structure is controlled at molecular level, the air-water interface is expected to offer a model environment for preparing films with controlled 2D framework by an appropriate matrix and under external control like surface pressure.

Nucleolipids are functionalized lipids with nucleosides or nucleotides moieties[17,18]. In aqueous environment, due to additional specific contributions of the polar heads to intermolecular interactions, *i.e.*, π-stacking and hydrogen bonds, the presence of a bioinspired functional polar headgroup affects the self-assembly properties, and therefore this type of molecules had been extensively studied over the past years[19].

Molecular recognition at the air-water interface between nucleolipids and their complementary bases dissolved in the subphase, has been widely studied and focused upon adenine and uracil/thymine moieties in nucleolipids and also cytosine- and guanine-functionalized nucleolipids by surface experimental techniques[20-26]. On this framework, the present work presents an approach combining experimental techniques, by surface pressure-area (π–A) isotherms, Brewster angle microscopy (BAM) and polarization-modulation infrared spectroscopy infrared sprectroscopy (PM-IRRAS), with molecular dynamics (MD) simulation techniques. This approach allows to describe in more detail the molecular recognition between cytosine and guanine molecules in an architecture prepared at the air-water interface by using a novel chemical system. Therefore, monolayers of cytosine-functionalized nucleolipid (CDP-DG) have been fabricated at the air-water interface where the aqueous subphase solves the complementary nitrogenous base at basic pH. Under compression, the molecular organization of cytosine-based nucleolipid (CDP-DG) monolayer is influenced by guanine presence in the subphase. The formation of the

complementary base paring in a monolayer is demonstrated and described by the combination of experimental and simulation techniques. The molecular organization implies a folding of the cytosine-based nucleolipid molecules in the monolayer during the guanine recognition. Furthermore, the molecular assembled is reproducible during several compression-expansion processes under set experimental conditions. Finally, mixed monolayers of CDP-DG and a phospholipid (DMPA) have been studied and a molecular segregation of DMPA molecules has been inferred by the additivity rule.

Experimental section

Materials. The nucleolipid 1,2-dipalmitoyl-sn-glycero-3-(cytidine diphosphate) (ammonium salt) powder (≥ 99%), CDP-DG, and phospholipid 1,2-dimyristoyl-sn-glycero-3-phosphate (sodium salt) (≥ 99%), DMPA, were purchased from Avanti Polar Lipids and used as received. The purine bases, guanine hydrochloride (> 99%) and adenine (98%) were obtained from Merck and used as well.

The basic subphase at pH 11 was adjusted by NaOH (> 99%) and supplied from Merck. The solutions for CDP-DG and DMPA were prepared in chloroform and $CHCl_3/CH_3OH$ 3/1, respectively, and used as spreading solvents. The pure solvents (Chromasol V® Plus) were purchased from Sigma Aldrich and used without further purification. Ultrapure water, produced by a Millipore Milli-Q unit, pre-treated by a Millipore reverse osmosis system (> 18.2 MΩ · cm), was used as a subphase. The subphase temperature was kept at 21 °C.

Methods. Two different models of Nima troughs (Nima Technology, Coventry, England) were used in this work, both provided with a Wilhelmy type dynamometric system using a strip of filter paper: a NIMA 611D with one moving barrier for the measurement of surface pressure (π)–area (A) isotherms and compression–expansion cycles, and a NIMA 601, equipped with two symmetrical barriers to record BAM images. The pure and mixed monolayers were compressed at a speed of 0.035–0.05 $nm^2 \cdot min^{-1} \cdot molecule^{-1}$.

Images of the film morphology were obtained by Brewster angle microscopy

(BAM) with a I-Elli2000 (Accurion GmbH, Germany) using a Nd:YAG diode laser with wavelength 532 nm and 50 mW, which can be recorded with a lateral resolution of 2 μm. The image processing procedure included a geometrical correction of the image, as well as a filtering operation to reduce interference fringes and noise. The microscope and the film balance were located on a table with vibration isolation (antivibration system MOD-2S, Accurion, Göttingen, Germany).

Monolayers of CDP-DG prepared on basic subphase at pH 11 in presence and absence of guanine were transferred onto glass substrates by Langmuir-Schaefer (LS) technique, *i.e.*, by horizontal touching method, at constant surface pressure ($\pi = 27$ mN/m). Therefore, multilayers (10 layers) by sequential monolayer transfer were assembled. The transfer ratio was closed to unity for all transferences.

Polarization-modulation infrared reflection absorption spectroscopy (PM-IRRAS) was performed using a KSV PMI 550 instrument (KSV, Biolin Scientific Oy, Helsinki, Finland), and equipped with a highly sensitive MCT-detector and ZnSe photoelastic modulator. The Langmuir trough was mounted so that the light beam reached the LS films at a fixed incidence angle of 76°. The incoming light is continuously modulated between s and p polarization at a high frequency. This allows the simultaneous measurement of spectra for the two polarizations, s and p, thus the effect of water vapor is largely reduced. In such a way, the PM-IRRAS signal (S) is the difference between s and p spectra, *i.e.* $S = \Delta R/R = (R_p - R_s)/(R_p + R_s)$, where R_p and R_s are the parallel p–and perpendicular s–polarized reflectances, respectively. The background spectrum of an uncoated glass substrate was recorded as the reference. In all the cases, the final spectrum was obtained by means of the accumulation of 600 scans. The spectra were recorded with 8 cm^{-1} resolution. All the experiments were done in a large class 100 clean room at the temperature of 21 °C.

Computer simulations. Molecular mechanics (MM) and molecular dynamics (MD) calculations were performed by using Forcite with Dreiding force field. The charge was incorporated by using Charge equilibration (QEq). A cutoff of 1.85 nm was used to calculate the LJ interactions and short-range electrostatic interactions.

For each MD simulation, the procedure was started with an optimized geometry followed by 20 ps of NVT dynamics to heat the system to 298 K. Finally, after each MD simulation, the geometry was again optimized. This routine was repeated at least 3 times for each system.

3D Periodical conditions were considered as follows: two lipid leaflets confining a water layer and forming a sandwich structure in which the lipid heads point toward the water layer with different orientations. The absence of interactions between the two lipid leaflets along the z axis was achieved by introducing an empty gap of 2–4 nm, as a function of surface area, above and below each lipid layers. The final dimensions of the computing box along z axes was 12.5 nm.

Results and Discussion

Surface pressure (π)–area (A) isotherms of CDP-DG nucleolipid at the air/water interface on different aqueous subphases. CDP-DG nucleolipid is a hybrid molecule composed of a nucleotide (cytidine diphosphate) and a lipophilic moiety (dipalmitoyl derivative acid), see molecular structure in Scheme 1. Such structure is expected to be able for lateral recognition of the complementary base pairing, that is, guanine in the subphase[27].

Accordingly, its surface behaviour has been studied at the air/water interface by means of Langmuir technique. Therefore, CDP-DG films were prepared at the air–water interface and π–A isotherms were registered on different aqueous subphases: pure water at pH 5.5, basic subphase at pH 11 both in absence and presence of guanine, and in presence of adenine. Such subphases has been set on basis of optimal solubility conditions for the complementary purine base, *i.e.*, guanine.

Fig. 1 shows the π–A isotherms under compression for a CDP-DG monolayer on water pH 5.5 (black line), basic subphase pH 11 in absence of guanine (red line) and basic subphase pH 11 containing guanine 10−4 M (green line).

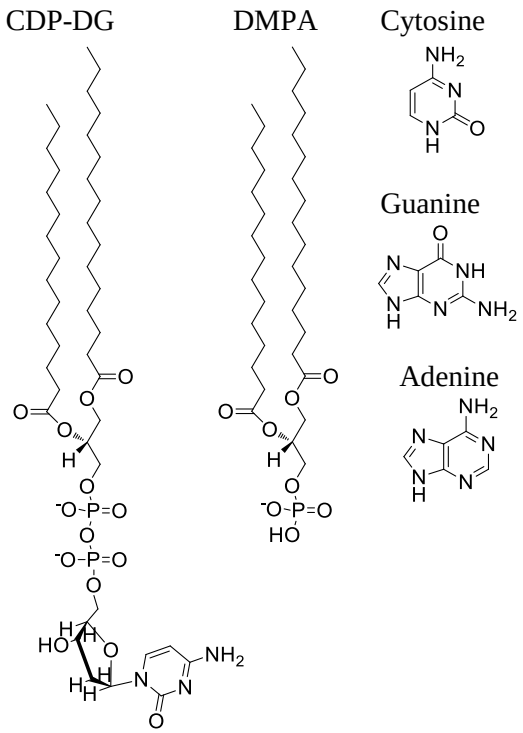

Scheme 1. Molecular structures of 1,2-dipalmitoyl-sn-glycero-3-(cytidine diphosphate), CDP-DG, dimyristoylphosphatidic Acid, DMPA, and purine and nitrogenous bases: cytosine, guanine and adenine.

As can be seen, in absence of purine base, an increase of subphase pH leads to two phenomena: (1) an expansion of the molecular area and (2) a shift of the phase transition from 75 $Å^2$/molecule and 20 mN/m for the film on pure water at neutral pH, up to around 85 $Å^2$/molecule and 30 mN/m on basic subphase at pH 11. Moreover, the presence of the guanine in the subphase (Fig. 1, green line) produces outstanding effects on the CDP-DG matrix as show the registered isotherms: (i) the π–A isotherm converges to that obtained on water pH 5.5 at very low ($\pi < 5$ mN/m) and high surface pressures ($25 < \pi < 35$ mN/m); (ii) two phase transitions are clearly distinguished, at low surface pressures ($5 < \pi < 10$ mN/m) and high surface pressures ($\pi > 35$ mN/m).

Furthermore, as molecular recognition control, the π–A isotherm of the CDP-DG

monolayer on aqueous subphase containing 10^{-4} M adenine was run. The π–A isotherm (Fig. 1, blue line) shows convergence at low and high surface pressures with the isotherm obtained in absence of nitrogenous base (Fig. 1, red line) and any phase transitions. These results are indicative of any interaction between cytosine group of nucleolipid and adenine, as expected.

By comparison such π–A isotherms obtained on water subphase in absence of guanine (Fig. 1, black line) and that on pH 11 and 10^{-4} M guanine (Fig. 1, green line), the phase transition registered at around 5 mN/m could be related to that observed on water, although is shifted to high surface area and low surface pressure. However, the phase transition at high surface pressures can be related to a molecular recognition between the cytosine group of the nucleolipid monolayer and the guanine molecules in the basic subphase.

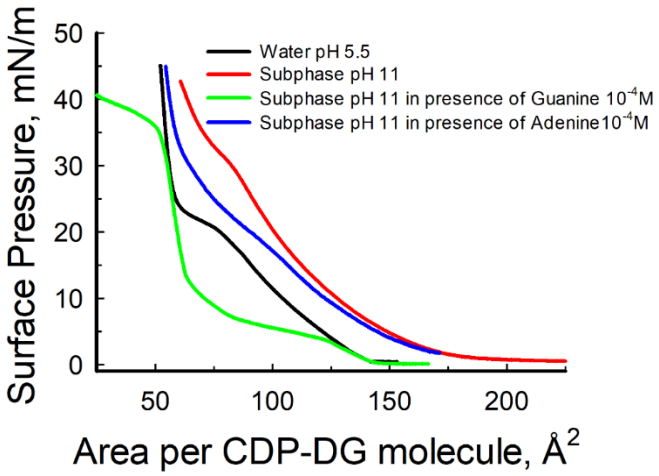

Fig 1. π–A isotherms of a CDP-DG monolayer prepared at air/water interface on different subphases: water (black line) and basic subphase pH 11 in absence (red line) and presence of purine bases, Guanine (green line) and Adenine (blue line), respectively.

Simultaneously to the π–A isotherms during the compression process, the morphological structure of the CDP-DG film at different subphases, has been directly visualized by BAM. The BAM images are shown in Fig. 2.

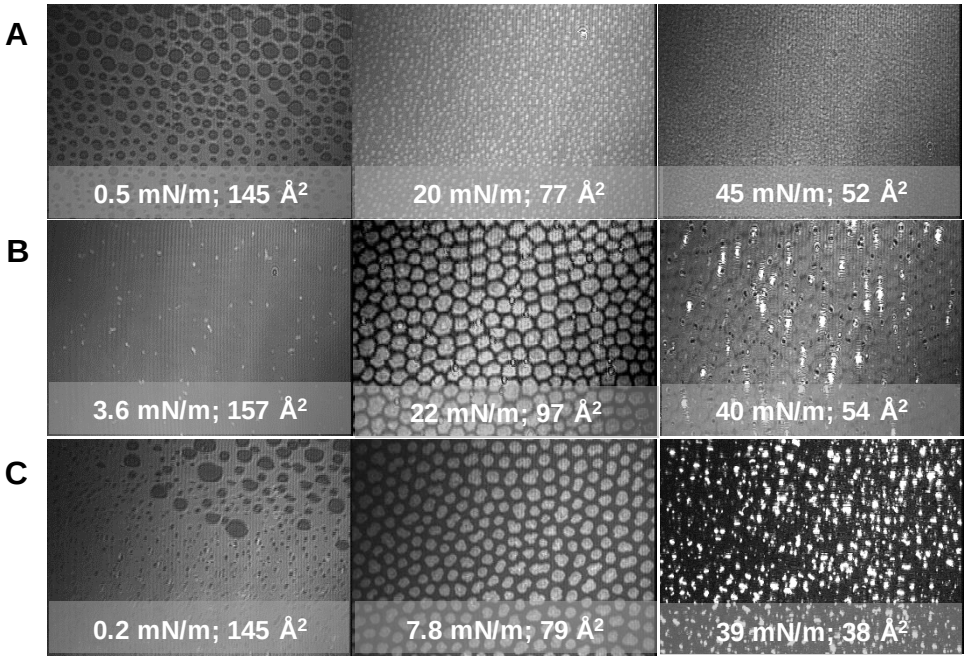

Fig. 2. BAM images of a CDP-DG monolayer prepared on different subphases: A) pure water pH 5.5; B) basic subphase pH 11 in absence of guanine; C) basic subphase pH 11 containing guanine 10^{-4} M. The molecular areas indicated in the images are expressed per CDP-DG molecule. Image width: 430 μm.

Fig. 2 shows the morphological features of the CDP-CG monolayer under compression on different aqueous subphases: the upper row shows the behaviour on pure water, the middle one corresponds to basic subphase pH 11, and the lower one to the presence of 10^{-4} M guanine.

On pure water (Fig. 2A), and at low surface pressure a gas phase is clearly observed and under compression the CDP-DG molecules form small circular domains that fused at high surface pressure. However, when the subphase pH increases (Fig. 2B), some small bright spots are detected at very large molecular areas and under compression irregular domains are formed until covering all the focused area. A behaviour in between those above is observed when guanine is present in the basic subphase (Fig. 2C), that is, gas phase at low surface pressure, formation of small irregular domains during the first phase transition and covering

all the focus area with a monolayer where many bright spots emerge during the second phase transition.

BAM images, as described previously from the π–A isotherm results, also show the different behaviour of the CDP-DG monolayer as a function of the subphase pH and notoriously different when guanine molecules are in the basic subphase. Details of the morphological characteristics of the CDP-DG film on basic subphase in presence of guanine during the compression process up to the collapse are given in SI1 (Supporting Information, SI).

As discussed above, the second phase transition registered at the π–A isotherm of the nucleolipid matrix on basic subphase containing guanine 10^{-4} M can be due to the specific interaction between guanine and cytosine, that occurs at high surface pressure. Therefore, to infer on this phenomenon, two compression-expansion cycles of a CDP-DG monolayer reaching the collapse at approximately 30 mN/m and 50 $Å^2$/molecule, were performed. The results are shown in Fig. 3.

Fig. 3 shows a great hysteresis between 1st and 2nd compression cycles when the collapse surface pressure is reached during the first compression process, and a significant shrinking of the isotherm during the second compression cycle is registered. This phenomenon may be ascribed to a conformational change of CDP-DG molecules arriving to the collapse surface pressure and in presence of guanine, complementary nitrogenous base of the cytosine polar group of the nucleolipid: before the collapse, the polar group of the nucleolipid molecules are oriented properly to bind the guanine molecules in basic subphase and extending their surface area. By contrary, after the collapse the polar groups of the CDP-DG molecules redirect ejecting the guanine molecules[28].

Therefore, to confirm the hypothesis above described, several bounded compression-expansion cycles have been made, and a monolayer of CDP-DG on a basic subphase pH 11 containing guanine 10^{-4} M has been compressed and expanded during three cycles up to 27 mN/m. The results are shown in Fig. 4. No hysteresis is registered. Thus, it can be confirmed that before the collapse, the orientation of the

polar group is directed to bind guanine molecules in the basic subphase.

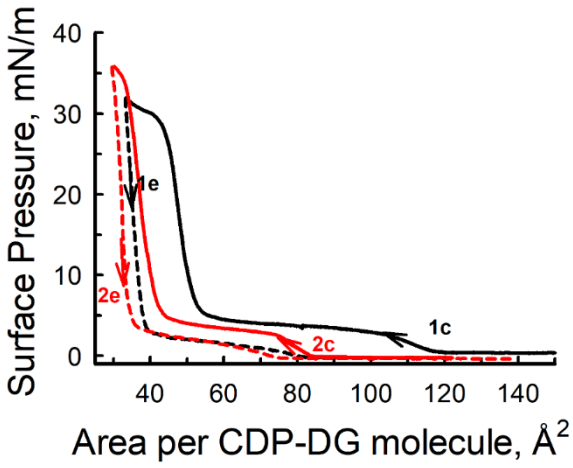

Fig. 3. Compression-Expansion cycles of a CDP-DG monolayer on a basic subphase pH 11 in presence of Guanine 10^{-4} M: 1st compression-expansion (1c-1e), black lines; 2nd compression-expansion (2c-2e), red lines.

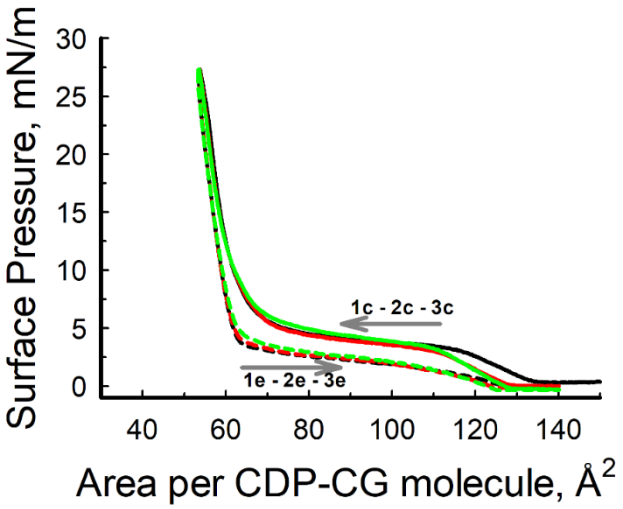

Fig. 4. Bounded expansion-compression cycles of CDP-DG on basic solution pH 11 containing Guanine 10-4M.

Details of the morphological characteristics of the CDP-DG film on basic subphase in presence of guanine during the compression process up to the surface pressure before collapse, are given in SI2. No differences between the bounded cycles were noticed.

PM-IRRAS of CDP-DG nucleolipid transferred by horizontal touching from the air/water interface to glass support. PM-IRRAS has been widely used for studying of monolayers formed by phospholipid molecules at the air-water interface[29-36] and the assignment of the corresponding bands to the different chemical groups has been described in detail, as well.

The binding of the guanine and polar group of the nucleolipid molecules is mainly due to the hydrogen bonds as expected for guanine-cytosine interaction. However, under basic conditions, subphase pH 11, which are necessary for the dissolution of guanine as absorbate, an intense negative band between 1800 and 1600 cm^{-1} in the PM-IRRAS spectra, also recorded on clean subphase (background), gives rise and it is similar to that described elsewhere[37]. This artefact makes impossible to analyze the spectral region of greatest interest at the air-water interface. Nevertheless, the existence of interactions between the nucleolipid monolayer and the guanine dissolved in the subphase can be proved on LS films once the modified substrate is rinsing with pure water to remove the large bands corresponding to water/NaOH absorption in the low wavenumber region as showed in SI3.

To confirm the binding of the guanine and polar group of the nucleolipid molecules is mainly due to the hydrogen bonds as expected for guanine-cytosine interaction, the CDG-DG film prepared on basic subphase pH 11 was transferred at constant surface pressure *ca.* 27 mN/m on glass support by Langmuir-Schaefer method, and PM-IRRAS spectra were measured.

Fig. 5 shows PM-IRRAS spectra corresponding to 10 LS layers of CDP-DG transferred from aqueous interface at pH 11 in absence (blue line) and presence (red line) of guanine, once the modified substrate has been rinsed with ultrapure water and dried under air flow, two times. Also, the selected PM-IRRAS signals of such

multilayers and their assignments are given in Table 1.

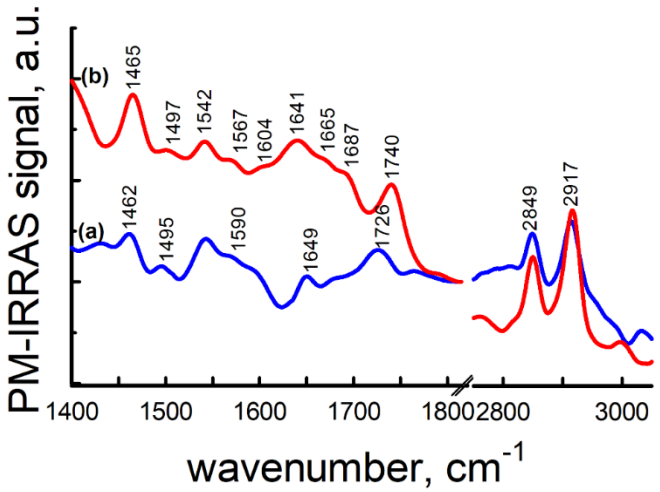

Fig. 5. PM-IRRAS spectra for 10 LS multilayers of CDP-DG film prepared at air-water interface at surface pressure *ca.* 27 mN/m and aqueous subphase pH 11: (a) in absence and (b) in presence of guanine 10^{-4} M, blue and red lines, respectively.

At high wavenumbers two characteristic signals of lipids with bands originated from C-H stretches at 2917 and 2848 cm^{-1} and assigned to the antisymmetric and symmetric CH_2 stretching modes [$\nu_a(CH_2)$ and $\nu_s(CH_2)$] of hydrocarbon chains, respectively, are detected for both films. These wavenumbers are characteristic of preferential all-trans conformers in highly ordered alkyl chains.

As previously described[39-45], the intensity of the tension vibrations of the methylene group depends on the orientation of the alkyl chains with respect to the glass substrate. However, as prepared LS CDP-DG films in the absence and presence of guanine those bands shown different height (see Fig. 5) and this fact should be mainly attributed to surface concentration rather than to orientation molecular variations (see Figure SI4). Accordingly to Fig. 1, at about 27 mN/m, the CDP-DG monolayer prepared at air/water interface on basic subphase pH 11 in absence (red line) has a larger area than that in presence of guanine (green line), about 89 vs. 57 A^2. Therefore, and taking into account that the transfer ratio of the LS films is

practically one, the surface concentration can be corrected by expressing the PM-IRRAS signal in a normalized manner, that is, multiplying the corresponding spectrum by its registered molecular area under surface pressure. Figure SI4 shows the normalized delta/sigma signal of the bands $\nu_a(CH_2)$ and $\nu_s(CH_2)$ and as can be seen for both LS films the spectra practically coincide.

Table 1. the major characteristic peaks of CDP-DG and CDP-DG/Guanine LS films and their possible assignments[a,b].

assignment	CDP-DG	CDP-DG/Guanine
$\nu_a(CH_2)$, asym stretch	2917	2917
$\nu_s(CH_2)$, sym stretch	2848	2850
ν(C=O), ester stretch	1726	1740
$\nu(C=O^{cytosine})$, stretch	1687	1689
$\nu(C=O^{guanine})$, stretch		1668
$\delta(NH_2)$, scissor mode	1649	1641
ν(C=N) + ν(C=C), ring stretch	1590	1605
ring stretch	1567, 1542, 1495	1567, 1542, 1497
$\delta(CH_2)$, scissor mode	1462	1465

[a] Band positions are given in cm^{-1}; [b] Reference Wang *et al*.[38]

At the region of low wavenumbers, a slightly different behaviour between those films is observed. Therefore, the vibrational frequency at 1726 cm^{-1} is assigned to the C=O stretching vibration [ν(C=O)], from the ester group and the band at 1462 cm^{-1} is caused by the scissor stretch of alkyl chains [$\delta(CH_2)$]. At the region 1490–1690 cm^{-1}, the small bans are related to the cytosine group stretching. Particularly, the signals at 1495, 1542 and 1567 cm^{-1} are arised from ring stretching vibration. Additionally, the shoulder at 1590 cm^{-1} is due to the coupled stretching vibration of C=N and C=C bonds in the cytosine moieties. Furthermore, the broad band detected at 1649 cm^{-1} can be mainly assigned to NH_2 scissoring vibration,

while the shoulder at 1687 cm^{-1} corresponds to the stretch mode of CO group belong to the cytosine [ν ($C=O^{cytosine}$)]. Nonetheless, both bands can be also governed by the hydrogen interactions between neighbour molecules [$C=O^{cytosine}$…H-$N^{cytosine}$-H].

By contrary, in the case of the CDP-DG multilayers fabricated from Langmuir monolayer of nucleolipid spread onto basic subphase containing guanine (Fig. 5, red line), the band at 1590 cm^{-1} vanishes and a new one at 1605 cm^{-1} emerges. This band can be related to the C=N stretching vibration links together C=C stretching modes from each cytosine and guanine rings. These different features for the two different multilayers suggest a reorganization and/or orientation change of the cytosine ring group in the nucleolipid molecule probably due to the formation of hydrogen bonds with the guanine molecules in the subphase [$C=N^{cytosine}$…H-$N^{guanine}$]. This binding is confirmed by the shift of the band at 1649 cm^{-1}–1641 cm^{-1} that notes the molecular recognition between guanine and cytosine by H-$N^{guanine}$-H…$O=C^{cytosine}$, and the appearance of a new band at 1668 cm^{-1} assigned to ν($C=O^{guanine}$) and coming from O=Cguanine…H-$N^{cytosine}$-H interaction.

Finally, it is noteworthy the shift of the C=O (ester group of the alkyl chains) stretching frequency happening from 1726 cm^{-1} to 1740 cm^{-1} when guanine molecules are in the aqueous subphase during the LS process, and corresponding to a dry ether group.

These results not only reproduce those published elsewhere[38,46], but additionally evidence the strong interaction between the ring groups of the cytosine and guanine par that leads to a framework where the orientation of the molecules in the monolayer avoids the hydration of the C=O groups during the horizontal transfer process.

Computer simulations. To predict structures and dynamics between biological adsorbed molecules and a main-group of inorganic molecules, Dreiding has been showed as a very suitable tool[47,48]. Thus, molecular mechanics calculations using the Dreiding force field were applied to self-assembled monolayer configurations of the nucleic acid base adenine adsorbed on graphite surfaces[49]. Also, Dreiding force field has been used for investigating a wide variety of DNA sequences and sizes

containing coding and non-coding, random and real, homogeneous or heterogeneous sequences in the range from 2 to 40 base pairs. Dreiding force field has been shown to improve the accuracy that the geometry of the hydrogen system adopts by using the 10–12 terms and includes the angle between the hydrogen donor (D), the hydrogen (H), and the hydrogen acceptor (A)[50]. Additionally, a series of porphyrinogens related to coproporphyrinogen-III have been modeled by molecular dynamics simulations (Dreiding force field). The results demonstrated that the porphyrinogen framework is highly flexible and can take on a number of conformations. Hydrogen bonding interactions to propionic acid side chains have a significant influence on the preferred conformations of these species, although this is overwhelmed by interactions with water molecules for solvated porphyrinogen[51].

On the basis of the potential suitability of Dreiding above described, here it has been applied for the simulation of DNA base-pairing.

Table 2. XYZ dimensions values of the computational box.

	x-axis nm	*y*-axis nm	π mN/m	A_{NL} nm^2
Absence	3.0	2.2	5	1.65
	2.14	1.53	30	0.82
Presence	2.42	1.82	5	1.10
	1.8	1.12	30	0.5

Each box was built incorporating 4 nucleolipid (CDP-DG (NL)) units per leaflets. The dimensions along the x- and y-axis depend on simulated surface pressures (5 and 30 mN/m). The dimensions obtained both in presence and absence of guanine are shown in Table 2. Snapshots of the system at low surface pressure have been depicted in SI5: in absence (SI5A) and in presence (SI5B) of guanine.

As above described, the nucleolipid isotherms at the air-water interface, in the absence or presence of the guanine at the aqueous subphase, show significant

differences. Briefly, those differences due to the presence of guanine are fundamentally three: (1) large reduction of the surface area per nucleolipid molecule;(2) decrease of the surface pressure at which the phase transition occurs, that is, 30 mN/m in the absence whilst 5 mN/m in the presence of guanine; and (3) drop of the collapse surface pressure.

The MD simulations show that at low surface pressure (5 mN/m), and in absence of guanine, the cytosine group is folded, so that its plane is located almost parallel to the interface. However, in presence of guanine, the polar group of the nucleolipid molecules at the matrix in the interface modify its conformation extending into the aqueous subphase, as a result of the formation of hydrogen bonds between cytosine and guanine. This phenomenon explains accordingly the contraction of the nucleolipid isotherm in guanine presence with respect to that measured in absence of the purine base, see Fig. 1.

Also, at high surface pressure, a surface area reduction is appreciated. Thus, at 30 mN/m, the surface area per CDP-DG molecule in guanine absence is ∼0.8 nm^2, while in guanine presence is approx. 0.5 nm^2. The MD simulation indicates that the nucleolipid undergoes a conformational change as a consequence of the formation of hydrogen bonds between cytosine and guanine, see Fig. 6. However, such shrinkage of the surface area cannot be explained because exclusively on the conformation change: strong repulsion between negatively charged phosphate groups of the NL units can be expected. The analysis of the results obtained by MD simulation shows that the units of guanine and cytosine are separately stacked at distances of the order of 0.33 nm, see Fig. 6. Thus, the stacking occurs not only between guanidine groups, but also between the cytosine groups belonging to the polar group of the nucleolipid molecules. The pi–stacking (also called π–π stacking) is a noncovalent attractive interaction between aromatic rings. This stacking not only stabilizes the monolayer, but also favors its contraction and partially compensates the repulsion energy between phosphate groups.

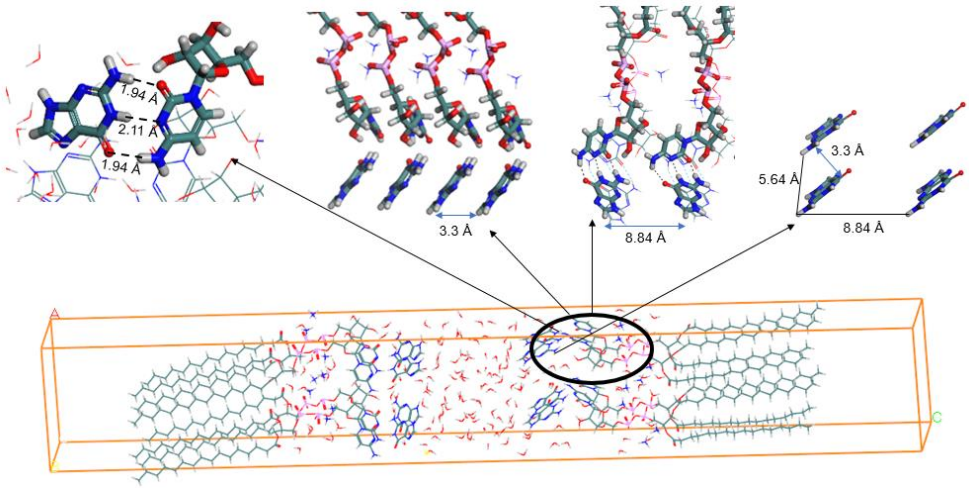

Fig. 6. MD simulation of the system CDP-DG in presence of guanine: (a) full system; (b) Hydrogen bond formation between guanine and cytosine groups; (c) lateral view of the periodic system; (d) frontal view of the periodic system; (e) view of the molecular organization of a system formed only by guanine molecules.

Furthermore, this strong stacking should be the reason for the decrease of the surface pressure at which the phase transition occurs when guanine is present in the aqueous subphase (~5 mN/m), compared to that registered in its absence (~30 mN/m).

As discussed above, the third effect of the guanine presence on the CDP-DG isotherm, see Fig. 1, is the drop of the collapse pressure. In previous works[52,53], it has been observed that certain well-organized monolayers may collapse toward trilayers where first and third monolayers organize the polar headgroups pointing to the aqueous subphase, whereas the intermediate layer displays the polar headgroups pointing to the air. In such a way, the polar groups of the monolayers further away from the water must be in contact. Those type of trilayers are stabilized by the strong attractive interactions between the head groups in contact[53]. Therefore, in the present work as previously described, the collapse of the CDP-DG isotherm may be favored by attractive interactions like stacking-type interactions between the guanine molecules of the alternating layers, see Fig. 6.

Dilution of CDP-DG monolayer by fabrication of mixed CDP-DG:DMPA films at the air-water interface. The combination of nucleic acid derivatives with lipids renders hybrid materials with interesting applications and can confers properties of interest to the system, like biocompatibility, biodegradability, etc. Also, to make easy the handling with synthetic amphiphilic nucleolipids, a dilution of the cytosine-based nucleolipid monolayer with a lipid is considered. Therefore, to organize the CDP-DG molecules in a lipid environment approaching to a membrane arrangement, the nucleolipid was mixed with DMPA phospholipid.

Previously, as reference, π–A isotherms of DMPA Langmuir films were prepared on different subphases: on pure water, basic subphase in absence and presence of guanine, and basic subphase with adenine (SI6). The results note differences between neutral or basic subphases, an expansion of the isotherms at low surface pressure upto reaching the phase transition at *ca.* 35 mN/m and shrinkage after the phase transition. Further, such effect is not related to the presence of the nitrogenous bases in the basic subphases, it seems to be related only with the increases of pH.

Simultaneously to the isotherms, BAM images were taken during the compression process (SI7). The morphological features of DMPA monolayer on the different basic subphases pH 11 in absence and presence of guanine 10^{-4} M are clearly different of the corresponding for DMPA on pure water[54]. The images show the effect on the domain formation under compression of the monolayer: in presence of guanine, the domains significantly reduce their size to form small dots and the anisotropy detected in the leave like domains typical of DMPA on water subphase disappears.

Following, mixed DMPA:CDP-DG films were prepared on different molar ratios (1:0, 5:1, 2:1, 1:1, 1:2 and 0:1). As an example, Fig. 7 shows the variation of π–A isotherms due to the dilution effect of DMPA molecules in the mixed DMPA:CDP-DG 1:1 monolayer fabricated at air/water interface with basic subphases in absence of purine derivatives (black line), as reference, and in presence of guanine 10^{-4} M (red line) and adenine 10^{-4} M (blue line). Furthermore, the selectivity interaction between nitrogeous pair bases in the mixed monolayer was also explored. The results

clearly demonstrate the specificity between nucleic bases in spite of the dilution of the nucleolipid monolayer with phospholipid molecules. Details of the π–A isotherms recorded on basic subphases in absence and presence of guanine 10^{-4} M, as well as the morphological characteristics are shown in SI8-SI10. The π–A isotherms were repeated at least three times and good reproducibility was obtained. From the isotherms shown in SI8-SI10 can note that the dilution of CDP-DG with DMPA is better when the nucleolipid concentration is higher.

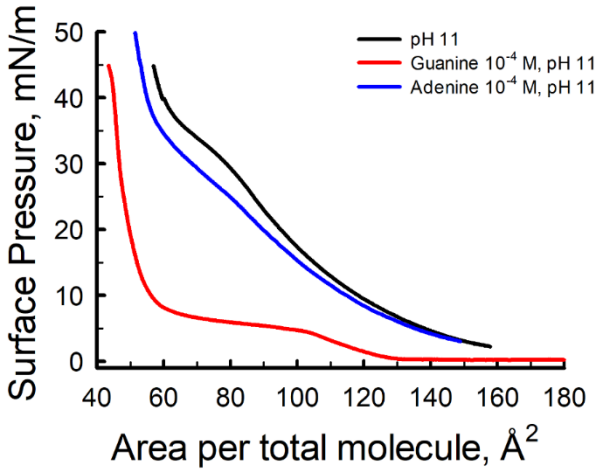

Figure 7. *π–A* isotherms of a mixed DMPA:CDP-DG 1:1 monolayer fabricated at air/water interface with basic subphases in absence of purine derivatives (black line), as reference, and in presence of Guanine 10^{-4} M (red line) and Adenine 10^{-4} M (blue line).

An understanding of the interaction between CDP-DG and DMPA is provided by means of a miscibility study. The nature of the miscibility can be investigated from the variation of mean molecular area, A_m, versus surface pressure, $A_m(\pi) = X_1A_1(\pi) + X_2A_2(p)$, Eq. (1), where A_i is the molecular area of the pure component *i* film at the relevant surface pressure and X_i is the molar fraction of the component *i* in the mixed film.

Coincident areas would correspond to a situation in which a pure DMPA monolayer coexists with the equimolecular mixed film at the air–water interface. Obviously, deviations from the additivity rule in the isotherms suggest that the

molecules are differently arranged along that pressures range. Deviations from the additivity rule are expected as a result of special molecular organization characteristics such as filling of the empty space by one component or changes in molecular packing as a result of interlocking of the different components. The size of the deviation, the form of the curves, and the mole fraction for which the maximum deviation occurs will depend strongly on the amphiphilic nature of the two components in the mixed layer[55-57].

The comparison between the experimental molecular areas (symbols) with the mean molecular areas, calculated by Eq. (1), at different surface pressures is shown in Fig. 8, in which it can be seen clearly that the mixed monolayers, in absence of guanine, do not follow the additivity rule. Miscibility results show a positive deviation behaviour over the ideality in basic subphase. The experimental molecular areas in all cases are larger than the corresponding calculated isotherm. Furthermore, the positive deviation from the additivity rule depends on the molar fraction of the CDP-DG in the mixture, becoming larger as the density of cytosine-based nucleolipid in the mixed film decreases.

As the mixed film is compressed, the distance between molecules in the monolayer decreases and their hydrophobic interactions increases. Consequently, the mixture of CDP-DG and DMPA exhibits a positive deviation from the additivity rule. When the mixed film is compressed further, those interactions become so strong that the amphiphilic molecules become less compatible and different regions can be formed, as detected in BAM images (SI10a).

Surprisingly, such phenomenon does not occurr when guanine is present in the basic subphase: as a funtion of the surface pressure, the deviation of the mixed monolayer with respect to the additivity rule is slightly negative at low surface pressure, almost coincident at intermediate surface pressures, and slightly positive at high π. This behaviour is in good agreement with the BAM images shown in SI10b. With guanine the molecular organization of the mixed film is because a hypothetical situation of two coexisting immiscible monolayers.

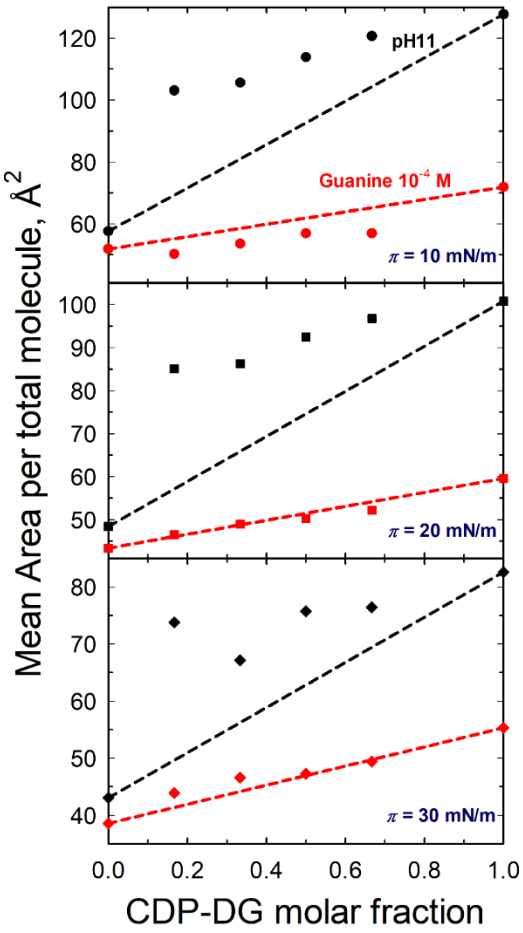

Fig. 8. Plots of area per molecule and deviations of ideal behaviour (lines) of a mixed DMPA:CDG-DP 1:1 film formed on basic subphase pH 11 in presence (red) and absence (black) of Guanine at 10 (circles), 20 (squares) and 30 mN/m (diamonds).

Conclusions

In this work, monolayers of a hybrid cytosine-based nucleolipid, CDP-DG, at basic subphase have been prepared at the air-water interface both in absence and presence of guanine by mechanical stimulus. The π–A isotherms and successive compression-expansion cycles highlight different organization of the CDP-DG in presence of guanine as a function of the surface pressure during the mechanical stimulus, that is, below or above phase transition. Differences were also directly

observed by BAM. Furthermore, PM-IRRAS spectra of Langmuir-Schaefer CDP-DG monolayers suggest a reorganization and/or orientation change of the cytosine ring group in the nucleolipid molecule probably due to the formation of hydrogen bonds with the guanine molecules in the subphase. These results also evidence the strong interaction between the ring groups of the cytosine and guanine par. Finally, computer simulations show how as a function of the surface pressure, in absence of guanine, the cytosine group is folded, so that its plane is located almost parallel to the interface. However, in presence of guanine, the polar group of the nucleolipid molecules at the matrix in the interface modify its conformation extending into the aqueous subphase, because of the formation of hydrogen bonds between cytosine and guanine.

The present work presents an approach combining experimental with molecular dynamics (MD) simulation techniques, that with respect to previous research, this approach allows to describe in more detail the molecular recognition between cytosine and guanine molecules in an architecture prepared at the air–water interface by using a novel chemical system.

Just like that, by combining surface experimental techniques, *i.e*., surface pressure (π) – area (A) isotherms, Brewster angle microscopy (BAM), infrared spectroscopy (PM-IRRAS) with computer simulations, not only the formation of the complementary base pairing (cytosine-guanine) established mainly by hydrogen bonds, is demonstrated, but also is provided the folding of the cytosine-based nucleolipid molecules in the monolayer is forced to change its orientation during the compression process and the guanine recognition in the basic subphase. Moreover, that change orientation is reversible during several compression-expansion processes under set experimental conditions.

Furthermore, the specific interaction between nitrogenous bases has been also demonstrated along the study of the CDP-DG monolayer fabricated at the air-water interface. Finally, the dilution of the cytosine-based nucleolipid monolayer with DMPA has resulted in mixed monolayers where a slight segregation between two molecules has been inferred by the additivity rule.

From what is reported, this approach can inspire the study of recognition in more complex 3D systems like bilayers, liposomes, QCM, etc.

References and Notes

1. L. Liu, D. Xia, L.H. Klausen, M. Dong, *Int. J. Mol. Sci*. **2014**, 15, 1901–1914.
2. C. Avitabile, C. Diaferia, B. Della Ventura, F.A. Mercurio, M. Leone, V. Roviello, *et al*., *Chem. - A Eur. J.* **2018**, 24, 4729–4735.
3. G. Zhu, Y. Xu, X. Cen, K.S. Nandakumar, S. Liu, K. Cheng, *Eur. J. Med. Chem.* **2018**, 144, 82–92.
4. X. Shen, D.R. Corey, *Nucleic Acids Res.* **2018**, 46, 1584–1600.
5. J. Baillet, V. Desvergnes, A. Hamoud, L. Latxague, P. Barthélémy, *Adv. Mater*. **2018**, 30, 1–24.
6. M. Angelerou, P.W.J.M. Frederix, M. Wallace, B. Yang, A. Rodger, D.J. Adams, *et al*., *Langmuir*. **2018**, 34, 6912–6921.
7. M. Ramani, T.D.T. Nguyen, S. Aryal, K.C. Ghosh, R.K. Delong, *J. Phys. Chem. C*. **2017**, 121, 15702–15710.
8. J. Willem de Vries, S. Schnichels, J. Hurst, L. Strudel, A. Gruszka, M. Kwak, *et al*., *Biomaterials*. **2018**, 157, 98–106.
9. A.P. Davis, *Nature*. **2010**, 464, 169–170.
10. H.R. Marsden, A. Kros, *Angew. Chemie - Int. Ed.* **2010**, 49, 2988–3005.
11. V. Amendola, G. Bergamaschi, A. Buttafava, L. Fabbrizzi, E. Monzani, *J. Am. Chem. Soc*. **2010**, 132, 147–156.
12. R.M. Leblanc, *Curr. Opin. Chem. Biol.* **2006**, 10, 529–536.
13. K. Ariga, T. Nakanishi, J.P. Hill, *Soft Matter*. **2006**, 2, 465–477.
14. K. Ariga, T. Michinobu, T. Nakanishi, J.P. Hill, *Colloid Interface Sci.* **2008**, 13, 23–30.
15. T. Mori, K. Okamoto, H. Endo, J.P. Hill, S. Shinoda, M. Matsukura, *et al.*, *J. Am. Chem. Soc*. **2010**, 132, 12868–12870.
16. H. Kitano, H. Ringsdorf, *Bull. Chem. Soc. Jpn*. **1985**, 58, 2826–2828.
17. D. Berti, C. Montis, P. Baglioni, *Soft Matter*. **2011**, 7, 7150–7158.
18. H. Rosemeyer, Chem. Biodivers. **2005**, 2, 977–1062.
19. C. Montis, Y. Gerelli, G. Fragneto, T. Nylander, P. Baglioni, D. Berti, *Colloids Surfaces B Biointerfaces*. **2016**, 137, 203–213.

20.M. Ahlers, H. Ringsdorf, H. Rosemeyer, F. Seela, *Colloid Polym. Sci.* **1990**, 268, 132–142.

21.J. Huang, Y. Liang, *Thin Solid Films*. **1998**, 326, 217–222.

22.C. Li, J. Huang, Y. Liang, *Langmuir*. **2001**, 17, 2228–2234.

23.T. Kondo, K. Ota, Y. Matsushita, R. Kimura, T. Kawai, *Colloids Surfaces A Physicochem. Eng. Asp.* **2006**, 273, 101–108.

24.X. Mulet, T. Kaasgaard, C.E. Conn, L.J. Waddington, D.F. Kennedy, A. Weerawardena, *et al*., *Langmuir*. **2010**, 26, 18415–18423.

25.B. Desbat, N. Arazam, S. Khiati, G. Tonelli, W. Neri, P. Barthélémy, *et al*., *Langmuir*. **2012**, 28, 6816–6825.

26.Y. Xin, X. Kong, X. Zhang, Z. Lv, X. Du, *Langmuir*. **2012**, 28, 11153–11163.

27.W. Lee, S. Matsika, *ChemPhysChem.* **2018**, 19, 1568–1571.

28.M. Kanduč, A. Schlaich, A.H. De Vries, J. Jouhet, E. Maréchal, B. Demé, *et al*., *Nat. Commun.* **2017**, 8.

29.M.N. Islam, Y. Ren, T. Kato, *Langmuir*. **2002**, 18, 9422–9428.

30.W.P. Ulrich, H. Vogel, *Biophys. J.* **1999**, 76, 1639–1647.

31.J. Saccani, S. Castano, F. Beaurain, M. Laguerre, B. Desbat, *Langmuir*. **2004**, 20, 9190–9197.

32.T.M. Nobre, F.J. Pavinatto, L. Caseli, A. Barros-Timmons, P. Dynarowicz-Łatka, O.N. Oliveira, *Thin Solid Films.* **2015**, 593, 158–188.

33.E.M. Adams, C.B. Casper, H.C. Allen, *J. Colloid Interface Sci.* **2016**, 478, 353–364.

34.J.C. Rodrigues, L. Caseli, *Thin Solid Films.* **2017**, 622, 95–103.

35.R. Wang, Y. Guo, H. Liu, Y. Chen, Y. Shang, H. Liu, *J. Colloid Interface Sci.* **2018**, 519, 186–193.

36.R. Marques De Oliveira, J. Ferreira, M.J.L. Santos, R.M. Faria, O.N. Oliveira, *ChemPhysChem.* **2011**, 12, 1736–1740.

37.R. Johann, D. Vollhardt, H. Möhwald, *Colloids Surfaces A Physicochem. Eng. Asp.* **2001**, 182, 311–320.

38.Y. Wang, X. Du, W. Miao, Y. Liang, *J. Phys. Chem. B.* **2006**, 110, 4914–4923.

39. R.M. Silverstein, F.X. Webster, D.J. Kiemle, D.L. Bryce, *Spectrometric Identification of Organic Compounds, 8th ed.,* John Wiley & Sons, New York, 2014.
40. R.G. Snyder, H.L. Strauss, C.A. Elliger, *J. Phys. Chem.* **1982**, 86, 5145–5150.
41. M.D. Porter, T.B. Bright, D.L. Aliara, C.E.D. Chidsey, *Chinese J. Oncol.* **1987**, 109, 3559–3568.
42. Y.T. Tao, *J. Am. Chem. Soc.* **1993**, 115, 4350–4358.
43. H. Byrd, S. Whipps, J.K. Pike, J. Ma, S.E. Nagler, D.R. Talham, *J. Am. Chem. Soc*. **1994**, 116, 295–301.
44. J. Fernández, J.J. Ruiz, L. Camacho, M.T. Martin, E. Muñoz, *J. Phys. Chem. B.* **2000**, 104, 5573–5578.
45. P. Lozano, A.J. Fernández, J.J. Ruiz, L. Camacho, M.T. Martín, E. Muñoz, *J. Phys. Chem. B.* **2002**, 106, 6507–6514.
46. W. Miao, X. Du, Y. Liang, *Langmuir.* **2003**, 19, 5389–5396.
47. S.L. Mayo, B.D. Olafson, W.A. Goddard, *J. Phys. Chem*. **1990**, 94, 8897–8909.
48. S. Vlachakis, Dimitrios; Bencurova, Elena; Papangelopoulos, Nikitas; Kossida, *Adv. Protein Chem. Struct. Biol.*, Elsevier, **2014**: pp. 269–313.
49. M. Edelwirth, J. Freund, S.J. Sowerby, W.M. Heckl, *Surf. Sci.* **1998**, 417, 201–209.
50. K. Sfyrakis, A. Provata, D.C. Povey, B.J. Howlin, *J Mol Model.* **2004**, 10, 185–197.
51. J. He, T. a. Kaprak, M. a. Jones, T.D. Lash, *J. Porphyr. Phthalocyanines*. **2005**, 9, 170–185.
52. M. Pérez-Morales, J.M. Pedrosa, M.T. Martín-Romero, D. Möbius, L. Camacho, T. Martín-Romero, *et al*., *J. Phys. Chem. B.* **2004**, 108, 4457–4465.
53. C. Rubia-Payá, E. Jimenez-Millán, J.J. Giner-Casares, G. Brezesinski, M.T. Martín-Romero, L. Camacho, *Langmuir.* **2013**, 29, 4796–4805.
54. H. Mohwald, *Annu. Rev. Phys. Chem*. **1990**, 41, 441–476.
55. G. De Miguel, M.T. Martín-Romero, J.M. Pedrosa, E. Muñoz, M. Pérez-Morales, T.H. Richardson, *et al*., *J. Mater. Chem*. **2007**, 17, 2914–2920.

56.J.J. Giner-Casares, M. Pérez-Morales, H.J. Bolink, E. Muñoz, G. de Miguel, M.T. Martín-Romero, *et al*., *J. Colloid Interface Sci.* **2007**, 315, 278–286.

57.J.J. Giner-Casares, M. Pérez-Morales, H.J. Bolink, N. Lardiés, E. Muñoz, G. De Miguel, *et al*., *J. Mater. Chem.*, **2008**, 18, 1681–1688.

Supporting Information

SI1. Morphological characteristics of the CDP-DG film on basic subphase pH 11 in presence of guanine 10^{-4} M during the first compression process up to the collapse (recording simultaneously with isotherms in Figure 3, 1c): from 0.4 mN/m and 137.3 $Å^2$/CDP-DG molecule, to 3 mN/m and 100 $Å^2$/CDP-DG molecule (first line); from 3.5 mN/m and 81 $Å^2$/CDP-DG molecule up to 30 mN/m and 38.2 $Å^2$/CDP-DG molecule (second line).

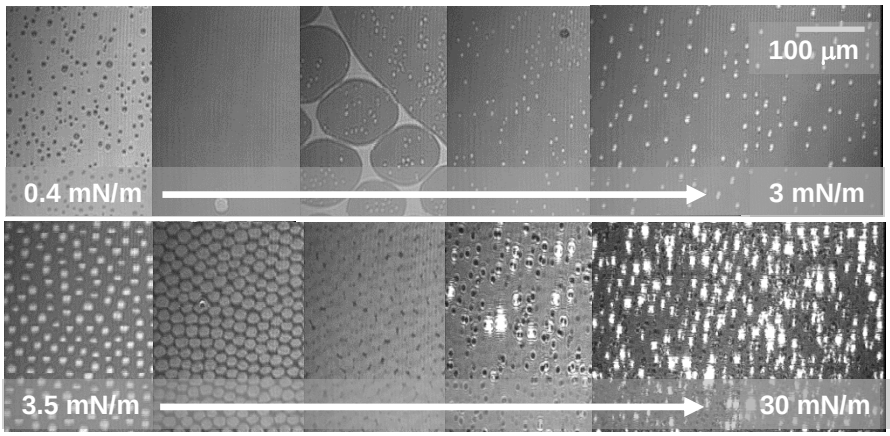

SI2. Morphological features of the CDP-DG film on basic subphase pH 11 in presence of guanine 10^{-4} M during the compression-expansion cycle to the molecular area before collapse (corresponding to the experience designed for Figure 4, bounded compression-expansion cycles). Image size: 430 μm width.

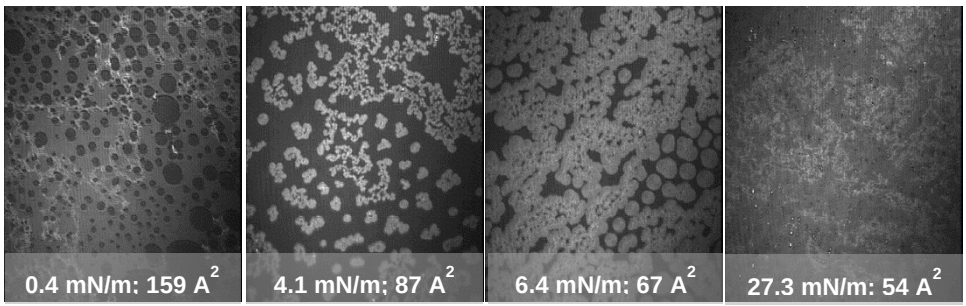

SI3. Interactions between the nucleolipid monolayer and the guanine dissolved in the subphase can be proved on LS films once the modified substrate is rinsing with pure water to remove the large bands corresponding to water/NaOH absorption in the low wavenumber region. SI3 figure shows PM-IRRAS signal of 10 Langmuir-Schaefer CDP-DG/Guanine films prepared at air-water interface, pH 11: unwashed (black line), washed onece (red line) and washed twice (blue line) protocol.

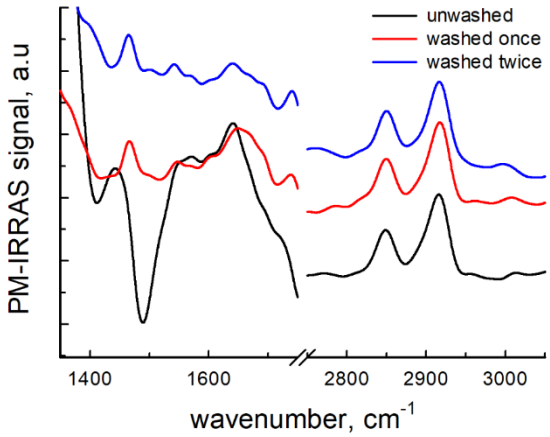

SI4. The different intensity of the tension vibrations of the methylene group of LS CDP-DG films in absence and presence of guanine depends on the orientation of the alkyl chains with respect to the glass substrate and should be mainly attributed to the surface concentration rather than to the molecular orientation. This attribution is proven by normalized the PM-IRRAS signal as shown in SI4 figure.

7

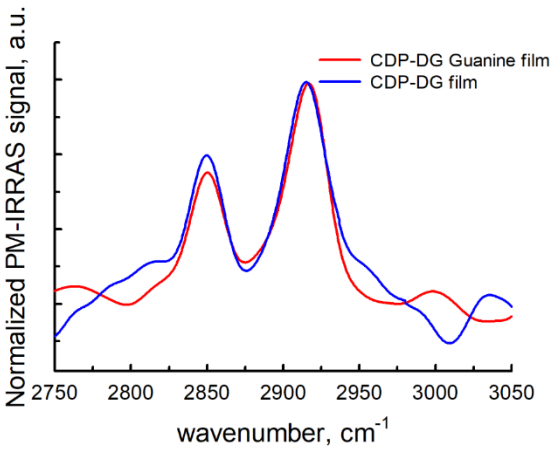

SI5. Snapshots of the system for low surface pressure in: absence (A) and presence (B) of guanine.

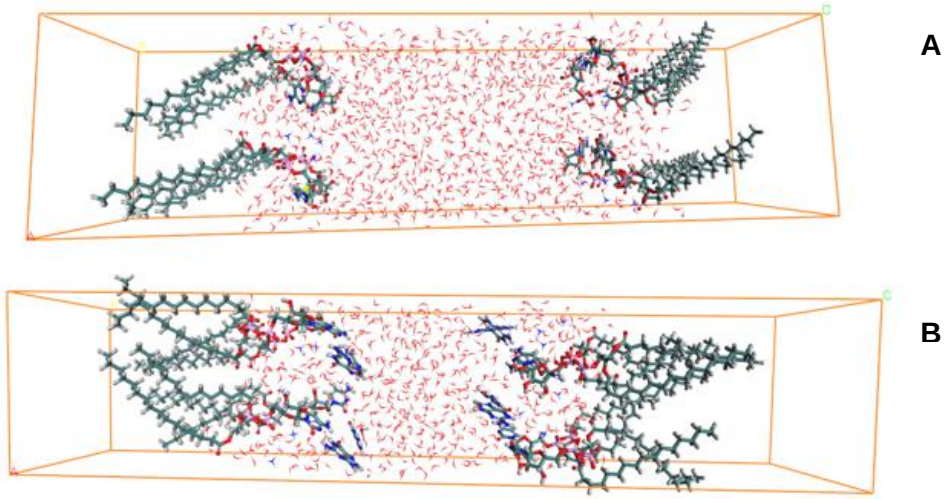

SI6. *π*–*A* isotherms of DMPA Langmuir films prepared on different subphase: pure water (black line); basic subphase pH 11: pure (red line), with guanine 10-4 M (green line), and with adenine 10-4 M (blue line).

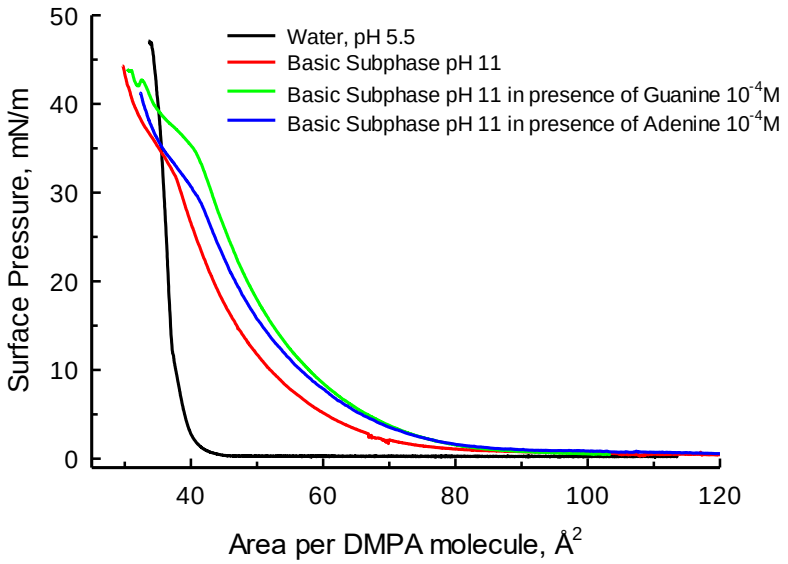

Study

of the effect of basic pH on DMPA monolayer: expansion reaching the phase transition at *ca.* 35 mN/m and shrinkage after the phase transition. The effect is not related to the presence of the nitrogenous bases in the basic subhases, it seems to be related only to the increasing of pH.

SI7. BAM images of DMPA monolayers organized on different basic subphases pH 11: (a) in absence of guanine; (b) in presence of guanine 10^{-4} M. Image size: 430 μm width.

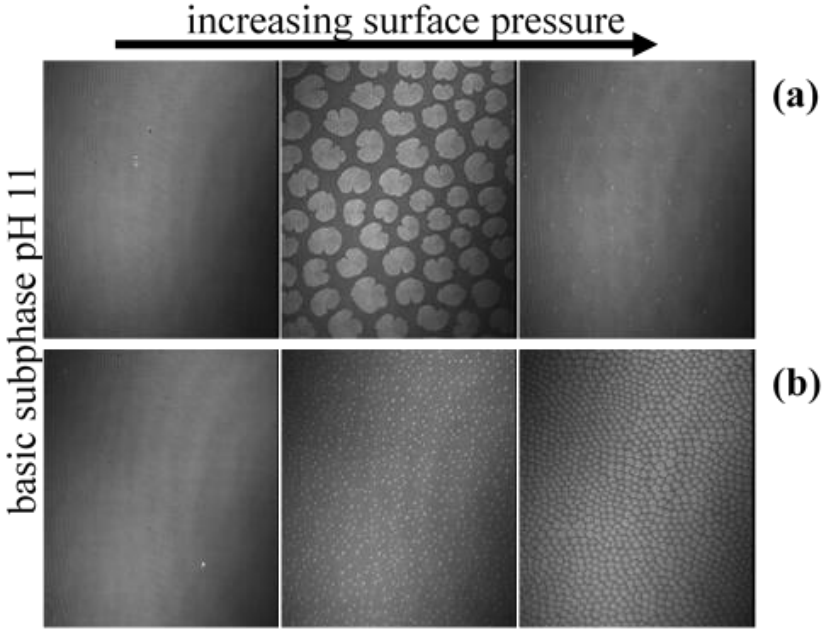

The morphological features of DMPA monolayer on the different basic subphases pH 11 in absence and presence of guanine 10^{-4} M (DMPA images on water has been previously published, Möhwald H. *Annu. Rev. Phys. Chem.* 1990, 41, 441) was monitoring by BAM. The images show a clear effect on the domain formation under compression of the monolayer: in presence of guanine, the domains significantly reduce their size to form small dots and the anisotropy detected in the leave like domains disappear.

SI8. Surface Pressure-Area isotherms of mixed DMPA:CDP-DG monolayers at various molar ratios prepared at air/water interface on basic subphase pH 11 in absence of guanine.

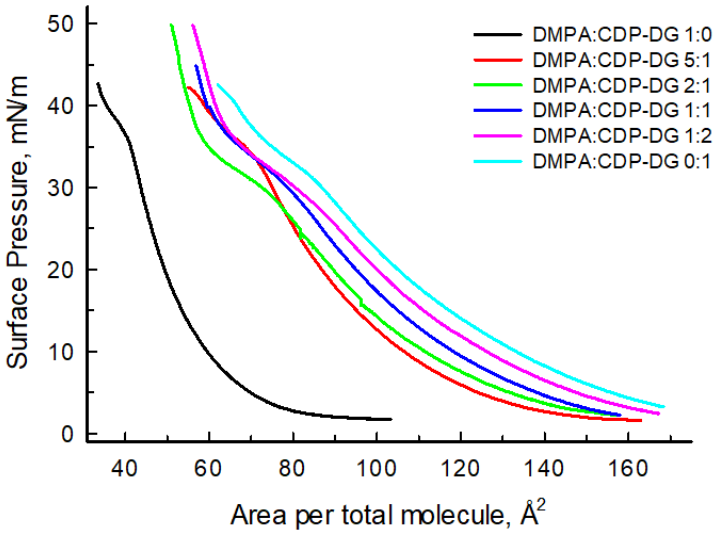

Examination of the effect of the molar ratio on the mixed monolayers registering the corresponding π—A isotherms: as increases the molar ratio of the nucleolipid in the mixture, increases the shift of the isotherm to higher area per molecule.

SI9. Surface Pressure-Area isotherms of mixed DMPA:CDP-DG monolayer at various molar ratios built at air/water interface on basic subphase pH and containing Guanine 10^{-4} M.

As in S6, the examination the effect of the molar ratio on the mixed monolayers registering the corresponding π–A isotherms in presence of guanine was done: the isotherms of the different mixtures show an intermediate behaviour with respect to the pure monolayers of DMPA and CDP-DG.

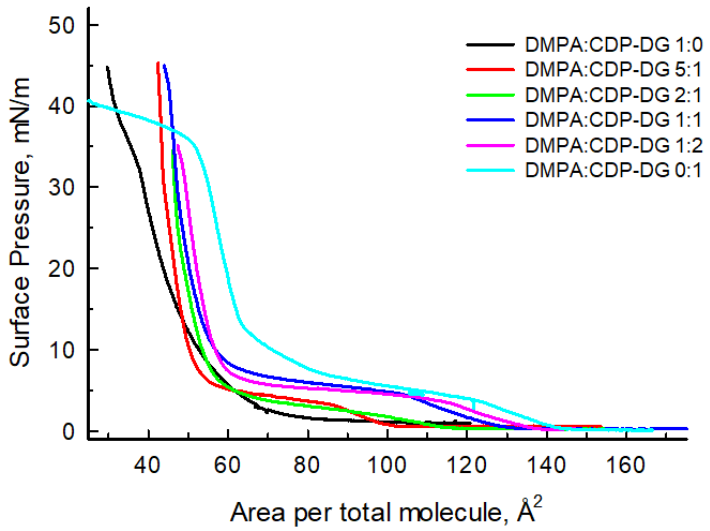

SI10. BAM images of mixed DMPA:CDP-DG 1:1 monolayers organized on different basic subphases pH 11: (a) in absence of guanine; (b) in presence of guanine 10^{-4} M. Image size: 430 μm width.

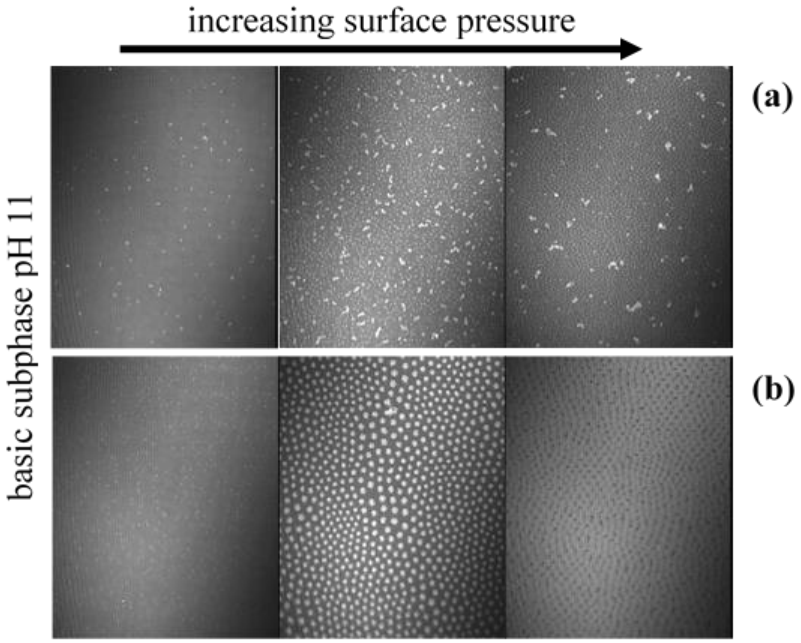

The morphological characteristics of the mixed DMPA:CDP-DG 1:1 monolayer on the different basic subphases pH 11 in absence (a) and presence (b) of guanine 10^{-4} M was recordered by BAM simultaneously to the surface pressure-area isotherms (Fig. 7 in the main body of the manuscript). Once more, the images show the influence of the cytosine-guanine interaction to the domain formation through the compression process.

Conclusiones

Conclusions

CONCLUSIONES

Al final de cada artículo detallados en el capítulo III de esta Memoria, se incluye un conjunto de conclusiones particulares al estudio desarrollado. En este apartado se presentan las conclusiones generales de toda la investigación realizada. Los resultados presentados a lo largo de esta Memoria contribuyen a la compresión de la formación y comportamiento de películas delgadas y abre nuevas perspectivas a futuras aplicaciones potenciales que exploten la funcionalidad de dichas películas, y establece el potencial uso de la técnica de Langmuir, Langmuir-Blodgett, Langmuir-Schaefer, así como diversas técnicas ópticas, como métodos de caracterización de dichos ensamblajes. En particular:

1. Se han establecido, por primera vez, las estructuras supramoleculares de diversos Fmoc-dipeptidos en sistemas 2D mediante auto-ensamblaje. Experimentalmente, se ha observado la relevancia del coeficiente de reparto, como magnitud macroscópica simple, que permite predecir sus propiedades en la interfase aire-agua.
2. Se ha comprobado el efecto de la secuencia y la estructura química de los distintos aminoácidos que forman los Fmoc-dipeptidos a la hora de interaccionar con una membrana modelo, y el efecto de la hidrofobicidad de éstos en dicha interacción.
3. Se ha demostrado el aumento de interacción entre quantum dots y membranas biológicas con el uso de ligandos fluorinados. Este aumento de la actividad en su superficie mediante interacciones hidrofóbicas facilita la internalización celular de los mismos.
4. Se ha constatado la interacción entre la citosina, presente en la cabeza polar de nuestro nucleolípido, y la guanina existente en el medio acuoso. Es más, se ha podido observar el efecto de este reconocimiento molecular en la orientación de la cabeza polar y como afecta al empaquetamiento del sistema. Finalmente, se ha aplicado positivamente a sistemas mixtos con fosfolípidos.

CONCLUSIONS

At the end of each article presented in this Thesis, Chapter III, there is a conclusion relevant to the work described in it. In this section, a summary of the more general conclusions related to the studies carried out is presented. All the results presented throughout this Thesis contribute to the understanding of the formation and behaviour of thin films and open new routes for their potential application in numerous systems due to their usefulness. Also, techniques like Langmuir, Langmuir-Blodgett, Langmuir-Schaefer as well as several optics techniques allow the characterization of the studied systems. Specifically:

1. For first time it has been stablished the supramolecular structure of diverse auto-assembled Fmoc-dipeptides in 2D systems. Furthermore, it has been observed experimentally the relevance of the partition coefficient as a simple macroscopic magnitude to predict their properties at the air-water interface.
2. It has been verified the effect of the sequence and the chemistry structure of the aminoacids that form the Fmoc-dipeptides in their interaction processes with a cellular model membrane alike the effect of their hydrophobicity in the interaction.
3. It has been demonstrated the increase in the interaction between quantum dots and biological membranes as a result of the use of fluorinated ligands. This rise in their surface activity, because of hydrophobic interactions, facilitate their cellular internalization.
4. It has been confirmed the interaction between the cytosine, presented in the polar head group of our nucleolipid, with the guanine existent in the aqueous subphase. Moreover, it has been observed of the effect of this recognition in the orientation of the polar head in the nucleolipid as well as the aftereffect in the system packaging. At last, these interactions have been applied positively in mixed systems with phospholipid molecules.

Apéndice

Appendix

- **Publicaciones derivadas directamente de la Tesis:**

– "*Unravelling the 2D self-assembly of Fmoc-dipeptides at fluid interfaces"* by Pablo G. Argudo, Rafael Contreras-Montoya, Luis Álvarez de Cienfuegos, Juan M. Cuerva, Manuel Cano, David Alba-Molina, María T. Martín-Romero, Luis Camacho and Juan J. Giner-Casares, *Soft Matter* **2018**, 14, 9343-9350.
JCR Impact Factor
Impact factor (2017): 3.709
Category: Materials Science, Multidisciplinary
Quartile (2017): 1

– "*Optimization of Amino Acid Sequence of Fmoc-Dipeptides for Interaction with Lipid Membranes"* by Pablo G. Argudo, Rafael Contreras-Montoya, Luis Álvarez de Cienfuegos, María T. Martín-Romero, Luis Camacho and Juan J. Giner-Casares, *J. Phys Chem. B* **2019**, 123, 3721-3730.
JCR Impact Factor
Impact factor (2017): 3.146
Category: Chemistry, Physical
Quartile (2017): 2

– "*Surface-active fluorinated quantum dots for enhanced cellular uptake*" by Pablo G. Argudo, Mónica Carril, María T. Martín-Romero, Juan J. Giner-Casares and Carolina Carrillo-Carrión, *Chem. Eur. J.* **2019**, 25, 195-199.
JCR Impact Factor
Impact factor (2017): 5.160
Category: Chemistry, Multidisciplinary
Quartile (2017): 1

– "*Fluorinated CdSe/ZnS quantum dots: Interactions with cell membrane*" by Pablo G. Argudo, María T. Martín-Romero, Luis Camacho, Mónica Carril, Carolina Carrillo-Carrión and Juan J. Giner-Casares, *Coll. And Surf. B* **2019**, 173, 148-154.
JCR Impact Factor
Impact factor (2017): 3.997
Category: Biophysics
Quartile (2017): 1

– "*Folding of cytosine-based nucleolipid monolayer by guanine recognition at the air-water interface*" by Pablo G. Argudo, Eulogia Muñoz, Juan J. Giner-Casares, María T. Martín-Romero and Luis Camacho, *Coll. And Int. Sci* **2019**, 537, 694-703.
JCR Impact Factor
Impact factor (2017): 5.091
Category: Chemistry, Physical
Quartile (2017): 1

submitted

- **Derivado de las publicaciones:**

– Back Cover: *Soft Matter*, Issue 46, 2018: "*Unravelling the 2D self-assembly of Fmoc-dipeptides at fluid interfaces"*

- **Becas y ayudas competitivas:**

– Beca de movilidad internacional "Doctorado Internacional hacia la excelencia" curso 2017/2018.

- **Comunicaciones orales y poster en congresos:**

– NanoUCO VI: "Monocapas mixtas de nucleolípido para reconocimiento de guanina en la interfase aire-agua", Córdoba (España), enero **2017**.

– VII Iberian Meeting on Colloids and Interfaces: "Phospholipid/nucleolipid mixed films for Guanine recognition at the air-water interface", Madrid (España), julio **2017**.

– 15th European Conference on Organized Films: "Interfacial self-assembly of dipeptides" & "Phospolipid/nucleolipid mixed films for guanine recognition at the air-water interface", Dresden (Alemania), julio **2017**.

– VI Congreso Científico de Investigadores en Formación de la UCO: "Folding of cytosine nucleolipid matrix by guanine recognition at the air-water interface", Córdoba (España), enero **2018**.

– Reunión de Jóvenes Investigadores en Coloides e Interfases IV: "Lipids as matrix for the cytosine-guanine interaction determination at the air-water interface", Córdoba (España), febrero **2018**.

– NanoUCO VII: "Fmoc-dipeptides, self-assembled structure at the air/water interface", Córdoba (España), enero **2019**.

– ESC2019: "A general route established for the 2D self-assembly of Fmoc-dipeptides" Varna (Bulgaria), junio **2019**.

– 16th European Conference on Organized Films: "Increase of the internationalization rate of Quantum Dots by fluorinated organic ligand" & "Promoting the interaction of Fmoc-dipeptides with lipid membranes by the adjustment of the hydrophobicity sequence", Paris (Francia), julio **2019**.

– 8th Iberian Meeting on Colloids and Interfaces: "Fmoc-dipeptides, air-water interface self-assembly and lipid membrane Interactions" Aveiro (Portugal), julio **2019**.